



Technische Universität München

Fakultät für Chemie

Between Metals and Salts:
Experimental and Computational Studies of Polar
Intermetallics, Zintl-Phases and Zintl-Ions

Jasmin Vanessa Dums

Vollständiger Abdruck der von der Fakultät für Chemie der Technischen Universität München zur Erlangung des akademischen Grades einer

Doktorin der Naturwissenschaften (Dr. rer. nat.)

genehmigten Dissertation.

Vorsitzende(r): Prof. Dr. Shigeyoshi Inoue

Prüfer der Dissertation:

1. Prof. Dr. Thomas F. Fässler
2. Prof. Dr. Tom Nilges

Die Dissertation wurde am 30.11.2021 bei der Technischen Universität München eingereicht und durch die Fakultät für Chemie am 08.02.2022 angenommen.

It's the questions we can't answer
that teach us the most.
They teach us how to think.
If you give a man an answer,
all he gains is a little fact.
But give him a question and
he'll look for his own answers.

-Patrick Rothfuss, *The Wise Man's Fear*

DANKSAGUNG

Besonders bedanke ich mich bei meinen Doktorvater

Prof. Dr. Thomas Fässler

für die Aufnahme im Arbeitskreis und für die Möglichkeit an diesem Lehrstuhl promovieren zu dürfen. Vielen Dank für die Möglichkeit ein solch abwechslungsreiches Thema bearbeiten zu dürfen, welches meine Interessen der Festkörperchemie und Theorie vereint.

Ganz besonders bedanke ich mich bei

Prof. Dr. Antti Karttunen.

Es war mir eine Freude nach Helsinki zu kommen und während meiner kompletten Arbeit stets so gut unterstützt zu werden in allen Fragen rund um die Theorie.

Ohne Antti wäre vieles nicht so zustande gekommen.

Vielen Dank auch an **Prof. Dr. Tom Nilges**, welcher im Seminar stets gute Tipps zu meinen Problemstellung gab.

Lieben Dank an **Manuela Donaubauer** für die Unterstützung bei bürokratischen und organisatorischen Belangen.

Meine Büro-Kollegen **Henrik, Stefan, Marina** und **David** möchte ich sehr für das angenehme Arbeitsklima danken und die vielen lustigen Gespräche und tollen Diskussionen. Insbesondere **Henrik**, welcher mir sehr bei experimentellen Fragen weitergeholfen hat.

Zudem vielen Dank an meine Kooperationspartner. Danke an **Nina** und **Ira**, welche mich so wundervoll an der Aalto Universität empfangen haben und mit denen sich eine tolle Freundschaft entwickelt hat denen Ländergrenzen egal sind. Auch dem ganzen **AK Karttunen** und **AK Karppinen** von der Aalto Universtät vielen Dank für das tolle Arbeitsklima und die Auflüge nach Nuuksio. Die Zeit in Helsinki war mit einer der schönsten meiner Promotion.

Danke an meine Kooperationspartner der Universität Cambridge von **AK Grey** für die vielen Messungen an meinen Proben. Ich bin glücklich, dass dabei ein so rundes Thema hervorging.

Meinen Dank gilt auch meinen Praktikanten Auzubildenden **David, Kevin, Michael, Anja, Lukas** und **Celina** für die tolle Unterstützung an meinen Themen.

Maria und **Tassilo** vielen Dank für die ganze EDX und DSC Messungen.

Vielen Dank der **Essensgruppe** und insbesondere **Michi** für die Offenbarung, dass der Campus mehr als nur die Mensa bietet.

Zudem der ganzen Gruppe **AK Fässler** vielen Dank. Es hat mich gefreut mit so vielen tollen Leuten gemeinsam an Projekten zu arbeiten und auch privat das Promotionsleben zu genießen. Danke Manuel, Thomas B., Christian, Christina, Kevin, Michi, David, Alex M., Tassilo, Yasmin, Stefan, Christoph, Thomas W., Done, Bene, Marina, Henrik, Lorenz, Wilhelm, Viktor, Felix, Lavinia, Kerstin, Thomas H., Alex H., Herta und Frau Schier.

Auch der gesamten Gruppe **AK Nilges** vielen Dank, dass ihr mich ab und zu bei euch aufgenommen habt und mich mit Kuchen versorgt habt.

Einen riesen Dank all meine Freunden die mich während dieser Zeit unterstützt haben. Ohne euch und der nötigen Ablenkung hätte ich das nie erreicht. Ganz besonders gilt dabei ein Dank der **Summer Breeze Gruppe**. Unser gemeinsamer Urlaub war stets ein Highlight im Jahr und ich freue mich auf viele weitere. Auch all die Personen die mich nicht nur während der Promotion unterstützt haben, sondern mich durch das Studium begleitet haben. Hierbei besonders der **FSI Chemie und Biochemie** der LMU München vielen Dank. Bei euch habe ich einen Rückzugsort gefunden, stets Rat bekommen zu persönlichen und zum Studium und zuletzt Freunde fürs Leben gefunden. Vielen Dank!

Außerdem gilt eine unglaublich großer Dank meinem Verlobten **Sascha Harm**. Du hast mich während meines kompletten Studiums und der kompletten Promotion unterstützt und den nötigen Rückhalt gegeben. Danke, dass du auch in schwierigen Zeiten bei mir warst und meine Launen ertragen hast. Ich freue mich auf unsere gemeinsame weitere Zeit.

Zuletzt möchte ich mich bei meiner **Familie** bedanken. Ihr habt immer an mich geglaubt und stets ermöglicht meine Träume umzusetzen. Ich kann mich glücklich schätzen euch zu haben und kann definitiv sagen, dass es mir ohne euch nicht möglich gewesen wäre das zu erreichen. Danke **Mama** und **Papa** und meinen Geschwistern **Christian, Benny** und **Melissa**.

List of Abbreviations

AO	Atom orbital
ASSLIB	All solid state Lithium ion battery
CC	Coupled cluster
CI	Configuration interaction
COSMO	Conductor-like screening model
CVE	Cluster valence electrons
DFT	Density functional theory
DOS	Density of States
DSC	Differential Scanning calorimetry
DZ	Double zeta
EDX	Energy dispersive X-ray spectroscopy
ELF	Electron localization function
fcc	face centered cubic
GGA	Generalized gradient approximation
GOF	Goodness of fit
HOMO	Highest occupied molecular orbital
HT	High temperature
IBO	Intrinsic bond orbital
k	klassengleich
KS	Kohn-Sham
LCAO	Linear combination of atomic orbitals
LDA	Local density approximation
LIB	Lithium ion battery
LT	Low temperature
LUMO	Lowest unoccupied molecule orbital
M	Metal
MO	Molecular orbital
NMR	Nuclear magnetic resonance
NPA	Natural population analysis
PCM	Polarizable continuum model
P-XRD	Powder X-ray diffraction
ppm	Parts per million
SC-XRD	Single Crystal X-ray diffraction
SCF	Self-consistent field
SEI	Solid electrolyte interface
S.O.F.	Site occupation factor
SVP	Split valence polarization

t	translationsgleich
TM	Transmission metal
Tt	Tetrel
TZ	Triple zeta
TZVP	Triple zeta valence + polarization
TZVPP	Triple zeta valence with two sets of polarization functions
XRD	X-ray diffraction

Abstract

Intermetallics show a large variety of possible compositions offering interesting chemical and physical properties for different applications such as battery materials. In this work such compounds were investigated by computational and experimental methods. The focus was mainly on typical ZINTL phases, which concept originally only refers to maingroup elements. In the course of the work it was investigated how this concept can be extended to polar intermetallic compounds. In particular, phases with lithium have been studied intensively due to their possible application in lithium-ion batteries. Therefore, structure-property relationships are a great tool to predict properties suitable for specific applications. For example, the very ionic nature of ZINTL phases building networks or layered structures stuffed by Li are promising candidates for Li-ion batteries. The following is a brief overview of the various topics, all based on polar intermetallic phases, which shows the versatility of these compounds.

The focus of this work was on synthesizing new materials by substitution of the Li-Ge and Li-Si binary phase system by transition metals.

In the ternary phase system Li-Ni-Ge two new compounds were found: $\text{Li}_{14}\text{Ni}_{8+x}\text{Ge}_{9-x}$ ($x = 0.3$) and $\text{LiNi}_{1+x}\text{Ge}$ ($x = 0.17$). $\text{Li}_{14}\text{Ni}_{8+x}\text{Ge}_{9-x}$ was first synthesized by Dr. Alexander Henze and further characterized in this work. The structure shows neat intermetallic clusters, which are connected *via* bridging Ge atoms to a three dimensional network offering channels filled by Li atoms. This structure was investigated by computational analysis to understand the nature of the compound and its metallic behavior. Secondly, $\text{LiNi}_{1+x}\text{Ge}$ is a layered structure with intercalated Li atoms. The substitution effect of silver was investigated in this work and three new compounds were obtained: $\beta\text{-Li}_2\text{Ag}_{1-x}\text{Ge}_{1+x}$, $\alpha\text{-Li}_2\text{Ag}_{0.8}\text{Ge}_{1.2}$ and $\gamma\text{-Li}_{2.53}\text{AgGe}_2$. Using group-subgroup relationships a Bärnighausen family tree was derived including also $\alpha\text{-Li}_{2.53}\text{AgGe}_2$ and $\alpha\text{-Li}_2\text{AgGe}$. The compound build a Ag-Ge anionic network similar to the structure of diamond, which channels stuffed by Li ions. The low-temperature phases build huge superstructures with ordered Ag and Ge positions, whereas for the high-temperature phases the positions are mixed. By using computational analysis driving forces to build such superstructures were simplified.

Last, in the Li-Ag-Si phase system the high-temperature phase $\beta\text{-Li}_{13}\text{Ag}_5\text{Ge}_6$ was synthesized. It shows the same structural behavior and motif as the heavier homologous in the Li-Ag-Ge phase system.

Another focus of this work was supporting other experimental work of ZINTL phases and ions with computational analysis. Characterization of the framework compound $\text{Li}_6\text{B}_{18}(\text{Li}_3\text{N})_x$ was done by calculated Raman spectra and additionally, the potential

use as electrolyte was investigated by simulating Li-ion diffusion. A very low energy barrier of about 20 kJ/mol was found. Besides, guest-free Li_6B_{19} and B_4C_2 models were derived and analyzed.

Ternary compounds Li_3AlP_2 , Li_3GaP_2 and Na_7TaP_4 synthesized by Tassilo Restle were investigated by band structure calculations and calculated Raman spectra.

Interestingly, is the influence of solvent molecules on compounds such as KBi. Here a metallization of the compound $\text{KBi}\cdot\text{NH}_3$ was observed and analyzed by computational methods. For various ZINTL ions such as $[\text{SnBi}_3^{5-}]$, clusters of the type $TM@Tt_9$, $[(\text{Ge}_9\{\text{Si}(\text{TMS})_3\}_2)^t\text{Bu}_2\text{P}$, $(\text{Si}/\text{Ge})_9\{\text{Si}(\text{TMS})_3\}_3^-$ and $[\text{Ge}_4\text{HZn}(\text{Ph})_2]^{3-}$ molecular orbital diagrams, charges, Raman spectra, etc. were computed and analyzed showing amazing characteristics like specific vibrations, which led to a nice tool of confirming the presence of endohedrally filled clusters or the presence of a $3c - 2e$ Ge-H-Ge bond.

Zusammenfassung

Intermetallische Verbindungen zeigen eine breite Vielfalt an möglichen Kompositionen, welche interessante chemische und physikalische Eigenschaften aufzeigen. In dieser Arbeit wurden diese Verbindungen theoretisch sowieso experimentell untersucht. Dabei lag ein Fokus vor allem auf typischen ZINTL-Phasen, welches Konzept sich ursprünglich nur auf Hauptgruppenelemente bezieht. Im Zuge der Arbeit wurde untersucht wie sich dieses Konzept auf polare intermetallische Verbindungen erweitern lässt. Insbesondere Phasen mit Lithium wurden intensiv studiert durch deren Anwendungsmöglichkeit in Lithium-Ionen-Batterien. Daher sind Struktur-Eigenschafts-Beziehungen ein gutes Werkzeug, um Eigenschaften vorherzusehen, welche sich für spezifische Anwendungen eignen. Zum Beispiel ist die sehr ionische Natur der ZINTL Phasen, welche mit Li gefüllte Netzwerke oder Schichtstrukturen ausbilden, ein vielversprechender Kandidat für Li-Ionen Batterien. Im Folgenden wird ein kurzer Überblick über die verschiedenen Thematiken alle beruhend auf polaren intermetallischen Phasen gegeben, welches die Vielseitigkeit dieser Verbindungen zeigt.

Der Fokus der Arbeit liegt auf der Synthese neuer Materialien durch Substitution der binären Li-Ge und Li-Si Phasensysteme durch Übergangsmetalle.

Im ternären Phasensystem Li-Ni-Ge konnten zwei neue Verbindungen gefunden werden: $\text{Li}_{14}\text{Ni}_{8+x}\text{Ge}_{9-x}$ ($x = 0.3$) und $\text{LiNi}_{1+x}\text{Ge}$ ($x = 0.17$). $\text{Li}_{14}\text{Ni}_{8+x}\text{Ge}_{9-x}$ wurde zuerst von Dr. Alexander Henze synthetisiert und weiter in dieser Arbeit charakterisiert. Die Struktur zeigt einzigartige intermetallische Cluster, welche verbrückend über Ge Atome miteinander ein dreidimensionales Netzwerk bilden. Dieses ist wiederum mit Li Atomen gefüllt. Diese Struktur wurde mittels quantenchemischer Rechnungen analysiert, um die Natur der Verbindung zu verstehen und dessen metallisches Verhalten. Die Verbindung $\text{LiNi}_{1+x}\text{Ge}$ ist eine schichtartig aufgebaute Struktur mit interkalierten Li Atomen.

Der Substitutionseffekt von Silber wurde in diese Arbeit untersucht und drei neue Verbindungen konnten erhalten werden: $\beta\text{-Li}_2\text{Ag}_{1-x}\text{Ge}_{1+x}$, $\alpha\text{-Li}_2\text{Ag}_{0.8}\text{Ge}_{1.2}$ und $\gamma\text{-Li}_{2.53}\text{AgGe}_2$. Mit Hilfe der Gruppe-Untergruppe Beziehungen wurde ein Bärnighausen Stammbaum hergeleitet, welcher auch die Verbindungen $\alpha\text{-Li}_{2.53}\text{AgGe}_2$ und $\alpha\text{-Li}_2\text{AgGe}$ beinhaltet. Die Verbindungen bilden anionische Ag-Ge Netzwerke aus, welche der Struktur von Diamant sehr ähneln und dessen Kanäle mit Li Atomen gefüllt sind. Die Tieftemperaturen der Strukturfamilie bilden riesige Überstrukturen mit geordneten Ag und Ge Positionen, während die Hochtemperaturphasen Mischbesetzungen ausbilden. Mit Hilfe von quantenchemischen Rechnungen konnten die treibenden Kräfte zur Ausbildung dieser Überstrukturen vereinfacht werden.

Zuletzt wurde auch im System Li-Ag-Si eine neue Hochtemperaturphase entdeckt. Diese Verbindung zeigt dieselben strukturellen Merkmale wie die des schwereren Homologen im Li-Ag-Ge Phasensystems.

Ein weiterer Fokus dieser Arbeit war es experimentelle Arbeit anderer ZINTL-Phasen und -Ionen mit quantenchemischen Rechnungen zu unterstützen. Hierbei wurde die Verbindung $\text{Li}_6\text{B}_{18}(\text{Li}_3\text{N})_x$ charakterisiert und zusätzlich Raman Spektren berechnet. Außerdem wurde die potenzielle Eignung als Elektrolyt untersucht und eine Li-Diffusion simuliert. Es konnte eine sehr niedrige Energiebarriere von ungefähr 20 kJ/mol bestätigt werden. Neben dieser Phase wurde auch die Gast-freien Li_6B_{19} and B_4C_2 Modelle untersucht.

Zu den ternären Verbindungen Li_3AlP_2 , Li_3GaP_2 und Na_7TaP_4 , welche von Tassilo Restle synthetisiert wurden, wurden Bandstruktur und Raman Rechnungen durchgeführt und analysiert.

Interessanterweise konnte an KBi der Effekt von Lösungsmittelmolekülen auf die Struktur und Eigenschaft gezeigt werden. Bei $\text{KBi}\cdot\text{NH}_3$ konnte eine Metallisierung beobachtet werden, welche mittels quantenchemischer Rechnungen weiter untersucht wurde.

Für verschiedene ZINTL Ionen wie $[\text{SnBi}_3]^{5-}$, Clustertyp $TM@Tt_9$, $[\text{Ge}_4\text{HZn}(\text{Ph})_2]^{3-}$, $[(\text{Ge}_9\{\text{Si}(\text{TMS})_3\}_2)^t\text{Bu}_2\text{P}]$ und $(\text{Si}/\text{Ge})_9\{\text{Si}(\text{TMS})_3\}_3^-$ wurde ein Molekülorbitaldiagramm erstellt, Ladungen und Raman Spektren berechnet und analysiert, welche faszinierende Charakteristika wie spezifische Schwingungen zeigte. Diese konnten als Werkzeug genutzt werden um die Anwesenheit von endohedralelen Cluster zu bestätigen. Zudem konnte in einer weiteren Verbindung die Existenz einer $3c-2e$ Ge-H-Ge-Bindung nachgewiesen werden.

Contents

I	Introduction	1
1	General Introduction	3
1.1	Motivation: Li-Ion Battery	3
1.1.1	Background and Conventional Lithium Ion Battery	4
1.2	Basics of Solid State Chemistry	6
1.2.1	ZINTL phases	7
1.2.2	HEUSLER phases	8
1.3	Bärnighausen family tree formalism or group-subgroup relationships	9
1.3.1	Group-subgroup relationships	9
II	Experimental Part	15
2	General Experimental Techniques	17
2.1	Starting Materials	17
2.2	Inertgas Techniques	18
2.2.1	Glovebox	18
2.2.2	SCHLENK Line	18
2.3	Preparing Ta-/Nb-ampules	18
2.4	Synthesizing precursors	19
2.5	Sample Preparation	19
2.6	Vertical Tube furnace	20
2.6.1	Low-Temperature-Synthesis	20
2.6.2	High-Temperature-Synthesis	20
2.6.3	Temperature Programs	21
2.7	Experimental Author Contribution	23
3	Characterization	25
3.1	Single Crystal X-ray Diffraction	25

3.2	Powder X-ray Diffraction and RIETVELD-Refinement	25
3.3	Thermal Analysis	26
3.4	Nuclear Magnetic Resonance (NMR) Spectroscopy	26
4	Computational Methods	29
4.1	Theoretical Background	29
4.1.1	The Electronic Structure Problem	29
4.1.2	The Born-Oppenheimer Approximation	30
4.1.3	Spin Orbitals and Slater Determinants	31
4.1.4	Hartree-Fock in a Nutshell	32
4.1.5	Post-Hartree-Fock methods	33
4.1.6	Basis Set	34
4.1.7	Density Functional Theory (DFT)	35
4.2	Periodic Systems	37
4.2.1	Structure Modeling	37
4.2.2	Used Functionals and Basis Sets	37
4.2.3	Structure Optimization and Frequency Calculation	38
4.2.4	One Electron Properties	40
4.2.5	Property Calculations	40
4.3	Molecular Systems	41
4.3.1	Structure modeling	41
4.3.2	Functional and Basis set	42
4.3.3	Optimization and Frequency Calculation	42
4.3.4	Property Calculations	43
III	Results and Discussions	47
5	Substitutional Effects in the Li-Ge	
	Binary System by Ni	49
5.1	Introduction	49
5.1.1	The Li-Ge-Ni phase system	49
5.1.2	Intermetalloid Clusters in Solid-State Chemistry	51
5.2	The Compound $\text{Li}_{14}\text{Ni}_{8+x}\text{Ge}_{9-x}$ ($x = 0.3$)	54
5.2.1	Synthesis of $\text{Li}_{14}\text{Ni}_{8+x}\text{Ge}_{9-x}$ ($x = 0.3$)	54
5.2.2	Characterization of $\text{Li}_{14}\text{Ni}_{8+x}\text{Ge}_{9-x}$ ($x = 0.3$)	55
5.2.3	Structure Description of $\text{Li}_{14}\text{Ni}_{8+x}\text{Ge}_{9-x}$ ($x = 0.3$)	58
5.2.4	Thermal behavior of $\text{Li}_{14}\text{Ni}_{8+x}\text{Ge}_{9-x}$ ($x = 0.3$)	61
5.2.5	Computational Analysis of $\text{Li}_{14}\text{Ni}_{8+x}\text{Ge}_{9-x}$ ($x = 0.3$)	62
5.3	The Compound $\text{LiNi}_{1+x}\text{Ge}$ ($x = 0.17$)	68

5.3.1	Synthesis of $\text{LiNi}_{1+x}\text{Ge}$ ($x = 0.17$)	68
5.3.2	Characterization of $\text{LiNi}_{1+x}\text{Ge}$ ($x = 0.17$)	68
5.3.3	Structure Description of $\text{LiNi}_{1+x}\text{Ge}$ ($x = 0.17$)	72
5.3.4	Thermal behavior of $\text{LiNi}_{1+x}\text{Ge}$ ($x = 0.17$)	74
5.3.5	Computational analysis of $\text{LiNi}_{1+x}\text{Ge}$ ($x = 0.17$)	75

6 Substitutional Effects in the Li-Ge

Binary System by Ag	79
6.1 Introduction	79
6.1.1 The binary system Li-Ge	79
6.1.2 The binary system Li-Ag	80
6.1.3 The binary system Ag-Ge	81
6.1.4 Substitution of Ag in the binary system Li-Ge	81
6.1.5 The compound $\alpha\text{-Li}_2\text{AgGe}$	84
6.1.6 The compound $\alpha\text{-Li}_{2.53}\text{AgGe}_2$	85
6.1.7 Towards new structure-related compounds	86
6.2 The Compound $\beta\text{-Li}_2\text{Ag}_{1-x}\text{Ge}_{1+x}$	87
6.2.1 Synthesis of $\beta\text{-Li}_2\text{Ag}_{0.8}\text{Ge}_{1.2}$	87
6.2.2 Characterization of $\beta\text{-Li}_2\text{Ag}_{0.8}\text{Ge}_{1.2}$	88
6.2.3 Structure Description of $\beta\text{-Li}_2\text{Ag}_{0.8}\text{Ge}_{1.2}$	92
6.2.4 Phase Width of $\beta\text{-Li}_2\text{Ag}_{1-x}\text{Ge}_{1+x}$	95
6.3 The Compound $\alpha\text{-Li}_2\text{Ag}_{0.8}\text{Ge}_{1.2}$	98
6.3.1 Synthesis of $\alpha\text{-Li}_2\text{Ag}_{0.8}\text{Ge}_{1.2}$	98
6.3.2 Characterization of $\alpha\text{-Li}_2\text{Ag}_{0.8}\text{Ge}_{1.2}$	98
6.3.3 Structure Description of $\alpha\text{-Li}_2\text{Ag}_{0.8}\text{Ge}_{1.2}$	101
6.4 The Compound $\gamma\text{-Li}_{2.53}\text{AgGe}_2$	103
6.4.1 Synthesis of $\gamma\text{-Li}_{2.53}\text{AgGe}_2$	103
6.4.2 Characterization of $\gamma\text{-Li}_{2.53}\text{AgGe}_2$	103
6.4.3 Structure Description of $\gamma\text{-Li}_{2.53}\text{AgGe}_2$	103
6.5 Group-Subgroup relationship of diamond-like structure in the Li-Ag-Ge phase system	105
6.6 Thermal Analysis	110
6.7 NMR Analysis	112
6.8 Computational Analysis of related diamond-like structure	113
6.8.1 Structure models	114
6.8.2 Structural parameter comparison	115
6.8.3 Band Structures and Electron Count	115
6.8.4 Population Analysis and Total Energies	117

7	Substitutional Effects in the Li-Si Binary System by Ag	125
7.1	Introduction	125
7.1.1	The binary system Li-Si	125
7.1.2	The binary system Ag-Si	126
7.1.3	Substitution of Ag in the binary system Li-Si	127
7.1.4	The Compound α -Li ₁₃ Ag ₅ Si ₆	129
7.2	The Compound β -Li ₁₃ Ag ₅ Si ₆	130
7.2.1	Synthesis of β -Li ₁₃ Ag ₅ Si ₆	130
7.2.2	Characterization of β -Li ₁₃ Ag ₅ Si ₆	130
7.2.3	Structure Description of β -Li ₁₃ Ag ₅ Si ₆	132
7.2.4	Thermal Analysis	132
8	The Framework Compound Li₆B₁₈(Li₃N)_x hosting Li₃N and chemi-inspired B₄C₂ structures	135
8.1	Introduction	135
8.2	The Compound Li ₆ B ₁₈ (Li ₃ N) _x	137
8.2.1	Experimental Part	137
8.2.2	Computational Analysis	138
8.2.3	Structure models of the type B ₄ C ₂	144
9	Computational Analysis of Low Dimensional Structures	149
9.1	Introduction	149
9.2	The Compounds Li ₃ TrP ₂ (Tr = Al, Ga)	150
9.2.1	Experimental Part	151
9.2.2	Computational Analysis	153
9.3	The Compound Na ₇ TaP ₄	155
9.3.1	Experimental Part	155
9.3.2	Computational Analysis	156
9.4	The Compound KBi·NH ₃	160
9.4.1	Experimental Part	160
9.4.2	Computational Analysis	161
9.5	The Anion [SnBi ₃] ⁵⁻	163
9.5.1	Experimental Part	164
9.5.2	Computational Analysis	165
10	Computational Analysis of deltahedral Clusters	171
10.1	Introduction	171
10.1.1	ZINTL phases of the type A ₄ E ₄ , A ₄ E ₉ and A ₁₂ E ₁₇	172

10.1.2	ZINTL phases in solution	172
10.1.3	Endrohedral Clusters	172
10.1.4	Ligand-stabilized Clusters	173
10.2	Bare Endohedral Clusters $TM@Tt_9$	173
10.2.1	$[Co@Ge_9]^{5-}$ and $[Ru@Sn_9]^{6-}$	173
10.2.2	Raman Studies of other Bare Endohedral Clusters of the type $TM@Tt_9$	180
10.3	Ligand-stabilized Ge/Si-Clusters	181
10.3.1	The Molecule $[(Ge_9\{Si(TMS)_3\}_2)^tBu_2P]$	181
10.3.2	The Molecule $[(Si/Ge)_9\{Si(TMS)_3\}_3]^-$	183
10.3.3	The Molecule $[Ge_4HZn(Ph)_2]^{3-}$	186
IV	Conclusion	195
11	Substitutional Effects	199
11.1	Substitutional Effects in the Li-Ge Binary System by Ni	199
11.2	Substitutional Effects in the Li-Ge Binary System by Ag	199
11.3	Substitutional Effects in the Li-Si Binary System by Ag	200
12	Computational Analysis of ZINTL phases and ions	201
12.1	The Framework Compound $Li_6B_{18}(Li_3N)_x$ hosting Li_3N and chemi- inspired B_4C_2 structures	201
12.2	Computational Analysis of Low Dimentional Structures	201
12.3	Computational Analysis of deltahedral Clusters	202
13	Appendix	203
13.1	Substitutional Effects in the Li-Ge Binary System by Ni	203
13.2	Substitutional Effects in the Li-Ge Binary System by Ag	223
13.3	Substitutional Effects in the Li-Si Binary System by Ag	235
13.4	The Framework Compound $Li_6B_{18}(Li_3N)_x$	236
13.5	The Compounds Li_2TrP_2 ($Tr = Al, Ga$)	247
13.6	The Compound Na_7TaP_4	250
13.7	The Compound $KBi \cdot NH_3$	254
13.8	The Anion $[SnBi_3]^{5-}$	259
13.9	Bare Endohedral Clusters $TM@Tt_9$	263
13.10	Basis Sets for periodic calculations	270

Part I

Introduction

General Introduction

In the periodic table about two thirds of the elements are metals and the large variety of metal elements offer a broad field of intermetallic structure by mixing them. Many of these compounds provide a attractive combination of physical and mechanical properties. Therefore, intermetallics can be used for many different applications like battery materials or magnetic applications.^[1]

Since the variety of possible intermetallic compounds is so high and rules of stable compounds are hard to figure out, the method of "trial and error" is mostly used. However, by getting to know more and more intermetallic compounds and studying their electronic nature and stability it is possible to synthesize new compounds target oriented. Computational studies of known and new structures are supporting to understand the driving forces. The goal is to synthesize new compounds with desired properties for specific applications on demand.

1.1 Motivation: Li-Ion Battery

Like mentioned above a possible application for intermetallics are as battery materials. The motivation for this thesis is to study new structures, which might be fit for Li-ion batteries.

The use of electronic devices is nowadays inevitable and have a broad area of applications starting from every days needs like lamps, running a fridge or washing machine to working applications as personal computer, laptop, smart phone to mobility as electric cars, trains and so on. To fulfill the energy on demand energy storage is crucial to receive the needed power whenever needed. Several countries have declared development plans, which lead to a increased need in energy storage.^[2] Additionally, due to pollution reasons the trend to renewable energies such as solar and wind base plants instead of fossil fuel and nuclear fission based power plants also increases the needs.^[3,4] The energy gained from such renewable energy plants is strongly varying and dependents on external circumstances, therefore energy storage buffering the output energy is required.^[5-7] Secondly, automotive industry is chang-

ing from gasoline based cars to hybrid or electric cars. In the automotive industry this could lead to a way to decrease CO₂ and NO_x emissions world-wide assuming proper infrastructure and recycling.^[8] Last, the demand of portable devices is increasing rapidly and small and light energy storage is needed.

Up to date different types of stationary energy storage are in use: pumped-storage hydroelectricity, molten salt thermal storage, compressed air storage, flywheels and electrochemical storage media (lead acid, vanadium flow, lithium-ion and sodium based batteries).^[9,10] But due to different properties like mobile storage and high specific energy density Li-ion batteries are gaining more and more attention. Therefore, the most common battery and state of the art battery for those requirements is lithium ion (secondary) battery.^[11] The demands are very high and most important ones are safety, high energy density and low cost.

1.1.1 Background and Conventional Lithium Ion Battery

The advantages of Li-ion batteries are for example a very low reduction potential of Li compared to other possible candidates, which leads to a high cell potential. Additionally, the charge per volume is very high since Li is a very small element. This offers the possibility of fast diffusion of the charge carrier. As Li is also very light and one of the many demands of battery materials is low weight this is another reason for Li-ion batteries and Li outmatches other candidates.

Having a look at the history of batteries, the first time the term "battery" was mentioned was by Benjamin Franklin in 1748 and was describing an array of Leyden jars, water filled glass jars with two metal electrodes serving as capacitors to store charges from electrostatic generators.^[12] Passing many years the discovery of the Voltaic pile (stack of metallic copper and zinc discs separated by brine soaked cloth) was in 1799^[13,14] and was further improved by John F. Daniell. The well-known lead-acid battery was investigated by Gaston Plante (1859) and finally batteries were categorized into two types: primary and secondary batteries. Primary batteries have only one use and cannot be recharged, whereas secondary batteries are rechargeable.

Batteries, secondary and primary, are build by two electrodes separated by an electrolyte, which is liquid for conventional Li-ion batteries. The electrode where the reduction reaction occurs is called cathode, consequently the anode is where the oxidation process takes place during discharge. For the charging process oxidation and reduction places are switched. The electrolyte is conducting for the charge carrier e.g. Li⁺, but non-conducting for electrons. This forces a current to flow outside the battery through a resistance to achieve neutral charge. In 1976 a Li-ion battery using Li metal as anode material, TiS₂ as cathode material and a solution of LiPF₆

in propylene carbonate as electrolyte was published. Recharging the battery could be carried out and open circuit potential of $V_{OC} \approx 2$ V were achieved.^[15-17] As anode material Lithium metal offers the highest anodic electrochemical potential energy and additionally its salts, like LiPF_6 dissolved in organic carbonate esters show a very good specific Li-ion conduction of $\sigma_{Li} > 10^{-1}$ S cm^{-2} at room temperature.^[18] The solution of electrolyte stabilizes the anode forming a solid electrolyte interface (SEI) by avoiding further decomposition of the electrolyte.^[19] The layered structure of TiS_2 is able to reversible intercalate Li-ions forming LiTiS_2 at its maximum. But further cathode materials were investigated throughout the years. A great discovery was the cathode material LiTmO_2 ($Tm = \text{Co, Ni}$) by Goodenough *et al.*^[20-22] Those compound offer high voltage Li-ion batteries up to 4 V. Nevertheless, a central issue of those Li-ion batteries is the Li metal. Although the SEI protects the electrolyte of further decomposition, the anode forms dendrites during many cycles. This causes a short-circuit, which is a huge safety issue and can end in overheating and explosion.^[23] To overcome this problem a new anode material was introduced: graphite. Graphite can intercalate Li up to LiC_6 .^[24,25] Finally, this set-up was commercially used and patented 1985 (Figure 1.1).^[26] SONY corporation marketed the first cell phone improving our every-day life in the early 1990s.

Although the set-up generally is still the same, nowadays, Li-ion batteries were

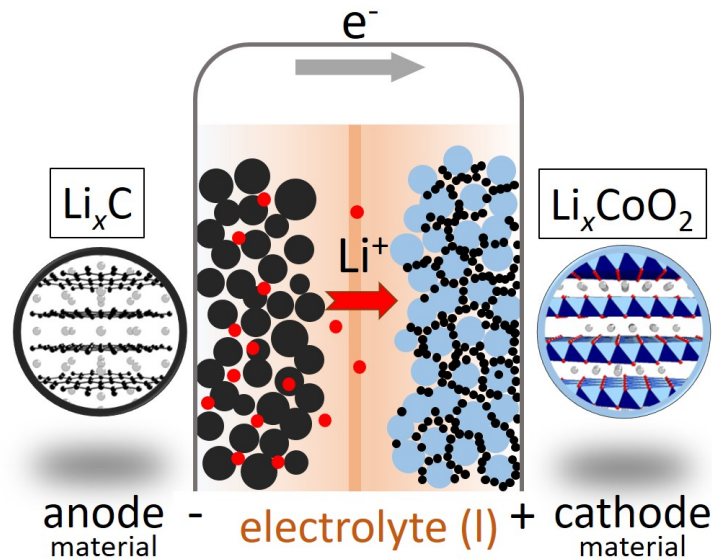


Figure 1.1: Scheme of conventional Li-ion battery cell. Cathode is made of Li_xCo_2 and anode of Li_xC with a liquid electrolyte such as LiPF_6 .

improved step by step. Mainly, the increase of the specific, volumetric and gravimetric, energy density and the power density was enhanced. This was achieved by e.g. nanostructuring, optimization of the electrolyte solution and new cathode ma-

materials. In chapter 6 and 7 the use of tetrel elements like Si and Ge are discussed as use for anode material to further improve the energy density. Using higher tetrels than carbon is a possibility to increase the theoretical specific capacity. Comparing carbon (372 mAhg^{-1}) to Si (4200 mAhg^{-1}) and Ge (1564 mAhg^{-1}) it is obvious, that there is potential for improving anode materials.^[27,28] Nevertheless, a central issue of Si and Ge as pure anode materials the huge volume change the material undergo by lithiation and delithiation of 270 % and 240 %, respectively. This leads to electrochemical grinding of the electrode and contact loss, which ends up in quick capacity fading.^[29] To overcome this issue different approaches have been tried like reduction of particle size or composite materials. Another option is to introduce a transition metal, which can establish a stable anionic network building layers or channels for Li-ions. Ideally, this network remains untouched during the charge/discharge process to avoid huge volume changes.

Recently, all-solid-state Lithium ion batteries raised huge interest. The liquid electrolyte in conventional Li-ion batteries can cause fire due to overheating and the flammable organic electrolyte.^[30-32] A solid electrolyte would offer several advantages like minimizing safety concerns and improving volumetric and gravimetric energy density. This means that the application of solid-state materials includes anode, cathode and electrolyte.

1.2 Basics of Solid State Chemistry

The term "solid state chemistry" can partly be described as the synthesis, structure, properties and reactivity of solid compounds, crystalline or amorphous, which are approximately unlimited expanded in all three directions (x , y and z).^[33] The compounds can be categorized in salts, homoatomic compounds and metals or intermetallics. In this thesis borderline cases of crystalline salts and intermetallics are discussed i.e. polar intermetallics.

Crystalline compounds are compounds with a specific ordering of atoms called crystal structure, which shows periodicity/translation symmetry. By the term intermetallics compounds/phases of two or more metallic elements are described, which can even be widened to semi-metallic elements. This offers a huge field of composition possibility accessing new properties, which are not observed in the single elements.^[34,35] The composition of intermetallic phases can be, in contrast to other solid state compounds like salts and covalent compounds, broader, therefore they can either have an exact composition or no exact stoichiometry (phase width). For example the composition of Cu_5Zn_8 ^[36] can vary from $\text{Cu}_{0.38}\text{Zn}_{0.66}$ to $\text{Cu}_{0.42}\text{Zn}_{0.58}$.

Understanding the electron structure and bonding situation of intermetallic compounds engaged chemists for decades. Intermetallics lack simple bonding or valence rules and closed-shell states or the electrons are mostly delocalized throughout the compound.^[37,38] Several rules were applied to explain driving forces and their stability. A way to apply certain rules is to categorize the compounds in different phases and subsequently understand stability, bonding situation and driving forces in those groups, since the field of intermetallics is huge due to the large variety of different metals and compositions. Therefore, intermetallics are categorized due to specific properties, elements or electron configurations in different phases like ZINTL phases (chapter 1.2.1), HEUSLER phases (chapter 1.2.2), HUME-ROTHERY phases or LAVES phases. In chapter 1.3 symmetry rules, which can be applied to show relationships between two or several crystalline compounds are explained. Those general rules were applied in this work to explain ordering and analyze new phases related to known compounds.

1.2.1 ZINTL phases

As mentioned above ZINTL phases are one of the main groups intermetallics are divided into. In general ZINTL phases are build of electropositive metals from the *s*-block and electronegative metals of Group 13.-14. elements. The large difference in electronegativity causes a formal electron transfer from the *s*-block metal to the 13.-14. elements.^[39] The charge transfer leads to a salt-like structure, but the anions itself form 3-dimensional networks or cluster units with covalent bonding character and defines the substructure. The anionic substructure build the same substructure like neutral or differently charged atoms with the same electron configuration. For instance, in NaTl Na transfers one electron to Tl ending up with Na^+Tl^- .^[40,41] Tl^- has the same electron configuration as carbon and therefore builds a diamond-like substructure with isolated sodium-ions in the tetrahedral voids. Other examples are KGe (Ge forms isolated tetrahedra according to P_4), CaSi_2 (Si forms undulated layers according to As) and LiAs (As forms screwed chains according to Se and Te). ZINTL phases are usually electron-precise and therefore have no phase width. Other typical properties of ZINTL phases are a high melting point, high heat of formation, poor electrical conductivity (usually semi-conductors) and brittleness.

ZINTL phases are named after the scientist Eduard Zintl, who was the first trying to apply rules explaining these group of compounds.^[42-45] The concept was improved by Klemm^[46,47] and Busmann,^[48,49] who generalized the rules and applied it to several binary and ternary compounds. Bonding and structure principles were associated with Zintl's assumptions. The Zintl-Klemm-Busmann concept explains anionic substructure by the rules of covalent compounds ($8-N$ rule). Following this the bonding

situation of such anionic substructures can be generalized and a bond order can be classified and 2-center-2-electron bonding and lone-pairs are observed.

Such electron counting rules as the 8- N rule improve the understanding of such complex compounds breaking it down into a simple formalism enabling structure prediction. An important electron counting rule to explain deltahedral clusters was established by Kenneth Wade and improved by Michael Mingos, which is used to classify boranes and carboranes.^[50,51] The Wade-Mingos rules describe structures with electron deficiency in clusters in simple terms by the number of skeletal electron pairs. After counting electrons the clusters are categorized in three groups *closo*, *nido* and *arachno* depending on the electron deficiency. Since this rule works extremely good for boranes and carboranes it was also extended for intermetallic cluster compounds.

For instance, similar to the famous boranes group 14 deltahedral clusters can be synthesized from ethylenediamine or liquid ammonia solutions and were thoroughly investigated during the last 30 years. Typical are the $[Tt_4^{4-}]$ and $[Tt_9^{4-}]$ clusters, which are described more detailed in chapter 10. These clusters all show delocalized bonding.

As mentioned above a typical property of ZINTL phases is low electric conductivity *aka.* semi-conducting behavior. According to this usually a band-gap is observed in the density of states (DOS) at the Fermi level, but sometimes due to lack of electrons the band gap is above the Fermi level or only a pseudo-gap (minimum at DOS) is observed. Still, the compounds show typical polar behavior by forming an anionic network or clusters following the ZINTL rule. These phases are called "metallic" or not electron-precise ZINTL phases.^[52] In chapter 6 and 7 typical not electron-precise ZINTL phases were investigated.

1.2.2 HEUSLER phases

HEUSLER phases have the general formula MM'_2X ($M, M' =$ transition metal; $X =$ group 3-5 element) named after Friedlich Heusler. In chapter 6 and 7 the compounds also show the typical structure of a HEUSLER phase on first sight, but show more characteristics of ZINTL phases, when investigated thoroughly.

1903 Friedrich Heusler first describes the phenomenon of ferromagnetism in the compound Cu_2MnAl .^[53] Noteworthy is, that non of the pure elements Cu, Mn and Al show this behavior. Passing time more compounds featuring the same behavior with the same stiochiometry and structure became known and they were finally named HEUSLER phases.^[54] These materials are especially interesting due to their properties like ferro- or antiferromagnetism. They crystallize in the Cu_2MnAl ($Fm\bar{3}m$) structure type. The interaction between the atoms is still not fully understood, but

leads to spin polarization and therefore ferromagnetism.

Additionally to the typical HEUSLER phase of the formula MM'_2X also semi-HEUSLER phases $MM'X$ became known. AgAsMg and LiAlSi are two representative of this class. The typical crystal structure is described in chapter 6.2.

1.3 Bärnighausen family tree formalism or group-subgroup relationships

In this thesis group-subgroup relationships play a big role. Especially in chapter 6 a so called Bärnighausen family tree is derived showing the structural relationship of several compounds, where symmetry reduction paired with chemical intuition and experimental data were used to finally determine a crystal structure. To understand the procedure of this work basics of crystallography are inevitable. Therefore, in chapter 1.3.1 group-subgroup relationships and symmetry reductions are discussed.

1.3.1 Group-subgroup relationships

In order to show relationships between crystal structures of different symmetries, the group-subgroup relationship can be applied. The symmetry reduction steps can be divided into two reduction types: *translationsgleich* (t) and *klassengleich* (k).

Translationsgleiche reduction means symmetry reduction without changing the original cell vectors. Consequently, the unit cell stays the same in size. The reduction takes place as lowering rotation axes from 4 to 2 for instance.

On the other hand, *klassengleiche* reduction is a reduction, where the crystal class stays the same, but translation symmetry changes by doubling the unit cell or loss of centering for instance. A special kind of *klassengleich* is isomorphic (i). This special kind is characterized by not changing the space group through reduction step, but only increasing the size of the unit cell.

Relationships of group-subgroups are displayed in a family tree or so-called Bärnighausen family tree.^[55-57] Higher symmetry space groups (aristotype) are on top of the scheme and arrows show the symmetry reduction to subgroups (hettotype). The arrows are further identified with the relationship to the subgroup by a shortcut indicating index and kind of reduction like $k2$, which means *klassengleiche* reduction with index 2. Additionally, new basis vectors of the subgroup unit cell is given in basis vectors of the former unit cell.

Fritz Laves already announced, that there is a tendency for crystalline solids compounds to achieve high symmetry.^[58] This symmetry principle was further improved by H. Bärnighausen:

1. In solid state is a distinct tendency to high symmetry positions of the atoms
2. Through special properties of atoms or their assemblies the highest possible symmetry can often not be achieved; the deviations of the ideal symmetry are usually quite small (pseudo symmetry)
3. For phase transitions and solid-state reactions that lead to products with lower symmetry often indirectly preserve symmetry properties of the starting compounds, namely by appropriate orientation of domains

1 accords also to G. O. Brunner who claimed, that atoms of the same type tend to have equivalent positions.^[59] To express this in a physical or chemical view, it can be phrased, depending on chemical composition, type of chemical bond, electron configuration of atoms, relative size of atoms, pressure, temperature, etc., there is an energetically favorable environment for atoms of a kind, that of all atoms of this sort are sought.

Due to the facts given complicated structure can be seen as descendant of simple high symmetrical structures. Reasons for symmetry reduction can be:

1. Atoms of an element in symmetry-equivalent positions substituted by atoms of several elements
2. atoms are substituted with vacancies or the other way around
3. Atoms of one element are substituted by those of another element, that requires changed bonding situation
4. Distortions by JAHN-TELLER-effects
5. Arise of new interactions
6. Distortions by covalent bonding
7. phase transitions

To analyze the relationship between two solids the *International Tables for Crystallography* can be used. Subgroups to each space group are given in this book with needed details like WYCKOFF splitting, new unit cell and atom positions, index and type of reduction. WYCKOFF splitting shows the new WYCKOFF positions in G_2 of a certain WYCKOFF position in G_1 . The splitting is often given in an additional table to the family tree, since the family tree itself does not include atom positions. Splitting of a WYCKOFF position offers a possibility for substitution of elements, because the former position could only be filled with one kind and the new structure

offers two or more possibilities. This often occurs for instance, if a high temperature phase only has a mixed position and the low temperature phase has a fully ordered structure. The so-called *coloring problem* can arise.^[60] In a fixed solid-state compound, there are several ways to distribute different atom types to the various lattice positions. Only one of many combinations shows the energetically favored structure. Therefore, understanding why a specific distribution of atoms has the lowest energy means solving the *coloring problem*. Solving the *coloring problem* is shown in chapter 6.

References

- [1] N. S. Stoloff, C. T. Liu, S. C. Deevi, *Intermetallics* **2000**, *8*, 1313–1320.
- [2] European Environment Agency, Improving Europe’s air quality - measures reported by countries, **2018**.
- [3] European Union, DIRECTIVE 2009/28/EC OF THE EUROPEAN PARLIAMENT AND OF THE COUNCIL of 23 April 2009 on the promotion of the use of energy from renewable sources and amending and subsequently repealing Directives 2001/77/EC and 2003/30/EC, **2009**.
- [4] REN21 Secretariat, *Renewables 2018 Global Status Report*, REN21, Paris, France, **2018**.
- [5] M. Kaltschmitt, W. Streicher, A. Wiese, *Erneuerbare Energien. Systemtechnik, Wirtschaftlichkeit, Umweltaspekte*, Springer, Berlin/Heidelberg, Germany, **2013**.
- [6] EWEA, *Wind Energy - The Facts - an Analysis of Wind Energy in the EU-25*, European Wind Energy Association, Brussels, Belgium, **2007**.
- [7] S. L. Piano, K. Mayumi, *Appl. Energy* **2017**, *186*, 167–176.
- [8] A. Unterstaller, Electric vehicles: a smart choice for the environment.
- [9] IRENA, *Electricity Storage and Renewables: Costs and Markets to 2030*, International Renewable Energy Agency, Abu Dhabi, United Arab Emirate, **2017**.
- [10] IEA, *Technology Roadmap: Energy storage*, International Energy Agency, Paris, France, **2014**.
- [11] J. B. Goodenough, K. S. Park, *J. Am. Chem. Soc.* **2013**, *135*, 1167–1176.
- [12] M. Bellis, History and Timeline of the Battery.
- [13] P. T. Keyser, *J. Near East. Stud.* **1993**, *52*, 81–98.
- [14] A. Volta, *Philos. Trans. RoyalSoc.* **1800**, *90*, 403–431.

- [15] M. S. Whittingham, *J. Chem. Soc. Chem. Commun.* **1974**, 328–329.
- [16] M. S. Whittingham, F. R. Gamble, *Mater. Res. Bull.* **1975**, *10*, 363–371.
- [17] M. S. Whittingham, *Science* **1976**, *192*, 1126–1127.
- [18] K. Xu, *Chem. Rev.* **2004**, *104*, 4303–4417.
- [19] D. Aurbach, Y. Gofer, J. Langzam, *J. Electrochem. Soc.* **1989**, *136*, 3198–3205.
- [20] K. Mizushima, P. C. Jones, P. J. Wiseman, J. B. Goodenough, *Mater. Res. Bull.* **1980**, *15*, 783–789.
- [21] J. Goodenough, K. Mizushima, T. Takeda, *Japanese J. Appl. Phys.* **1980**, *19*, 305–313.
- [22] M. G. Thomas, P. G. Bruce, J. B. Goodenough, *Solid State Ionics* **1985**, *17*, 13–19.
- [23] M. S. Whittingham, *Chem. Rev.* **2004**, *104*, 4271–4302.
- [24] M. S. Whittingham, A. J. Jacobson, *Intercalation chemistry*, Academic Press, New York, **1982**, pp. 19–52.
- [25] R. Yazami, P. Touzain, *J. Power Sources* **1983**, *9*, 365–371.
- [26] A. Yoshino, US Patent No. 4, 668, 595 and JP9769585, **1985**.
- [27] C. J. Wen, R. A. Huggins, *J. Solid. State. Chem.* **1981**, *37*, 271–278.
- [28] G. R. Goward, N. J. Taylor, D. C. S. Souza, L. F. Nazar, *J. Alloys Comp.* **2001**, *329*, 82–91.
- [29] L. Baggetto, P. H. L. Notten, *J. Electrochem. Soc.* **2009**, *156*, A169–A175.
- [30] T. M. Bandhauer, S. Garimella, T. F. Fuller, *J. Electrochem. Soc.* **2011**, *158*, R1.
- [31] Q. Wang, P. Ping, X. Zhao, G. Chu, J. Sun, C. Chen, *J. Power Sources* **2012**, *208*, 210–224.
- [32] Y. Miao, P. Hynan, A. Von Jouanne, A. Yokochi, *Energies* **2019**, *12*, 1074.
- [33] A. F. Holleman, N. Wiberg, E. Wiberg, *Lehrbuch der Anorganischen Chemie*, 102., de Gruyter, Berlin, **2007**, p. 1401.
- [34] M. Nakamura, *MRS Bull.* **1995**, *20*, 33–39.
- [35] J. D. Corbett, *Inorg. Chem.* **2010**, *49*, 13–28.
- [36] A. J. Bradley, J. Thewlis, *Proc. R. Soc. London Ser. A* **1926**, *112*, 678–692.
- [37] R. E. Rundle, *J. Am. Chem. Soc.* **1947**, *69*, 1327–1331.
- [38] R. E. Rundle, *J. Chem. Phys.* **1949**, *17*, 671.

- [39] T. F. Fässler, *Zintl Phases: Principles and Recent Developments*, Springer, Berlin/Heidelberg, Germany, **2011**.
- [40] E. Zintl, A. Woltersdorf, *Z. Electrochem.* **1935**, *41*, 876–879.
- [41] G. Grube, A. Schmidt, *Z. Elektrochem. Angew. P.* **1936**, *42*, 201–209.
- [42] E. Zintl, G. Brauer, *Z. Phys. Chem.* **1933**, *20B*, 245–271.
- [43] E. Zintl, W. Dullenkopf, *Polyantimonide, Polywismutide und ihr Übergang in Legierungen*, 16B, **1932**, p. 183.
- [44] E. Zintl, S. Neumayr, *Über den Gitterbau von NaIn und die Deformation der Atome in Legierungen*, 20B, **1933**, p. 272.
- [45] E. Zintl, *Angew. Chem.* **1939**, *52*, 1–6.
- [46] W. Klemm, *Proc. Chem. Soc.* **1959**, *329*.
- [47] W. Klemm, *Naturwis.* **1950**, 150–155.
- [48] E. Busmann, *Z. Anorg. Allg. Chem.* **1961**, *313*, 90–106.
- [49] W. Klemm, E. Busmann, *Z. Anorg. Allg. Chem.* **1963**, *319*, 297–311.
- [50] K. Wade, *J. Chem. Soc.* **1971**, 792–793.
- [51] D. M. P. Mingos, *Nat. Phys. Sci.* **1972**, *236*, 99–102.
- [52] R. Nesper, *Prog. Solid St. Chem.* **1990**, *20*, 1–45.
- [53] F. Heusler, *Verh. Deutsche Physikalische Gesellschaft* **1903**, *5*, 219.
- [54] G. Sauthoff, *Intermetallics*, Wiley-VCH, Weinheim, **1995**, pp. 83–90.
- [55] H. Bärnighausen, Group-subgroup relationships between space groups: A useful tool in crystal chemistry, **1980**.
- [56] U. Müller, *Z. Anorg. Allg. Chem.* **2004**, *630*, 1519–1537.
- [57] U. Müller, *Anorganische Strukturchemie, Vol. 6. Auflage*, **2008**.
- [58] F. Laves, *Phase Stability in Metals and Alloys*, McGraw-Hill, New York, **1967**.
- [59] G. O. Brunner, *Acta Crystallogr. A.* **1971**, *27*, 338.
- [60] G. J. Miller, *European Journal of Inorganic Chemistry* **1998**, 523–536.

Part II

Experimental Part

General Experimental Techniques

In the following sections all general experimental techniques are described and explained. All materials are listed and all used equipment are specified.

Glassware was dried in an drying oven at 100 °C for at least a day before usage.

2.1 Starting Materials

All used chemicals are listed in Table 2.1 including name, formula, shape, supplier and purity. All samples were synthesized directly or *via* a precursor from the listed elements. For some synthesis the tetrel (*Tt*) elements were ball-milled before usage using a planetary ball mill (Retsch, PM100). In this case a batch of about 30 g *Tt* element was processed at 150 rpm for 2 h in an 80 mL WC milling jar with 25×10 mm balls. Lithium rods were stripped from their passivation layer of lithium oxide and lithium nitride by peeling off the layer by a knife.

Table 2.1: Name, formula, shape, supplier and purity of starting materials

Name	Formula	Shape	Supplier	Purity [%]
Germanium	Ge	Pieces	EVOCHEM	99.999
Lithium	Li	Rods	ROCKWOOD LITHIUM	99
Nickle	Ni	Wire	ALFA AESAR	99.98
Nickle	Ni	Powder	CHEMPUR	99.99
Silicon	Si	Granules	WACKER	99.9
Silver	Ag	Wire	CHEMPUR	99.9
Silver	Ag	Powder	CHEMPUR	99.9

2.2 Inertgas Techniques

2.2.1 Glovebox

All materials and products were handled in a glovebox (MBRAUN, $O_2 < 1$ ppm, $H_2O < 1$ ppm) to avoid contamination and exclude air and moisture, because in particular all products show sensitivity to air and moisture. Argon (Ar) gas (Argon 4.8, WESTFALEN, 99.998 vol.%) was used as inert gas in all cases, which was dried over three columns filled with BTS-catalyst, P_2O_5 and molecular sieve, respectively, before usage.

2.2.2 SCHLENK Line

For evacuating reaction-tubes for high temperature synthesis a so-called SCHLENK line was used. This apparatus can be used to connect either a vacuum pump (VACUUBRAND GmbH & Co. KG, $p < 10^{-3}$ mbar) or inert gas to the used silica or aluminumoxide tube. Ar gas (Argon 4.8, WESTFALEN, 99.998 vol.%) was used as inert gas in all cases, which was dried over three columns filled with BTS-catalyst, P_2O_5 and molecular sieve, respectively, before usage. For evacuating reaction-tubes vacuum and inert gas was applied alternately for three times each.

2.3 Preparing Ta-/Nb-ampules

The appropriate reaction container for high-temperature reaction containing reactive substances e.g. alkali metals has to be chosen carefully. Alkali metals diffuse into glass or silica material, which becomes brittle, and causes loss of alkali metal during the reaction. Therefore those materials are unfit for ampules in this case. Niobium (Nb) and tantalum (Ta) ampules are mostly inert to the samples up to very high temperatures (about 900 °C). Nb tends to react at lower temperatures than Ta, but is also much cheaper. Therefore, depending on the reaction temperature and used elements for reaction either Ta or Nb was chosen as ampule material. In both cases during the heating inert gas atmosphere was needed, because Ta for example already reacts with oxygen at about 300 °C.

The ampules were prepared by Ta/Nb tubes (CHANGSHA SOUTH TANTALUM NIOBIUM Co., LDT., Ta/Nb > 99.95 %, $\varnothing = 10$ mm, wall-thickness 0.5 mm, cut in 3 mm or 5 mm pieces) and caps/bottoms provided by the in-house workshop from panels (CHANGSHA SOUTH TANTALUM NIOBIUM Co., LDT., Ta/Nb > 99.95 %, thickness 0.5 mm). All parts were washed *via* a four-step procedure with different solutions in a ultrasonic bath for 15 min each:

- (1) Water

- (2) Acetic acid (99.8 %)

- (3) Water

- (4) Acetone (technical)

Subsequently all parts were dried at 120 °C over night.

The bottoms of the ampules were pressed onto the tubes by a manual hydraulic press (SPECAC) and welded to the ampules using a water-cooled arc welder (EDMUND BÜHLER GmbH, MAM-1) located in the glove box. Afterwards ampules were filled by samples and sealed with a cap by arc welding, which is described in detail in 2.5.

2.4 Synthesizing precursors

For some synthesis a precursor was necessary. This technique enables a possible melting point decrease in case of the Ni-Ge system and offers a mixing of both metals on an atomic scale and therefore decreases the reaction temperature and reaction duration. Ni melts at 1455 °C, whereas depending on the stoichiometry Ni-Ge-alloy the melting point decreases below 800 °C.^[1] The *Tt* and transition metal (*TM*) was placed in a copper crucible, which could be installed in the arc-welder. For this procedure only pieces or wires of metals were used, because powders would tend to drop out of the crucible due to quick heating. The samples were heated for about 3-7 s by slowly circling around the pile of metals in the middle of crucible in the beginning and subsequently slowly moving to the middle in order to melt the outer parts first. After this step a metal regulus was gained. The regulus was turned at least twice and welded again for 3-7 s until a homogeneous regulus was achieved. In case the regulus was not homogeneous the procedure was repeated until it was achieved.

2.5 Sample Preparation

Samples were prepared in the glovebox. In case of using precursors *Tt* and *TM* were prepared as described in 2.4. The obtained regulus was weighted after this

procedure in order to identify the lost weight during the procedure. Afterwards the regulus was placed in the appropriate metal ampule and cut Li was added on top. The ampule was carefully sealed by arc welding to avoid loss of Li during the heating.

Sample preparation without precursors were carried out using powders of *Tt* and *TM*. A metal ampule was loaded with a mixture of both metals. Subsequently cut Li was added on top and the ampule was carefully sealed by arc welding to avoid loss of Li during the heating.

In case of a high-temperature phase synthesis 150 mg of corresponding low temperature phase was grounded in an achate-mortar and added to a appropriate metal ampule. The ampule was carefully sealed by arc welding.

2.6 Vertical Tube furnace

Two different procedures were necessary depending on a low- or high-temperature synthesis.

2.6.1 Low-Temperature-Synthesis

The sealed metal ampules were placed inside a large silica tube ($\varnothing = 35$ mm) equipped with a 40/45 ground glass joint and a stopcock containing an extra inner silica tube (2.1). This silica tubes fit several metal ampules for parallel synthesis under the same conditions. The silica tubes were evacuated and flushed with Ar gas at least three times each ending with evacuating to result in low pressure during the synthesis. This prevents oxidation of the metal ampules as mentioned in 2.3 and a high-temperature influenced pressure build-up.

The tubes were placed in a vertical resistance tube furnace (HTM Reetz LOBA 1200-40-600, EURO THERM 2416 controller). The detailed heating program is given in 2.2.

2.6.2 High-Temperature-Synthesis

In case of high-temperature phase synthesis a different procedure was necessary. The ampules had to be quenched in cold water quickly to avoid phase transition to low-temperature phases. The silica tube used for the regular synthesis is not appropriate for this, because the opening produce takes quite long and the air flow would cool down the metal ampule to slowly when opening the silica tube. Therefore a different container was needed providing Ar atmosphere with pressure compensation. A aluminumoxid tube ($\varnothing = 35$ mm) equipped with a 40/45 ground metal joint and

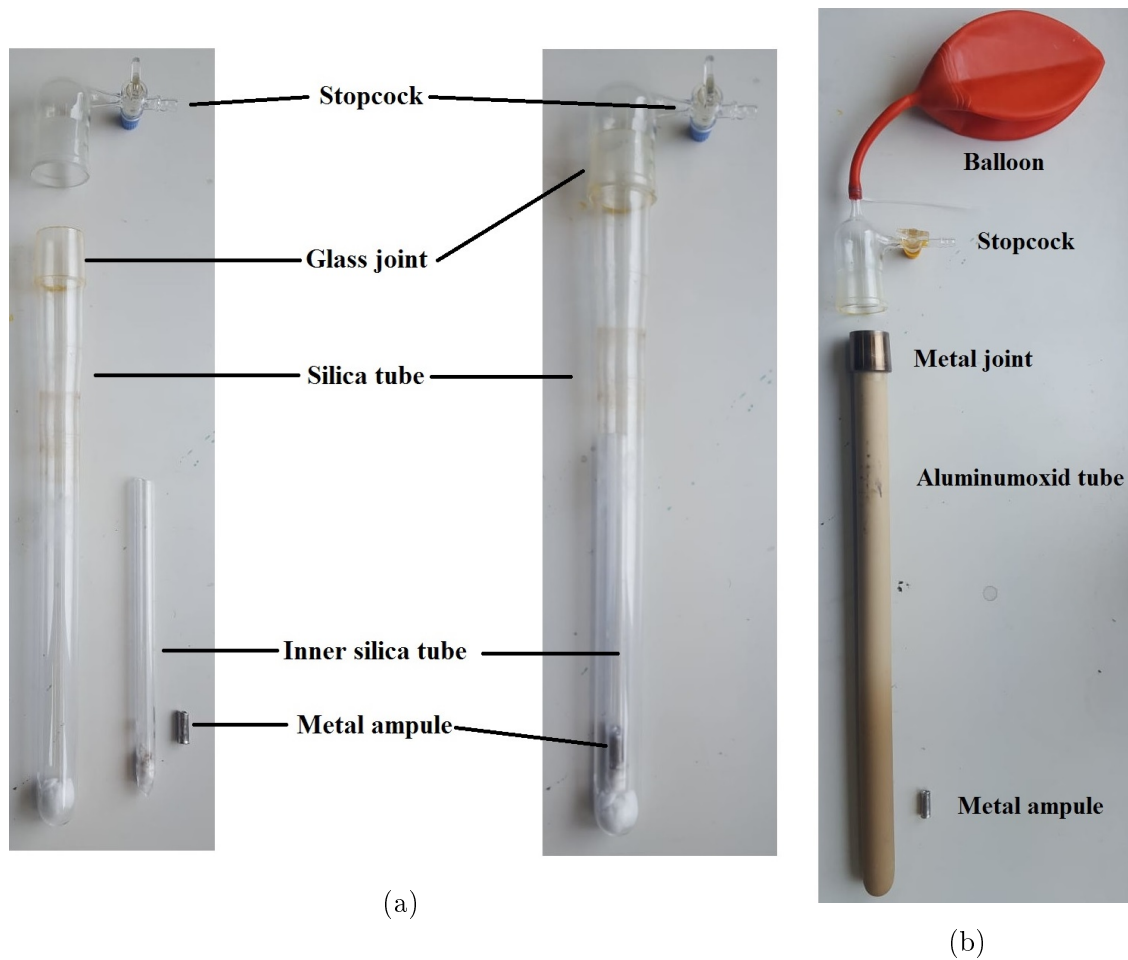


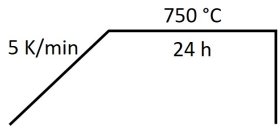
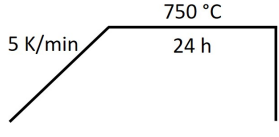
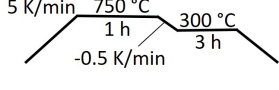
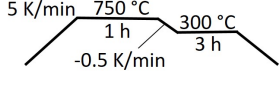
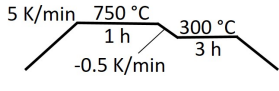
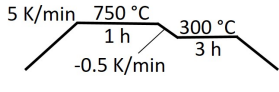
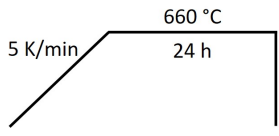
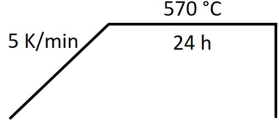
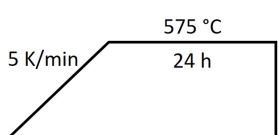
Figure 2.1: (a) Used silica tube showing all used parts next to each other and assembled silica tube. (b) Used disassembled aluminumoxid tube.

a glass cap with an attached balloon for pressure compensation shown in Figure 2.1 was used. After placing the metal ampule in the aluminumoxid tube, it was evacuated and flushed with Ar gas at least three times each ending with Ar gas. The tube was placed in a vertical resistance tube furnace. After ending the synthesis the tube was opened inside of the furnace and the metal ampule was quickly dumped in a bowl containing ice and water.

2.6.3 Temperature Programs

In Table 2.2 are all temperature programs for all furnace synthesis given.

Table 2.2: Compound, weighted materials, ampule material, kind of reaction tube and temperature program for all furnace syntheses

Compound (Chapter)	Starting Materials	Ampule	Reaction Tube	Temperature program
$\text{Li}_{14}\text{Ni}_{8+x}\text{Ge}_{9-x}$ (5.2)	Ni+Ge (pre-melted), Li	Nb	Silica	
$\text{LiNi}_{1+x}\text{Ge}$ (5.3)	Ni+Ge (pre-melted), Li	Nb	Silica	
$\alpha\text{-Li}_2\text{Ag}_{0.8}\text{Ge}_{1.2}$ (6.3)	Li, Ag, Ge	Ta	Silica	
$\alpha\text{-Li}_{2.53}\text{AgGe}_2$ (6.5)	Li, Ag, Ge	Ta	Silica	
$\alpha\text{-Li}_2\text{AgGe}$ (6.5)	Li, Ag, Ge	Ta	Silica	
$\alpha\text{-Li}_{13}\text{Ag}_5\text{Si}_6$ (7.1.4)	Li, Ag, Si	Ta	Corundum	
$\beta\text{-Li}_2\text{Ag}_{0.8}\text{Ge}_{1.2}$ (6.2)	$\alpha\text{-Li}_2\text{Ag}_{0.8}\text{Ge}_{1.2}$	Ta	Corundum	
$\gamma\text{-Li}_{2.53}\text{AgGe}_2$	$\alpha\text{-Li}_{2.53}\text{AgGe}_2$ (6.4)	Ta	Corundum	
$\beta\text{-Li}_{13}\text{Ag}_5\text{Si}_6$ (7.2)	$\alpha\text{-Li}_{13}\text{Ag}_5\text{Si}_6$	Ta	Corundum	

2.7 Experimental Author Contribution

Table 2.3: Experimental Contributions of other people for this thesis

Person	Compound (Chapter)	Contribution
A. Henze	$\text{Li}_{14}\text{Ni}_{8+x}\text{Ge}_{9-x}$ (5.2)	Synthesis, SC measurement and refinement, EDX measurement
M. F. Groh, S. P. Emge and K. Griffith	Li-Ag-Ge-System (6)	NMR-measurements
L. M. Scherf and T. Restle	$\text{Li}_6\text{B}_{18}\text{Li}_3\text{N}$ (8)	All experimental work
T. Restle	Li_3TrP_2 (9.2), Na_7TaP_4 (9.3)	All experimental work
K. Mayer	$\text{KBi}\cdot\text{NH}_3$ (9.4.2)	All experimental work
K. Mayer	$[\text{SnBi}_3^{5-}]$ (9.5)	All experimental work
B. Witzel	$[\text{TM}@\text{Tt}_9]$ (10.2)	All experimental work
F. Geitner	$[(\text{Ge}_9\{\text{Si}(\text{TMS})_3\}_2)^t\text{Bu}_2\text{P}]$ (10.3.1)	All experimental work
M. Giebel	$[(\text{Si}/\text{Ge})_9\{\text{Si}(\text{TMS})_3\}_3]^-$ (10.3.2)	All experimental work
T. Henneberger	$[\text{Ge}_4\text{HZn}(\text{Ph})_2]^{3-}$ (10.3.3)	All experimental work
Antti Karttunen		Basis sets for solid state calculations

Characterization

3.1 Single Crystal X-ray Diffraction

For structure determination Single-crystal X-ray Diffraction (SC-XRD) was used. This tool is one of most convenient way for structure solution of newly found compounds.

In the glovebox a few milligram of the sample was transferred to a petri-dish and a drop of perfluorinated ether was added on top. In the ether a crystal was carefully selected using a microscope and separated from the sample. The selected crystal was carefully mounted on a glass needle and transferred into a glass capillary (diameter=0.1 mm or 0.3 mm depending on the crystal size). Subsequently the glass capillary was sealed using a electrically heated tungsten wire and mounted on a StadiVari diffractometer (STOE & Cie).

The StadiVari diffractometer is equipped with a fine focused radiation source and a Dectris Pilatus 300 K detector.

Structures were solved with direct methods with the ShelXS software and refined with full-matrix least squares on F^2 with the program ShelXL.^[2] Graphical illustration of crystal structures was done with the Diamond 3 software.^[3]

3.2 Powder X-ray Diffraction and RIETVELD-Refinement

Powder X-ray Diffraction (P-XRD) was used for two different purposes identifying crystalline materials.

First it was used to determine already know compounds in the sample by comparing the theoretical pattern of known compounds with the measured diffractogram of the sample.

The second purpose was to determine newly found compounds, where no SC-XRD was possible due to bad crystal quality, or reassure the structure, which was found by SC-XRD. For this purpose a RIETVELDT-refinement was carried out using the obtained P-XRD data.

For both procedures small amounts of the sample was thoroughly grounded in an achate mortar to secure very small grain size. This is important to obtain a better statistical intensities of the crystalites and therefore sharper peaks in the diffractogram. Additionally the small grain size is important in order to transfer the powder to a glass capillary (diameter=0.3 mm). Usage of bigger capillaries was avoided, because this would cause also bigger absorption problems. The filled capillary was sealed using an electrically heated tungsten wire and additionally sealed by capillary wax.

Depending on the elements $\text{Mo}_{K\alpha 1}$ ($\lambda = 0.71073 \text{ \AA}$) or $\text{Cu}_{K\alpha 1}$ ($\lambda = 1.54056 \text{ \AA}$) radiations was chosen. Each diffractometer was equipped with a Ge(111) monochromator and a Dectris Mythen 1K detector. Data were calibrated with an external Si standard to ensure comparability of cell parameters.

For data processing the software WinXPow, Origin and Jana2006 was used.^[4-6]

3.3 Thermal Analysis

In order to investigate the thermal behavior Differential Scanning Calorimetry (DSC) was performed. Different phase transitions such as melting, crystallization, phase changes and decompositions can be observed in those measurements.

About 50 to 100 mg of sample was filled in an custom-built pre-cleaned niobium crucible. The crucibles were obtained from the precision mechanics workshop at TU Munich. The loaded crucible was sealed by arc welding and an additional empty crucible was sealed as reference. The measurement was performed by Tassilo Restle on a DSC 404 Pegasus (NETZSCH). The heating circles are given in the respective chapter of the investigated compound.

The crucibles were loaded into the measuring chamber of the DSC machine, which was subsequently evacuated and refilled with Ar three times each. Measurements were then carried out under a constant gas flow of $75 \text{ mL}\cdot\text{min}^{-1}$. The PROTEUS Thermal Analysis software package was employed for measurement control and evaluation.^[7] Additionally Origin was used for data processing.^[5]

3.4 Nuclear Magnetic Resonance (NMR) Spectroscopy

For all ^6Li -NMR measurements a Bruker 700 MHz (16.4 T) magnet with Avance III console and a single-channel Bruker 4 mm X MAS probe was used with a regular zg/one-pulse pulse program and a single $\pi/2$ pulse, a delay of 30-120 s between pulses and an MAS speed of 10-12.5 kHz was applied.

The NMR samples were prepared in an Ar-filled MBraun glovebox ($p(\text{O}_2)/p^0 < 1$

ppm, $p(\text{H}_2\text{O})/p^0 < 1$ ppm) and were mixed and grinded with dried KBr in a ratio of 1:1 (by weight) in agate mortars. The samples were packed into standard 4 mm ZrO_2 rotors with Vespel or ZrO_2 caps.

For raw data handling and processing Bruker Topspin (v3.2 and v3.6.1) was used.^[8] All experiments were carried out and analyzed by Dr. M. F. Groh, S. P. Emge and K. Griffith in the chair of C. P. Grey (University of Cambridge).

Computational Methods

The significance of computational chemistry increases since methods of solving the many body problem improve constantly. Predicting and explaining properties of new materials, such as metallic behavior, Li-mobility or just fundamental bonding principles get more accurate and computational resources are available to solve larger systems without taking weeks of calculations. Supporting experimental work with computational methods has become a standard in chemistry to reassure, interpret and understand experimental data. Overall, computational chemistry helps experimental chemists to explain their structures behavior and giving new ideas for hypothetical compounds, which might be able to synthesize. Therefore, in this thesis a major part was to investigate the experimentally gained compounds by computational work.

4.1 Theoretical Background

This chapter focuses on the theoretical background of the computational work in this thesis. It will discuss different methodologies like Hartree-Fock, Møller-Plesset perturbation theory, coupled cluster, and density functional theory for solving the many electron problem approximately.^[9]

4.1.1 The Electronic Structure Problem

The starting point and basis of computational chemistry was the development of the Schrödinger wave function (Ψ). This function contains all information of a system, but does not refer to any physical meanings. But by calculating the scalar product with its complex conjugate $\Psi(r, t)\Psi^*(r, t)$ it bears the idea where to find a particle at a position r at the time t . This concept is called the Born interpretation or Born rule. The time-dependent Schrödinger's equation is given by equation 4.1.

$$i\hbar\frac{\delta}{\delta t}\Psi(r, t) = \hat{H}\Psi(r, t) \quad (4.1)$$

Where \hat{H} is the Hamiltonian operator for a system of nuclei and electrons. Assuming \hat{H} does not depend on time, $\Psi(r, t)$ can be written as a product $\psi(r)\phi(t)$. This allows us to write a time-independent Schrödinger equation 4.2.

$$\hat{H}\psi(r) = E\psi(r) \quad (4.2)$$

where $\psi(r)$ is the eigenfunction of the time-independent Hamiltonian with eigenvalue E . The Hamiltonian includes nuclei and electrons, which are described by position vectors R_A and r_i , respectively. Distances between the i th electron and A th nucleus is given by r_{iA} . The same is notation is used between nuclei and electrons. Therefore, equation 4.3 describes \hat{H} for a N electron and M nuclei system.

$$\hat{H} = -\sum_{i=1}^N \frac{1}{2} \nabla_i^2 - \sum_{A=1}^M \frac{1}{2M_A} \nabla_A^2 - \sum_{i=1}^N \sum_{A=1}^M \frac{Z_A}{r_{iA}} + \sum_{i=1}^N \sum_{j>i}^N \frac{1}{r_{ij}} + \sum_{A=1}^M \sum_{B>A}^M \frac{Z_A Z_B}{R_{AB}} \quad (4.3)$$

where M_A is the ratio of the mass of nucleus A to the mass of an electron, and Z_A is the atomic number of nucleus A . ∇_i^2 and ∇_A^2 are the Laplacian operators, which involve differentiation with respect to the coordinates of the i th electron or A th nucleus. The Hamiltonian can be divided in five terms. The first one is assigned to the kinetic energy of electrons, the second one refers to the kinetic energy of nuclei, third is the coulomb attraction between electrons and nuclei and forth and fifth are terms of the repulsion between electrons and nuclei, respectively. Unfortunately equation 4.2 can only be solved exactly for one-electron systems. Therefore, approximations have to be used to solve the equation as accurate as possible for many-electron systems.

4.1.2 The Born-Oppenheimer Approximation

This approximation is central in computational chemistry. Two fundamental principle are used by the Born-Oppenheimer approximation.^[10]

- Nuclei are much heavier than electrons
- Nuclei are much slower than electrons

This allows the approximation of electrons moving through a field produced by fixed nuclei. Therefore, it means the second term of equation 4.3 can be neglected, and the last term can be treated as a constant for a nuclear coordinates. The resulting terms are called electronic Hamiltonian \hat{H}_{elec} given in equation 4.4.

$$\hat{H}_{elec} = -\sum_{i=1}^N \frac{1}{2} \nabla_i^2 - \sum_{i=1}^N \sum_{A=1}^M \frac{Z_A}{r_{iA}} + \sum_{i=1}^N \sum_{j>i}^N \frac{1}{r_{ij}} \quad (4.4)$$

Therefore, using the electronic Hamiltonian in the Schrödinger equations 4.5 gives the electronic wave function (equation 4.6).

$$\hat{H}_{elec}\psi_{elec} = E_{elec}\psi_{elec} \quad (4.5)$$

$$\psi_{elec} = \psi_{elec}(r_i, R_A) \quad (4.6)$$

The wave function describes the motion of the electrons. Thereby, it depends *explicitly* on the coordinates of the electrons (r_i) by also *parametrically* on the coordinates of the nuclei (R_A). This also applies for the electronic energy. In the end, the total energy is given by:

$$E_{tot} = E_{elec} + \sum_{A=1}^M \sum_{B>A}^M \frac{Z_A Z_B}{R_{AB}} \quad (4.7)$$

However, one should always have in mind that the Born-Oppenheimer approximation has its limits and is not universality valid.

The most difficult part of solving equation 4.5 is the electron-electron interaction ($\frac{1}{r_{ij}}$). This includes all the quantum effects of the electrons. Many Methods have been developed to have a approximate solution of this part. These are briefly described in chapter 4.1.5.

4.1.3 Spin Orbitals and Slater Determinants

Noteworthy is, that to completely specify an electron, it is required to relate a spin (ω) to each electron. Therefore, two spin functions are introduced: $\alpha(\omega)$ and $\beta(\omega)$ corresponding to spin up and down. This spin functions are complete and orthonormal.

All together these are described by four coordinates . x will describe all four four coordinates collectively ($x = \{r, \omega\}$). Two types of orbitals are introduced therefore:

- *spatial orbitals* $\psi_i(r)$: Is a function of the position vector r in space. The spatial distribution $|\psi_i(r)|^2 dr$ is the probability of finding electrons in a small volume element dr .
- *spin orbital* $\chi(x)$: Describes both spin and space (spatial) coordinates. For each spatial orbital only two spin orbitals can be assigned ($\chi(x) = \psi(r)\alpha(\omega)$ or $\chi(x) = \psi(r)\beta(\omega)$).

Constructing a wave function of N electrons a basic form could be as a product of N spin orbitals $\chi(x)$ (Hartree product). But since electrons are considered fermions, they obey the Pauli exclusion principle or antisymmetry. The meaning of this is that the wave function of a many-electrons system has to be antisymmetric with respect to the interchange of the coordinates x shown in equation 4.8.

$$\phi(x_1, \dots, x_i, \dots, x_j, \dots, x_N) = -\phi(x_1, \dots, x_j, \dots, x_i, \dots, x_N) \quad (4.8)$$

To fulfill the requirement of antisymmetry Slater determinants are useful. They satisfy the antisymmetric condition through an appropriate linear combination of Hartree products, which are non-interacting electron function. The Slater determinant for a N electron system is given in equation 4.9.

$$\Psi(x_1, x_2, \dots, x_N) = (N!)^{-1/2} \begin{vmatrix} \chi_i(x_1) & \chi_j(x_1) & \dots & \chi_k(x_1) \\ \chi_i(x_2) & \chi_j(x_2) & \dots & \chi_k(x_2) \\ \cdot & \cdot & & \cdot \\ \cdot & \cdot & & \cdot \\ \cdot & \cdot & & \cdot \\ \chi_i(x_N) & \chi_j(x_N) & \dots & \chi_k(x_N) \end{vmatrix} \quad (4.9)$$

By interchanging the coordinates of two electrons, which equals interchanging the rows, The Slater determinant will change the sign. Furthermore, the Slater determinant also include, that there cannot be a electron with the same spatial and spin function. This could mean two identical columns and leads to the determinant being zero. A convenient way to notate a Slater determinant is by only showing the diagonal elements given in equation 4.10.

$$\Psi(x_1, x_2, \dots, x_N) = |\chi_i(x_1)\chi_j(x_2) \cdots \chi_k(x_N) \rangle \quad (4.10)$$

Since the order of electrons is always x_1, x_2, \dots, x_N it results in equation 4.11

$$\Psi(x_1, x_2, \dots, x_N) = |\chi_i\chi_j \cdots \chi_k \rangle \quad (4.11)$$

4.1.4 Hartree-Fock in a Nutshell

The Hartree-Fock approach is one of the central approaches in quantum chemistry and is also the basis of many other more accurate methods.

The Hartree-Fock method uses a Slater determinant as an approximation of the ground-state wave function of a N -electron system (equation 4.11). As explained in chapter 4.1.3 is assures the the Pauli exclusion principle.

By using the variation principle the "best" wave function is evaluated, which is given by the lowest possible energy (equation 4.12).

$$E_0 = \frac{\langle \Psi_0 | \hat{H} | \Psi_0 \rangle}{\langle \Psi_0 | \Psi_0 \rangle} \quad (4.12)$$

The energy is minimized by the choice of spin orbital. By this method the Hartree-Fock equation 4.13 is obtained.

$$f(i)\chi(x_i) = \epsilon\chi(x_i) \quad (4.13)$$

where $f(i)$ is an effective one-electron operator, which is called the *Fock* operator. It is described in equation 4.14.

$$f(i) = -\frac{1}{2}\nabla_i^2 - \sum_{A=1}^M \frac{Z_A}{r_{iA}} + \nu^{HF}(i) \quad (4.14)$$

The average potential experienced by the i th electron due to other electrons is given by $\nu^{HF}(i)$. This is the basis to overcome the many-electron problem in the Schrödinger equation and is replaced by a one-electron problem in which electron-electron repulsion is treated like a average potential of all electrons on one electron. To solve the Hartree-Fock equation a iterative approach is used and the procedure is called self-consistent field (SCF). A initial guess of spin orbitals is needed and is used to calculate the average field seen by each electron. The eigenvalue problem is solved for a new set of spin orbitals. These new spin orbitals are used for the next cycle to calculate the average field and is repeated until a pre-determined convergence criterion is reached.

4.1.5 Post-Hartree-Fock methods

Hartree-Fock was used as basis for other wave-function based methods. Those methods try to solve the major problem, that Hartree-Fock method neglects electron correlation beyond exchange. Löwdin defines the missing electron correlation as difference between the exact energy and the Hartree-Fock energy of a many-electron system (equation 4.15).^[11]

$$E_{corr} = E_{exact} - E_{HF} \quad (4.15)$$

E_{corr} is always negative since E_{exact} is always lower than E_{HF} . Although the correlation energy is usually a very small part of the total energy it can be crucial if it comes to relative energies. Since a computational chemist mostly looks at relative energies for physical and chemical interest this part shouldn't be easily neglected. For example Hartree-Fock is not able to describe dissociation of H_2 sufficiently.^[12]

Three methods, which try to overcome this problem, are configuration interaction (CI),^[13] Møller-Plesset perturbation theory^[14,15] and coupled cluster (CC).^[16,17] But due increase of system size those methods also become very expensive.

CI uses a linear combination of Slater determinants rather than a single one. By doing this more than one electron configurations are considered for the wave functions e.g. excited states. In case of *Full-CI* all excited states are considered.

Møller-Plesset perturbation theory describes the electron correlation as a perturbation. Usually second order (MP2) perturbations are used.

CC uses a cluster-operator to treat the electron correlation problem.

4.1.6 Basis Set

In order to solve the electronic Schrödinger equation basis set as initial guess are necessary. We are using basis sets, which describe the electronic structure of single atoms. To describe this electronic structure basically any type of functions are possible. Still, one has to consider, that some might be more appropriate than others. The basis set should allow for low computational cost, but still be as accurate as possible. Since the basis set also will describe some physical behavior it should follow some basics like becoming zero, if the distance between nucleus and electron becomes too large.

Gaussian functions proved to be very useful for basis sets in the early years of computational quantum chemistry due to the fact that single Gaussian functions (primitive Gaussian functions, p-GTO) can be contracted to new Gaussian function (contracted Gaussian function, c-GTO) and the functionals can be solved analytically. This means a reduced computational effort since several coefficients turn into one. In equation 4.16 and 4.17 the general form of Gaussian functions and its contraction is shown, respectively.

$$g(\zeta, l_x, l_y, l_z, x, y, z) = N e^{-\zeta r^2} x^{l_x} y^{l_y} z^{l_z} \quad (4.16)$$

$$g(c) = \sum_i^k a_i g(p) \quad (4.17)$$

where $g(c)$ is c-GTO and $g(p)$ is p-GTO.

The minimum basis set of an atom is the one according to the number of atomic orbitals. In case of an hydrogen this would only require a single s -function. In case of first row p -block elements two s -functions and a set of p -functions are required. But for practical use the minimum basis set is usually not sufficient. The next level of basis set is called double zeta basis (DZ). For this basis set type all basis functions are doubled. Using three sets of basis function per atomic orbital this is called triple zeta (TZ), which is the type used in this thesis.

But there are still further improvements of basis set like polarization or diffuse functions. This is usually needed for higher basis sets like TZ. The polarization allows for distortions by adding functions with higher angular momentum. Hydrogen, for example, would be also described by p orbitals. It is called polarization, because consider a hydrogen in an uniform electric field. The electron can now be attracted to one direction causing a distortion in the spherical s -orbital shape. The atom has been polarized.

Throughout this thesis mostly TZVP (**T**riple **Z**eta **V**alence **P**olarization) was used. For molecular calculations the Karlsruhe basis sets were used (def2-TZVP) and for periodic systems a basis set derived from the Karlsruhe basis set was used. **Antti**

Karttunen from Aalto university did all manipulation of the Karlsruhe basis sets. Other used basis set were def2-SVP (Split valence polarization) and def2-TZVPP (Valence triple-zeta with two sets of polarization functions). All basis set are given in the appendix 13.

4.1.7 Density Functional Theory (DFT)

The above mentioned Hartree-Fock and Post-Hartree-Fock methods are all many-body wave-function based. This means especially for larger system a huge computational effort, since $3N$ spatial variables and spin variable are needed, where N is the number of electrons. This exceed the computational resources for post-Hartree-Fock methods quickly and computational analysis would be limited to small systems. Density Functional Theory (DFT) offers a solution for this problem. This method is not electron wave-function but electron density ($\rho(r)$) based. This central quantity can be described by only 3 dimensions regardless of the system size. For this reason nowadays DFT is the most used quantum chemical approach. In the follow sections the black-box DFT is explained briefly. DFT methods were used throughout this thesis.

Thomas and Fermi first worked on using the electron density.^[18,19] The electron density is defined in equation 4.18 and is the probability of finding any of N electron in a certain range of volume r .

$$\rho(r) = N \int \dots \int |\Psi(x_1, x_2, \dots, x_N)| ds_1 x_2 \dots x_N \quad (4.18)$$

By integrating over the electron density in this certain volume the total number of electrons is given (equation 4.19).

$$N = \int \rho(r) dr \quad (4.19)$$

Like in the wave-function based methods we now define single therms of the energy like kinetic energy of the electrons, electron-electron interaction and electron-nucleus interaction. Therefore, the kinetic energy is derived from quantum statistical theory of a uniform electron gas given in equation 4.20 with $C_F = \frac{3}{10}(3\pi^2)^{2/3} = 2.871$.

$$T[\rho] = C_F \int \rho^{5/3}(r) dr \quad (4.20)$$

The total energy is given in equation 4.21 including electron-electron interaction and electron-nucleus interaction as second and last therm.

$$E[\rho] = C_F \int \rho^{5/3}(r) dr - Z \int \frac{\rho(r)}{r} dr + \frac{1}{2} \int \int \frac{\rho(r_1)\rho(r_2)}{|r_1 - r_2|} dr_1 dr_2 \quad (4.21)$$

This shows, that it is possible to determine the energy by only using the electron density.

After the beginning of thinking about electron density instead of a wave function Hohenberg and Kohn published two major results in 1964:^[20]

- for any system of interacting particles, the electron density uniquely determines the external potential, thereby implying that the ground state energy of the system is a unique functional of the electron density
- variational principle can be applied

But the theorem lacks how to obtain ground state energy from electron density and electron density itself. Therefore, Kohn and Sham introduced an auxiliary system of non-interacting electrons. The electrons are influenced by an effective one-electron potential, the so-called Kohn-Sham potential.^[21] Using the functional of the electron density the ground state energy of the real system can be expressed shown in equation 4.22.

$$\begin{aligned} E(\rho) &= E^T(\rho) + E^V(\rho) + E^J(\rho) + E^{XC}(\rho) \\ &= E^T(\rho) + \int d^3q \rho(r) \nu_0(r) + \frac{1}{2} \int d^3r' \frac{\rho(r)\rho(r')}{|r-r'|} + E^{XC}(\rho) \end{aligned} \quad (4.22)$$

where $E^T(\rho)$ is the kinetic energy of the auxiliary system, $E^V(\rho)$ is the electron-nucleus attraction, $E^J(\rho)$ is the Coulombic repulsion between electrons and $E^{XC}(\rho)$ is the exchange-correlation energy. The last part includes all corrections to the first three terms.

The ground state electronic density of the real system can be described with the auxiliary one-electron orbitals $\varphi(r)$

$$\rho_0(r) = \sum_{i=1}^N |\varphi_i(r)|^2 \quad (4.23)$$

The one-electron orbitals $\varphi(r)$ are called Kohn-Sham orbitals and are solved according to the methodology of the Hartree-Fock approach solving the one-electron Kohn-Sham equation 4.24.

$$\left(-\frac{\nabla^2}{2} + \nu_s[\rho](r)\right)\varphi_i(r) = \epsilon_i\varphi_i(r) \quad (4.24)$$

In the case of $E^{XC}(\rho)$ the exact form of this function is unknown. Therefore, several main approaches have been developed to approximate this term like:

- local density approximation (LDA)
- generalized gradient approximation (GGA)
- hybrid methods

For all approaches the term is split into a sum of exchange $E^X(\rho)$ and correlation $E^C(\rho)$. The simplest approximation is LDA, which assumes that electron density behaves like a uniform electron gas. The value of the potential at some point depends only on the value of electron density at that point. This can be improved by taking the spin into account ending up with local spin density approximation (LSDA), where α and β spin is given as a sum of electron densities. Still, this method is not sufficient for a lot of systems and improvements are made by GGA method. This method includes the gradient of electron density not just the electron density itself. The last method is a combination of DFT and wave-function method and therefore a hybrid of both. Fractions of Hartree-Fock exchange are combined with LDA/GGA-type. These type of functional is widely used in computational chemistry and also for most systems in this thesis, namely the PBE0^[22,23] functional by Perdew, Burke and Ernzerhof. But also a GGA functional, PBE,^[22,23] is used for some calculations in this thesis in particular for metallic systems.

4.2 Periodic Systems

All calculations on periodic systems were carried out with the CRYSTAL program package (versions CRYSTAL14 or CRYSTAL17).^[24,25]

4.2.1 Structure Modeling

Several periodic systems were investigated by computational analysis. For experimentally synthesized structures the initial structure was taken from the experimental findings. In case of superstructure building symmetry reduction was done with the help of Bilbao Crystallographic Server^[26–28] and/or International Tables for Crystallography.^[29] For structure manipulation like adding vacancies or displacing atoms the ATOMREMO, ATOMSUBS, and ATOMDISP tools implemented in CRYSTAL were used. The initial structure of chemi-inspired models were taken from the original experimental structure and atoms were substituted manually in the input file.

FINDSYM was used to determine the space group of superstructures, derived structures or after any structure manipulations.^[30] For visualization JMol,^[31] Diamond 3.0^[32] and VESTA^[33] were used.

4.2.2 Used Functionals and Basis Sets

In chapter 4.1.7 it is already mentioned, that DFT was used throughout this thesis. In case of periodic systems the LCAO approach is used dependent on the lattice

constant for each crystalline orbital ψ_i . As there are infinite numbers of atoms due to the periodicity the translational symmetry is used. The system does not change as long as shifts are n times the lattice constant, when n is an integer. With this information the Bloch's theorem or Floquet's theorem in case of one-dimension can be derived given in equation 4.25.

$$\psi_k(r) = e^{ikr}u_k(r) \quad (4.25)$$

Where k is the wave vector and $u_k(r)$ is a periodic function with the same periodicity as the crystal. Using the concept of plane waves with wave vector q it shows that crystalline orbitals are a linear combination of Bloch functions (equation 4.26).

$$\psi(r) = \sum_q c_q e^{iqr} \quad (4.26)$$

Using DFT methods the choice of an appropriate functional is very important. For example in case of band structure calculations the GGA functional PBE tends to underestimate the band gap, whereas the hybrid functional PBE0 tends to overestimate the band gap. PBE0 with 25% exact Hartree-Fock exchange has proven to have good performance for those systems investigated in this thesis.^[22,23]

The general concept of basis sets has been introduced in chapter 4.1.6. The SVP and TZVP basis set used for periodic systems are created by Prof. Dr. Antti Karttunen, Aalto University (Finland). All basis sets are given in the appendix. In case of heavier elements, like Bi, a scalar-relativistic effective core potential was used. The core electrons were described by a pseudopotential instead of treating them as single particles. Through this modification scalar relativistic effects were taken into account and a decrease of computational time was achieved.

4.2.3 Structure Optimization and Frequency Calculation

If not stated otherwise all periodic systems were optimized with CRYSTAL14 or CRYSTAL17 within the constraints imposed by the space group symmetry. For some structures the geometry optimization did not fully converge. In this case the lowest point in energy was chosen and a single-point calculation was subsequently carried out.

For non-conducting compounds a frequency calculation was carried out in order to determine the character of the stationary point at Γ -point. Additionally Raman spectra were calculated in case experimental data was available of the structure.

Optimization Procedure

For the geometry optimization a Quasi-Newton optimization was applied. This means every time the total energy is calculated gradients are evaluated and a second

derivative matrix, so-called Hessian matrix, is build using the gradients. Therefore, all distances and angles of the structures are varied within constraints given by the space group symmetry until a local minimum of the total energy due to the convergence criteria is achieved.

As initial Hessian matrix a model Hessian proposed by Schlegel with an update by using the BFGS algorithm is used.^[34]

For each Newton step direction and length of step is controlled by the Trust Radius scheme. In some cases NOTRUSTR was used, which removes the trust radius control.

Choice of k -point Sampling

In the crystal program package shrinking factors are used to define the k -point sampling of the first Brillouin zone. For isotropic unit cells two factors are needed IS and ISP. The factor IS generates a commensurate grid of k points in reciprocal space according to Monkhorst and Pack.^[35] ISP is used for a denser k point net (Gilat net) in the evaluation of the Fermi energy and density matrix. Calculations become more accurate with a higher k -point sampling, but calculations also need a higher computational effort with a higher k -point sampling. The appropriate IS was usually chosen due a general scheme shown in Table 4.1. Usually, first calculations were also carried out with a higher shrink than listed to assure that the actual shrink is accurate. In case of highly anisotropic unit cells, anisotropic shrinking factors were used for the different cell parameters. In case of conducting state of the compound ISP was chosen to be 2*IS, if the state was non-conducting ISP=IS.

Table 4.1: Shrink usually used according to lattice constant a , b or c of primitive cell

a, b or c / Å	IS
<4	12
4-6	8
6-8	6
8-12	4
12-18	2
<18	1

Numerical Accuracy and Computational Parameters

For all calculations on periodic systems a tight tolerance factor (TOLINTEG) of 8, 8, 8, 8, 16 was used. Those parameters control the accuracy of the calculation of the bielectronic Coulomb and exchange series. When the overlap between two atomic orbitals becomes smaller than 10^{-ITOL} , the corresponding integral is disregarded or evaluated in a less precise way for ITOL is one of the five parameters defined as:

- (1) overlap threshold for Coulomb integrals
- (2) penetration threshold for Coulomb integrals

- (3) overlap threshold for HF exchange integrals
- (4) pseudo-overlap
- (5) pseudo-overlap

Additional keywords

For possible conducting states or other reasons some keywords were added to help the system to converge:

- (1) FMIXING: percent of Fock/KS matrices mixing
- (2) SMEAR: a finite temperature Fermi smearing of the electronic occupation
- (3) BROYDEN: energy stabilization

The keywords are described in detail in the Crystal manual.^[36]

Frequency Calculation

In general the same settings were used for geometry optimization and frequency analysis.

Generally, for the frequency calculation two displacements for each atom along each Cartesian direction was used (NUMDERIV 2).

In case of imaginary frequencies the structure was scanned along the imaginary frequency using SCANMODE and reoptimized with this distortion in a lower space group according to the distortion. Those procedure was repeated until no imaginary frequency was present.

4.2.4 One Electron Properties

Band structure, density of states (DOS) and band gaps were obtained by CRYSTAL14 or CRYSTAL17 properties package. For visualization a python script by Marco Lorenz and changed by Jasmin Dums was used.^[37] For band structure analysis paths derived from Curtarolo *et al.* were used, if not stated otherwise.^[38]

4.2.5 Property Calculations

After calculating the total energy of a system and therefore obtaining the density matrix P , it is possible to derive further properties of the system for example charge distribution. A variety of methods are available for doing a so-called population analysis. In this thesis three different methods were used.

A population analysis was performed for all compounds. Therefore one, two or all of the following methods were used:

- (1) Mulliken's atomic gross charges^[39]
- (2) Natural Population Analysis^[40]
- (3) Hirshfeld Analysis^[41]

(1) is always carried out after a optimization or single point calculation. The methods bases on the relationship between charge density and number of electrons. The approach of Mulliken is to substitute the spin orbitals for the atom centered basis functions. That allows to derive equation 4.27, in which electron density is assigned to certain atom centered basis functions:

$$N_{el} = \sum_{\mu} \sum_{\nu} P_{\mu\nu} S_{\nu\mu} = \sum_{\mu} (PS)_{\mu\mu} \quad (4.27)$$

The net charge q_A of the atom A is obtained by subtraction of PS from the nuclear charge Z_A of the respective atom (equation 4.28).

$$q_A = Z_A - \sum_{\mu \in A} (PS)_{\mu\mu} \quad (4.28)$$

This method is rather basis-set dependent and susceptible to misinterpretations.^[42] Therefore, to interpret the values always another method was used to check the results.

(2) is a second wave-function based method. It uses so-called "natural orbitals" and is less basis set dependent.^[43] The third used approach (3). This method is based on partitioning the total electron density distribution of the system to its constituent atoms with overlapping atomic contributions.

4.3 Molecular Systems

For all non-periodic systems the Gaussian09 or TURBOMOLE program package was used.^[44,45]

4.3.1 Structure modeling

The molecular units were obtained from experimental data using JMol and Diamond 3.0. Long residues, which were substituted by smaller ones were drawn by hand and subsequently optimized. This was also done for any kind of structure modification.

4.3.2 Functional and Basis set

The same functional were used as for periodic system described in chapter 4.2.2. In case of basis sets also the Karlsruhe basis set were used, but additionally the basis set def2-TZVPP was taken for some calculations.

4.3.3 Optimization and Frequency Calculation

Using the program package TURBOMOLE the molecules were optimized within the constraints imposed by the point group. In case of Gaussian09 no constraints were applied. In some cases the structure could not be optimized, therefore only a single point calculation using the structural parameters of the experimental data was performed.

For some systems in Gaussian09 the standard self-consistent field (SCF) did not converge and therefore a quadratically convergence SCF procedure was applied (keyword SCF=XQC).

For TURBOMOLE calculations a Multipole-accelerated resolution-of-the-identity technique was used to speed up the calculations.^[46-48]

Numerical Accuracy and Computational Parameters

For Gaussian09 calculations normal convergence criteria were used (OPT). For special cases also OPT=TIGHT or OPT=VERYTIGHT and a tighter DFT integration grid (GRID=ULTRAFINE) were used.

For Turbomol calculations always a tighter DFT integration grid m_4 was used. Additionally, resolution-of-the-identity (RI) approximation and multipole-accelerated RI-J approximation was always switched on.

Charge Compensation

In case of TURBOMOLE the negative charges of molecules was countered by using a continuum solvation model (conductor-like screening model, COSMO).^[49]

Using the program package Gaussian09 a solvent field generated by a polarized continuum model (keyword SCRF=PCM) was applied.^[50] The solvent field of water was used, if not stated otherwise in the specific sections.

Frequency Calculation

In general the same settings were used for geometry optimization and frequency analysis. This method was used for two reasons: (1) to determine the character of the stationary point and (2) for Raman investigations.

4.3.4 Property Calculations

As already described in chapter 4.2.5 for periodic systems the same population analysis methods were applied for non-periodic system: Mulliken's atomic gross charges, Natural Population Analysis and Hirshfeld Analysis.

Additionally, for some molecules a molecular orbital diagram was derived and evaluated. The information was gained from information in the checkpoint-file transferred to "cube-files" of Gaussian09 calculations or by the use of TmoleX, a graphical interface for TURBOMOLE, for TURBOMOLE calculations.

Further, electron localization function (ELF) and intrinsic bond orbitals (IBO) were analyzed for some cases.^[51]

References

- [1] A. Nash, P. Nash, *J. Phase Equilib.* **1987**, *8*, 255–264.
- [2] G. M. Sheldrick, *Acta Crystallogr. A.* **2008**, *64*.
- [3] K. Brandenburg, DIAMOND, Program for X-Ray Structure Analysis, **2005**.
- [4] WinXPOW V3.0.2.1. Darmstadt, **2011**.
- [5] OriginPro 9.1G, Northampton, MA, USA, **2013**.
- [6] V. Petricek, M. Dusek, L. Palatinus, *Z. Kristallogr. - Cryst. Mater.* **2014**, *229*, 345–352.
- [7] PROTEUS Thermal Analysis V4.8.2, Selb, **2006**.
- [8] Topspin, Software for NMR Spectral Analysis, Rheinstetten, Germany, **2019**.
- [9] A. Szabo, N. Ostlund, *Modern Quantum Chemistry*, Dover Publications, Inc., Mineola/New York, **1996**.
- [10] M. Born, R. Oppenheimer, *Ann. Phys.* **1927**, *84*.
- [11] P. O. Löwdin, *Adv. Chem. Phys.* **1959**, *2*, 207.
- [12] B. Santra, A. Michaelides, M. Scheffler, *J. Chem. Phys.* **2007**, *127*, 184104.
- [13] C. D. Sherrill, H. F. Schaefer, *Adv. Quantum Chem.* **1999**, *34*, 143–269.
- [14] A. P. Scott, L. Radom, *J. Phys. Chem.* **1996**, *100*, 16502–16513.
- [15] C. Möller, M. S. Plesset, *Phys. Rev.* **1934**, *46*, 618–622.
- [16] J. Čížek, *J. Phys. Chem.* **1966**, *45*, 4256–4266.
- [17] J. Čížek, J. Paldus, *Int. J. Quan. Chem.* **1971**, *5*, 359.
- [18] L. H. Thomas, *Proc. Camb. Phil. Soc.* **1927**, *23*, 542–548.

- [19] E. Fermi, *Rend. Accad. Lincei*. **1927**, *6*, 602.
- [20] P. Hohenberg, W. Kohn, *Phys. Rev.* **1964**, *136*, B864.
- [21] W. Kohn, L. J. Sham, *Phys. Rev.* **1965**, *140*, A1133.
- [22] J. P. Perdew, K. Burke, M. Ernzerhof, *Phys. Rev. Lett.* **1996**, *77*, 3865.
- [23] C. Adamo, B. F., *J. Chem. Phys.* **1999**, *110*, 6158–6170.
- [24] R. Dovesi, A. Orlando, A. Erba, C. M. Zicovich-Wilson, B. Civalleri, S. Casassa, M. Maschio, M. Ferrabone, M. De La Pierre, P. D’Arco, Y. Noel, M. Causa, M. Rerat, B. Kirtman, *Int. J. Quantum Chem.* **2014**, *114*, 1287.
- [25] R. Dovesi, A. Erba, R. Orlando, C. M. Zicovich-Wilson, B. Civalleri, L. Maschio, M. Rerat, S. Casassa, J. Baima, S. Salustro, B. Kirtman, *WIREs Comput. Mol. Sci.* **2018**, *8*, e1360.
- [26] M. I. Aroyo, J. M. Perez-Mato, D. Orobengoa, E. Tasci, G. de la Flor, A. Kirov, *Bulg. Chem. Commun.* **2011**, *43*, 183–197.
- [27] M. I. Aroyo, J. M. Perez-Mato, C. Capillas, E. Kroumova, S. Ivantchev, G. Madariaga, A. Kirov, H. Wondratschek, *Z. Krist.* **2006**, *221*, 15–27.
- [28] M. I. Aroyo, A. Kirov, C. Capillas, J. M. Perez-Mato, H. Wondratschek, *Acta Cryst.* **2006**, *A62*, 115–128.
- [29] *International Tables for Crystallography: Symmetry Relations between Space Groups, Vol. A1*, (Eds.: H. Wondratschek, U. Müller), **2004**.
- [30] H. T. Stokes, D. M. Hatch, *J. Appl. Cryst.* **2005**, *38*, 237–238.
- [31] Jmol 14.0.11, **2014**.
- [32] K. Putz, K. Brandenburg, *Diamond - Crystal and Molecular Structure Visualization*, Bonn, **2014**.
- [33] K. Momma, F. Izumi, *J. Appl. Cryst.* **2008**, *41*, 653–658.
- [34] C. G. Broyden, *Math. Comput.* **1965**, *19*, 577–593.
- [35] H. J. Monkhorst, J. D. Pack, *Phys Rev B* **1976**, *13*, 5188.
- [36] R. Dovesi, V. R. Saunders, C. Roetti, R. Orlando, C. M. Zicovich-Wilson, F. Pascale, B. Civalleri, K. Doll, N. M. Harrison, I. J. Bush, P. D’Arco, M. Llunell, M. Causa, Y. Noel, **2014**, 382.
- [37] M. Lorenz, *Band Structure and Density of States Script*, Torino, **2014**.
- [38] W. Setyawan, S. Curtarolo, *Comput. Mater. Sci.* **2010**, *49*, 299–312.
- [39] R. S. Mulliken, *J. Chem. Phys.* **1955**, *23*, 1833–1840.
- [40] A. E. Reed, R. B. Weinstock, F. Weinhold, *J. Chem. Phys.* **1985**, *83*, 735–746.

- [41] F. L. Hirshfeld, *Theor. Chim. Acta* **1977**, *44*, 129–138.
- [42] R. S. Mulliken, W. C. Ermler, *Diatomic Molecules*, Academic Press, New York, **1977**.
- [43] J. Meister, W. H. E. Schwarz, *J. Phys. Chem.* **1994**, *98*, 8245–8252.
- [44] M. J. Frisch, G. W. Trucks, H. B. Schlegel, G. E. Scuseria, M. A. Robb, J. R. Cheeseman, G. Scalmani, V. Barone, G. A. Petersson, H. Nakatsuji, X. Li, M. Caricato, A. Marenich, J. Bloino, B. G. Janesko, R. Gomperts, B. Mennucci, H. P. Hratchian, J. V. Ortiz, A. F. Izmaylov, J. L. Sonnenberg, D. Williams-Young, F. Ding, F. Lipparini, F. Egidi, J. Goings, B. Peng, A. Petrone, T. Henderson, D. Ranasinghe, V. G. Zakrzewski, J. Gao, N. Rega, G. Zheng, W. Liang, M. Hada, M. Ehara, K. Toyota, R. Fukuda, J. Hasegawa, M. Ishida, T. Nakajima, Y. Honda, O. Kitao, H. Nakai, T. Vreven, K. Throssell, J. A. Montgomery, J. E. Peralta, F. Ogliaro, M. Bearpark, J. J. Heyd, E. Brothers, K. N. Kudin, V. N. Staroverov, T. Keith, R. Kobayashi, J. Normand, K. Raghavachari, A. Rendell, J. C. Burant, S. S. Iyengar, J. Tomasi, M. Cossi, J. M. Millam, M. Klene, C. Adamo, R. Cammi, J. W. Ochterski, R. L. Martin, K. Morokuma, O. Farkas, J. B. Foresman, D. J. Fox, Gaussian 09, Wallingford CT, **2016**.
- [45] TURBOMOLE, **2018**.
- [46] K. Eichkorn, H. Öhm, M. Häser, R. Ahlrichs, *Chem. Phys. Lett.* **1995**, *240*, 283–290.
- [47] M. Sierka, R. Ahlrichs, *J. Chem. Phys.* **2003**, *118*, 9136–9148.
- [48] F. Weigend, *Phys. Chem. Chem. Phys. Lett.* **2006**, *8*, 1057–1065.
- [49] A. Klamt, G. Schuurmann, *J. CHEM. SOC. Perkin Trans.* **1993**, *2*, 799–805.
- [50] V. Barone, M. Cossi, *J. Phys. Chem. A* **1998**, *102*, 1995.
- [51] G. Knizia, *J. Chem. Theory Comput.* **2013**, *9*, 4834–4843.

Part III

Results and Discussions

Substitutional Effects in the Li-Ge Binary System by Ni

5.1 Introduction

5.1.1 The Li-Ge-Ni phase system

The ternary system Li-Ni-Ge was investigated in order to investigate new compounds with potential use as anode materials. The phase diagram was rarely investigated to date. Only two ternary compounds, LiNi_6Ge_6 ^[1] and LiNi_2Ge ^[2] were published. In this work we managed to discover two additional compounds, $\text{Li}_{14}\text{Ni}_{8+x}\text{Ge}_{9-x}$ ($x = 0.3$) and $\text{LiNi}_{1+x}\text{Ge}$. Known LiNi_2Ge crystallizes in the space group $Fm\bar{3}m$. The structure is built by a fcc packing of Ge atoms, which octahedral voids are filled by Li atoms and tetrahedral voids by Ni, respectively. One can describe the structure as cubes of Ni alternately filled by Li and Ge atoms. This cubic arrangement can also be found in $\text{Li}_{14}\text{Ni}_{8+x}\text{Ge}_{9-x}$, which is discussed later on in chapter 5.2. LiNi_6Ge_6 (space group $P6/mmm$) can be described as a layered structure derived from the B35-type structure FeGe. The six-membered-rings of Ni are occupied by Li in every other layer, which drives the Ge atoms located above or below to move toward each other forming Ge-dumbbells.

Both known compounds have a quite low Li content of 25 at% and less. Introducing Li to a network of late-transition-metals and group 14 metals, Li acts as scissors cutting the binary solid state structure by intercalating Li. Therefore channels filled by Li, layered structures or isolated units are obtained. In this work the aim was to synthesize compounds with higher Li content. The synthesized compounds are discussed in the following section 5.3 ($\text{LiNi}_{1+x}\text{Ge}$) and 5.2 ($\text{Li}_{14}\text{Ni}_{8+x}\text{Ge}_{9-x}$).

All known compounds including binaries and the ones investigated in this thesis are shown in the ternary phase diagram in Figure 5.1, additionally an excerpt of every ternary phase is shown. A list of all ternary and binary compounds including reference and space group is given in Table 5.1.

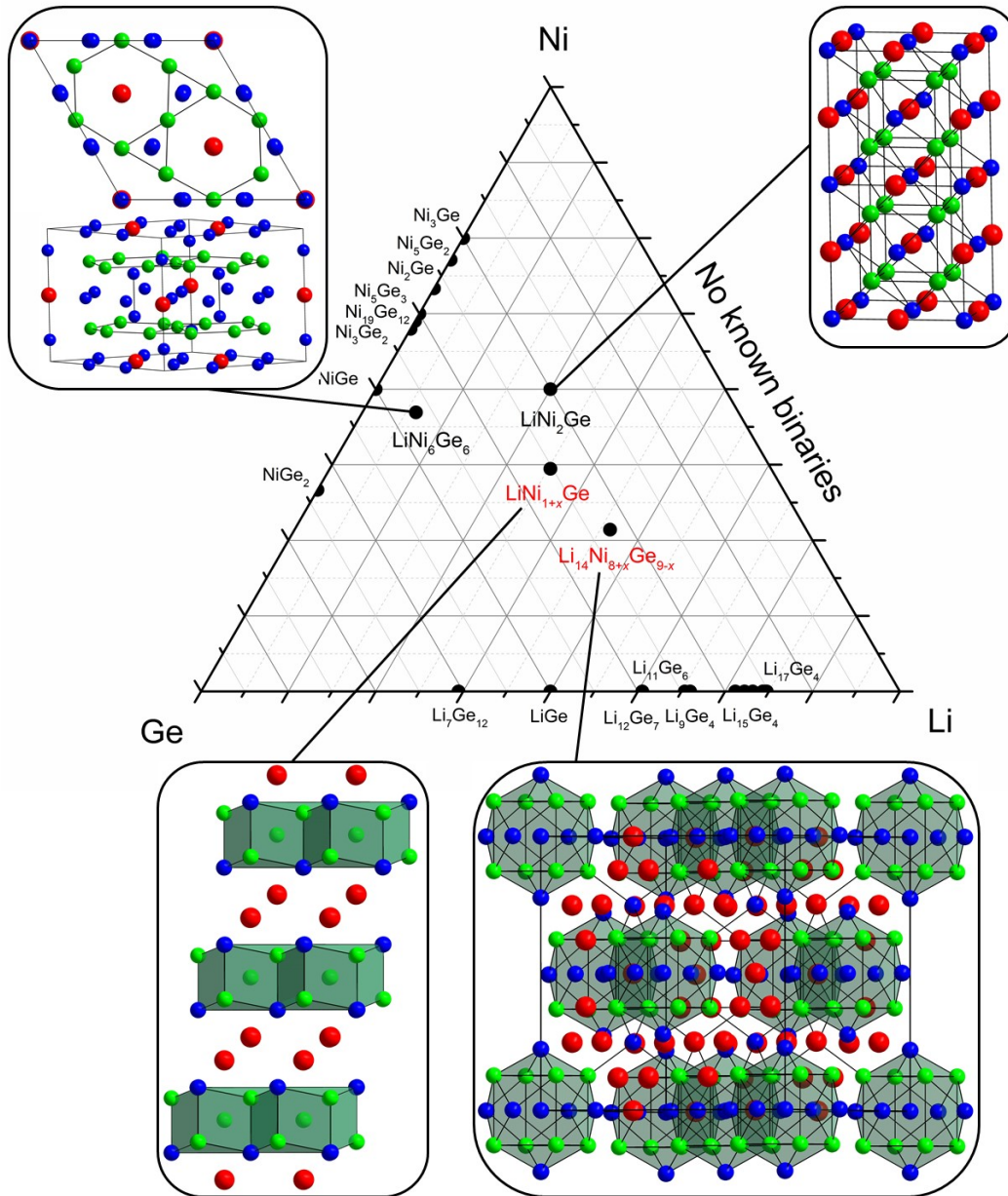


Figure 5.1: Ternary composition diagram of the phase system Li-Ni-Ge including all known binaries. For clarity not all Li-Ge-compounds were assigned. A full list of all compounds is given in Table 5.1. At the corners the pure elements Li, Ni and Ge are located. Compounds investigated in this thesis are given in red and an excerpt of the crystal structure of all ternary compounds is given. Li, Ni and Ge atoms are shown in red, green and blue, respectively. Structures written in red were investigated in this work.

Table 5.1: All known binary and ternary compounds in the Li-Ni-Ge phase diagram

Compound	Space Group	Ref.
Li ₇ Ge ₁₂	P2/n	[3]
LiGe	I4 ₁ md	[4]
HP-LiGe	I4 ₁ a/P6 ₃ /mmc	[5]/[6]
Li ₁₂ Ge ₇	Pnma	[7]
Li ₉ Ge ₄	Cmcm	[8]
Li ₇ Ge ₃	P3 ₂ 2	[9]
Li ₁₃ Ge ₄	n.a. ^[a]	[10]
Li ₁₅ Ge ₄	I44d	[11]
Li _{4.1} Ge	Cmcm	[12]
Li _{16.95} Ge ₄	F43m	[13]
Li ₁₇ Ge ₄	F43m	[12]
HP-NiGe ₂	Cmca	[14]
NiGe	Pnma	[15]
Ni ₃ Ge ₂	P6m2	[16]
Ni ₁₉ Ge ₁₂	C2	[16]
Ni ₅ Ge ₃	C2	[16]
Ni ₂ Ge	Pnma	[16]
Ni ₅ Ge ₂	P6 ₃ /cm	[17]
Ni ₃ Ge	Pm3m	[18]
Ni ₃ Ge	Fd3m	[17]
LiNi ₆ Ge ₆	P6/mmm	[1]
LiNi ₂ Ge	Fm3m	[2]
LiNi _{1+x} Ge ($x = 0.17$)		[b]
Li ₁₄ Ni _{8+x} Ge _{9-x} ($x = 0.3$)	Fm3m	[b]

^[a] no crystal structure was published

^[b] this thesis

5.1.2 Intermetalloid Clusters in Solid-State Chemistry

Chemistry of metal clusters are increasingly interesting for investigations due to their special characteristics lying between molecular and solid-state chemistry.^[19]

This field of interest became popular in the 1960s, when J. Lewis published a review discussing metal-metal bonding.^[20] Up to this time already many homoatomic metal clusters were known such as [Re₃Cl₁₂]³⁻^[21] and [Mo₆Cl₈]⁴⁺,^[22] but only very few heteroatomic metal clusters (WMo(C₅H₅)₂(CO)₆^[23] and MnRe(CO)₁₀^[24]). Additionally heteroatomic clusters were limited to biatomic clusters only at this time

and the clusters, homo- and heteroatomic, were always ligand-stabilized. A year later F. A. Cotton first used the term *metal atom cluster compounds* to describe this class of compounds and defined it as "those containing a finite group of metal atoms which are held together entirely, mainly, or at least to a significant extent, by bonds directly between the metal atoms even though some non-metal atoms may be associated intimately with the cluster".^[25] Additionally he points out, that up to this time mainly the elements Ta, Mo, W and Re are forming those kind of clusters, although already other *metal atom cluster compounds* possessing Ni for example were known. A general rule of why those clusters were formed could not be specified. Several possibilities were considered like a low formal oxidation state. A long time this field of interest was limited to transition elements only. But especially as the huge main group metal cluster Al_{77} was published by Gellman *et al.* main group metal clusters were investigated more thoroughly.^[26] After the discovery of the Al_{77} cluster, further group 13 metal clusters were investigated and a new term was introduced by Schnepf calling this kind of intermediate species between molecules and bulk materials *metalloid clusters*, which means that discrete areas of the cluster units exhibit a structural motifs similar to solid-state metals, although there the clusters itself are no 3-dimensional periodic systems^[19,27]

The expression was further extended in the view of polyhedral cages encapsulating another metal atom to *intermetalloid clusters*. In particular group 14 Zintl cluster anions filled with an endohedral d-block metal atom.^[28] It is noteworthy, that still this metal clusters are restricted mainly to homoatomic and pseudo-heteroatomic systems. This now offers a broad field of heteroatomic d- and p-block metal clusters.^[29] Additionally those endohedral clusters are very energetically stable and can without ligand-free stabilization, whereas most of other *metalloid* or *intermetalloid clusters* are still ligand-stabilized. $[\text{E}_9(\text{CH}=\text{CH}_2)]^{3-}$ ($\text{E} = \text{Ge}, \text{Sn}$) is a simple example for an ligand

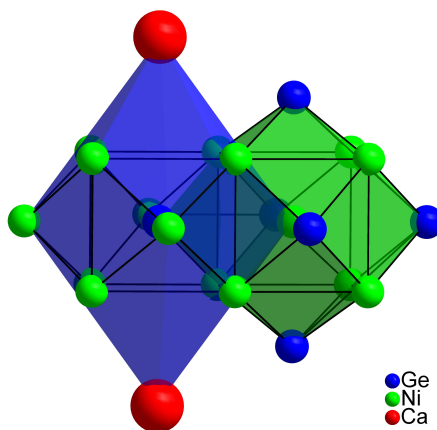


Figure 5.2: Excerpt of the CaNi_5Ge_3 crystal structure showing the rhombic dodecahedral surrounding of the endohedral Ni in green and Ge in blue. Ge, Ni and Ca atoms are represented as spheres in blue, green and red, respectively.

stabilized endohedral cluster. Especially for larger systems a central atom is stabilizing the *intermetalloid cluster* due to the occupancy of a larger void.^[28] Favored are group 14 cages containing 9-, 10- or 12-atoms. Also larger cluster with 17 or 18 atoms are possible. A noteworthy *intermetalloid cluster* is the onion-like $\text{Sn@Cu}_{12}\text{@Sn}_{20}$, exhibiting a central Sn-atoms surrounded by twelve Cu-atoms, which is again surrounded by 20 Sn-atoms.^[30] The cluster $[\text{Ru@Sn}_9]^{6-}$ and $[\text{Co@Ge}_9]^{5-}$ are discussed later in this thesis (10.2) with a more detailed list of these clusters.

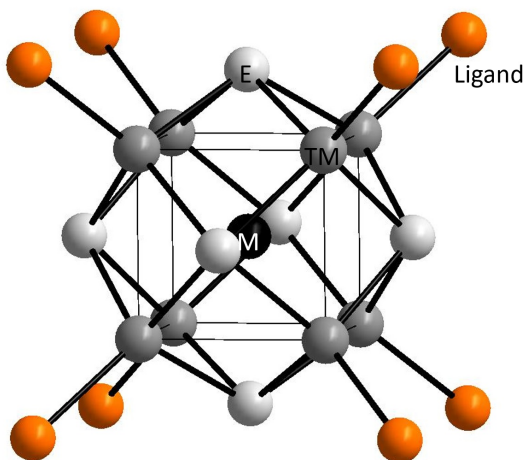


Figure 5.3: Structure of $[M@TM_8E_6]$ (M = (semi)-metal, TM = transition metal, E = semi-metal or ligand).

Another type of metal clusters are molecular rhombic dodecahedral clusters of a general formula $[M@TM_8E_6]$ (M = (semi)-metal, TM = transition metal, E = semi-metal or ligand) built by a cube of transition metal atom, in our case Ni, which is capped on each plane by a semi-metal or ligand (Figure 5.3). This clusters can be filled by a central atom, but also empty clusters exist. Tabel 5.2 and 5.3 gives an insight of the Ni-containing clusters with and without central atom. All the listed compounds are obtained by a solution-based synthesis, in contrast to the one described in this thesis. From solid-state chemsity the compound CaNi_5Ge_3 is known.^[31] This structure does not exhibit isolated rhombic dodecahedra, but layers of cuboids containing alternating endohedral Ni and Ge atoms. The cuboid filled by Ni is capped by 6 Ge atoms (one is the endohedral Ni of the next Ni_6 -cuboid), which forms a rhombic dodecahedra. Whereas the Ge filled cuboid is capped by 4 Ni atoms (one is the endohedral Ge of the next Ni_6 -cuboid) and two Ca atoms. This rhombic dodecahedra is distorted due to the Ca atoms (Figure 5.2).

Table 5.2: Non-centered rhombic dodecahedral clusters with $M = \text{Ni}$, their valence electron counts (CVE) and interatomic distances in the rhombic dodecahedra

Cluster	CVE	$M-E$ [\AA]	$M-M$ [\AA]	ref
$[\text{Ni}_5\text{Fe}_3\text{S}_6\text{I}_8]^{4-}$	110	n.a.	2.68	[32]
$[\text{Ni}_8(\text{PPh})_6(\text{PPh}_3)_4\text{Cl}_4]^+$	115	n.a.	2.58	[33]
$\text{Ni}_8(\text{PPh})_6(\text{PPh}_3)_4\text{Cl}_4$	116	2.21	2.61	[34]
$\text{Ni}_8(\text{PPh})_6(\text{PPh}_3)_4\text{Br}_4$	116	n.a.	2.61	[34]
$\text{Ni}_8\text{S}_6(\text{PPh}_3)_6\text{Cl}_2$	118	2.21	2.68	[35]
$\text{Ni}_8(\text{PPh})_6(\text{CO})_8$	120	2.18	2.65	[36]
$\text{Ni}_8\text{S}_6(\text{PPh}_3)_8$	120	n.a.	2.70	[37]
$\text{Ni}_8\text{Se}_6(\text{P}n\text{-Bu}_3)_8$	120	n.a.	2.70	[38]
$\text{Ni}_8(\text{PPh})_6(\text{PPh}_3)_4(\text{CO})_4$	120	2.19	2.67	[34]
$\text{Ni}_8(\text{PPh})_6(\text{AsPh}_3)_4(\text{CO})_4$	120	n.a.	n.a.	[39]

Table 5.3: Centered rhombic dodecahedral clusters with $M = \text{Ni}$, their valence electron counts (CVE) and interatomic distances in the rhombic dodecahedra

Cluster	CVE	$M-E$ [\AA]	$M-M$ [\AA]	ref
$[\text{Ge@Ni}_8\text{Ge}_6]^{6-}$	114	2.40	3.00	[a]
$\text{As@Ni}_8\text{As}_6(\text{PPh}_3)_8$	119	2.32	2.89	[40]
$[\text{Ni@Ni}_8\text{Ge}_6]^{6-}$	120	2.40	3.00	[a]
$\text{Ni@Ni}_8\text{As}_6(\text{PPh}_3)_5\text{Cl}_3$	121	n.a.	2.81	[41]
$\text{Ni@Ni}_8\text{As}_6(\text{PPh}_3)_6\text{Cl}_2$	122	2.21	2.81	[41]
$\text{Ni@Ni}_8\text{P}_6(\text{PCy}_3)_6\text{Cl}_2$	122	n.a.	2.80	[42]
$\text{Ni@Ni}_8(\text{Ge-Et})_6(\text{CO})_8$	124	2.36	2.67	[43]
$\text{Ni@Ni}_8\text{Te}_6(\text{PEt}_3)_8$	130	2.55	2.86	[44]

[a] this thesis

5.2 The Compound $\text{Li}_{14}\text{Ni}_{8+x}\text{Ge}_{9-x}$ ($x = 0.3$)

5.2.1 Synthesis of $\text{Li}_{14}\text{Ni}_{8+x}\text{Ge}_{9-x}$ ($x = 0.3$)

The starting materials Ni and Ge were pre-melted by arc-welding described in chapter 2.4. The obtained regulus was transferred to a niobium ampule and peeled Li was added on top afterwards. The ampule was sealed by arc-welding and transferred into a silica tube. The silica tube was evacuated and put into a vertical resistance tube furnace. The samples were heated to 750 °C and tempered for 24 hours. Afterwards they were quenched in a water/ice-mixture. After opening the ampules, the

product appeared as metallic lustrous pinkish silver powder, which was sensitive to air and moisture. SC-XRD and P-XRD-measurement were performed, as well as, thermal investigates by DSC measurements.

Table 5.4: Masses and molar masses of the used chemicals, Mass loss by arc-welding was neglected

Chemical	Formula	Mass [mg]	Molar mass [mmol]
Germanium	Ge	253	3.48
Nickle	Ni	204	3.48
Lithium	Li	43	6.15

5.2.2 Characterization of $\text{Li}_{14}\text{Ni}_{8+x}\text{Ge}_{9-x}$ ($x = 0.3$)

The compound was characterized by SC-XRD-measurements. The preparation was performed like described in chapter 3.1. For the measurement a 0.3 mm diameter capillary was used. A face-centered cubic cell was found containing rhombic dodecahedral cluster units. Selected crystallographic data is given in Table 5.5 and 5.6. Additional crystallographic data is given in the appendix (Table 13.16 and 13.17). Additionally, EDX measurements were carried out to determine the Ge:Ni ratio. A Ge:Ni ratio of 0.49:0.51(7) was found, which in general matches the expected ratio for $x = 0.3$.

Additionally P-XRD-measurements were performed to check the composition of the bulk. In this case $\text{Cu}_{K\alpha 1}$ ($\lambda = 1.54056 \text{ \AA}$) radiation was used. The powder pattern compared with the theoretical pattern of the SC-XRD-data is shown in Figure 5.4.

Table 5.5: Crystal data and structure refinement

Formula	$\text{Li}_{14}\text{Ni}_{8.3}\text{Ge}_{8.7}$
Formula weight ($\frac{g}{mol}$)	1220.16
Space group	$Fm\bar{3}m$ (no. 225)
Z	4
Unit cell parameters (\AA)	$a = 11.77340(10)$
Volume (\AA^3)	1631.95(4)
$P_{calc}(\frac{g}{cm^3})$	4.949
abs. coeff.	25.04
F(000)	2211
Crystal shape/color	block/pinkish silver
Temperature (K)	150
Θ range/deg	3.46-32.39
Index Range in hkl	$-17 \leq h \leq 17$ $-16 \leq k \leq 17$ $-9 \leq l \leq 17$
Reflections collected	2829
Unique reflections	185
Reflections with $I > 2\sigma(I)$	177
Data / parameter	185/X/18
GOF on F^2	1.349
R_1, wR_2 ($I \geq 2\sigma(I)$)	0.0222, 0.0583
R_1, wR_2 (all data)	0.0243, 0.0589
Largest diff. peak and hole	1.02, -0.69

Table 5.6: Atomic coordinates and equivalent isotropic displacement parameters for $\text{Li}_{14}\text{Ni}_{8.3}\text{Ge}_{8.7}$

Atom	Wyck.	x	y	z	S.O.F.	$U_{eg}/\text{\AA}^2$
Ge1	24e	0	0.22368	0.52957	1	0.007(1)
Ge2/Ni2	4a	0	0	0	0.69(9)/0.31(9)	0.005(1)
Ge3	8c	$\frac{1}{4}$	$\frac{1}{4}$	$\frac{1}{4}$	1	0.007(1)
Ni1	32f	0.12721	0.12721	0.12721	1	0.006(1)
Li1	32f	0.37845	0.12155	0.12155	1	0.020(3)
Li2	24d	$\frac{1}{4}$	$\frac{1}{4}$	0	1	0.020(4)

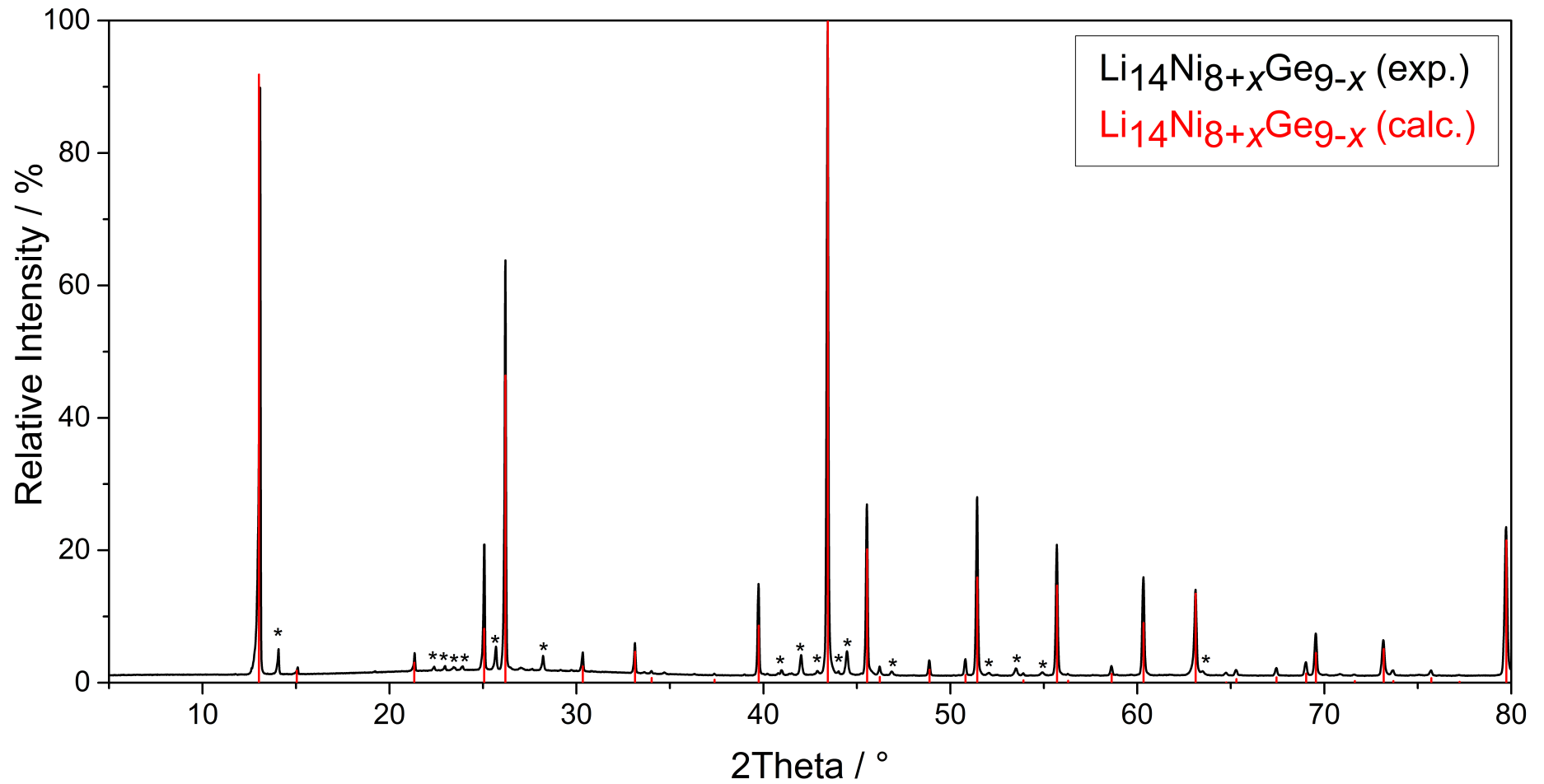


Figure 5.4: Experimental P-XRD diffractogram (black) with the theoretical pattern of $\text{Li}_{14}\text{Ni}_{8.3}\text{Ge}_{8.7}$ (red). Minor unknown sidephases are marked with an asterisk.

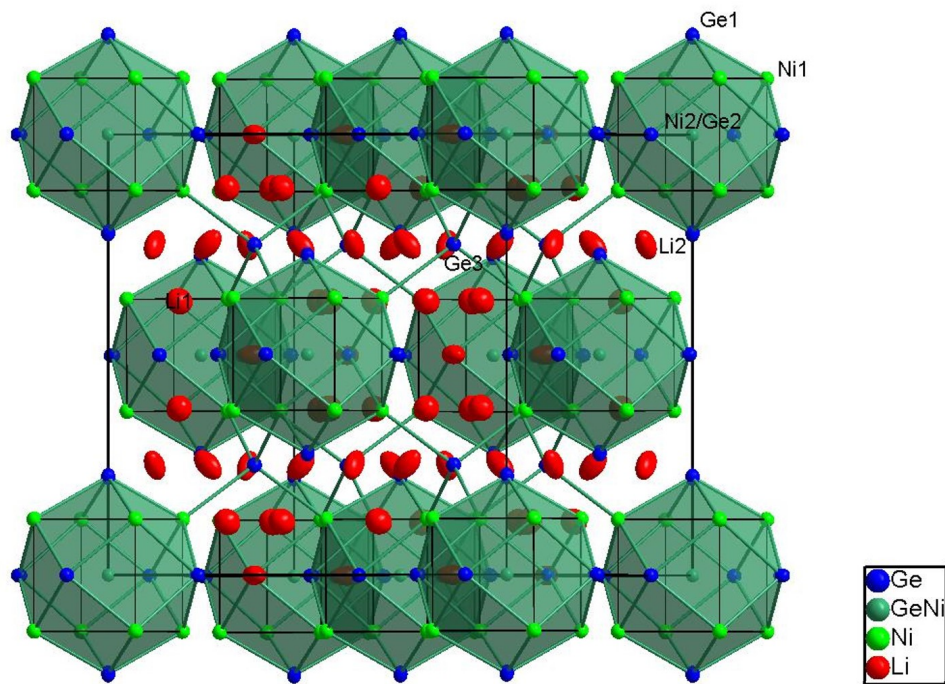
5.2.3 Structure Description of $\text{Li}_{14}\text{Ni}_{8+x}\text{Ge}_{9-x}$ ($x = 0.3$)

$\text{Li}_{14}\text{Ni}_{8.3}\text{Ge}_{8.7}$ crystallizes in its own structure type in the space group $Fm\bar{3}m$ (No. 225). The structure is built up from a face-centered cubic (fcc) packing of rhombic dodecahedral (Ni_8Ge_6) clusters, which are connected by Ge atoms and Li_8 cubes (see Figure 5.5 and 5.6). It can be derived from a Heulser alloy as a hierarchical variant, in which the clusters have a fcc type arrangement, Li cubes occupy the octahedral voids and the bridging Ge occupy all tetrahedral voids. The rhombic dodecahedral clusters are made of eight Ni1 atoms arrange in a cube-like fashion and each square-side is capped a Ge1 atom. SC-XRD measurements show a mixed occupancy of Ge2/Ni2 of the central position of the Ni_8 -cube in a ratio of 0.69/0.31(9). This can be considered as significant due to 3σ rule. But additionally one has to take into account, that Ge and Ni only differ by four electrons, which complicates the distinction of those atoms by XRD-methods. The EDX measurements of a generally Ge:Ni ratio of 0.49:0.51(7) matches the ratio found for this position. Due to the XRD measurements there is no sign of a superstructural ordering and occupying the position with solely Ni or Ge led to significantly worse solutions in the structure refinement. The rhombic dodecahedra form a network connected by a Ge3 position, which occupies the tetrahedral void of the fcc structure. Therefore a 3D-network is archived. This can also be seen as a polyanionic substructure, which derives from the fluorite structure. The Li atoms, which are not located as a cube in the octahedral voids, are arranged as a cuboctahedral surrounding of the Ni_8Ge_6 -cluster.

The cluster network $(\text{Ni}/\text{Ge})@\text{Ni}_8\text{Ge}_6$ has different types of bonding. In case of Ge-Ni bonds three kinds are present: (1) Ni1-Ge1 (2.403(1) Å), (2) Ni1-Ge2/Ni2 (2.594(1) Å) and (3) Ni1-Ge3 (2.504(1) Å). For Ni1-Ge1 the distance is in the range of the Ni-Ge bond length in NiGe (2.33 to 2.49 Å).^[45] The second type Ni1-Ge2/Ni2 is discussed later in this section. In case of the Ni1-Ge3, which is bridging the cluster units, the distance is slightly longer, which indicates a weaker bond.

For the Ni1-Ni1 distance in the Ni_8 -cube no bond should be considered due to a very long bond length of 2.995(1) Å. In comparison metallic Ni shows a bond length of 2.49 Å.^[46]

This results match the results of other cluster systems like $(\text{Ni}/\text{Ge})@\text{Ni}_8\text{Ge}_6$. These clusters are known from solution-based synthesis like **(1)** $[\text{Ni}@\text{Ni}_8(\text{GeEt})_6](\text{CO})_8$, **(2)** $[\text{As}@\text{Ni}_8\text{As}_6](\text{PH}_3)_8$ and **(3)** $[\text{Ni}@\text{Ni}_8\text{Te}_6](\text{PH}_3)_8$ (see also Table 5.2 and 5.3). Their general structure is shown in Figure 5.3 with a general structure of $[M@TM_8E_6]$ ($M = (\text{semi})\text{-metal}$, $TM = \text{transition metal}$, $E = \text{semi-metal or ligand}$). For example **(1)**, in which the Ni-Ge bond length is 2.36 Å, while Ni-Ni distances are 2.67 Å.^[43] Due to packing effects the Ni-Ni distances are longer, while other known clusters were only found in solution based synthesis. This clusters mostly contain



b

Figure 5.5: Unit cell with highlighted Ni_8Ge_6 clusters of the compound $\text{Li}_{14}\text{Ni}_{8+x}\text{Ge}_{9-x}$. Li, Ni, Ge and Ni/Ge mixed positions are represented as ellipsoids at the 90 % probability level in red, green, blue and teal respectively. In chapter 13.1 further structure pictures are shown.

isolated clusters mostly natural charged, we present a network of highly negatively charged clusters. This very high negative charge of -8 can also be a reason for the long Ni-Ni distance.^[47]

The clusters **(2)** and **(3)** show similar interatomic distances with a Ni-As bond length of 2.32 Å and a Ni-Te bond length of 2.55 Å. The respective Ni-Ni distances are longer compared to **(1)** (2.89 Å and 2.87 Å, respectively) and can be considered as non-binding. Other compounds with their valence electron count (CVE) exhibiting the same rhombic dodecahedron cluster are listed in Table 5.2 and 5.3. The influence of the ligands are probably very important to the stability of the compounds as they donate necessary electrons in the case of ethyl ligands. In our structure the needed electrons are provided by the surrounding Li, each donating an electron, which makes the $(\text{Ni}/\text{Ge})@\text{Ni}_8\text{Ge}_6$ cluster the first highly charged rhombic dodecahedron. The distances of the central position Ni2/Ge2 to the cluster unit (Ni_8Ge_6) are longer than in NiGe and the high coordination number of the central position Ni2/Ge2 already indicates that no 2-center-2-electron bonds should be considered. (2.594(1) Å for Ni2/Ge2-Ni1 and 2.634(1) Å for Ni2/Ge2-Ge1).

The Li-Li distances in the compound range from 2.57(1) Å for Li1-Li2 to 2.86(2) Å

for Li1-Li1. This is much shorter than Li-Li distances in body-centered-cubic Li with 3.05 \AA ,^[48] but longer than Li-Li distances in highly ionic compounds like Li₂.53AgGe₂ with 2.49 \AA ^[49] or Li₁₂Ge₇ with 2.41 \AA .^[7] Therefore, Li is considered as Li⁺. This might be due to the space the Li atoms are given in the large channels between the clusters and could cause the enlarged anisotropic replacement parameter for Li2 in one direction. The ellipsoids of this atom point towards the unoccupied octahedral voids as well as the lone pairs of the Ge1 atoms in the cluster. This may cause additional attraction to the cationic Li besides the given space in this direction. Coordinations of atoms are shown in the appendix.

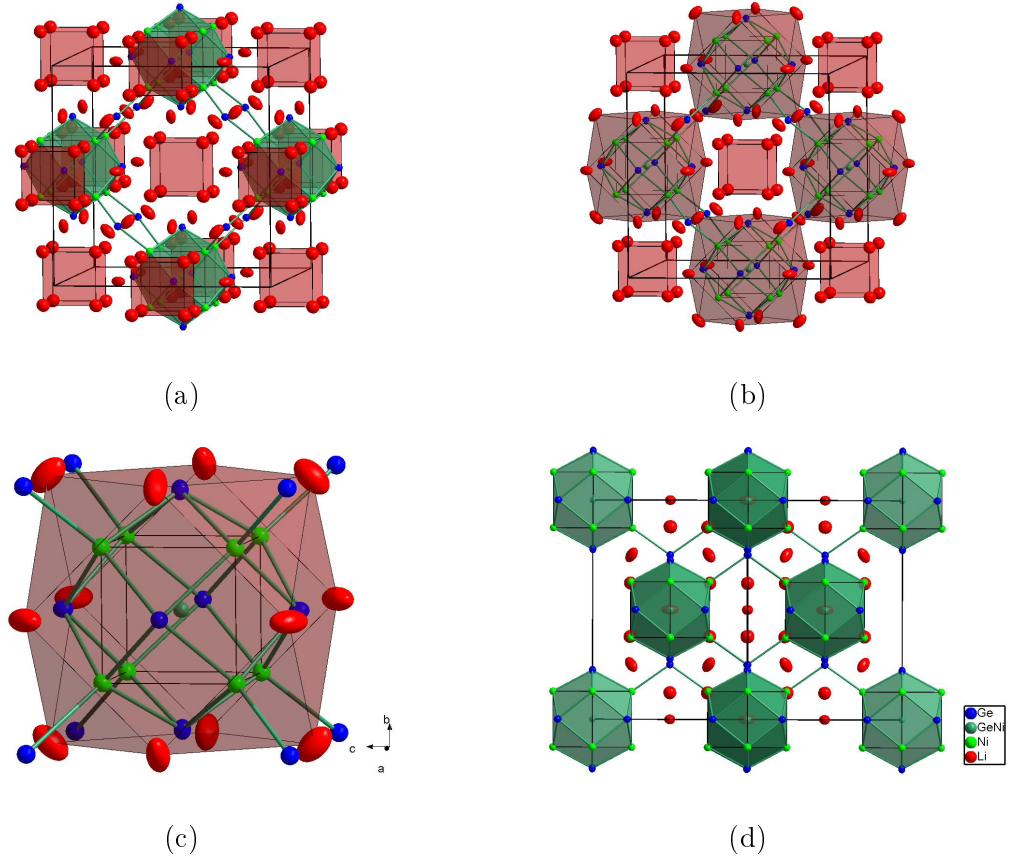


Figure 5.6: (a) Unit cell with highlighted Ni_8Ge_6 clusters and Li_8 cubes of the compound $\text{Li}_{14}\text{Ni}_{8+x}\text{Ge}_{9-x}$. (b) The cuboctahedral coordination sphere of Li_2 atoms as well as the Li_1 cubes in the octahedral voids are marked with red polyhedra. (c) ($\text{Ni}/\text{Ge}@\text{Ni}_8\text{Ge}_6$) cluster with cuboctahedral surrounding of Li_2 atoms (red polyhedron) and Ge_3 atoms capping the triangular faces of the cuboctahedron in the compound $\text{Li}_{14}\text{Ni}_{8+x}\text{Ge}_{9-x}$. (d) Unit cell of $\text{Li}_{14}\text{Ni}_{8+x}\text{Ge}_{9-x}$ in nearly bc-direction highlighting the Li filled channels in the structure. Covalent bonds are marked with thick teal lines. Thin lines represent the coordination of Li atoms. Li, Ni, Ge and Ni/Ge mixed positions are represented as ellipsoids at the 90 % probability level in red, green, blue and teal respectively.

5.2.4 Thermal behavior of $\text{Li}_{14}\text{Ni}_{8+x}\text{Ge}_{9-x}$ ($x = 0.3$)

The thermal behaviour was investigated using a DSC apparatus (Details see 3.3). In an Ar-filled glovebox, a Nb crucible was loaded with 50 mg of $\text{Li}_{14}\text{Ni}_{8+x}\text{Ge}_{9-x}$ containing small remains of an unknown side phase. The sample was heated in Ar flow with a heating rate of $5 \text{ K} \cdot \text{min}^{-1}$ to $1000 \text{ }^\circ\text{C}$ and subsequently cooled down by the same rate to $150 \text{ }^\circ\text{C}$. The procedure was repeated. The sample was recovered in an Ar-filled glovebox and examined by P-XRD-experiments.

During the first heating cycle a partly decomposition of $\text{Li}_{14}\text{Ni}_{8+x}\text{Ge}_{9-x}$ to $\text{Li}_{15}\text{Ge}_4$ and an unknown side phase is shown at 708°C . The remains of $\text{Li}_{14}\text{Ni}_{8+x}\text{Ge}_{9-x}$ melt at about 741°C . $\text{Li}_{14}\text{Ni}_{8+x}\text{Ge}_{9-x}$ recrystallizes during the cooling procedure at 708°C , whereas $\text{Li}_{15}\text{Ge}_4$ crystallizes at about 667°C .^[11] During the second heating cycle the melting point of $\text{Li}_{15}\text{Ge}_4$ appears at 682°C . The melting point of $\text{Li}_{14}\text{Ni}_{8+x}\text{Ge}_{9-x}$ almost vanishes due to the decomposition happening at 708°C . For the second cooling cycle only the melting point of $\text{Li}_{15}\text{Ge}_4$ occurs. The decomposition of $\text{Li}_{14}\text{Ni}_{8+x}\text{Ge}_{9-x}$ seems to be kinetically inhibited, because it takes two cycles to fully decompose the compound. The DSC measurement including onsets of peaks is shown in Figure 5.7.

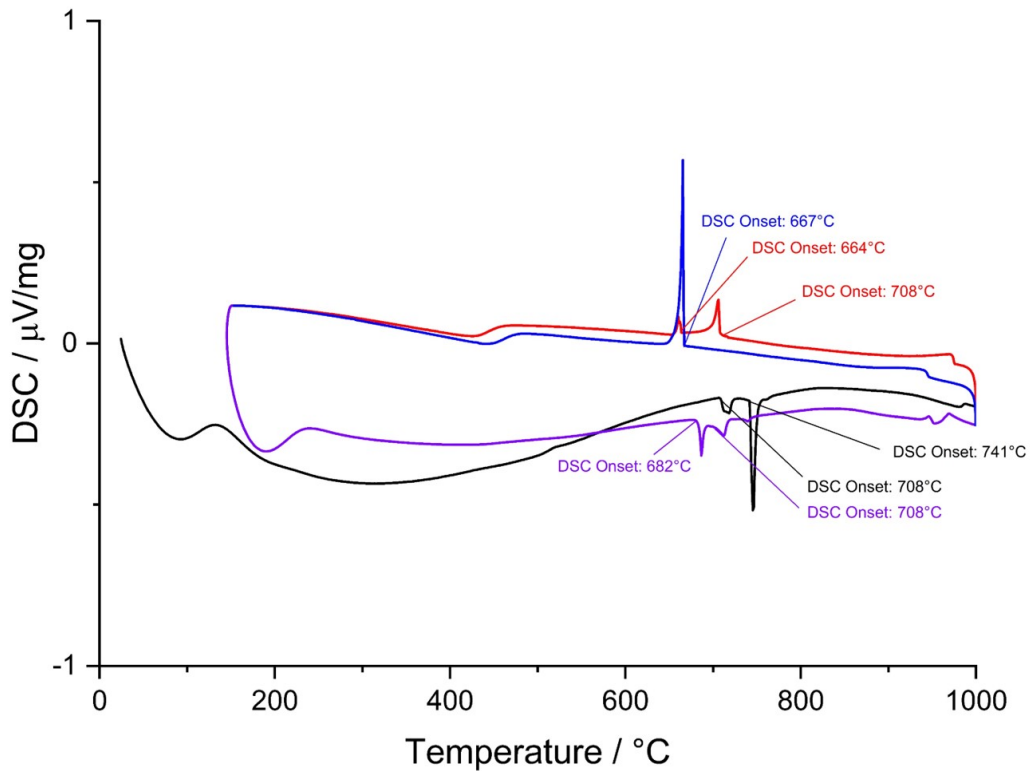


Figure 5.7: Thermogramm of $\text{Li}_{14}\text{Ni}_{8+x}\text{Ge}_{9-x}$ containing minor sidephases. The first and second heating traces are shown as black and purple lines, respectively. The first and second cooling traces are shown in red and blue, respectively.

5.2.5 Computational Analysis of $\text{Li}_{14}\text{Ni}_{8+x}\text{Ge}_{9-x}$ ($x = 0.3$)

Periodic Systems Calculations

The computational analysis for the structures $\text{Li}_{14}\text{Ni}_8\text{Ge}_9$, $\text{Li}_{14}\text{Ni}_9\text{Ge}_8$, $\text{Li}_{14}\text{Ni}_{8.25}\text{Ge}_{8.75}$, $\text{Li}_{14}\text{Ni}_{8.75}\text{Ge}_8$ and $\text{Li}_{14}\text{Zn}_8\text{Ge}_9$ was carried out using the Crystal14 program package

and hybrid density functional methods. A hybrid exchange correlation functional after Perdew, Burke and Ernzerhof (PBE0) and split-valence + polarization level basis sets derived from the Karlsruhe basis sets for all considered elements Li, Ni, Ge and Zn (full basis set details are given in the appendix) was applied. Detailed information about computational method is given in chapter 4. The starting geometry was taken from experimental data and all structures were fully optimized within the constraints imposed by the space group symmetry. The optimization of $\text{Li}_{14}\text{Ni}_{8.25}\text{Ge}_{8.75}$ did not reach a local minimum. Therefore, the lowest point in energy was chosen and a single-point calculation was subsequently carried out. Optimized geometry of all calculation are given in the appendix (Table 13.3-13.8). Band structure, density of states (DOS), as well as, Mulliken population analysis calculations were performed.

In computational analysis it is not possible to use mixed positions, therefore idealized model systems have to be built with a composition close to the actual system. In our case first two very simple models were investigated using a full occupancy of either Ge or Ni for the central position of $X2$ in the intermetalloid cluster ($\text{Li}_{14}\text{Ni}_8\text{Ge}_9$ (**A**) and $\text{Li}_{14}\text{Ni}_9\text{Ge}_8$ (**B**)). The third model (**C**) was built to imitate the mixed position with an Ni:Ge ratio of 0.25:0.75, which is within the error of the experimental findings of 0.31:0.69(9). A decrease of the symmetry was necessary to split up the Wyck-

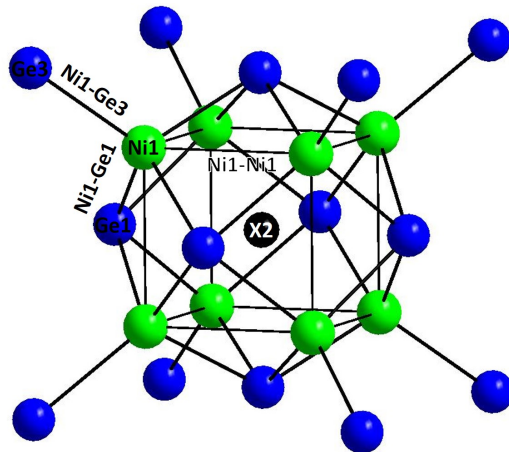


Figure 5.8: Cluster unit showing atom labels and bond labels.

off position of $X2$ ($4a$) in two sites Ni ($1a$) and Ge ($3c$). For the composition $\text{Li}_{14}\text{Ni}_{8.25}\text{Ge}_{8.75}$ (**C**) with the space group $Pm\bar{3}m$ (no. 221) detailed structural data is given in Figure 13.2 in the appendix. Additionally, calculations for a non-filled cluster $\text{Li}_{14}\text{Ni}_8\text{Ge}_8$ (**D**) and a partly-filled cluster $\text{Li}_{14}\text{Ni}_{8.75}\text{Ge}_8$ (**E**) using the same model as for $\text{Li}_{14}\text{Ni}_{8.25}\text{Ge}_{8.75}$ were carried out. For all calculations, the detailed atomic distances were compared to the experimental data as shown in Table 13.9 and 13.10. Summarized deviation of atomic distances are listed in Table 5.7.

For the structural optimization in the original space group, models B and D show the smallest deviations with respect to the experiment. But still the deviation of Ni1-Ge3 distance from the experimental data is over 2% for these compositions. **A** shows large deviations of up to 5%. **C**, which should imitate the mixed position according to the experimental findings has large deviations as well. A more accurate

Table 5.7: All structure models for quantum chemical calculations with element at $X2$ position and deviation of distances between atoms with respect to experimental data. Position $X2$ is shown in Figure 5.8. The detailed structure comparison values and structure parameters are given in Tables 13.3-13.10

Structure	Position $X2$ (Occupancy)	Deviation of atomic distances
$\text{Li}_{14}\text{Ni}_8\text{Ge}_9$ (A)	Ge (1.0)	0.4-5.0%
$\text{Li}_{14}\text{Ni}_9\text{Ge}_8$ (B)	Ni (1.0)	0.2-2.0%
$\text{Li}_{14}\text{Ni}_{8.25}\text{Ge}_{8.75}$ (C)	Ni/Ge (0.25 /0.75)	0.0-5.0%
$\text{Li}_{14}\text{Ni}_8\text{Ge}_8$ (D)		0.9-2.8%
$\text{Li}_{14}\text{Ni}_{8.75}\text{Ge}_8$ (E)	Ni (0.75)	0.3-2.0%
$\text{Li}_{14}\text{Zn}_8\text{Ge}_9$ (F)	Ge (1.0)	

model exhibiting an even bigger cell could be needed, but it would not be computationally feasible. Modelling a mix of **B** and **D** using partial occupation of only Ni of the $X2$ position one yields the composition **E**, which cluster voids are partly filled by Ni. The atomic distances for this composition are in reasonable agreement with the experimental findings. Keeping in mind, that is hard to distinguish Ni from Ge in single crystal diffraction, as well as, a mixed position from a partly occupied position of one element, these results indicate a partial Ni occupancy of the center position $X2$.

Mulliken partial charges and bond overlaps were calculated in order to investigate the chemical bonding. Charges and overlaps are shown in the Table 13.11 and 13.12. The bond between Ni1-Ge1 and Ni1-Ge3 have similar in strength for **D**, although the bond length is shorter for Ni1-Ge1 (bond overlap populations: 0.17 and 0.16). For filled clusters **A** and **B**, the bond overlap population of Ni1-Ge1 becomes even smaller compared to Ni1-Ge3 (0.13 for Ni2, 0.13 for Ge2 and 0.18 for Ni2/0.18 for Ge2, respectively). The overlap of Ni1-Ni1 confirms, that there is no bond (less than 0.04 for all structures). This suggests that the structure does not exhibit isolated $[\text{Ni}_8\text{Ge}_6]$ clusters with Ge3 in the tetrahedral voids, but a network of clusters connected by Ge3.

The density of states (DOS) and band structure show all structures to be conducting (Figure 13.3-13.8). The band structure of **A** shows a pseudo-bandgap above the Fermi level (about 3 eV), which indicates a possibility for substitution in order to yield a semiconductor. The count of electrons needed to reach the pseudo-bandgap was estimated to be 16 per formula unit, which could be obtained for example by a substitution of Ni by Zn. Quantum chemical calculations for $\text{Li}_{14}\text{Zn}_8\text{Ge}_9$ (**F**) were carried out at the DFT-PBE0/SVP level of theory. The band structure and DOS

show a semiconductor with a bandgap of 0.7 eV.

This calculations show, that we have a network of rhombic dodecahedral intermetalloid clusters connected by Ge3 and show a possible substitution for achieving a semi-conducting system $\text{Li}_{14}\text{Zn}_8\text{Ge}_9$. Additionally the results rise a question about the central position. They indicate a partly position, but a mixed position of Ni and Ge.

Molecular Systems Calculations

For molecular calculations a suitable excerpt was needed. To satisfy the loose end at the Ge3 atoms three hydrogen atoms were added to compensate the cut of bonds. The model clusters $[\text{Ni}@\text{Ni}_8\text{Ge}_6(\text{GeH}_3)_8]^{6-}$ (**G**) and $[\text{Ge}@\text{Ni}_8\text{Ge}_6(\text{GeH}_3)_8]^{6-}$ (**H**) were investigated using the Turbomole V7.1 program package, DFT-PBE0 method and def2-TZVP basis sets for all considered elements Ni, Ge and H. For compensation of the negative charges, a continuum solvation model COSMO was applied. Multipole-accelerated resolution-of-the-identity technique was used to speed up the calculations. For detailed information about computational methods see chapter 4. After optimization both models were investigated by frequency analysis in order to reassure character of a stationary point to be a minimum. For both clusters minor imaginary frequencies less than $45i \text{ cm}^{-1}$ were found, which did not vanish after using a tighter DFT integration grid and a higher convergence criteria. The frequencies belong to bending vibrations of the GeH_3 groups and have no impact to the cluster itself. Additionally, those frequency can be caused by the missing crystal surrounding of such highly charged clusters, where the surrounding was replaced by a solvation model.

Property calculations like natural population analysis, as well as, an intrinsic bonding orbital (IBO) analysis were carried out. IBOs allow to simplify complex wave functions by constructing localized orbitals that are easier to connect with fundamental chemical concepts. The interpretation of the IBOs is simple: if an IBO describes a purely covalent two-atomic bond, each atom would contribute 50%. The further the atomic contributions are from 50%, the more ionic the bond is.

Some selected IBO descriptions are given in Table 5.8 and Table 13.14 and 13.15 shows several IBO illustration, which are not shown in this section.

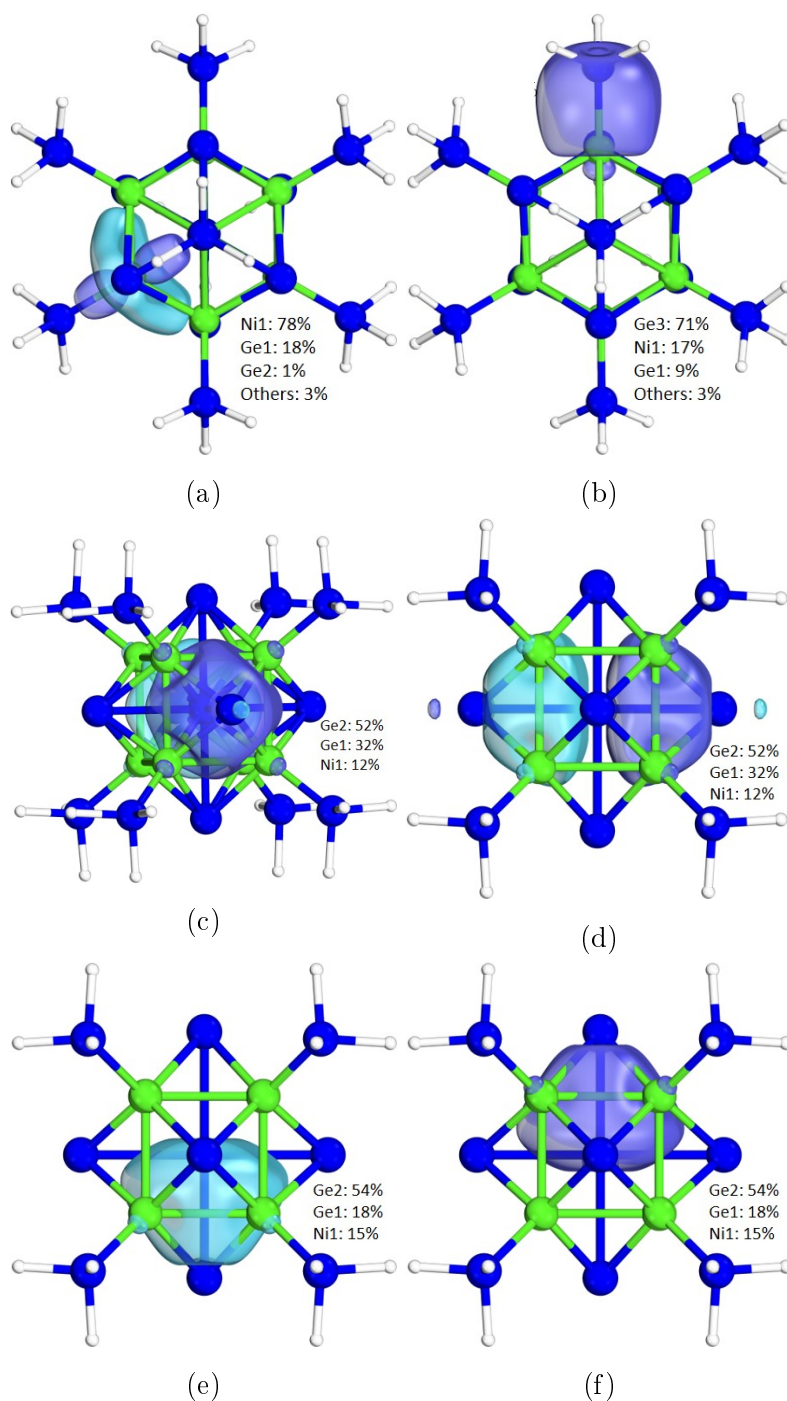


Figure 5.9: (a): IBO-325 of $[\text{Ge}@Ni_8\text{Ge}_6]^{6-}$ showing a dz^2 -like orbital at Ni1. Ge and Ni are colored blue and green, respectively. Contribution of each atom to the IBO: Ni1 78 %, Ge1 18 %, Ge2 1 %, Others 3 %. (b): IBO-300 of $[\text{Ge}@Ni_8\text{Ge}_6]^{6-}$ showing a bonding orbital between Ge3 and Ni1. Contribution of each atom to the IBO: Ge3 71 %, Ni1 17 %, Ge1 9 %. (c): IBO-291 and (d) IBO-292 of $[\text{Ge}@Ni_8\text{Ge}_6]^{6-}$ showing a p -like orbital at Ge2 bonding to Ge1 in x or y direction, respectively. Contribution of each atom to the IBO: Ge2 52 %, Ge1 32 %, Ni1 12 %. (e): IBO-283 and (f) IBO-284 of $[\text{Ge}@Ni_8\text{Ge}_6]^{6-}$ showing a orbital at Ge1 in z direction. Contribution of each atom to the IBO: Ge2 54 %, Ge1 18 %, Ni1 15 %. Ge and Ni are colored blue and green, respectively.

Table 5.8: Summarized description of IBOs of structures **G** and **H**. All relevant IBOs are shown in the appendix (Table 13.14 and 13.15)

Structure	# IBOs	Description
G	364-366	Delocalized at Ni ₈ Ge ₆ -Cluster unit, each orbital is only $\frac{2}{3}$ filled
G	361-363	<i>d</i> -shaped orbital of cluster unit mainly localized at Ge1 atoms
G	337-344	<i>dz</i> ² -shaped orbital at Ni1 atoms forming a bond towards Ge1 atoms
G	284-291	σ -shaped bonding of Ni1 and Ge3 atoms
G	278-283	Lone pair of Ge1 with small interaction towards Ni1 atoms
H	365-367	<i>d</i> -shaped orbital of cluster unit mainly localized at Ge1 atoms
H	325-332	<i>dz</i> ² -shaped orbital at Ni1 atoms forming a bond towards Ge1 atoms
H	293-300	σ -shaped bonding of Ni1 and Ge3 atoms
H	291-292	<i>p</i> -shaped orbital of cluster unit in <i>x</i> and <i>y</i> direction
H	285-290	Lone pair of Ge1
H	283-284	Combining both orbitals: <i>p</i> -shaped orbital of cluster unit in <i>z</i> direction

Most of the IBOs are almost identical for **G** and **H**. The *dz*²-shaped orbital at Ni1 indicates a Ni1-Ge1 bond and the Ni1-Ge3 bond is shown by a σ -shaped bond. Both of those bonds appear rather weak according to IBOs, which are mostly located at one atom. Both models also show *d*-shaped orbitals for the whole cluster. Although it appears delocalized mostly Ge1 contributes to the IBO. Another common orbital is the lone pair of Ge1. For **H** only Ge1 has a contribution to this orbital, but for **G** there is an additional contribution of Ni1. Noteworthy is the bonding of Ge1-Ge2 as this only occurs in **H**, where the degenerate state of *O_h*-symmetry is distorted. This is shown by IBO 291 and 292, where a *p*-orbital at Ge2 is forming an σ -bond to 4 Ge1 atoms instead of all 6 Ge1 atoms. The other two Ge1 atoms are not bonding in those degenerate orbitals, but IBOs at lower energies are found (IBO 283 and 283), which is shown in Figure 5.9. The two models also differ for the HOMO orbitals. **G** shows a completely delocalized *f*-shaped orbital. In total there are three *f*-shaped orbitals occupied by $\frac{2}{3}$.

To sum up the molecular calculation of **G** shows the "metallic" behavior even for

the molecule, whereas **H** shows a distortion to achieve a kinetically more stable molecule. The actual distortion in the solid is probably avoided due to the surrounding environment in the compound.

5.3 The Compound $\text{LiNi}_{1+x}\text{Ge}$ ($x = 0.17$)

5.3.1 Synthesis of $\text{LiNi}_{1+x}\text{Ge}$ ($x = 0.17$)

The starting materials Ni and Ge were pre-melted by arc-welding described in 2.4. The obtained regulus was transferred to a niobium ampule and peeled Li was added on top afterwards. The ampule was sealed by arc-welding and transferred into a silica tube. The silica tube was evacuated and put into a vertical resistance tube furnace. The samples were heated to 750 °C and tempered for 24 hours. Afterwards the silica tube was removed from the oven and quenched in water. After opening the ampules, the product appeared as metallic lustrous purple silver powder, which was sensitive to air and moisture. SC-XRD and P-XRD-measurement were performed, as well as, thermal investigates by DSC measurements.

Table 5.9: Masses and molar masses of the used chemicals

Chemical	Formula	Mass [mg]	Molar mass [mmol]
Germanium	Ge	148	2.04
Nickle	Ni	138	2.35
Lithium	Li	14	2.02

5.3.2 Characterization of $\text{LiNi}_{1+x}\text{Ge}$ ($x = 0.17$)

The compound was characterized by SC-XRD-measurements. The preparation was performed like described in 3.1. For the measurement a 0.1 mm diameter capillary was used. Single crystals revealed a hexagonal unit cell and the structural determination leads to Ni-Ge layers, that are separated by Li atoms. Selected crystallographic data is given in Table 5.10 and 5.11. Ge could be refined on the Ni2 position, as well, with a partial occupation of 28 %. Due to comparison of other similar structures like SrNi_3Ge_2 , where always Ni can be found on this position, EDX measurements and computational data, which is discussed in this chapter later, Ni and not Ge was determined to be located at this position. The R_1 and wR_2 values did not change significantly depending on Ge and Ni, but became significantly worse in case of a mixed position. EDX measurements were performed to determine the w-% for Ni and Ge, which are showing 48(6) w-% and 52(6) w-%, respectively. This results in a sum formula of $\text{LiNi}_{1.14}\text{Ge}$ suggesting Ni to be located in the Ni-Ge-layers.

Table 5.10: Single crystal data and structure refinement

Formula	LiNi_{1.17}Ge
Formula weight ($\frac{g}{mol}$)	148.25
Space group	$R\bar{3}m$ (no. 166)
Z	24
Unit cell parameters (\AA)	$a = 4.0807(6)$ $c = 18.799(4)$
Volume (\AA^3)	271.10(8)
$P_{calc}(\frac{g}{cm^3})$	5.4397
abs. coeff.	28.138
F(000)	406
Crystal shape/color	block/silver
Temperature (K)	250
Θ range	3.25-50.74
Range in hkl	-8/8 -8/5 -40/40
Reflections collected	3768
Unique reflections	279
Data / parameter	279/14
GOF on F^2	0.996
$R_1, wR_2 (I \geq 2\sigma(I))$	0.0277, 0.0407
R_1, wR_2 (all data)	0.0556, 0.0441
Largest diff. peak and hole	0.940 and -1.559

Additionally P-XRD-measurements were performed to reassure the found structure. In this case $\text{Cu}_{K\alpha 1}$ ($\lambda = 1.54056 \text{ \AA}$) radiation was used. The powder pattern compared with the theoretical pattern of the SC-XRD-data is shown in Figure 5.10.

Table 5.11: Atomic coordinates and equivalent isotropic displacement parameters for $\text{LiNi}_{1.17}\text{Ge}$

Atom	Wyck.	x	y	z	S.O.F.	$U_{eg}/\text{\AA}^2$
Ge1	6 <i>c</i>	0	0	0.40999(2)	1	0.01006(9)
Ni1	6 <i>c</i>	0	0	0.28220(3)	1	0.01041(10)
Ni2	3 <i>a</i>	0	0	0	0.33	0.0120(5)
Li1	6 <i>c</i>	0	0	0.1409(5)	1	0.0184(15)

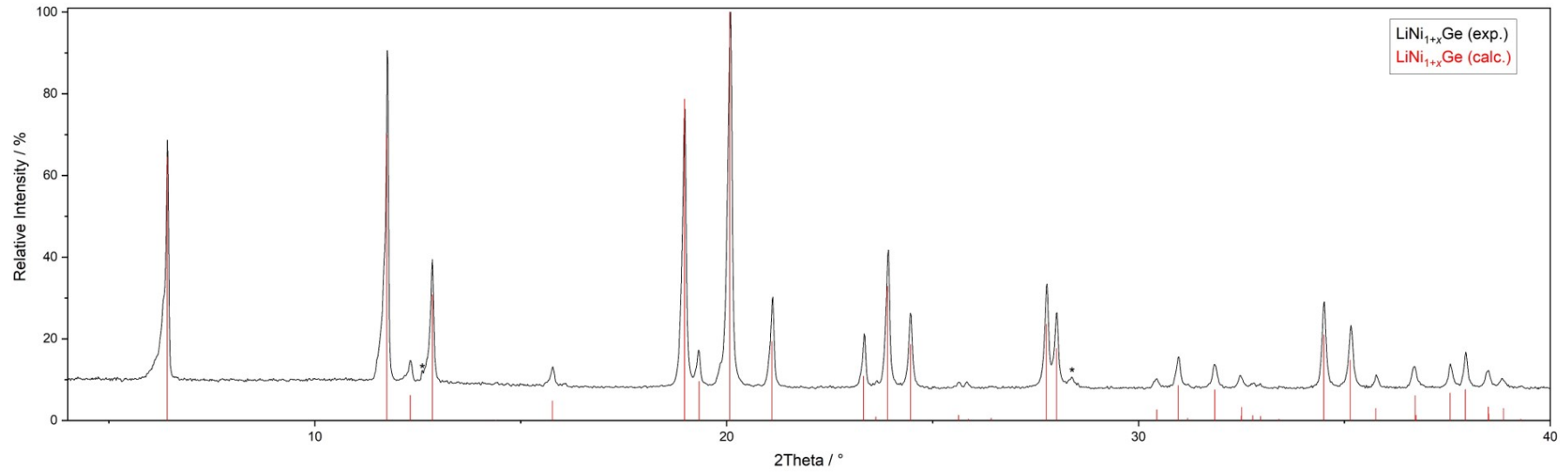


Figure 5.10: Experimental P-XRD diffractogram (black) with the theoretical pattern of $\text{LiNi}_{1+x}\text{Ge}$ ($x = 0.17$) (red). Minor sidephases are marked with an asterisk.

5.3.3 Structure Description of $\text{LiNi}_{1+x}\text{Ge}$ ($x = 0.17$)

The compound $\text{LiNi}_{1+x}\text{Ge}$ ($x = 0.17$) crystallizes like the compounds $\text{Li}_{2.35}\text{Si}$ and Li_4ZrGe_2 in a Li_5Tl_2 structure type.^[50–52] It can also be described as a filled variant of the hexagonal CaSi_2 .

The structure consists of puckered Ni-Ge double-deck layers, which is partial filled by Ni atoms (0.33). The center Ni atom is surrounded by two six-membered ring of alternating Ni and Ge atoms (Figure 5.11). This kind of layers is known from several structures like SrNi_3Ge_2 (Figure 5.13) or CaAl_2Si_2 . The later one CaAl_2Si_2 crystallizes as a defect version with no center atom in the Al_6Si_6 -polyhedra.^[53] These kind of structures belong to the large structure related family derived from the AlB_2 -type. The layers show a ABC stacking shown in Figure 5.12 a and b. The three layers A,

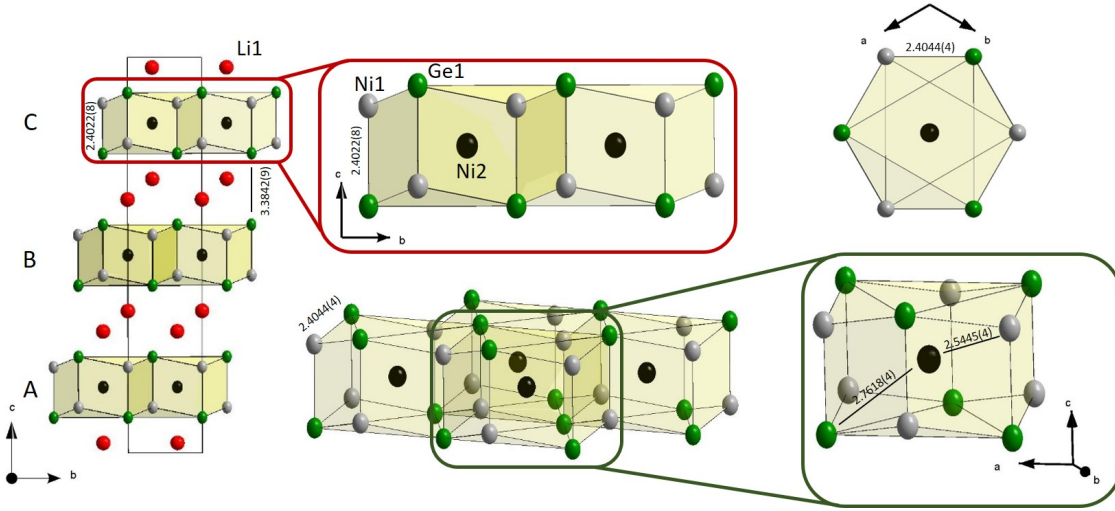


Figure 5.11: Structure of $\text{LiNi}_{1+x}\text{Ge}$. On the left side the unit cell is shown. The blue and red rectangles show close ups of layers and cluster units. And the top right pictures shows the top view of a cluster unit along c . The structure shows a ABC layered structure assigned in the illustration. Li, Ni1, Ni2 and Ge1 are represented as ellipsoids at the 90 % probability level in red, grey, black and green, respectively. The partial occupied position is shown in black. Thin black lines indicate polyhedra borders. For a better clarity Ni1 and Ni2 is marked by different colors.

B and C are represented in red, yellow and blue polyhedra. A top view in this illustration shows the dislocation of the stacked layers. In Figure 5.12 the coordination of Li atoms is shown as well. They are tetrahedrally coordinated in between the layers by one Ni atom and three Ge atoms.

The interatomic distance Ge1-Ni1 of 2.4022(8) Å and 2.4044(4) Å is in line with distances found in SrNi_3Ge_2 (2.36–2.40 Å) shown in 5.13. The structure $\text{Li}_{14}\text{Ni}_{8+x}\text{Ge}_{9-x}$ discussed in chapter 5.2 shows a Ni1-Ge1 distance of 2.403(1) for a typical Ge-Ni

bond. For example NiGe exhibits Ni-Ge bond lengths between 2.33 and 2.49 Å.^[45] This shows a classic Ni-Ge bond for Ge1-Ni1 in LiNi_{1+x}Ge (Pauling single bond length for Ni-Ge: 2.45 Å).^[bla]

The Ge1-Ni2 distance is longer and no bond should be considered (2.7618(4) Å). The distance is also in line with the data of SrNi₃Ge₂ (2.71 Å).

Between Ni1 and Ni2 also no bond should be considered (Ni1-Ni2: 2.5445(4) Å). Again, the distances matches with data received for SrNi₃Ge₂ (2.56 Å) and is also longer compared to elemental Ni (2.49 Å).^[46]

Between the layers Li is located, which ends up in a interlayer distance (Ge1-Ge1) of 3.3842(9) Å. This is significantly shorter than in SrNi₃Ge₂ (4.39 Å), where Sr atoms are located between the layers. The Sr atoms are much bigger than Li atoms. Although, for each Sr atom in SrNi₃Ge₂ two Li atoms occur in LiNi_{1+x}Ge the different size of atoms leads to the different interlayer distance.

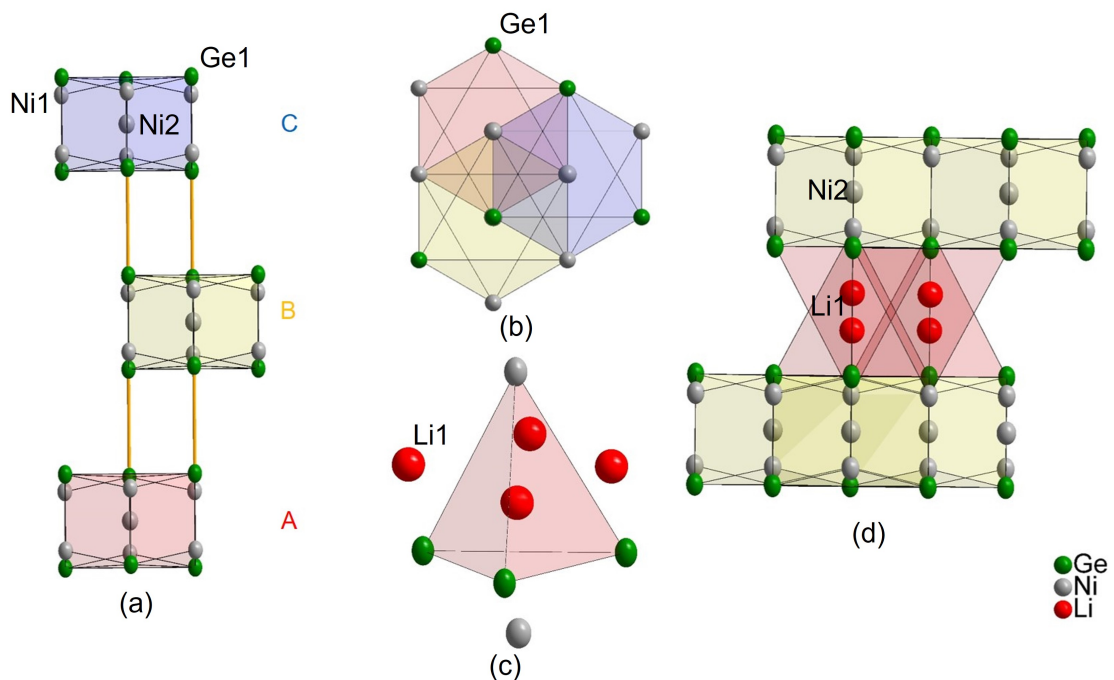


Figure 5.12: Structure of LiNi_{1+x}Ge. (a): the dislocation of the layers ist shown in blue, yellow and red, which are representing the differend layers A, B and C. (b): Top view of (a). (c) and (d): tetrahedral coordination of the Li atom is shown. Li, Ni and Ge are represented as as ellipsoids at the 90 % probability level in in red, grey and green, respectively.

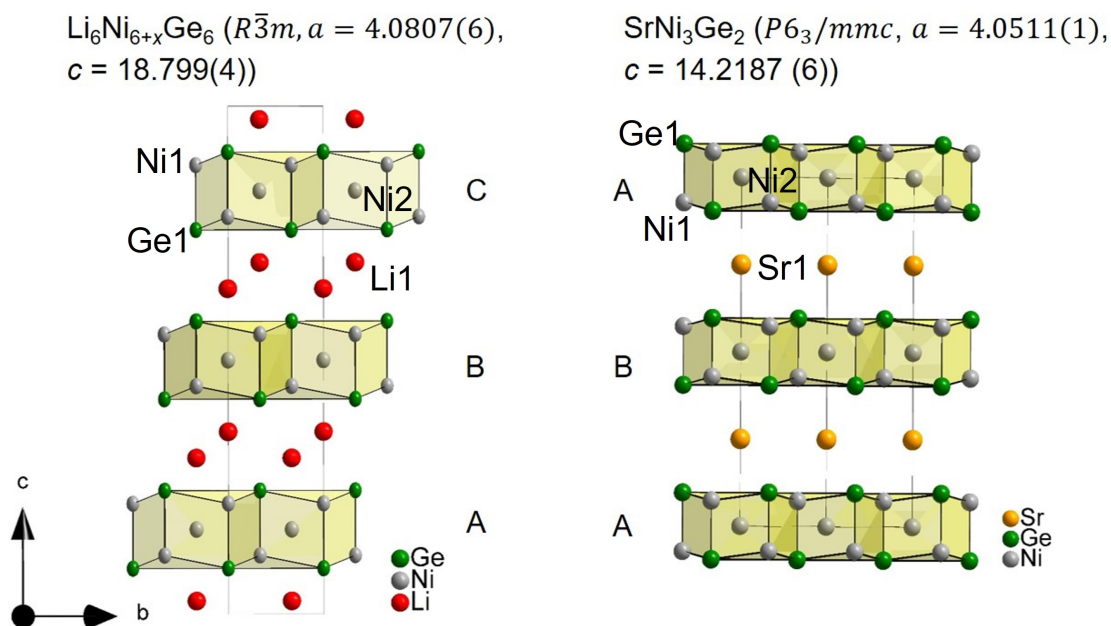
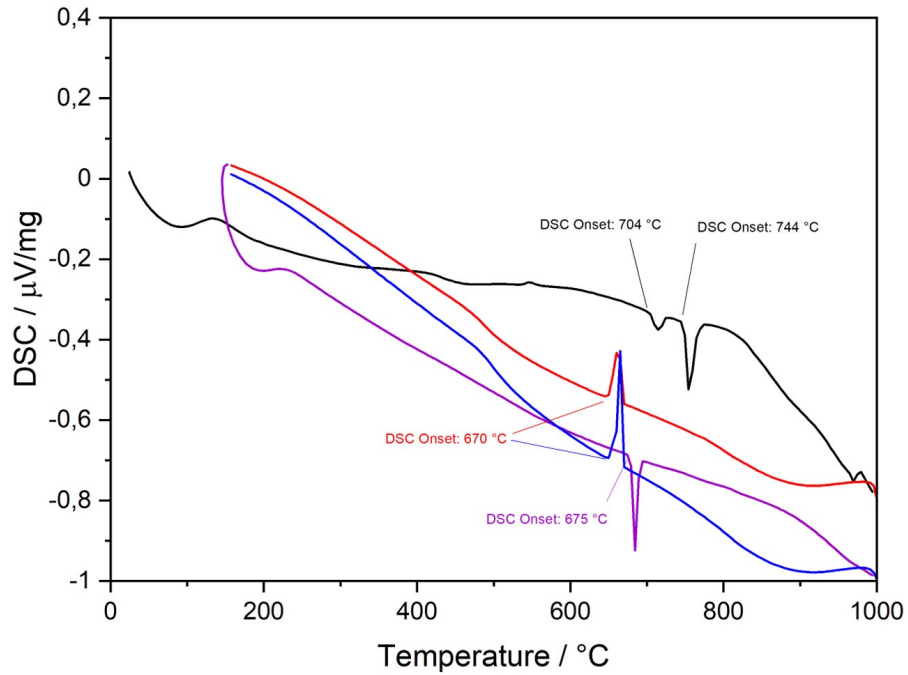


Figure 5.13: Structure of $\text{LiNi}_{1+x}\text{Ge}$ (left) and SrNi_3Ge_2 (right) showing different stacking of layers. Li, Sr, Ni and Ge are represented as ellipsoids at the 90 % probability level for $\text{LiNi}_{1+x}\text{Ge}$ and spheres for SrNi_3Ge_2 in red, yellow, grey and green, respectively.

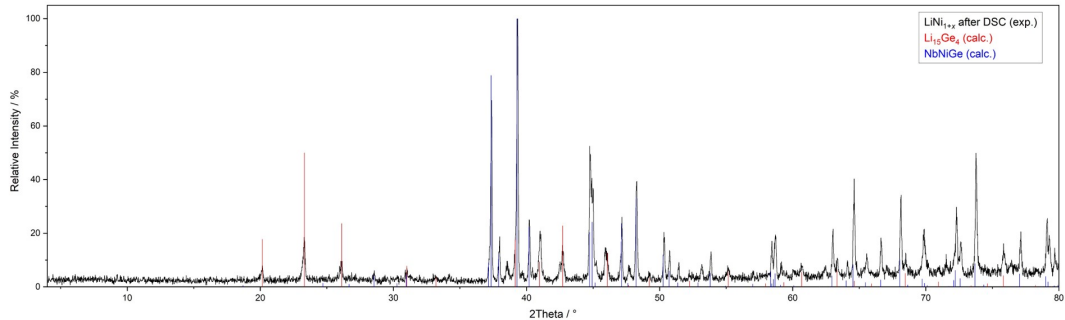
5.3.4 Thermal behavior of $\text{LiNi}_{1+x}\text{Ge}$ ($x = 0.17$)

The thermal behaviour was investigated by DSC measurement (Details see 3.3). In an Ar-filled glovebox, a Nb crucible was loaded with 50 mg of $\text{LiNi}_{1+x}\text{Ge}$ containing small remains of an unknown side phase. The sample was heated in Ar flow with a heating rate of $5 \text{ K} \cdot \text{min}^{-1}$ to $1000 \text{ }^\circ\text{C}$ and subsequently cooled down by the same rate to $150 \text{ }^\circ\text{C}$. The procedure was repeated. The sample was recovered in an Ar-filled glovebox and examined by P-XRD-experiments.

During the first heating cycle (black) the compound $\text{LiNi}_{1+x}\text{Ge}$ reacts with the ampule material Nb to NbNiGe and $\text{Li}_{15}\text{Ge}_4$ at $704 \text{ }^\circ\text{C}$. At $744 \text{ }^\circ\text{C}$ the melting starts in the first cycle. In the second heating cycle (purple) the reaction to NbNiGe and $\text{Li}_{15}\text{Ge}_4$ is not present any more, since all of compound $\text{LiNi}_{1+x}\text{Ge}$ did already react. At $675 \text{ }^\circ\text{C}$ the new melting point is present. The cooling cycles (red and blue) both show the melting point at $670 \text{ }^\circ\text{C}$. The DSC measurement including onsets of peaks is shown in Figure 5.14. DSC measurements in quartz ampules were performed, but due to intercalation of Li in the ampule material the ampule became brittle.



(a)



(b)

Figure 5.14: (a) Thermogramm of $\text{LiNi}_{1+x}\text{Ge}$ containing minor sidephases. The first and second heating traces are shown in black and purple, respectively. The first and second cooling traces are shown in red and blue, respectively. (b) Experimental P-XRD diffractogram of sample after DSC measurement (black) and theoretical pattern of $\text{Li}_{15}\text{Ge}_4$ ^[11] and NbNiGe .^[54]

5.3.5 Computational analysis of $\text{LiNi}_{1+x}\text{Ge}$ ($x = 0.17$)

The computational analysis for the structures $\text{LiNi}_{1.5}\text{Ge}$ (Ni at the central position), $\text{LiNiGe}_{1.5}$ (Ge at the central position) and LiNiGe (no central position) was carried out using the Crystal17 program package and density functional methods. A GGA functional after Perdew, Burke and Ernzerhof (PBEXC) and split-valence + po-

larization level basis sets derived from the Karlsruhe basis sets for all considered elements Li, Ni and Ge (full basis set details are given in the appendix) was applied. Detailed information about computational method is given in chapter 4. The starting geometry was taken from experimental data and all structures were fully optimized within the constraints imposed by the space group symmetry.

The cell parameters were compared for all models with respect to experimental data (Table 5.12). The results clearly show, that the experimental data is matching the model $\text{LiNi}_{1.5}\text{Ge}$ suggesting Ni to be located at the central position between the layers.

Table 5.12: Cell parameter a and b for $\text{LiNi}_{1.5}\text{Ge}$ (Ni at the central position), $\text{LiNiGe}_{1.5}$ (Ge at the central position) and LiNiGe (no central position), as well as, experimental data are shown in Å and as deviation (Δd) from experimental data in percentages

	$\text{LiNi}_{1.5}\text{Ge}$		$\text{LiNiGe}_{1.5}$		LiNiGe		Experimental Data $d / \text{Å}$
	$d / \text{Å}$	$\Delta d / \%$	$d / \text{Å}$	$\Delta d / \%$	$d / \text{Å}$	$\Delta d / \%$	
a	4.0565	0.01	4.0318	1.20	4.0521	0.70	4.0807
c	18.8865	0.00	22.4989	-19.68	17.0816	9.14	18.7990

References

- [1] W. Buchholz, H. Schuster, *Z. Anorg. Allg. Chem.* **1981**, *482*, 40–48.
- [2] H. Schuster, A. Mewis, *Z. Naturforsch.* **1969**, *24b*, 1190.
- [3] F. Kiefer, T. F. Fässler, *Solid State Sciences* **2011**, *13*, 636–640.
- [4] E. Menges, V. Hopf, H. Schäfer, A. Weiss, **1969**, *21*, 1351–1352.
- [5] J. Evers, G. Oehlinger, G. SEXTL, H. â. Becker, *Angew. Chem. Int. Ed.* **1987**, *26*, 76–78.
- [6] J. Evers, G. Oehlinger, *Angew. Chem. Int. Ed.* **2001**, *40*, 1050–1053.
- [7] H. G. von Schnering, R. Nesper, J. Curda, K.-F. Tebbe, *Angew. Chem.* **1980**, *92*, 1070–1070.
- [8] V. Hopf, H. Schäfer, A. Weiss, *Z. Naturforsch. B* **1970**, *25*, 653.
- [9] A. Grüttner, R. Nesper, H. G. von Schnering, *Acta Cryst.* **1981**, *A37*, C161.
- [10] R. Nesper, Habilitation, Universität Stuttgart, **1988**.
- [11] Q. Johnson, G. S. Smith, D. Wood, *Acta Cryst.* **1965**, *18*, 131.

- [12] M. Zeilinger, T. F. Fassler, *Dalton Transactions* **2014**, *43*, 14959–14970.
- [13] G. R. Goward, N. J. Taylor, D. C. S. Souza, L. F. Nazar, *J. Alloys Compd.* **2001**, *329*, 82.
- [14] H. Takizawa, K. Uheda, T. Endo, *Journal of Alloys and Compounds* **2000**, *305*, 306–310.
- [15] H. Pfisterer, K. Schubert, *Die Naturwissenschaften* **1950**, *37*, 112–113.
- [16] M. Ellner, T. Gödecke, K. Schubert, *J. less-common Met.* **1971**, *24*, 23–40.
- [17] S. Bhan, H. Kudielka, *Z. Metallkd.* **1978**, *69*, 333–336.
- [18] T. Suzuki, Y. Oya, S. Ochiai, *Metall. Trans. A* **1984**, *15 A*, 173–181.
- [19] A. Schnepf, H. Schnöckel, *Angew. Chem. Int. Ed.* **2002**, *41*, 3532–3552.
- [20] J. Lewis, *Pure and Appl. Chem.* **1965**, *10*, 11–36.
- [21] J. A. Bertrand, F. A. Cotton, W. A. Dollase, *J. Am. Chem. Soc.* **1963**, *85*, 1349–1350.
- [22] C. Brosset, *Arkiv. Kemi* **1949**, *1*, 353.
- [23] E. W. Abel, A. Singh, G. Wilkinson, *J. Chem. Soc.* **1960**, 1321.
- [24] N. N. Nesmeyanov, K. N. Anisimov, N. E. Kolobova, I. S. Kolomniker, *Izv. Akad. Nauk SSSR.* **1963**, 194.
- [25] F. A. Cotton, *Q. Rev. Chem. Soc.* **1966**, *20*, 389–401.
- [26] A. Ecker, E. Weckertt, H. Schnackel, *Nature* **1997**, *387*, 379–381.
- [27] A. Schnepf, G. Stösser, H. Schnöckel, *J. Am. Chem. Soc.* **2000**, *122*, 9178–9181.
- [28] T. F. Fässler, S. D. Hoffmann, *Angew. Chem. Int. Ed.* **2004**, *43*, 6242–6247.
- [29] K. Mayer, J. Weßing, T. F. Fässler, R. A. Fischer, *Angew. Chem. Int. Ed.* **2018**, *57*, 14372–14393.
- [30] S. Stegmaier, T. F. Fässler, *J. Am. Chem. Soc.* **2011**, *133*, 19758–19768.
- [31] L. Siggelkow, V. Hlukhyy, B. Wahl, T. F. Fässler, *Eur. J. Inorg. Chem.* **2011**, *9*, 4012–4024.
- [32] W. P. Saak, *Angew. Chem. Int. Ed. Engl.* **1991**, *30*, 881.
- [33] D. Fenske, J. Ohmer, J. Flachgenei, K. Merzweiler, *Angew. Chem. Int. Ed. Engl.* **1988**, *27*, 1277.
- [34] D. Fenske, R. Basoglu, J. Hachgenei, F. Rogel, *Angew. Chem. Int. Ed.* **1984**, *23*, 160–162.

- [35] D. Fenske, J. Flachgenei, J. Ohmer, *Angew. Chem. Int. Ed. Engl.* **1985**, *24*, 706.
- [36] L. D. Lower, L. F. Dahl, *J. Am. Chem. Soc.* **1976**, *98*, 5046–5047.
- [37] D. Fenske, J. Z. Magull, *Z. Naturforsch.* **1990**, *45b*, 121.
- [38] D. Fenske, H. Krautscheid, M.-H. Muller, *Angew. Chem. Int. Ed. Engl.* **1992**, *31*, 321.
- [39] E. Furet, J. H. Le, A.; Beuze, J. Saillard, *J. Am. Chem. Soc.* **1994**, *116*, 274–280.
- [40] K. Vogt, PhD thesis, **1994**.
- [41] D. Fenske, J. Ohmer, K. Merzweiler, *Angew. Chem. Int. Ed. Engl.* **1988**, *27*, 1512.
- [42] D. Fenske, C. Persau, *Z. Anorg. Allg. Chem.* **1991**, *593*, 61–68.
- [43] J. P. Zebrowski, R. K. Hayashi, A. Bjarnason, L. F. Dahl, *J. Am. Chem. Soc.* **1992**, *114*, 3121–3123.
- [44] J. Brennan, T. Siegrist, S. Stuczynski, M. Steigerwald, *J. Am. Chem. Soc.* **1989**, *111*, 9240–9241.
- [45] H. Pfisterer, K. Schubert, *Metallkd.* **1950**, *41*, 358–367.
- [46] H. E. Swanson, E. Tatge, *Acta Crystallogr. A.* **1954**, *7*, 464.
- [47] R. Gautier, F. Ogliaro, J.-F. Halet, J.-Y. Saillard, E. J. Baerend, *Eur. J. Inorg. Chem.* **1999**, *7*, 1161–1168.
- [48] J. Donohue, *The Structures of the Elements*, Wiley, New York, **1974**.
- [49] A. Henze, V. Hlukhyy, T. F. Fässler, *Inorg. Chem.* **2015**, *54*, 1152–1158.
- [50] H. G. von Schering, R. Nesper, K. F. Tebbe, J. Curda, *Z. Metallkd.* **1980**, *71*, 357–363.
- [51] G. M. Zatorska, V. V. Pavlyuk, V. M. Davydov, *J. Alloy. Compd.* **2004**, *367*, 80–84.
- [52] J. Stoehr, W. Mueller, H. Schaefer, *Studies in Inorganic Chemistry* **1983**, *3*, 753–756.
- [53] R.-D. Hoffmann, R. Pöttgen, *Z. Kristallogr.* **2001**, *216*, 127–145.
- [54] W. Jeitschko, A. G. Jordan, P. A. Beck, *R. Metall. Soc. AIME* **1969**, *245*, 335.

Substitutional Effects in the Li-Ge Binary System by Ag

6.1 Introduction

The ternary system Li-Ag-Ge was investigated in order to discover new compounds meeting the requirements for new Li-ion-battery materials as higher capacities and better cycling stability.^[1,2] In particular ZINTL-phases, as described in chapter 1.2.1 show structural features due to their very ionic behavior, which could be suitable for efficient battery materials such as solid electrolytes or electrode materials.

6.1.1 The binary system Li-Ge

Li-rich compounds containing group 14 elements (*Tt*) were investigated thoroughly in the last decade and Si became a potential candidate as anode material due to the very high specific capacity of about $4200 \frac{\text{mA}\cdot\text{h}}{\text{g}}$ ($\text{Li}_{17}\text{Si}_4$, see also chapter 7.1.1).^[3-6] However, silicon anodes lack in mechanical stability due to the volume change of about 300% during the lithiation process, which ends up in electrochemical grinding of the anode material.^[7] Therefore, its heavier homologue Ge has raised some interest. Noteworthy is, that Ge-containing compounds show up to 400 times higher Li diffusivity than Si at room temperature. Nevertheless, also Ge has the issue of material pulverization due to high volume change (250%).^[8,9] Several Li-Ge binaries are known to date listed in Table 6.1 and their structural motif regarding the connectivity of Ge atoms is shown in Figure 6.1. By raising the Li-content towards very Li-rich compounds over 50% Ge cannot build an anionic network anymore providing the stability during lithiation process. Ge is either present as isolated Ge or molecular fragments like rings, dumbbells, triangles, octahedra or tetrahedra, which are not interconnected anymore.

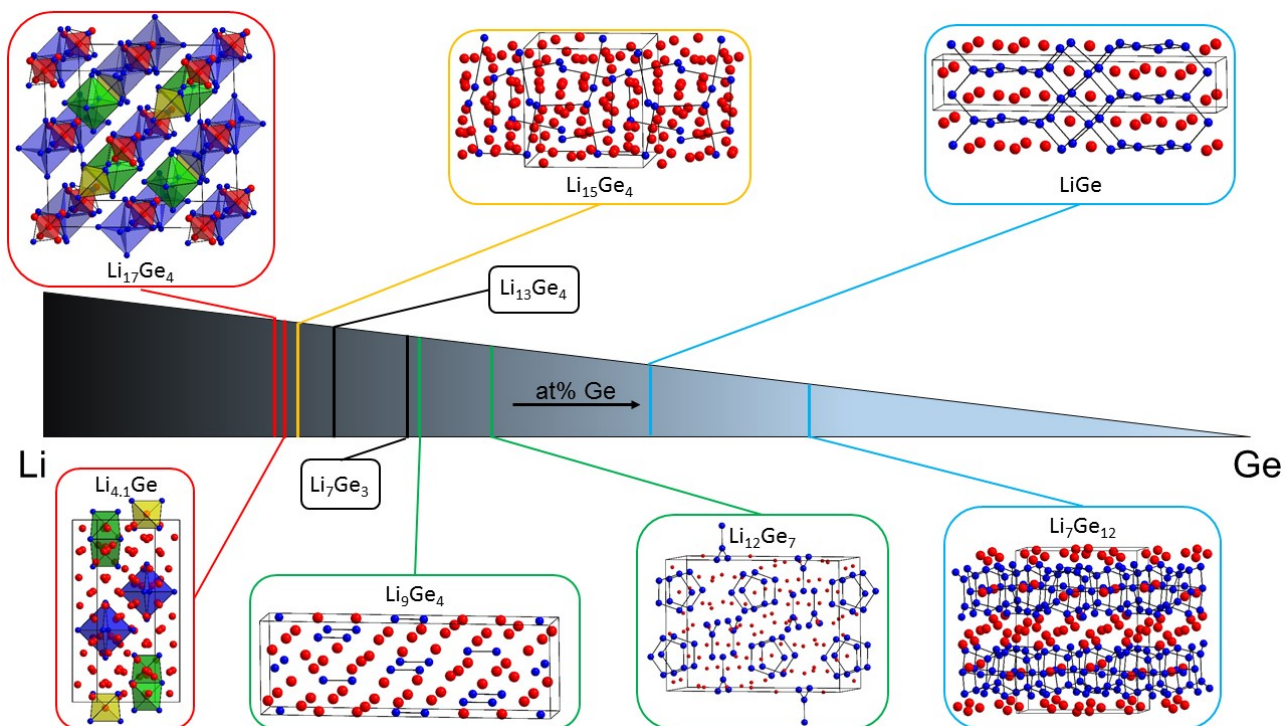


Figure 6.1: Fragments of the crystal structures of binary Li-Ge phases. The phases are color-coded according to the dimensionality of the anionic Ge framework: Ge octa- or tetrahedra (red), isolated Ge atoms (yellow), no detailed structure available (black), two-dimensional molecular units like dimer, triangles or rings (green) and two-dimensional layers (light blue). For clarity most of the Li atoms were removed in the structure $\text{Li}_{17}\text{Ge}_4$.

6.1.2 The binary system Li-Ag

The Li-Ag phase systems shows typical HUME-ROTHERY intermetallic phases in an untypical way.^[10-12] HUME-ROTHERY phases follow the rule of valence electron concentration ($\frac{e}{a}$). Unique is here the situation of $\frac{e}{a}$, which is always 1, because Li and Ag are both monovalent atoms (e is number of valence electrons and a is atoms per formula). Usually the structural motif changes with $\frac{e}{a}$, but in this case the typical structure motifs of HUME-ROTHERY phases are existent without a change of $\frac{e}{a}$. The Li-Ag phase system shows four HUME-ROTHERY phases β , γ_1 , γ_2 and γ_3 . All phases are having a phase width, which is again typical for HUME-ROTHERY phases and the γ -phases are separated by a two-phase region in between. The β -phase crystallizes in a typical CsCl-fashion, whereas the structure of γ -phases crystallize in the structure of γ -brass Cu_5Zn_8 .^[13] The phase diagram is shown in the appendix.

6.1.3 The binary system Ag-Ge

The Ag-Ge phase system exhibits a very simple eutectic form with a very low solubility of Ag in Ge and Ge in Ag. Only one phase Ag_4Ge was reported and analyzed by P-XRD obtaining only the tetragonal cell parameters of $a = 5.099$ and $c = 7.009$.^[14,15] The phase diagram is given in the appendix (Figure 13.10).

6.1.4 Substitution of Ag in the binary system Li-Ge

To overcome the electrochemical grinding of Li-Ge materials of the lithiation and delithiation process discussed in chapter 6.1.1 the integration of a transition metal (TM) was used to stabilize the anionic network. The substitution of Ge by Ag leads to electron deficiency and, therefore, to formation of two- and three-dimensional polyanionic networks. These networks provide cages, channels or layers for Li-ions. Additionally, by introducing a TM the complexity increases, because of the rising numbers of possible structures and atom distributions. In combination with chemical intuition this allows a better target-oriented and, therefore, efficient investigation of structures.^[16]

For ternary silicides Anani and Huggins already reported a better voltage profile and a higher reversible capacity by introducing a TM compared to the binary system of Li-Si.^[17,18] Cu- and Ag-containing composite-compounds were investigated by electrochemical analysis. The Cu-containing compounds synthesized by deposition of Cu on a Si surface with subsequently annealing showed a very high capacity of over $1400 \frac{\text{mAg}}{\text{g}}$ for the first cycle, but quickly fading after 15 cycles.^[19] Whereas Li-Ag-Si compounds showed hardly any capacity fading after 50 cycles, but the total capacity is only $280 \frac{\text{mAg}}{\text{g}}$. The sample was prepared by ball-milling receiving a uniform dispersion of Si in ductile Ag.^[20] An overview of Li- TM - Tt compounds was reported by Pöttgen *et al.* showing also a better stability against moisture of the ternary compounds compared to the Li- Tt compounds.^[21,22] The materials were investigated due to their electrochemical properties and especially the compounds Li_2AuSn_2 ,^[23,24] LiAg_2Sn ^[25,26] and $\text{Li}_3\text{Rh}_4\text{Si}_4$ ^[21] showed very high lithium mobility. In this work the ternary system with $TM = \text{Ag}$ was investigated. In particular the NaTl-like structures $\alpha\text{-Li}_2\text{AgGe}$, $\alpha\text{-Li}_{2.53}\text{AgGe}_2$ and new structure-related compounds were analyzed.^[27] An overview of all ternary compounds in the Li-Ag-Ge phase system is given in Figure 6.3 and Table 6.1. Additionally Figure 6.2 shows the structures with respect to their Li-content showing the same trend to isolated molecular units with very high percentage of Li as in the binary system Li-Ge. $\text{Li}_{12}\text{AgGe}_4$ ^[28] with a atm.%-Li of 70.6% shows linear Ge-Ag-Ge units and Ge-Ge dumbbells. Nevertheless, $\beta\text{-Li}_2\text{AgGe}$ (atm%-Li=50) exhibits a neat anionic network

with channels for Li-ion. In the following chapters 6.1.5 and 6.1.6 the structure of the already known compounds α - Li_2AgGe and α - $\text{Li}_{2.53}\text{AgGe}_2$ are described.

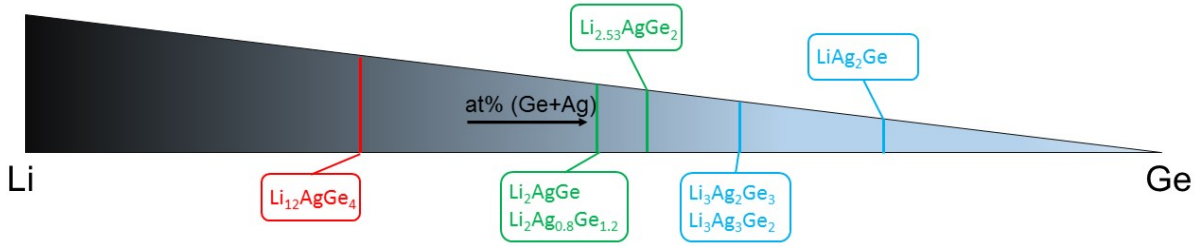


Figure 6.2: All known ternary compounds of the Li-Ag-Ge system according to their Li content. The structures are divided in three different categories: Molecular units of Ag and Ge (red), NaTl-like anionic substructure with channels for Li-ions (green) and three-dimensional structures without channels for Li-ions (light-blue).

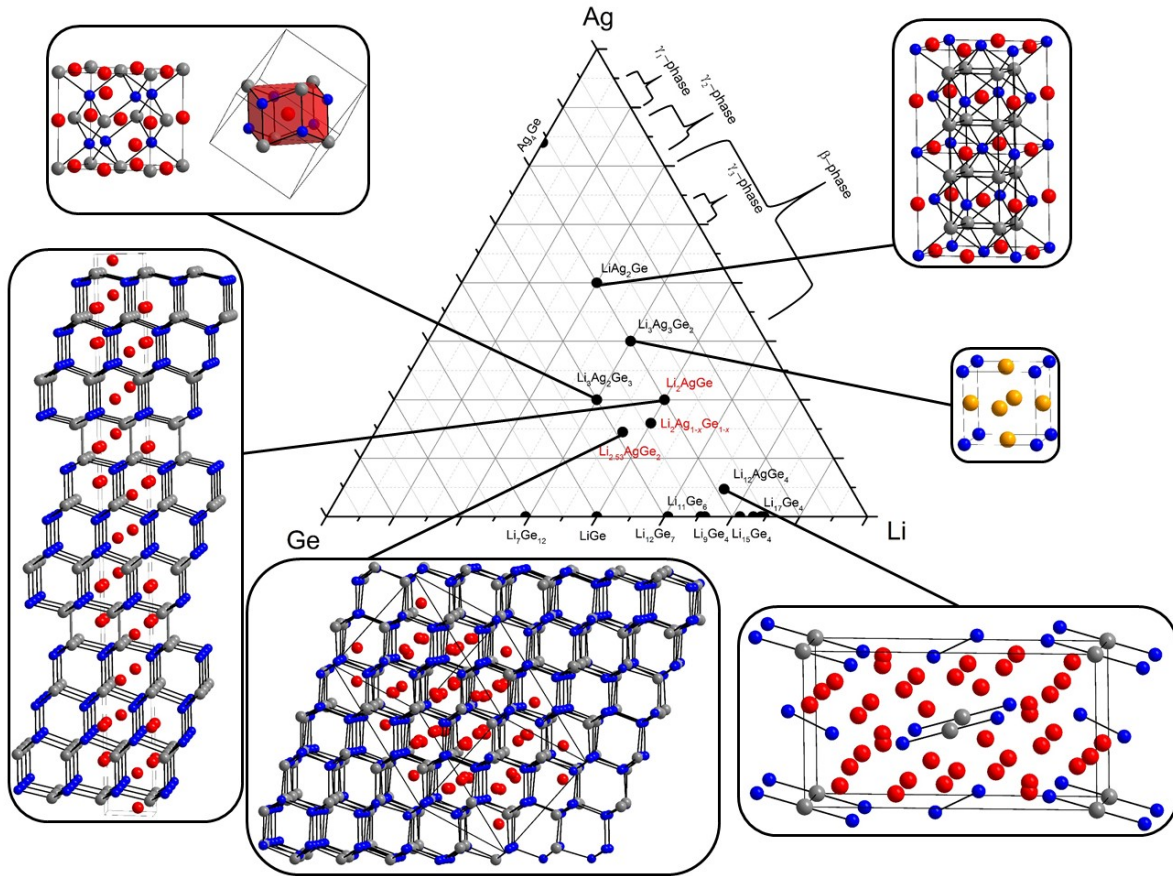


Figure 6.3: Ternary composition diagram of the phase system Li-Ag-Ge including all known binaries. For clarity not all Li-Ge-compounds were assigned. A full list of all compounds is given in Table 6.1. At the corners the pure elements Li, Ag and Ge are located. Compounds investigated in this thesis are given in red and an excerpt of the crystal structure of all known ternary compounds is given. Li, Ag, Ge and a Li/Ag mixed position are shown in red, grey, blue and orange, respectively.

Table 6.1: All known binary and ternary compounds in the Li-Ag-Ge phase diagram

Compound	Space Group	Ref.
Li ₇ Ge ₁₂	P2/n	[29]
LiGe	I4 ₁ md	[30]
HP-LiGe	I4 ₁ a/P6 ₃ /mmc	[31] / [32]
Li ₁₂ Ge ₇	Pnma	[33]
Li ₉ Ge ₄	Cmcm	[34]
Li ₇ Ge ₃	P3 ₂ 2	[35]
Li ₁₃ Ge ₄	n.a. ^[a]	[36]
Li ₁₅ Ge ₄	I44d	[37]
Li _{4.1} Ge	Cmcm	[5]
Li _{16.95} Ge ₄	F43m	[38]
Li ₁₇ Ge ₄	F43m	[5]
Ag ₄ Ge	n.a. ^[a]	[14] / [15]
Ag-Li (β -phase)	Pm3m	[10]
Ag-Li (γ_1 -phase)	I43m	[10]
Ag-Li (γ_2 -phase)	I43m	[10]
Ag-Li (γ_3 -phase)	I43m	[10]
Li ₁₂ AgGe ₄	Pbam	[28]
LiAg ₂ Ge	Fm3m	[39]
Li ₃ Ag ₃ Ge ₂	Pm3m	[39]
Li ₃ Ag ₂ Ge ₃	P4 ₂ /nnm	[39]
α -Li ₂ AgGe	R3m	[27]
α -Li ₂ Ag _{0.8} Ge _{1.2}	I4 ₁ /amd	[b]
β -Li ₂ Ag _{1-x} Ge _{1+x}	Fd3m	[b]
α -Li _{2.53} AgGe ₂	I4 ₁ /a	[27]
γ -Li _{2.53} AgGe ₂	Fd3m	[b]

^[a] no crystal structure was published

^[b] this thesis

6.1.5 The compound α -Li₂AgGe

As mentioned above this compound α -Li₂AgGe found by Henze *et al.* was investigated in this thesis by thermal and computational analysis. Especially, the computational analysis was carried out to understand the driving force to build such big superstructures. The principle of the coloring problem in the polyanionic network is discussed in this work taking the relative energies and bonding situations into account. In this section the structure is described.

The structure, which crystallizes in the space group $R\bar{3}m$, is shown in Figure 6.4. The structure type is a fully ordered variant of Li₁₃Ag₅Si₆.^[40] The Ag and Ge atoms form a diamonds-polytype-like polyanionic network and Li atoms are stuffed in the channels, which are arranged in a diamond-like fashion, too. The coordination environment and channels stuffed with Li ions are shown in Figure 6.5. The structure can also be derived from the NaTl structure with Ag and Ge on Tl positions. This structure is achieved by transforming the NaTl structure into the trigonal crystal system and subsequently quadruplicate the axes along c direction. This transformation is described in detail on chapter 6.5 with the structural relation to other compounds in this phase system.

The inter atomic distances of Ag-Ge, Ge-Ge and Ag-Ag are 2.752 Å, 2.537 Å and 2.969 Å, respectively. The Ag-Ge distances are in line with a typical bond length of a Ag-Ge bond observed in LiAg₂Ge. Also the Ge-Ge distances are in a typical range or even shorten than the bond length of Ge-Ge dumbbell in Li₁₃Ge₄. At last, the Ag-Ag distance matches the distances also found in Li₁₃Ag₅Si₆. All bonds length are discussed with respect to the coloring problem in the computational analysis (Chapter 6.8). The interatomic Li-Li distance range from 2.648 to 2.753 Å.

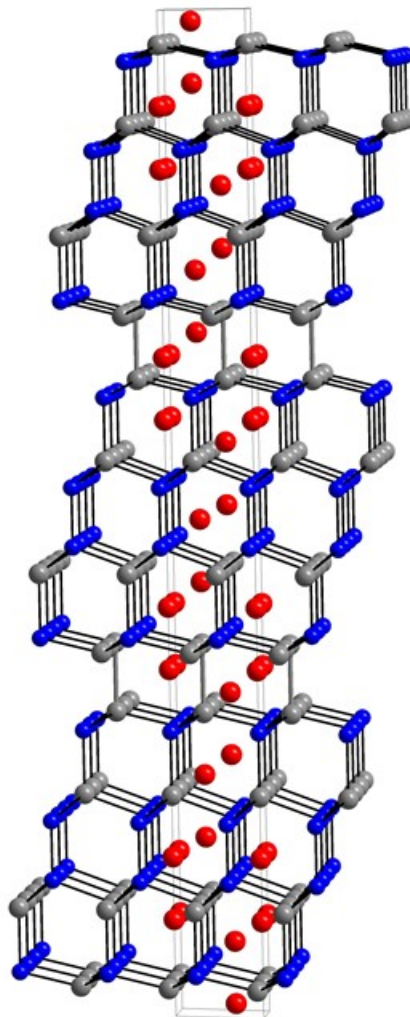


Figure 6.4: Excerpt of the crystal structure of α -Li₂AgGe showing the NaTl-like anionic Ag/Ge-substructure stuffed with Li-ions. Li, Ag and Ge are shown in red, grey and blue, respectively.

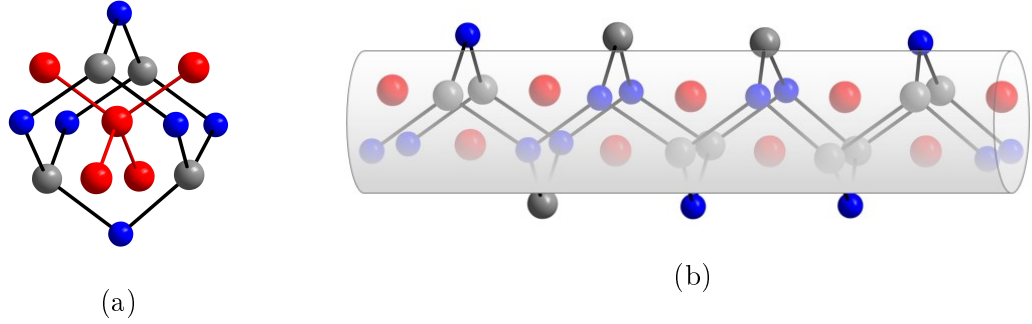


Figure 6.5: (a) Coordination environment of Li in α -Li₂AgGe. (b) Channel provided by the anionic Ag-Ge network for Li-ions. Li, Ag and Ge are shown in red, grey and blue, respectively.

6.1.6 The compound α -Li_{2.53}AgGe₂

α -Li_{2.53}AgGe₂ is the second known compound exhibiting this NaTl-like structure in the Li-Ag-Ge phase system. Like α -Li₂AgGe, this compound was investigated by thermal and computational analysis in this work. The thermal analysis led to a new phase γ -Li_{2.53}AgGe₂ with the same structural features and the computational work was used to understand the bonding situation of the compound. In this section the crystal structure is briefly discussed.

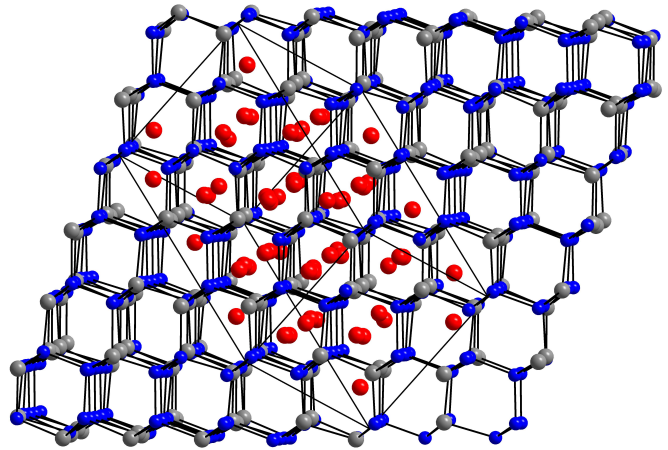


Figure 6.6: Excerpt of the crystal structure of α -Li_{2.53}AgGe₂ showing the NaTl-like anionic Ag/Ge substructure stuffed with Li-ions. Li, Ag and Ge are shown in red, grey and blue, respectively.

The crystal structure of α -Li_{2.53}AgGe₂ is illustrated in Figure 6.6 showing the NaTl-like motif. The compound crystallizes in its own structure type in space group $I4_1/a$ with fully ordered Ge and Ag positions. Noteworthy is the situation of Li atoms. In α -Li₂AgGe the Li atoms itself are arrange in a diamond-like fashion. In the case of α -Li_{2.53}AgGe₂ the diamond-like motif of Li atoms exhibits Li-vacancies, whereas Li2 (16*f*), Li3 (16*f*) and Li (16*f*) are fully occupied, Li1 (8*e*) is only partial occupied with a S.O.F. of 0.32. Even considering a fully occupancy of Li1 positions would result in the

formula " $\text{Li}_{2.8}\text{AgGe}_2$ " and Li defect positions with respect to the diamond-type Li-substructure. Including the $4b$ position located at $(0, 0.25, 0.675)$ would complete the diamond-type Li-substructure and the formula " Li_3AgGe_2 ". These Li vacancies are shown in Figure 6.7 and show a possible path for Li mobility.

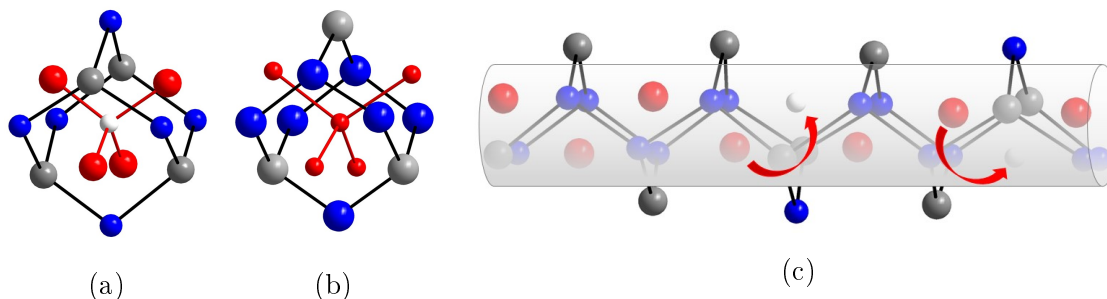


Figure 6.7: (a) Coordination environment of Li-vacancy at $4b$ position of $\alpha\text{-Li}_{2.53}\text{AgGe}_2$. (b) Coordination environment of Li. (c) Channel provided by the anionic Ag-Ge network for Li-ions with Li-vacancies. Possible Li-mobility is shown with red arrows. Li, Ag, Ge and Li-vacancy are shown in red, grey, blue and white, respectively.

The interatomic distances match the distances already reported for $\alpha\text{-Li}_2\text{AgGe}$ in chapter 6.1.5 with a Ge-Ge and Ag-Ge distance of 2.579 to 2.618 Å and 2.650 to 2.850 Å, respectively.

6.1.7 Towards new structure-related compounds

This chapter gives an overview of all investigated compounds including known and new compounds, as well as, structure models investigated by computational analysis.

Three new compounds $\beta\text{-Li}_2\text{Ag}_{0.8}\text{Ge}_{1.2}$ (chapter 6.2), $\alpha\text{-Li}_2\text{Ag}_{0.8}\text{Ge}_{1.2}$ (chapter 6.3) and $\gamma\text{-Li}_{2.53}\text{AgGe}_2$ (chapter 6.4.1) were found with the same structural motif based on the NaTl-structure-type. During the thermal analysis (DSC) high-temperature-phases were discovered and were subsequently target-oriented synthesized. In addition several models were developed for computational analysis showing the coloring problem of some structures. All structures were connected *via* the Bärnighausen family tree formalism (see chapter 1.3 for theoretical background and chapter 6.5 for the family tree with detailed reduction steps).

An overview of all structures is given in Table 6.2. All synthesized compounds are labeled from (1) to (5) and all models are labeled with a three letter code implying the crystal system and a number. The labels were used throughout the thesis.

All structural details to the structure models are given in chapter 6.8.

Table 6.2: Overview of all synthesized compounds and structure models

Synthesized Compound	Comment	Label
β -Li ₂ Ag _{1-x} Ge _{1+x}	new high-temperature phase	(1)
γ -Li _{2.53} AgGe ₂	new high-temperature phase	(2)
α -Li ₂ Ag _{0.8} Ge _{1.2}	new low-temperature phase	(3)
α -Li _{2.53} AgGe ₂	known low-temperature phase	(4)
α -Li ₂ AgGe	known low-temperature phase	(5)
Model Stoichiometry	Related Experimental Structure	Label
Li ₂ AgGe	1 and 2	Cub1
Li ₂ AgGe		Tet1
Li ₂ Ag _{0.8} Ge _{1.2}	3	Tet2
Li ₂ Ag _{0.8} Ge _{1.2}	3	Tet3
Li _{2.8} AgGe ₂	4	Tet4
Li _{2.6} AgGe ₂	4	Tet5
Li ₂ AgGe	5	Tri1
Li ₂ AgGe	5	Tri2
Li ₂ AgGe	5	Tri3

6.2 The Compound β -Li₂Ag_{1-x}Ge_{1+x}

6.2.1 Synthesis of β -Li₂Ag_{0.8}Ge_{1.2}

β -Li₂Ag_{0.8}Ge_{1.2} was synthesized by a high temperature route described in chapter 2.6.2. The elements (chapter 2.1) were mixed in a tantalum ampule in the expected ratio and the sealed ampule (chapter 2.5) was transferred to a corundum tube, which was equipped with an attached balloon for pressure compensation. The corundum tube was evacuated and heated to 660 °C under Ar and held for 24 h. Subsequently it was rapidly cooled down by transferring the ampule directly to an iced water bath. After opening the ampules, the product appeared as metallic lustrous silver powder, which was sensitive to air and moisture. SC-XRD, P-XRD-measurement and NMR analysis were performed.

Table 6.3: Masses and molar masses of the used chemicals for $\beta\text{-Li}_2\text{Ag}_{0.8}\text{Ge}_{1.2}$

Chemical	Formula	Mass [mg]	Molar mass [mmol]
Germanium	Ge	233	3.20
Silver	Ag	230	2.14
Lithium	Li	37	5.34

6.2.2 Characterization of $\beta\text{-Li}_2\text{Ag}_{0.8}\text{Ge}_{1.2}$

The compound was characterized by SC-XRD measurements. The preparation was performed analogously to the procedure described in chapter 3.1 and a 0.3 mm diameter capillary was used for the measurement. A face-centered cubic cell was found exhibiting a NaTl-like structure motif. Selected crystallographic data is given in Table 6.4 and 6.5. Additional crystallographic data is given in the appendix (Table 13.18 and 13.19)

Additionally, the structure was investigated by P-XRD experiments with subsequently RIETVELD-refinement. Pseudo-Voigt was chosen for the peak profile and the asymmetry correction was fitted by divergence. The background was determined manually. The structure was refined using an absorption correction of a cylindrical sample (1.6). All cell parameter, atomic positions and isotropic displacement parameters were refined freely, as well as, site occupations of Ag and Ge. The data is shown in Table 6.10 and Figure 6.12.

Table 6.4: Single crystal data and structure refinement of β -Li₂Ag_{0.8}Ge_{1.2}

Formula	β -Li ₂ Ag _{0.8} Ge _{1.2}
Formula weight/ $\frac{g}{mol}$	187.28
Space group	$Fd\bar{3}m$ (no. 227)
Z	2
Unit cell parameters/ \AA	$a = 6.2068(7)$
Volume/ \AA^3	239.11(8)
$\rho_{calc}/\frac{g}{cm^3}$	2.601
abs. coeff./ mm^{-1}	10.596
F(000)	164
Crystal shape/color	block/grey silver
Temperature (K)	150
Θ range/deg	5.691-56.474
Index Range in hkl	$-14 \leq h \leq 13$ $-12 \leq k \leq 14$ $-14 \leq l \leq 8$
Reflections collected	2590
Unique reflections	102
reflections with $I > 2\sigma(I)$	96
Data/restraints/parameter	102/0/4
GOF on F^2	1.545
R_1, wR_2 ($I \geq 2\sigma(I)$)	0.0300, 0.0752
R_1, wR_2 (all data)	0.0316, 0.0762
Largest diff. peak and hole	0.964, -1.507

Table 6.5: Atomic coordinates and equivalent isotropic displacement parameters of β -Li₂Ag_{0.8}Ge_{1.2}

Atom	Wyck.	x	y	z	S.O.F.	$U_{eg}/\text{\AA}^2$
Ge1	8a	0.1250	0.1250	0.1250	0.49(12)	0.0136(3)
Ag1	8a	0.1250	0.1250	0.1250	0.51(12)	0.0136(3)
Li1	8b	0.3750	0.3750	0.3750	1	0.030(6)

Table 6.6: RIETVELD structure refinement details of β -Li₂Ag_{0.8}Ge_{1.2} from P-XRD measurements at room temperature

Formula	β-Li₂Ag_{0.8}Ge_{1.2}
T/K	300
Formula weight/ $\frac{g}{mol}$	187.3
Space group	$Fd\bar{3}m$ (no. 227)
Z	2
Unit cell parameters/ \AA	$a = 6.23615(6)$
Volume/ \AA^3	242.515(4)
$\rho_{calc}/\frac{g}{cm^3}$	2.5648
$\lambda/\text{\AA}$	0.70926
2 Θ range/deg	10.8- 49.943
R _w (all)	2.31%
R _{wp}	3.46%
R _{exp}	2.14%
χ^2	2.61
GOF	1.62

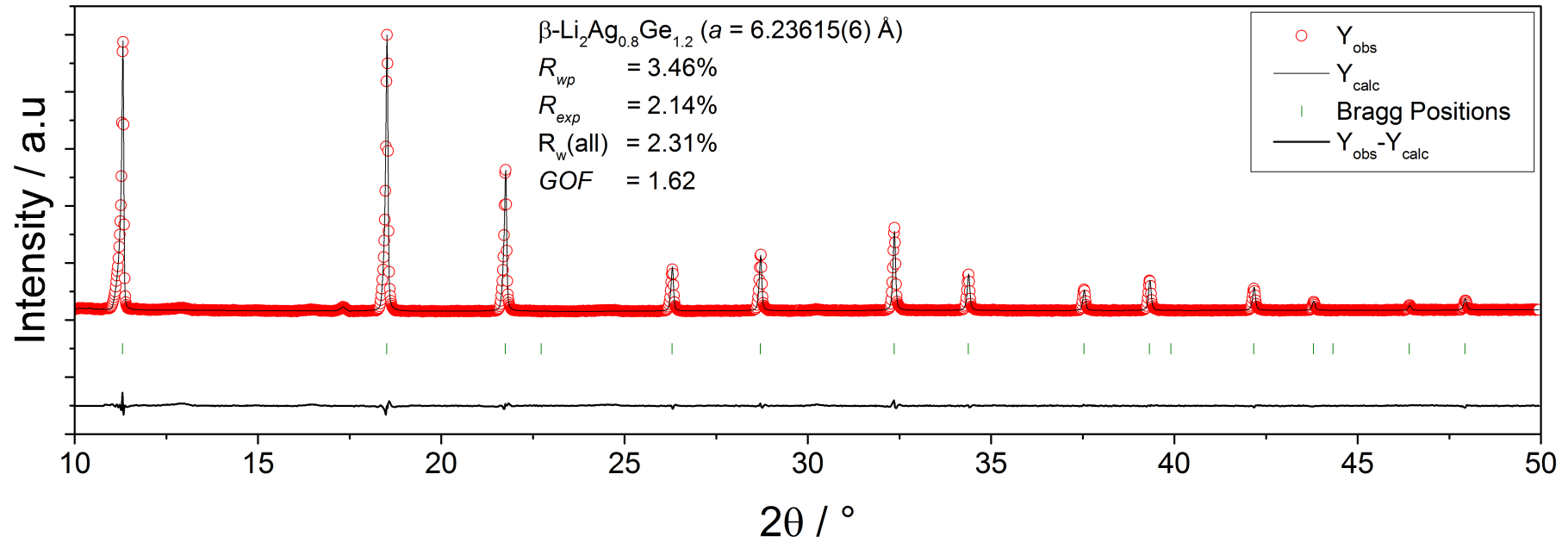


Figure 6.8: RIETVELD-refinement of $\beta\text{-Li}_2\text{Ag}_{0.8}\text{Ge}_{1.2}$ from powder P-XRD diffraction data ($\lambda = 0.7107$ Å) at room temperature. Red circles show observed intensities Y_{obs} , the black line shows the calculated intensities Y_{calc} , blue line reveal the difference of observed and calculated intensities ($Y_{obs} - Y_{calc}$), and green marks indicate BRAGG positions of $\alpha\text{-Li}_2\text{Ag}_{0.8}\text{Ge}_{1.2}$. The region from 17.1 to 17.55° has been excluded, because this peak belongs device issues and is not part of the measured powder.

6.2.3 Structure Description of $\beta\text{-Li}_2\text{Ag}_{0.8}\text{Ge}_{1.2}$

Compound $\beta\text{-Li}_2\text{Ag}_{0.8}\text{Ge}_{1.2}$ (**1**) crystallizes as a version of the NaTl structure type with a disordered site occupation on Wyckoff-position $8a$ of Ag/Ge in space group $Fd\bar{3}m$ (no. 227). The Ag/Ge position has a mixed occupancy with no signs of superstructure ordering. The disordered structures are rather common for high-temperature phases, since there is usually a tendency for unordered structures with higher temperatures due to higher entropy.

The NaTl-like structure can be derived from the cubic CsCl structure-type. CsCl crystallizes in a cubic primitive structure with an occupied cubical void as shown in Figure 6.19a. The cell parameters a , b and c have to be doubled to gain a superstructure consisting of eight smaller cubes. Both atomic sites of the CsCl superstructure are now occupied alternately with two different atoms in each subcube. The derived model can be described with a general formula of $ABCD$, which is shown in Figure 6.19b. This general structure gives several possibilities to occupy the four different sites. As discussed in chapter 1.3 this shows a typical case of the coloring problem in a simple case and raises the question of how to distribute the atoms in the cell and why they are taking those sites.

Going back to ternary systems, this allows for an occupation of two atom sites with the same atom. The book *Anorganische Strukturchemie* by U. Müller discusses two typical phases that can be achieved with this kind of CsCl-superstructure.^[41] The first phase, known as HEUSLER-phase, can be derived by either $C = D$ or $A = B$ resulting in the formula A_2CD (Figure 6.9c). HEUSLER-phases are discussed as part of the introduction in chapter 1.2.2. A typical example is TiCo_2Si .^[42] For those phases B and C usually is a transition metal and A a main group element of group 13-15. Therefore, Li would be rather unusual to occupy this positions, but some cases are known. For example Li_2AgMg ,^[43] containing Li-atoms is a HEUSLER-phase. The other phase, which has a few representative crystallizing with this kind of motif, are ZINTL-phases (see chapter 1.2.1 for more information). In this case $B = D$ or $A = C$ as shown in Figure 6.9d. For ZINTL-phases alkali-metals like Li are very typical to achieve the salt-like structure. Li_2AgSb is an example crystallizing as a AB_2C structure, with $A = \text{Sb}$, $B = \text{Li}$ and $C = \text{Ag}$. In the case of $\beta\text{-Li}_2\text{Ag}_{0.8}\text{Ge}_{1.2}$, one observes shows metallic behavior, which is very untypical since ZINTL-phases are typically semi-conductors.

The occupation of B and D with an identical atom hints to for a ZINTL phase as well, since for HEUSLER C and D would be occupied with the same element. At the same time, A and C are also occupied by the same element in **1** due to the mixed Ag/Ge position, which ends up in the NaTl structure type. NaTl itself is a metallic ZINTL phase. Several examples are given with their site occupation in Table 6.7.

This lead to the assumption that the compound is neither a typical HEUSLER phase, nor a typical ZINTL-phase and represents a polar intermetallic compound and therefore not an electron precise ZINTL phase. In chapter 6.8 the electronic structure is discussed in more detail including computational chemistry. In Figure 6.9e a unit cell of the compound is shown in thick lines, whereas the thinner dashed lines shows the eight CsCl-subunits.

The Ag/Ge atoms form a diamond-like network with an interatomic distance of

Table 6.7: Examples for structures derived from a ABCD-structure with given A , B , C and D occupation, assigned phase-type and reference

Compound	A	B	C	D	Phase	Ref.
β -Li ₂ Ag _{0.8} Ge _{1.2}	Ag/Ge	Li	Ag/Ge	Li		[a]
NaTl	Tl	Na	Tl	Na	ZINTL	[44]
Li ₂ AgSb	Sb	Li	Ag	Li	ZINTL	[45]
Li ₂ AgSb	Sb/Ag	Li	Sb/Ag	Li	ZINTL	[46]
Li ₂ ZnGe	Ge	Zn	Li	Li	HEUSLER	[47]
Li ₂ ZnGe	Ge	Li	Zn/Li	Zn/Li	HEUSLER	[48]
LiNi ₂ Sn	Sn	Li	Ni	Ni	HEUSLER	[49]
TiCo ₂ Si	Si	Ti	Co	Co	HEUSLER	[42]
Li ₂ AuBi	Au	Li	Bi	Li	ZINTL	[50]
MnCu ₂ Al	Al	Mn	Cu	Cu	HEUSLER	[51]
MgAgAs	As		Mg	Ag	HALF-HEUSLER	[52]
Na ₂ CdPb	Cd	Na	Pb	Na	ZINTL	[53]
Li ₂ AgMg	Ag	Li	Li/Mg	Li/Mg	HEUSLER	[43]
Li ₂ CdSb	Cd	Sb	Li	Li	HEUSLER	[54]
Li ₂ ZnSb	Sb	Zn/Li	Li	Zn/Li		[55]
Li ₃ Bi	Bi	Li	Li	Li		[56]
Diamond	C		C			[57]
CsCl	Cs	Cs	Cl	Cl		[58]

[a] this thesis

2.6876(3) Å (Figure 6.9f). The interatomic distance is in line with the values found for other distances in Li-Ag-Ge structures. In the case of **(5)**, which exhibits a similar structure motif with ordered Ag and Ge positions, the Ag-Ge distances are about 2.75 Å, whereas the Ge-Ge and Ag-Ag distances are 2.537 Å and 2.969 Å, respectively. Since this new compound has a mixed position with all possible arrangements it should be in the range of Ge-Ge, Ag-Ag and Ag-Ge inter atomic distances, but closest to the Ge-Ge bond length due to the higher Ge content. This matches very well. The Ag-Ge bond length of **4** varies between 2.650 Å and 2.850

Å. In this structure only a Ge-Ge (2.579-2.618 Å) bond is found, whereas no Ag-Ag bonds are observed in this structure. The Ge-Ge bond is shorter than in **1**, but then again **1** contains additionally Ag-Ge and Ag-Ag bonding due to the mixed position, which would elongate the bond. $\text{Li}_{12}\text{AgGe}_4$ exhibits also Ge-Ge and Ag-Ge bonds as dumbbells and a linear Ge-Ag-Ge unit. Both bonds, 2.546 Å (Ge-Ge) and 2.510 Å (Ag-Ge), are shorter than the bond in **1**. This can be explained by fact, that in $\text{Li}_{12}\text{AgGe}_4$ molecular units separated from each other are present and no network exists. In this Li-surrounding the units are able to arrange more freely compared to a rigid network. Additional Ag-Ag bonds elongate the network in our compound due to a longer bond length. The values, which can be found in elemental Ag^[59] and α -Ge^[60] also match with the experimental finding (2.889 Å and 2.445 Å, respectively), which should be in between both values.

Summarizing the Ag/Ge-Ag/Ge bonds are in good accordance to the values found in literature and an average of a Ag-Ge, Ge-Ge and Ag-Ag bond can be found, which states the fact of an completely disordered site. An extended list of Ag-Ag, Ge-Ge and Ag-Ge bond length can be seen in Table 6.8.

The Li-Li distance is the same 2.6876(3) Å as for Ag/Ge-Ag/Ge, due to the symmetry. Li is intercalated in the Ag/Ge-network forming another diamond-like pattern. The distance is in the range of other similar structures like **(5)** (2.648 to 2.753 Å) and **(4)** (2.492-3.019 Å), but shorter than in the elemental body-centered cubic (bcc) Li (3.05 Å). This is because Li in our case and the other two examples in the Li-Ag-Ge system is mostly ionic Li^+ , whereas in the elemental case it is Li^0 .

Table 6.8: Interatomic distances for Ag-Ag, Ge-Ge and Ag-Ge of various compounds

Compound	d(Ag-Ag) / Å	d(Ag-Ge) / Å	d(Ge-Ge) / Å
β - $\text{Li}_2\text{Ag}_{0.8}\text{Ge}_{1.2}$ (1)	2.69	2.69	2.69
γ - $\text{Li}_{2.53}\text{AgGe}_2$ (2)	2.68	2.68	2.68
α - $\text{Li}_2\text{Ag}_{0.8}\text{Ge}_{1.2}$ (3)		2.70-2.71	2.69
α - $\text{Li}_{2.53}\text{AgGe}_2$ (4)		2.65-2.85	2.58-2.62
α - Li_2AgGe (5)	2.97	2.75	2.54
$\text{Li}_{12}\text{AgGe}_4$		2.55	2.51
α -Ge			2.45
$\text{Li}_{13}\text{Ge}_4$			2.62
CaGe			2.59
Ag	2.89		
LiAg_2Ge		2.74	
Summ of covalent radii		2.65	

6.2.4 Phase Width of $\beta\text{-Li}_2\text{Ag}_{1-x}\text{Ge}_{1+x}$

The mixed Ag/Ge position in $\beta\text{-Li}_2\text{Ag}_{0.8}\text{Ge}_{1.2}$ is indicating a possible phase width compared to the low-temperature phase, which exhibits a fully ordered structure. Therefore synthesis with different ratio Ag:Ge for the general formula $\beta\text{-Li}_2\text{Ag}_{1-x}\text{Ge}_{1+x}$ ($x = 0.1, 0.2, 0.25,$ and 0.3) was carried out. The products were investigated by P-XRD experiments with $\text{Mo}_{k\alpha_1}$ -radiation as described in chapter 3.2 indicating a trend for larger 2Θ with higher Ag content. All diffraction patterns were indexed and the cell parameters were compared (Figure 6.11). A Vegard-plot is shown in Figure 6.10. For the case $x = 0.3$ already side phases occur indicating this formula already above a border case of the phase width. Therefore a small phase width between $x = 0.1$ and <0.3 is present.

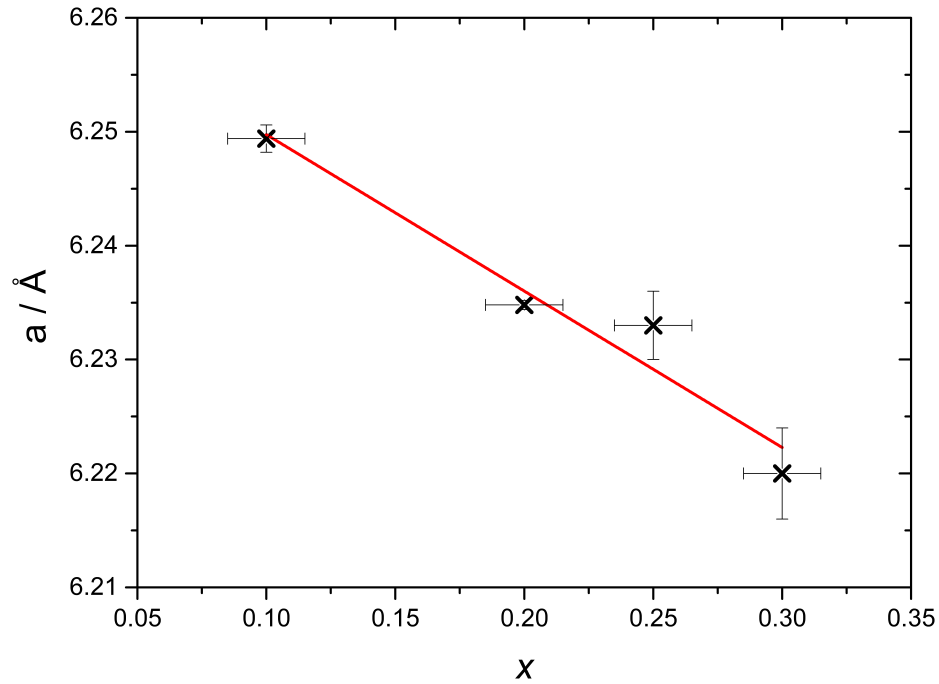


Figure 6.10: Vegard-Plot of $\beta\text{-Li}_2\text{Ag}_{1-x}\text{Ge}_{1+x}$ ($x = 0.1, 0.2, 0.25,$ and 0.3). Errors in a and x parameter is implied by vertical and horizontal lines.

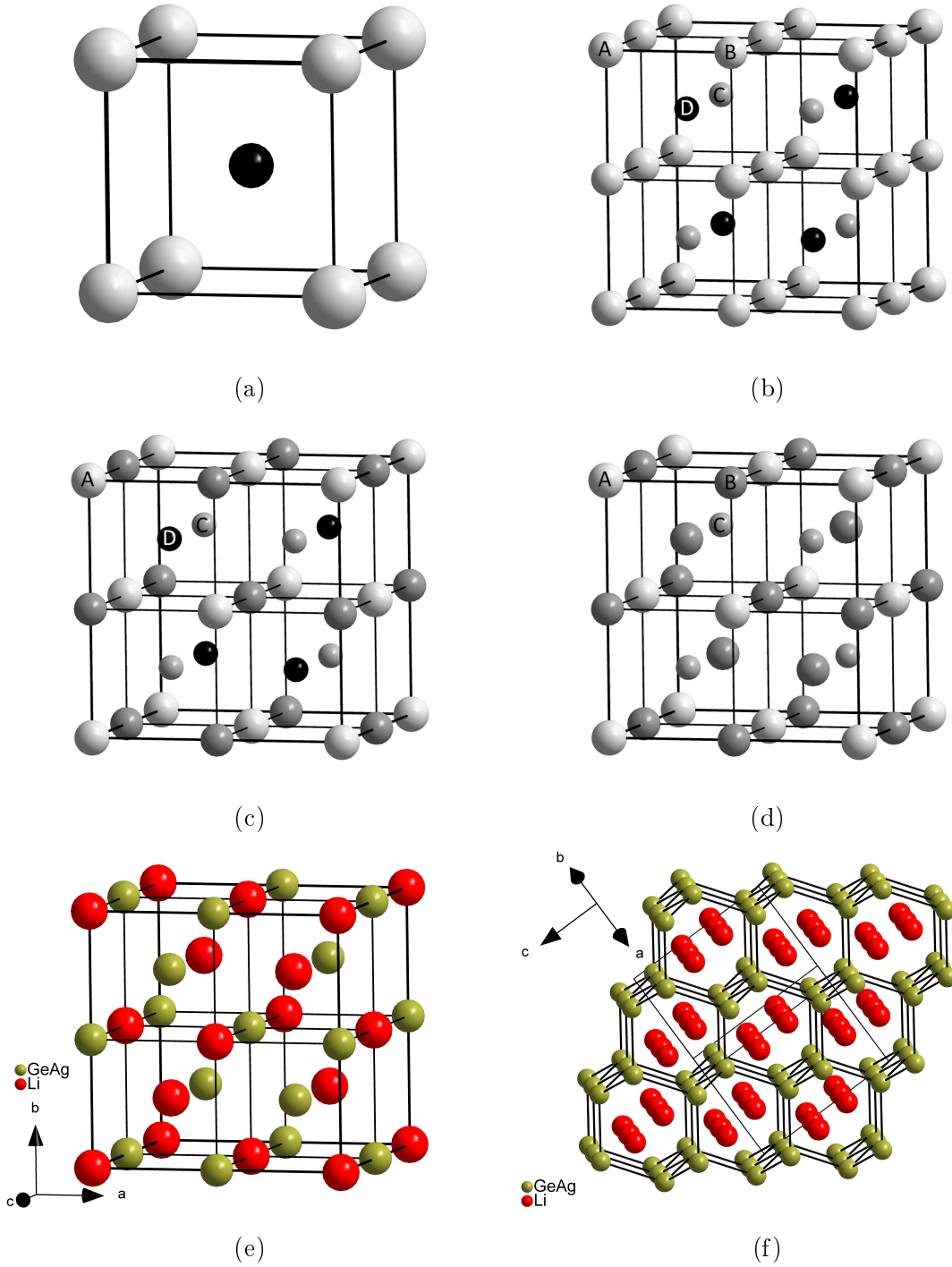


Figure 6.9: (a) Unit cell of a CsCl structure type showing the primitive cubic cell with filled cubic void. (b) Unit cell of an $ABCD$ structure derived from a CsCl structure by doubling all cell parameters a , b and c . (c) A_2CD structure of a typical HEUSLER phase. (d) AB_2C structure of a ZINTL phase like Li_2AuBi . (e) Unit cell of **(1)**. Li is shown in red and Ag/Ge in dark yellow. The thinner lines show the CsCl-like substructure. (f) Structure of **(1)** showing the diamond-like network of Ag/Ge. Li is shown in red and Ag/Ge in purple. The thinner lines show the unit cell borders.

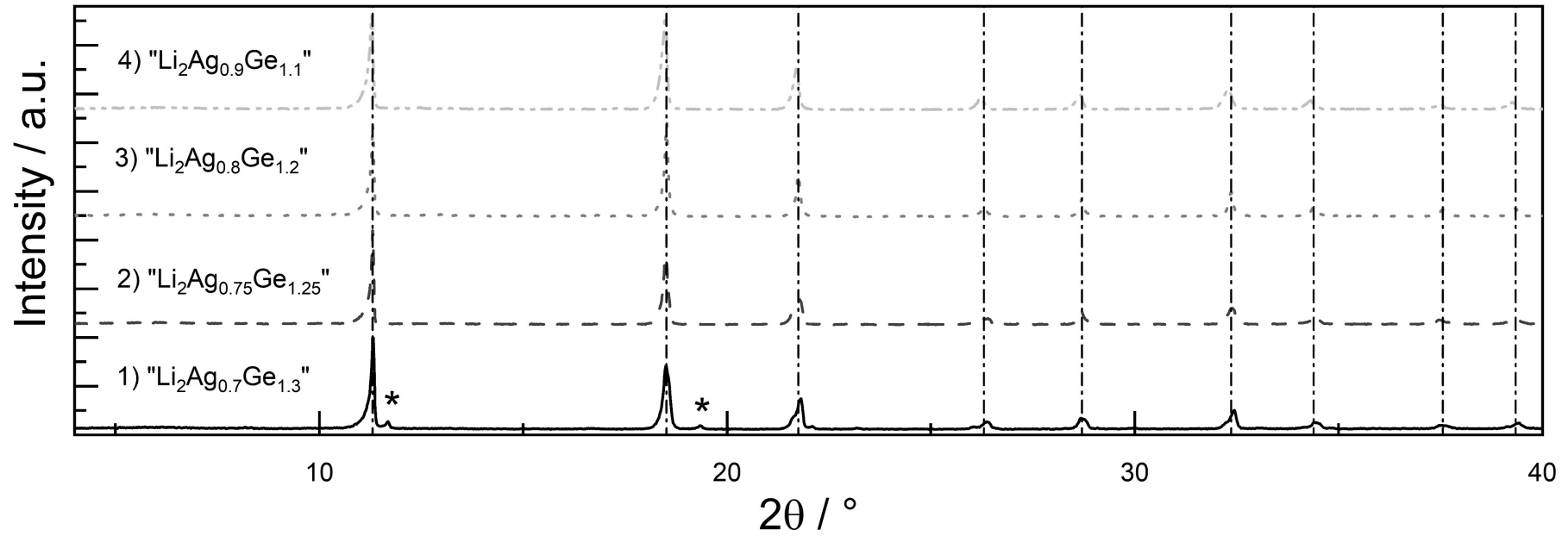


Figure 6.11: P-XRD pattern of β - $\text{Li}_2\text{Ag}_{1-x}\text{Ge}_{1+x}$ with different stoichiometry ($x = 0.1, 0.2, 0.25, \text{ and } 0.3$). Reflexes of β - $\text{Li}_2\text{Ag}_{0.8}\text{Ge}_{1.2}$ are shown by vertical lines. A clear trend is visible for larger 2θ with higher Ag content. Side phase is marked by asterisk.

6.3 The Compound $\alpha\text{-Li}_2\text{Ag}_{0.8}\text{Ge}_{1.2}$

6.3.1 Synthesis of $\alpha\text{-Li}_2\text{Ag}_{0.8}\text{Ge}_{1.2}$

$\alpha\text{-Li}_2\text{Ag}_{0.8}\text{Ge}_{1.2}$ (**3**) was synthesized by a high temperature route described in chapter 2.6.1. The elements (chapter 2.1) were mixed in a tantalum ampule in the expected ratio and sealed by arc welding (chapter 2.5). The ampule was transferred into a silica tube, which was evacuated and heated to 750 °C in a vertical resistance tube furnace. The temperature was held for 1 h and subsequently cooled down to 300 °C with $0.5 \frac{\text{K}}{\text{min}}$. The oven was switched off after the sample was kept at 300 °C for 3 h. After opening of the ampule, the product appeared as metallic lustrous silver powder, which was sensitive to air and moisture. P-XRD-measurement and NMR analysis were performed.

Table 6.9: Masses and molar masses of the used chemicals for $\alpha\text{-Li}_2\text{Ag}_{0.8}\text{Ge}_{1.2}$

Chemical	Formula	Mass [mg]	Molar mass [mmol]
Germanium	Ge	233	3.20
Silver	Ag	230	2.14
Lithium	Li	37	5.34

6.3.2 Characterization of $\alpha\text{-Li}_2\text{Ag}_{0.8}\text{Ge}_{1.2}$

The compound $\alpha\text{-Li}_2\text{Ag}_{0.8}\text{Ge}_{1.2}$ was primary characterized by P-XRD-measurements with RIETVELD-refinement. The preparation was performed as described in chapter 3.2. For all measurements a 0.3 mm diameter capillary was used. For **3** an absorption correction of a cylindrical sample was applied (2.5). Pseudo-Voigt was chosen for the peak profile and the asymmetry correction was fitted by divergence. The background was determined manually. All cell parameter and atomic positions were refined freely. For Ag and Ge all displacement parameter were refined anisotropic, whereas the Li positions were coupled and refined isotropic.

Additionally, SC-XRD-measurements (chapter 3.1) were applied, which showed a poor crystal quality. Therefore, the crystal structure could not be refined by single crystal methods, but the parameters of the tetragonal unit cell were gained as $a = \sim 4 \text{ \AA}$ and $c = \sim 30 \text{ \AA}$. In Figure 6.12 the P-XRD-pattern with RIETVELD-refinement is shown and in Table 6.10 and 6.11 the details are listed. The cell parameters at room temperature were refined as $a = 4.38778(6) \text{ \AA}$ and $b = 31.6056(6) \text{ \AA}$.

Table 6.10: RIETVELD structure refinement details of α -Li₂Ag_{0.8}Ge_{1.2} from P-XRD measurements at room temperature

Formula	α -Li ₂ Ag _{0.8} Ge _{1.2}
T/K	300
Formula weight/ $\frac{g}{mol}$	187.3
Space group	$I4_1/amd$ (no. 141)
Z	10
Unit cell parameters/ \AA	$a = 4.38778(6)$ $c = 31.6056(6)$
Volume/ \AA^3	608.491(16)
$\rho_{calc}/\frac{g}{cm^3}$	5.1109
$\lambda/\text{\AA}$	0.70926
2 Θ range/deg	9-49.943
R _w (all)	2.32%
R _{wp}	3.58%
R _{exp}	1.88%
χ^2	3.61
GOF	1.90

Table 6.11: Atomic coordinates and equivalent isotropic displacement parameters of α -Li₂Ag_{0.8}Ge_{1.2}

Atom	Wyck.	x	y	z	S.O.F.	$U_{eg}/\text{\AA}^2$
Ge1	8e	0	0.25	0.17391(19)	1	0.005(3)
Ge2	4b	0	0.25	00.375	1	0.005(2)
Ag1	8e	0	0.25	0.17391(19)	1	0.037(2)
Li1	8e	0	0.25	0.0680(19)	1	0.030(5)
Li2	8e	0	0.25	0.271(2)	1	0.030(5)
Li3	4a	0	0.75	0.125	1	0.030(5)

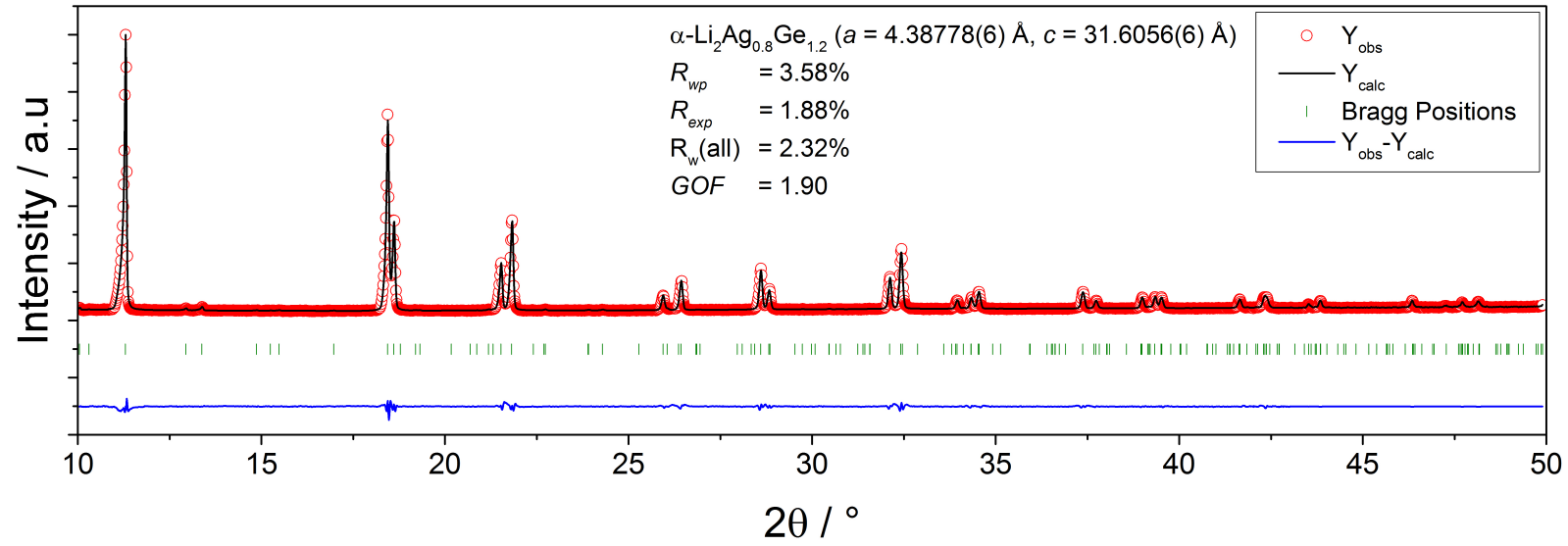


Figure 6.12: Rietveld-refinement of $\alpha\text{-Li}_2\text{Ag}_{0.8}\text{Ge}_{1.2}$ from powder P-XRD diffraction data ($\lambda = 0.7107 \text{ \AA}$) at room temperature. Red circles show observed intensities Y_{obs} , the black line shows the calculated intensities Y_{calc} , blue line reveal the difference of observed and calculated intensities ($Y_{obs} - Y_{calc}$), and green marks indicate BRAGG positions of $\alpha\text{-Li}_2\text{Ag}_{0.8}\text{Ge}_{1.2}$.

6.3.3 Structure Description of $\alpha\text{-Li}_2\text{Ag}_{0.8}\text{Ge}_{1.2}$

The compound $\alpha\text{-Li}_2\text{Ag}_{0.8}\text{Ge}_{1.2}$ **3** crystallizes in its own structure type in the space group $I4_1/amd$ (no. 141). All atomic positions are completely occupied and fully ordered. No phase width was found. By adding more Ge or Ag to the synthesis side phases occur and no change in the atomic cell parameters of the compound is observed.

The structure can be derived from its high-temperature phase **1** described in chapter 6.2 by converting the cubic cell into the tetragonal space group no. 141 and subsequently quintupling the c -axis. This transformation allows the original mixed Ag/Ge position to order in the exact ratio of 0.8:1.2 fitting the stoichiometry of the compound and shows the tendency to order structures by lowering the temperature. Hence, the driving force to build up this large structure is to keep the structural motif, but at the same time fully order the mixed position.

The structure can be seen as a superstructure of the CsCl structure-type as shown in Figure 6.13. Along the c -axis five different subunits of the type X_2YZ are shown building a $XYZZ'Y'$ structure, where the Li always takes the same position (A), but Ag and Ge are switching between B and C position. Layers are assigned as a and b , meaning that either Ag or Ge is occupying the position in that layer, respectively. The single X_2YZ subunits are slightly distorted.

Due to the special arrangement of the position, again, a diamond-like network is built by Ge and Ag atoms (Figure 6.14a). Compared to the high-temperature phase all positions are now fully ordered, which

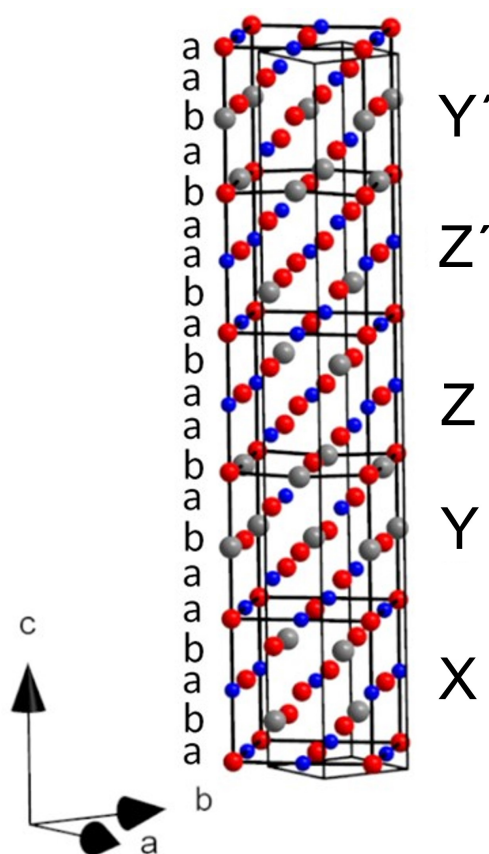


Figure 6.13: $\alpha\text{-Li}_2\text{Ag}_{0.8}\text{Ge}_{1.2}$ shown as a superstructure of the X_2YZ -structure in $XYZZ'Y'$ -layers. Li is always occupying the X position, whereas Ge and Ag switch within the X_2YZ -subunit between Y and Z position. Layers in a X_2YZ -subunit occupied by Ag and Ge is assigned as a and b , respectively. Li, Ag and Ge are shown in red, grey and blue spheres.

mean that one can distinguish between Ag-Ge, Ge-Ge and Ag-Ag bonds unlike in the high-temperature phase **(1)**. The later one, Ag-Ag bond, is not preferred due to the absence in the whole structure. This kind of bond can be observed in the similar structure Li_2AgGe , which builds the same structure motif also fully ordered. In **5** the Ag-Ag bond also seems less stable, which is shown by a high interatomic distance of 2.969 Å. This is discussed later on as part of the electronic structure analysis. Ag-Ge and Ge-Ge bonds are both present in the structure. Noteworthy is the Ge-Ge bond, which only occurs in ${}^1_{\infty}[\text{Ge}_2]$ zig-zag chains along the a or b axis (Figure 6.14b). This also occurs in another structure CaGe . The Ge-Ge interatomic distance in our structure is 2.6874 Å and significantly longer than in CaGe (2.592 Å), **5** (2.537 Å) and **4** (2.579-2.618 Å). The Ag-Ge distance (2.7030 Å and 2.7114 Å) is slightly longer than in its high-temperature phase (2.6878 Å), but in the high temperature phase this is an average of Ag-Ge, Ge-Ge and Ag-Ag bonds, where the Ge-Ge contribution probably leads to this shorter length. Compared to the other low-temperature phases **5** and **4** the distance is in line (2.75 Å and 2.65-2.85 Å, respectively). The Li-Li distances vary from 2.6156 to 2.7967 Å. These high difference are probably due to the network built by the Ag and Ge atoms. The Li are more or less isolated in the voids built by this network resulting again in a diamond-like structure motif. In **4** the variation is even higher from 2.492 to 3.019 Å.

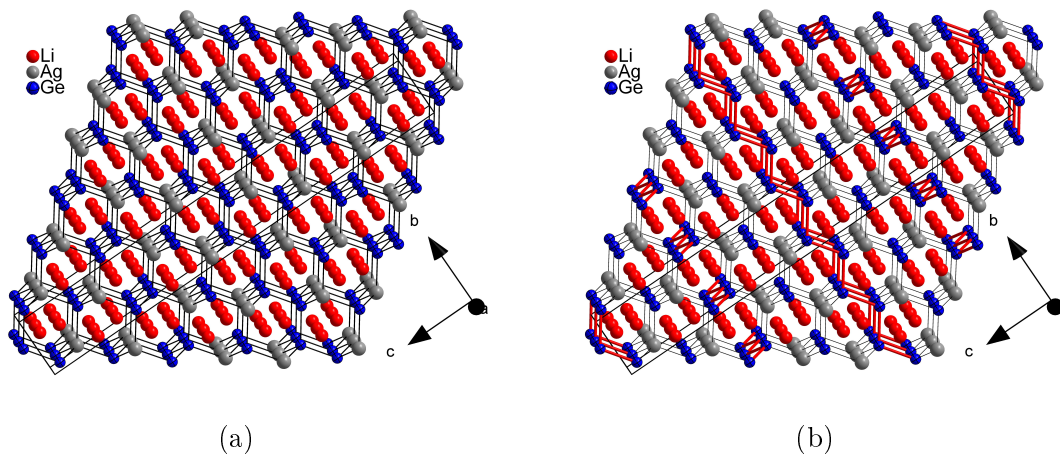


Figure 6.14: (a) The typical diamond-like structure is shown, which Li intercalated channels. (b) The Ge-Ge bonds are shown as thicker red lines to make the arrangement as ${}^1_{\infty}[\text{Ge}_2]$ zig-zag chains along the a or b axis clear.

6.4 The Compound γ -Li_{2.53}AgGe₂

6.4.1 Synthesis of γ -Li_{2.53}AgGe₂

γ -Li_{2.53}AgGe₂ was synthesized by a high temperature route described in chapter 2.6.2. 150 mg of the low-temperature phase α -Li_{2.53}AgGe₂ (**4**) was sealed in a tantalum ampule. The ampule (chapter 2.5) was transferred to a corundum tube, which was equipped with an attached balloon for pressure compensation. The corundum tube was evacuated and heated to 570 °C under Ar and held for 24 h. Subsequently it was rapidly cooled down by transferring the ampule directly to an iced water bath. After opening the ampules, the product appeared as metallic lustrous silver powder, which was sensitive to air and moisture. SC-XRD-measurement, P-XRD-measurement and NMR analysis were performed.

α -Li_{2.53}AgGe₂ was synthesized by a high temperature route described in chapter 2.6.1. The elements (chapter 2.1) were mixed in a tantalum ampule in the expected ratio and sealed by arc welding (chapter 2.5). The ampule was transferred into a silica tube, which was evacuated and heated to 750 °C in a vertical resistance tube furnace. The temperature was held for 1 h and subsequently cooled down to 300 °C with 0.5 $\frac{\text{K}}{\text{min}}$. The oven was switched off after the sample was kept at 300 °C for 3 h. After opening of the ampule, the product appeared as metallic lustrous silver powder, which was sensitive to air and moisture.

6.4.2 Characterization of γ -Li_{2.53}AgGe₂

The compound was characterized by SC-XRD measurements. The preparation was performed analogous to the procedure described in chapter 3.1 and a 0.3 mm diameter capillary was used for the measurement. Indexing of the reflections lead to a cubic cell. A face-centered cubic cell was found exhibiting a NaTl-like structure motif like for compound **2** (see chapter 6.2). Selected crystallographic data is given in Table 6.12 and 6.13. Additional crystallographic data is given in the appendix (Table 13.20 and 13.21).

6.4.3 Structure Description of γ -Li_{2.53}AgGe₂

The title compound **2** crystallizes in the space group $Fd\bar{3}m$ (no. 227) as **1**. The structure is shown in Figure 6.16. Like in **1** the Ag/Ge position is totally mixed with no sign of superstructure ordering and was set to a Ag:Ge ratio of 1:2. This ratio was chosen since as the low-temperature phase (**4**) was taken as educt, which was undergoing the phase transition and quenched at 843 K. Afterwards there were

Table 6.12: Single crystal data and structure refinement of γ -Li_{2.53}AgGe₂

Formula	γ -Li _{2.53} AgGe ₂
Formula weight/ $\frac{g}{mol}$	270.71
Space group	$Fd\bar{3}m$ (no. 227)
Z	1.33
Unit cell parameters/ \AA	$a = 6.1866(7)$
Volume/ \AA^3	236.79(5)
$\rho_{calc}/\frac{g}{cm^3}$	1.363
abs. coeff./ mm^{-1}	5.129
F(000)	85
Crystal shape/color	block/grey silver
Temperature (K)	150
Θ range/deg	5.71-46.60
Index Range in hkl	$-12 \leq h \leq 12$ $-12 \leq k \leq 12$ $-9 \leq l \leq 12$
Reflections collected	966
Unique reflections	70
reflections with $I > 2\sigma(I)$	65
Data/restraints/parameter	70/0/5
GOF on F^2	1.171
R ₁ , wR ₂ ($I \geq 2\sigma(I)$)	0.0328, 0.0666
R ₁ , wR ₂ (all data)	0.0355, 0.0678
Largest diff. peak and hole	5.469, -4.469

no signs of side phases, which concludes in the same stoichiometry as the low temperature phase. (Figure 6.15) The occupation of Li was refined freely, although the occupation should be the same as the low temperature phase. A S.O.F. of 0.8 for Li1 was obtained, which ends up in a Li_{2.41}AgGe₂ stoichiometry. Taking the aberration into account, this is in accordance to the data known from the low-temperature phase (**4**) (α -Li_{2.53}AgGe₂). Therefore the final stoichiometry for **2** is Li_{2.53}AgGe₂. Basically the same structure description as for **1** applies here as well (chapter 6.2.3). The structure can again be derived from the CsCl structure and builds a diamond-like network of the Ag and Ge atoms. The channels provided by the anionic network is filled with Li-atoms, which are arranged in a defect diamond-like motif due to the partial occupation of Li1.

The Ag/Ge-Ag/Ge distance is 2.6789(3) \AA , which is slightly shorter than in (**1**). This can be explained due to two reasons. First the fact of the under-occupation of

Table 6.13: Atomic coordinates and equivalent isotropic displacement parameters of γ -Li_{2.53}AgGe₂

Atom	Wyck.	x	y	z	S.O.F.	$U_{eg}/\text{\AA}^2$
Ge1	8a	0.1250	0.1250	0.1250	0.67	0.0105(3)
Ag1	8a	0.1250	0.1250	0.1250	0.33	0.0105(3)
Li1	8b	0.3750	0.3750	0.3750	0.8(3)	0.011(14)

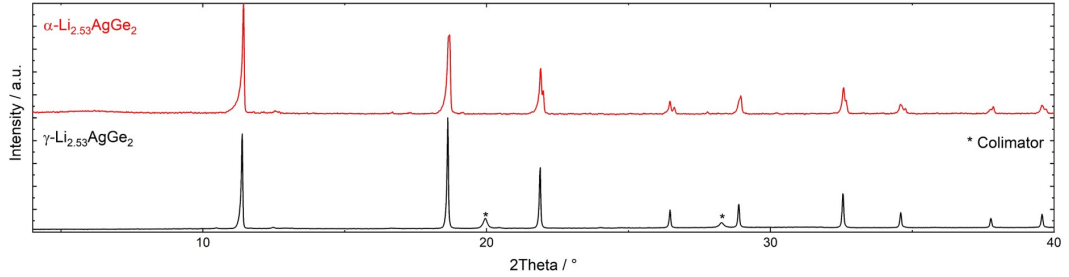


Figure 6.15: PXRd of α -Li_{2.53}AgGe₂ (top) and γ -Li_{2.53}AgGe₂ (bottom). Peaks marked by asterisk are caused by the colimator

Li atoms allows the structure to shrink a little bit and second the higher Ge content results in a higher percentage of Ge-Ge bonds than Ag-Ag bond. Like discussed Ge-Ge bonds are in general shorter than Ag-Ag bonds, which shortens the cell parameters.

The Li-Li bond is also 2.6789(3) Å due to symmetry rules. Therefore, the distance is probably mostly influenced by the Ag-Ge network and not by the Li itself, since they are located isolated in the channels. The distance is again smaller than in **1**, but for example **3** shows even smaller Li-Li distances of 2.6156 Å.

Since **1** exhibits a phase width of the Ag:Ge ratio **2** can be seen as an extreme case of **1** with Li defects. This is discussed in the following section.

6.5 Group-Subgroup relationship of diamond-like structure in the Li-Ag-Ge phase system

In this section the structural relationship of all five compounds **1-5** is discussed and illustrated in a Bärnighausen family tree. Additionally, structure models derived from the synthesized compounds were built and added to the scheme. Each symmetry reduction step is described in detail. General information about the Bärnighausener family tree or group-subgroup relationship tree is given in chapter 1.3.

This formalism is used to show the structural relationship of different compounds

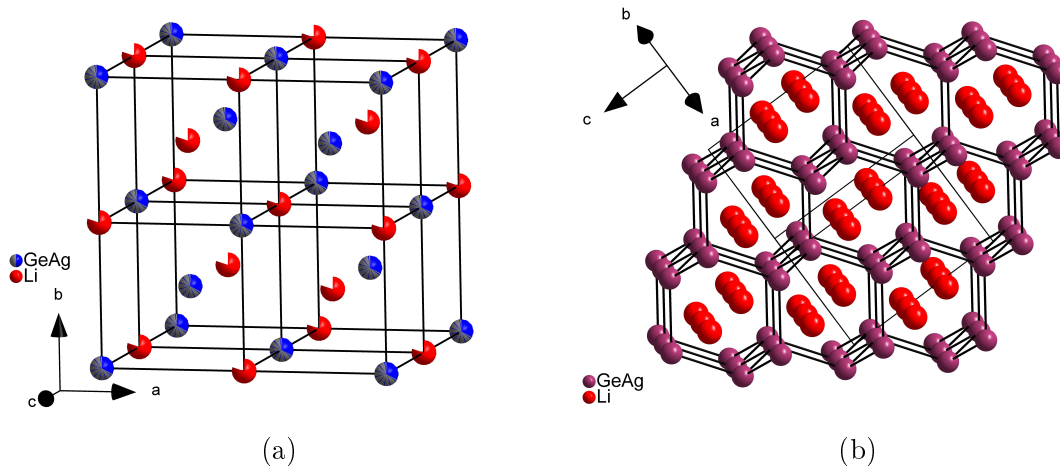


Figure 6.16: (a) A unit cell of (1). Li is shown in red/white according to partial occupation and Ag/Ge in grey/blue according to site occupation at a 90% probability level. The thinner lines show the CsCl-derived substructure. (b) Structure of (1) showing the diamond-like network of Ag/Ge. Li is shown in red and Ag/Ge in purple. The thinner lines show the unit cell borders.

and can even be used to predict certain structures, such as, high- or low-temperature phases of already know structures. The principle is to start with a high symmetry structure called aristotype and lower the symmetry step by step by ordering mixed sites of atoms, substitute atoms or distort the structure and therefore derive more complicated structures called hettotypes. Due to the ordering of mixed position the question of the coloring problem arises, which is discussed taking other modeled structures into account in chapter 6.8.

In this work the formalism was also used to determine the structure of α - $\text{Li}_2\text{Ag}_{0.8}\text{Ge}_{1.2}$, which could not be refined by single-crystal diffraction due to poor crystal quality (chapter 6.3). The derived model was used for RIETVELD-refinement to confirm the structure by experimental data.

The family tree is shown in Figure 6.17. In the scheme the translationsgleiche (t) and isomorphe (i), which is a special form of klassengleiche (k), setting is indicated as well as the index of the symmetry reduction, the vectors of the cell transformation and the Wyckoff position transformation. The Wyckoff splitting due to the symmetry reduction is shown in Figure 6.18.

Table 6.14: Possible atom distribution of Ag and Ge due to the coloring problem

positions	Tet2	Tet3
$4b$	Ge	Ge
$8e$	Ge	Ag
$8e$	Ag	Ag

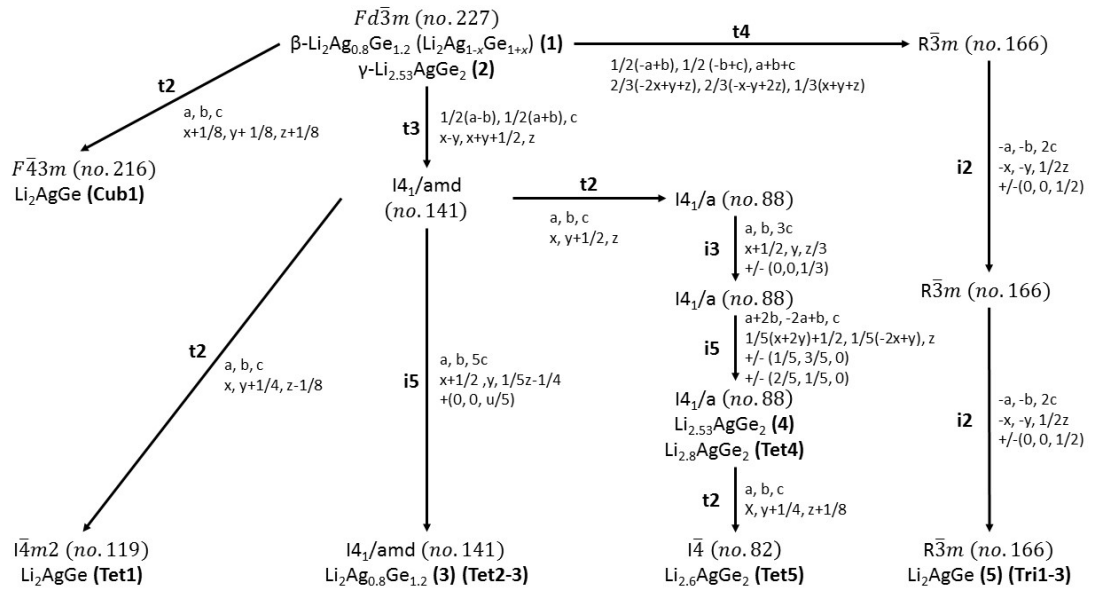


Figure 6.17: Group-subgroup relationships shown by the Bärnighausen family tree formalism. The aristotype in space group $Fd\bar{3}m$ is shown at top of the tree. By symmetry reduction described next to the arrows the hettotypes are derived. Synthesized compounds are labeled by numbers from (1) to (5), whereas all theoretical models for quantum chemical calculations are labeled by a three letter code naming the crystal system and a number.

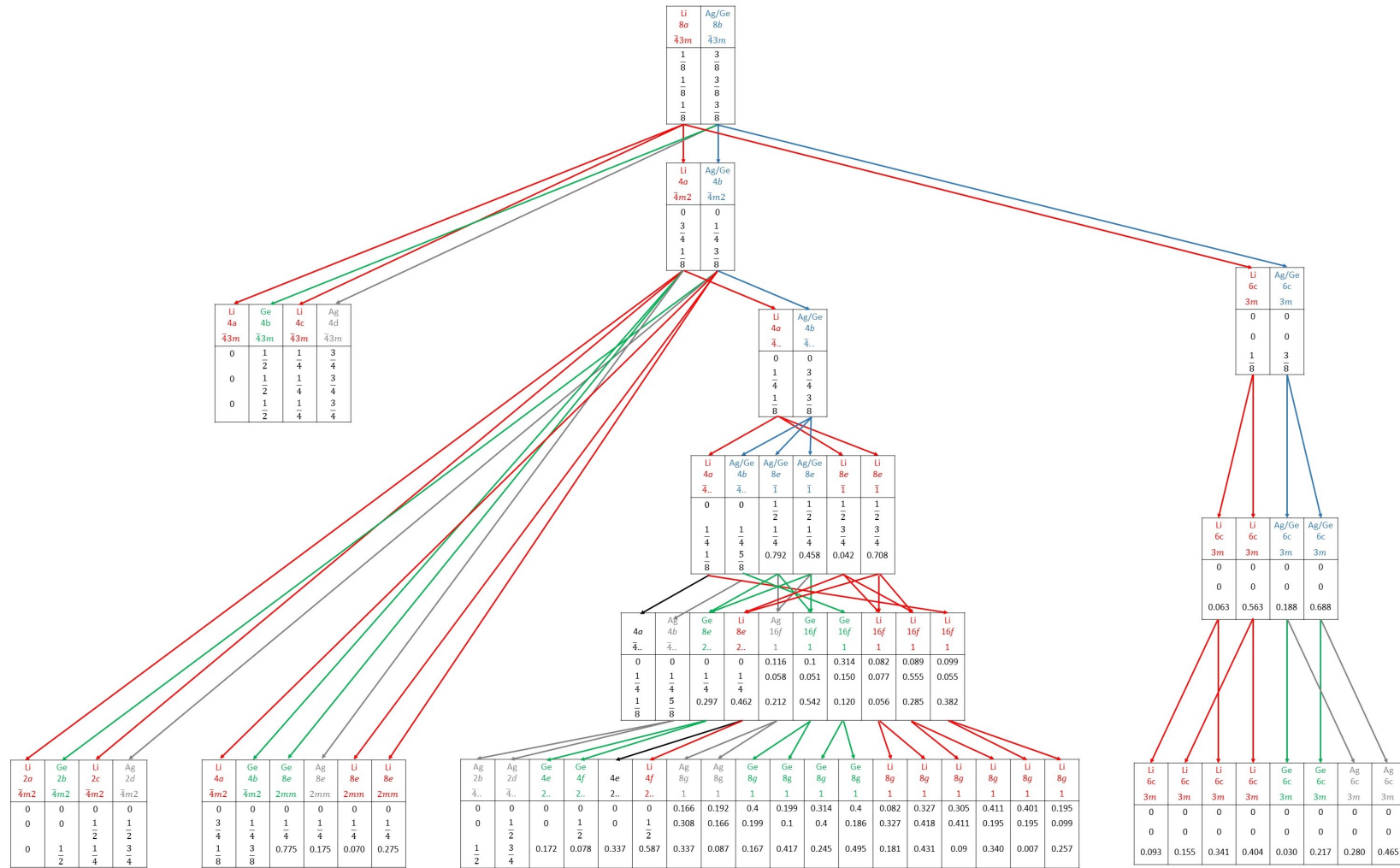


Figure 6.18: Addition to the Bärnighausen family tree this scheme is showing the Wyckoff position splitting. Li positions are shown in red, Ag in grey, Ge in green, mixed Ag/Ge in blue and vacancies in black. Most of the positions were calculated due to symmetry reductions rules, except structures with crystallographic data. In this case the experimental parameters were used in the tables.

On top of the scheme are β -Li₂Ag_{1-x}Ge_{1+x} (**1**) and γ -Li_{2.53}AgGe₂ (**2**) both having space group $Fd\bar{3}m$ as aristotype. The structures differ in the composition of their mixed Ag/Ge sites and partial occupation of the Li site. **1** also exhibits a phase width for the ratio of Ag and Ge, which is described in chapter 6.2.4 in this work. Therefore, **2** can also be seen as an extreme variant of **1** having a partial occupation of the Li site as well. Since an ordered model for partial or mixed occupation is required for quantum chemical calculations, a simple ordered model having a 1:1 ratio of Ag and Ge was derived ending up in space group $F4\bar{3}m$ (**Cub1**) by a $t2$ transformation. This structure has alternating Ag and Ge atoms with only heteroatomic bonds.

Maintaining the low temperature phase α -Li₂Ag_{0.8}Ge_{1.2} (**3**) of (**1**) a two-step symmetry decrease was needed. From single-crystal data the small tetragonal cell after the first transformation was and indications of a superstructure by an elongated c axis, which was estimated to be times 5, was known. First, the symmetry was decreased to the demanded tetragonal crystal system, which was found in experimental data. Subsequently a isomorphic transformation for the superstructure by elongating the c axis by the time of 5 was carried out. This splits the $8b$ position (Ag/Ge) of **1** into a $4b$, $8e$ and a second $8e$ position. At this point the coloring problem has to be included. The three different positions provide several options to distribute the Ag and Ge atoms. From experimental data a atom ratio of 0.8:1.2 (Ag:Ge) is known. Including this information two possible options are left shown in Table 6.14. **Tet2** of the two models could be assigned as the real cell by subsequently RIETVELD refinement ending up with **3**. The difference of the two cells are discussed in the following chapter 6.8. Also the smaller tetragonal cell was investigated by quantum chemical calculations using a simple ordered model with a 1:1 ratio of Ag and Ge. For this a $t2$ symmetry reduction to space group $I\bar{4}m2$ (**Tet1**) was necessary to split the $8b$ position (Ag/Ge) into a $4b$ (Ge) and $4d$ (Ag) position. This cell **Tet1** exhibits a diamond-like network of alternating Ge and Ag atoms with only heteroatomic bonds.

For α -Li_{2.53}AgGe₂ (**4**) the first step is the same transformation as for α -Li₂Ag_{0.8}Ge_{1.2} resulting in a tetragonal crystal system, but having a different transformation for the second step ($t2$) ending up in the demanded space group $I4_1/a$. After the final

Table 6.15: Possible atom distribution of Ag and Ge due to the coloring problem of structure α -Li₂AgGe

positions	Tri1	Tri2	Tri3
6 c	Ge	Ge	Ge
6 c	Ag	Ag	Ge
6 c	Ge	Ag	Ag
6 c	Ag	Ge	Ag

space group was reached the cell undergoes two further isomorphic transformation ending up in the final cell parameters of **4** and **Tet4**. Since in **4** a partial occupation of one Li site is present, we derived another model for this structure (**Tet5**). This reduction is splitting the Wyckoff position of the partially occupied $8e$ position into $4e$ and $4f$, where only $4f$ was occupied for **Tet5**.

The last structure α -Li₂AgGe (**5**) can be derived from the aristotype by undergoing a t_4 transformation to the rhombohedral space group $R\bar{3}m$ and subsequently two identical isomorphic transformations, which combined elongate the c -axis by times four. Interestingly the first elongation of the c -axis would already be enough to build a structure model for a totally ordered structure, which splits the mixed $8b$ position of **1** into two $6c$ positions. In the case of occupying one of the $6c$ positions with Ag and the other with Ge only heteroatomic bonds would occur. The second elongation of the cell offers several options for atom distributions since each $6c$ splits again in two $6c$ positions ending up with four $6c$ for the occupation of Ag and Ge. The different models achieving a 1:1 ratio of Ag and Ge obtained from experimental data could be derived showed in Table 6.15. The main difference of the structures is the different amount of Ag-Ge, Ge-Ge and Ag-Ag bond. In chapter 6.8 these models are compared and discussed. All unit cells of the models are shown in the appendix.

6.6 Thermal Analysis

All low-temperature phases were investigated by DSC experiments. The samples were handled as described in chapter 3.3. The thermograms are shown in Figure 6.19.

Compound **5** shows two peaks during the heating and cooling procedure. The first one at about 597.5 °C is assigned to the phase transition from α - to the unknown β -phase. Attempts to synthesis the β -phase fails due to the very small temperature window between transition and melting point at 677.8 °C. Due to the Bärnighausen family tree it is expected to be similar to the phases **1** and **2**.

In the case of compound **3** again two peaks are present. The transition from α - to β -phase is at lower temperature than for **5** (545.7 °C) and the melting point is at 673.5 °C. All phases could be synthesized in this case.

Table 6.16: Ag:Ge ratio, average temperature of first and second phase transition, and melting point of **3-5**

Composition	Ag:Ge ratio	1st phase transition / °C	2nd phase transition / °C	Melting point / °C
Li ₂ AgGe	1:1	597.5		677.8
Li ₂ Ag _{0.8} Ge _{1.2}	1:1.5	545.7		673.5
Li _{2.53} AgGe ₂	1:2	512.6	531.9	639.2

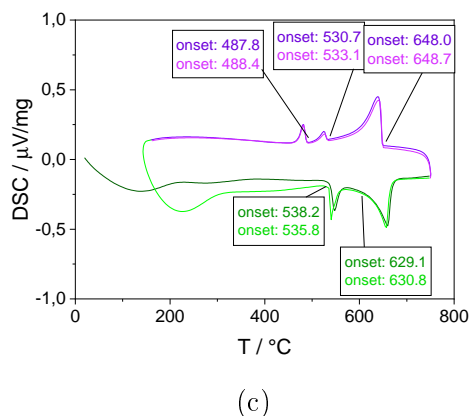
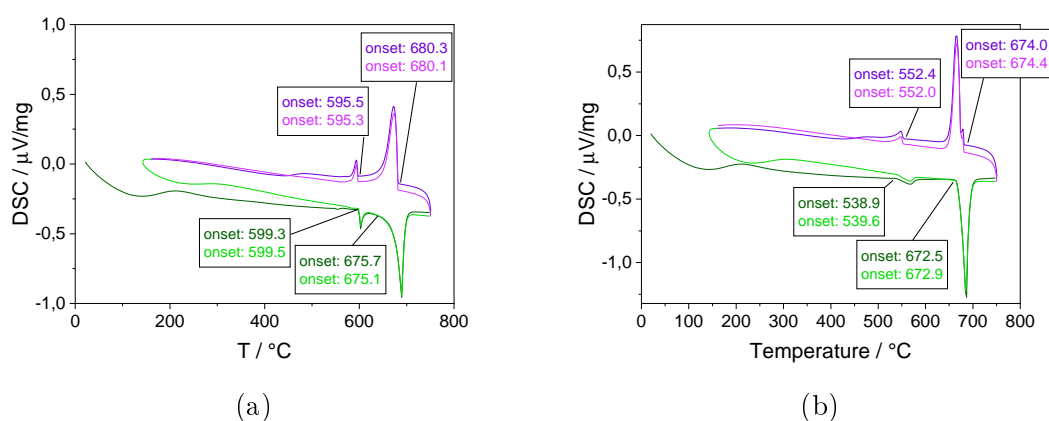


Figure 6.19: DSC thermogram of (a) α -Li₂AgGe (**5**) (b) α -Li₂Ag_{0.8}Ge_{1.2} (**3**) and (c) α -Li_{2.53}AgGe₂ (**4**). Lines and numbers indicate the onset temperatures of the corresponding thermal effects. The 1st and 2nd heating circle is shown in green and light green, respectively. The 1st and 2nd cooling circle is shown in violet and light violet, respectively.

Compound **4** is the only one showing more than two peaks during the process. In this case two phase transitions occur. Both transition points are lower than the one of **3** (512.6 °C and 531.9 °C). The phase between this two transition point could

not be identified, but according to the Bärnighausen family tree it could be one of the three cell during the symmetry reduction process from the aristotype towards **4**. The second transition is only seen during cooling and probably overlaps with the peak of the first transition for the heating process. Especially in the second heating cycle a shoulder of the first transition peak can be observed, which belongs to the second transition.

In general a trend towards lower melting and transition point with higher Ge-content could be observed. The data is also represented in Table 6.16.

6.7 NMR Analysis

NMR studies were carried out to get an insight in Li ion mobility. The experiments were carried out at the university of Cambridge in the chair of Prof. Clare P. Grey assisted by Dr. M. F. Groh, S. P. Emge and Dr. K. Griffith.

All five samples **1-5** were analyzed by ^6Li MAS-NMR spectra recorded at ambient temperature (Figure 6.20) to investigate their local structure. The samples were mixed with dry KBr to facilitate high spinning speed and to mitigate spinning-induced heating, because they showed slight resistance to spinning. This was expected for metallic compounds. The observed signals for all samples cover the range of 0 to 15 ppm. For metallic samples 15 pm is a very low shift and closer to what is usually observed for diamagnetic Li compounds. Neat Li metal, for example, shows shifts of around 250 ppm.^[61] This suggest a very ionic, electronically insulated Li environment with the unpaired electrons centered on the Ag-Ge network. This fact is supported by the rather long T1 times, necessitating recycle delays typical for diamagnetic Li compounds.

3 shows two signals in the approximate ratio of 1:4, which represents the three crystallographically independent sites of Li on Wyckoff positions $4a$, $8e$ and $8e$ (ratio 1:2:2). The two $8e$ shifts combine to one signal. **1** also shows two signals, albeit with slightly different shifts. Although **1** features only one crystallographically independent site due to disorder, the differences in local structure that are invisible for X-ray diffraction lead to several NMR signals, indicating that local environments similar to **3** are retained upon phase transition.

The ^6Li NMR spectra of the other phases **2**, **4**, and **5** feature only one observable signal. The signal for **5** is significantly wider than for any other investigated phases. This phase has four crystallographically independent sites, which are probably shifted only slightly different leading to only one broad signal.

In contrast, the spectra of **2** and **4**, which are corresponding high- and low-temperature phases show only one rather narrow signal. **4** consists of four independent Li posi-

tions, but due to Li-vacancies Li ion mobility can be considered facilitating Li-ion hopping.

Also **2** does contain Li vacancies and therefore does not show any local structure as the very similar **1**.

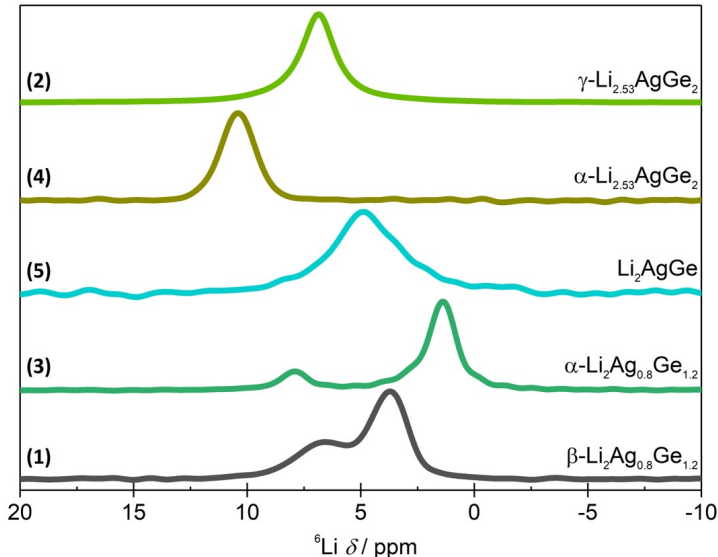


Figure 6.20: ${}^6\text{Li}$ MAS-NMR of five different phases of the Li-Ge-Ag phase system. Spectra were recorded at a spinning speed of 12.5 kHz (**1-4**) or 10 kHz (**5**).

6.8 Computational Analysis of related diamond-like structure

In this part the computational analysis of all compounds **1-5** including their derived structure models are discussed. The structural parameters are compared and band structure calculations were carried out for each model. Mulliken overlap population is taken into account explaining the driving forces of the huge superstructures.

The structures were investigated by quantum chemical methods using DFT-HSE06/TZVP level of theory. For each experimental achieved structure one or several models were built in order to investigate the driving force especially for the huge superstructures. As described in the sections before one driving force for the low-temperature phases is the ordering of the Ag/Ge sites, but the question how exactly they order is part of the coloring problem. Here, substructure units are discussed due to the bond behavior of the Ag/Ge atoms for the different models. All modeled structure and their associated experimental compound is shown in Table 6.2.

6.8.1 Structure models

The most simple model **Cub1** is associated with the high temperature phases **1** and **2**. Since all Ag/Ge sites are fully mixed and in case of **2** a partial occupation for Li position is present, a ordered model was derived. As a simple model the ordering of Ag and Ge sites with equal occupation 1:1 was chosen. The partial occupation of Li of **2** was not modeled.

The structure model is shown in Figure 13.16 and the optimized cell parameters are given in Table 13.22. In this model only heteroatomic bonds occur.

Tet1 also shows a very simple cell like **Cub1**. Basically this cell shows the same arrangement of alternating Ag and Ge atoms, but with an tetragonal distortion. The structure model is shown in Figure 13.17 and the optimized cell parameters are given in Table 13.23.

Tet2 and **Tet3** are both structure models for compound **3**. In this case the formalism group-subgroup relationships was used to identify the experimental synthesized structure (see chapter 6.5). According to the gained cell parameters by XRD-experiments and atoms ratios used in the synthesis two possible structures were obtained (**Tet2** and **Tet3**, see also Table. 6.14). Both structures are illustrated in Figure 13.18 and the optimized cell parameters are given in Table 13.24. In principle they differ only in the amount and arrangement of Ag-Ge, Ag-Ag and Ge-Ge bonds. **Tet2** exhibits Ag-Ag bonds, whereas **Tet3** does not show this kind of bond. In chapter 6.3 it is shown, that in **Tet3**, which is at the end the experimental obtained structure, ${}^1_{\infty}[\text{Ge}_2]$ zig-zag chains are built.

For a model of **4** the partial occupation of the $8e$ Li position must be considered. The first model **Tet4** has a fully occupied position, whereas for **Tet5** the $8e$ position was split due to symmetry reduction to a $4e$ and $4f$ position. In this model only the $4f$ position was occupied. In general a $\text{Li}_{2.8}\text{AgGe}_2$ (**Tet4**) and $\text{Li}_{2.6}\text{AgGe}_2$ (**Tet5**) stoichiometry was achieved. The structures of both models are given in Figure 13.19 and the optimized cell parameters are given in Table 13.25.

At last the three models **Tri1-3** for compound **5** were derived. The experimental structure with fully ordered Ag and Ge positions is known (chapter 6.1.5), but to understand why the atoms are ordered in this fashion, two other models were derived with the same ratio of Ag and Ge, but the atoms were distributed differently (see Table 6.15). All structures are illustrated in Figure 13.20 and the optimized cell parameters are given in Table 13.26. The amount of Ag-Ge, Ag-Ag and Ge-Ge bonds differs for each model. **Tri3** could be identified as the experimentally obtained structure.

6.8.2 Structural parameter comparison

The structural parameters of the modeled representing the same compound were compared to the associated experimental gained parameters to reassure the level of theory.

The deviation of cell parameters a and b , as well as, interatomic distances of Ag-Ag, Ag-Ge and Ge-Ge bonds are given in Table 6.17. For the interatomic distances the maximal deviation of a length is given in case of several interatomic distances. For

Table 6.17: Model for computational analysis and their associated structure, as well as, deviations of cell parameters an interatomic distances from experimental data

Model	Associated Structure	Deviation of a /%	Deviation of c /%	Deviation Ag-Ag/%	Deviation Ge-Ge/%	Deviation Ag-Ge/%
Cub1	(1)	-1.27				-1.27
Cub1	(2)	-1.61				-1.61
Tet2	(3)	-2.25	3.16		0.56	-1.14
Tet3	(3)	-3.71	3.54		-1.36	1.66
Tet4	(4)	-1.50	-1.20		-2.08	-1.72
Tet5	(4)	-0.92	-0.70		-0.29	-1.00
Tri1	(5)	-3.11	-2.99	5.36	-13.24	2.14
Tri2	(5)	-0.30	-1.47	3.17	-4.09	-2.44
Tri3	(5)	-0.65	-0.33	-1.86	-0.73	-0.50

Cub1 the parameters are in line with experimental findings for **1** and **2**. Additionally, one has to consider the different Ag:Ge ratio in the model, which affects the cell parameters. For **3** the parameters of **Tet2** match slightly better than the ones of **Tet3**, but still a quite high deviation of b is present (3.16%). The model **Tet5**, which imitates the Li-vacancies present in **4**, shows very good match, all deviations being less than 1%. Also **Tet4**, which contains lesser Li-vacancies, shows good accordance with **4**. The three models **Tri1**, **Tri2**, and **Tri3** clearly show, that **Tri3** is the best match for the experimental findings showing less than 1% deviation for both cell parameters a and b . The structural comparison of the models compared to the experimental structures shows in general good accordance at the chosen level of theory.

6.8.3 Band Structures and Electron Count

For all structure models band structure calculations were carried out. In this section only the band structures of selected models are shown (Figure 6.21), but all other

band structures are given in the appendix (Figures 13.11-13.15). The band structure of **Cub1** (Figure 6.21a) shows metallic behavior like all other band structures, but in this case a band gap above the Fermi level can be observed. In the other band structures only pseudo gaps or a very low density of states are shown above the Fermi level due to more complicated situations. The electron lack to reach the band gap was estimated to be one for the formula Li_2AgGe and would therefore than achieve a true ZINTL-phase. To verify this assumption the structure model Li_2ZnGe was calculated isostructural to **Cub1**. The initial parameters for the calculations were taken from **Cub1**, whereas Ag was substituted by Zn, and subsequently optimized. The band structure of cubic Li_2ZnGe shows a band gap of 0.4 eV. Counting electrons of the structures this is in line with the *Zintl* concept. Each Li transfers one electron to the [AgGe]-network, which would result in a -2 charge. The $[\text{AgGe}]^{2-}$ builds a diamond-like or α -Ge-like network, but for an electron isovalent structure to α -Ge, $[\text{AgGe}]^{3-}$, it misses exactly one electron. The **Cub1** band structure shows this very clearly, but all other band structures also show the indications of this fact. The amount of electrons lacking differs with the Ag:Ge ratio, depending on how many electrons are needed to be isovalent to α -Ge.

To state this theory several examples of ZINTL- and HEUSLER-phases with their electron count of the metal network unit compared to α -Ge is given in Table 6.18.

Table 6.18: Example compounds with network subunit, missing electron count to achieve isovalent structure to α -Ge and phase type

Compound	Network Unit	Missing Electrons	Phase
Li_2AgGe	$[\text{AgGe}]^{2-}$	1	
Li_2AgSb	$[\text{AgSb}]^{2-}$	0	ZINTL
Li_2AuBi	$[\text{AuBi}]^{2-}$	0	ZINTL
Na_2CdPb	$[\text{CdPb}]^{2-}$	0	ZINTL
Li_2AgMg	$[\text{AgMg}]^{2-}$	3	HEUSLER
Li_2CdSb	$[\text{CdSb}]^{2-}$	-1	HEUSLER
Li_2ZnSb	$[\text{ZnSb}]^{2-}$	-1	

The difference in electrons if compared to the tetravalent α -Ge structure is given as missing electrons. In the case of additional electrons the number is negative. It clearly shows, that if the network-unit is isovalent to α -Ge it tends to build the structure motif of α -Ge and therefore shows the typical ZINTL-phase behavior. But if the electron count does not match the one of α -Ge it tends to build a HEUSLER phase instead. Table 6.18 shows two exceptions of this theory: 1) Li_2ZnSb should show a HEUSLER-phase, but builds a ternary variant of the NaTl structure instead,

and 2) our compounds, which lack electrons to achieve a true ZINTL-phase, but nevertheless still adopt the structure motif of α -Ge.

6.8.4 Population Analysis and Total Energies

In this section the HIRSHFELD charges and MULLIKEN overlap population of each model is discussed with respect to their arrangement of Ag and Ge atoms in the network. Additionally, the total energies of selected models, which have the same Li:Ag:Ge ratio are compared showing, that the experimental obtained structures are energetically favored.

The HIRSHFELD partial charges are given in Table 6.19. A trend to more ionic Li and Ag ions is visible with higher Ge content, whereas Ge becomes less negative. This states the trend towards an electron-precise MULLIKEN-phase. The amount of missing electrons is reduced by a higher Ge content due to the fact that the valence electron count converges towards α -Ge of the anionic network.

Table 6.19: Average HIRSHFELD charges for selected models

Model	Formula	Average Li charge	Average Ag charge	Average Ge charge
Cub1	Li ₂ AgGe	0.87	-0.30	-1.44
Tet1	Li ₂ AgGe	0.86	-0.30	-1.42
Tri3	Li ₂ AgGe	0.85	-0.36	-1.33
Tet2	Li ₂ Ag _{0.8} Ge _{1.2}	0.89	-0.36	-1.25
Tet5	Li _{2.6} AgGe ₂	0.99	-0.48	-1.05

The total energies of **Tet2** and **Tet3** were compared showing, that **Tet2** (experimental confirmed structure) is energetically favored. In case of models **Cub1**, **Tet1** and **Tri1-3** **Tri3** shows the lowest total energy, which again is the experimental confirmed low-temperature structure. The total energies are illustrated in Figure 6.22.

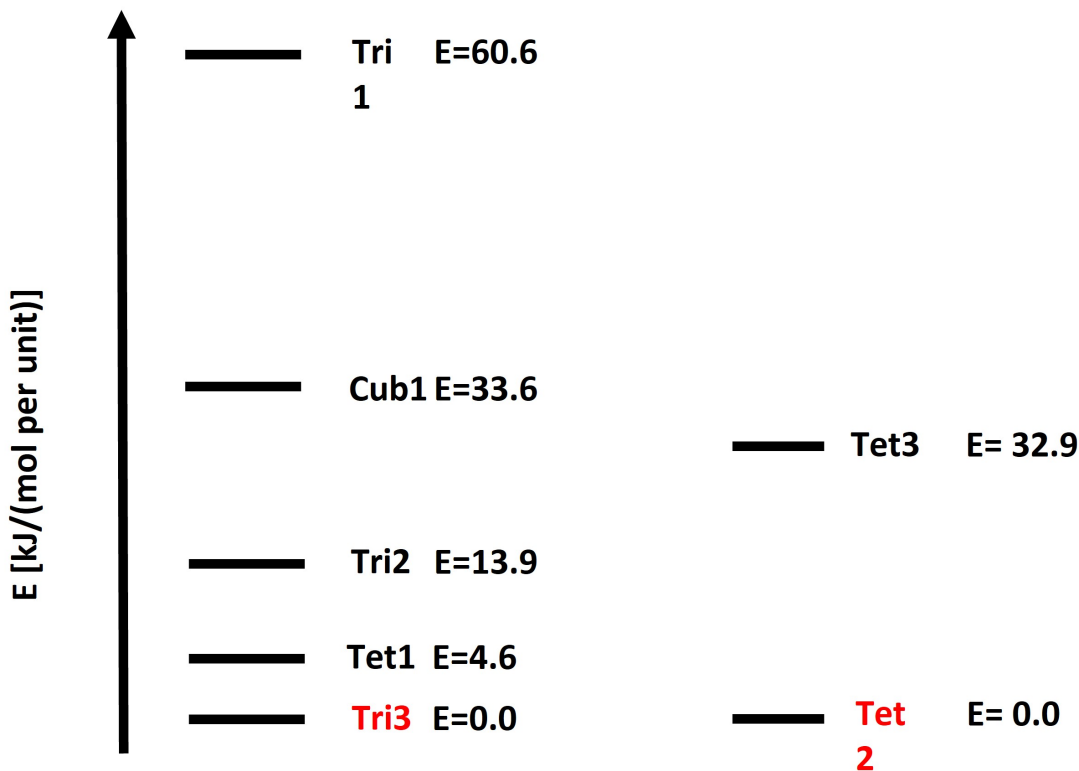
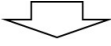
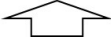
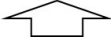


Figure 6.22: Relative energies of **Cub1**, **Tet1-3** and **Tri1-3** in kJ/mol per unit. **Tet4-5** were not included due to different stoichiometry.

The question of the coloring problem arises now: Why are some structures favored with respect to other. To answer this, one has to have a look at the Ag-Ge, Ag-Ag and Ge-Ge bond. In general, heteroatomic bonds are more favored. Thus structures with a higher number of heteroatomic bonds should be energetically favored. Additionally, we assume the ordering of Ag and Ge atoms as a driving force for all low-temperature phases. This matches for **Tet2**, which exhibits more heteroatomic bonds than **Tet3** (Table 6.20). Additionally, the MULLIKEN overlaps populations are about the same for Ag-Ge and Ge-Ge bonds, but Ag-Ag bonds do not exist at all. The homoatomic Ge-Ge bond in **Tet2** seems to be stabilized due to chain-building. Infinite 1-D zig-zag chains in *a* and *b* direction with short Ge-Ge bonds similar to those in CaGe confirm this fact.

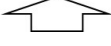
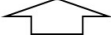
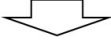
In the case of the trigonal models **Tri1-3** the situation is more complex. Following the rule of more heteroatomic bonds, the simple **Cub1** or **Tet2** model would already achieve only heteroatomic bonds with the matching stoichiometry, but still **Tri3** is energetically favored. Comparing only the trigonal models, **Tri3** has more heteroatomic bonds and less homoatomic bonds (Table 6.21). The high MULLIKEN

Table 6.20: Trend of number of bonds for Ag-Ge, Ag-Ag and Ge-Ge bonds with bond length and MULLIKEN overlap populations for **Tet2-3**

TetX	Bond	# of bonds	Length / Å	MULLIKEN overlap population / e-
Tet2	Ag-Ge		2.71-2.74	0.16-0.17
Tet3	Ag-Ge		2.69	0.16
Tet2	Ag-Ag		2.89	0.13
Tet3	Ag-Ag			
Tet2	Ge-Ge		2.66	0.11
Tet3	Ge-Ge		2.7147	0.116

overlap population of Ge-Ge bonds (0.20) building Ge-Ge dumbbells is compensating the unfavorable Ag-Ag bond. The Ag-Ag distance is rather long, with very low overlap, suggesting almost non-bonding situation. To conclude, the structure is stabilized by building Ge-Ge dumbbells and compensating the neighboring Ag atoms in the network by driving them further away, that they are almost non-bonding and do not destabilize the structure.

Table 6.21: Trend of number of bonds for Ag-Ge, Ag-Ag and Ge-Ge bonds with bond length and MULLIKEN overlap populations for **Tri1-3**

TetX	Bond	# of bonds	Length / Å	MULLIKEN overlap population / e-
Tri1	Ag-Ge		2.69	0.16
Tri2	Ag-Ge		2.71-2.72	0.16-0.16
Tri3	Ag-Ge		2.66-2.77	0.16-0.18
Tri1	Ag-Ag		2.81-2.82	0.13
Tri2	Ag-Ag		2.87	0.13
Tri3	Ag-Ag		3.02	0.09
Tri1	Ge-Ge		2.77-2.86	0.05-0.08
Tri2	Ge-Ge		2.59-2.63	0.16-0.18
Tri3	Ge-Ge		2.54	0.20

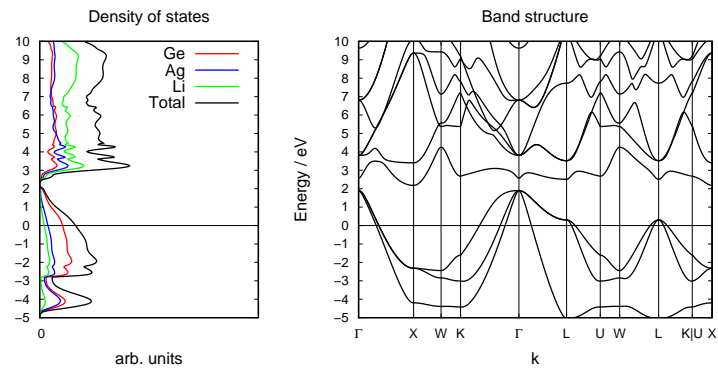
References

- [1] J.-M. Tarascon, M. Armand, *Nature* **2001**, *414*, 359–367.
- [2] J. B. Goodenough, Y. Kim, *Chem. Mater.* **2010**, *22*, 587–603.
- [3] M. Zeilinger, D. Benson, U. Häussermann, T. F. Fässler, *Chem. Mater.* **2013**, *25*, 1960–1967.

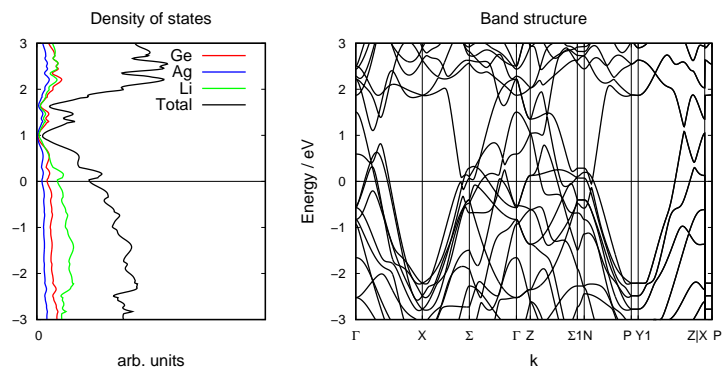
- [4] M. Zeilinger, I. M. Kurylyshyn, U. Häussermann, T. F. Fässler, *Chem. Ma* **2013**, *25*, 4623–4632.
- [5] M. Zeilinger, T. F. Fassler, *Dalton Transactions* **2014**, *43*, 14959–14970.
- [6] T. D. Hatchard, J. R. Dahn, *J. Electrochem. Soc.* **2004**, *151*, 838–842.
- [7] M. N. Obrovac, L. Christensen, *Electrochemical and Solid-State Letters* **2004**, *7*, 93–96.
- [8] C. S. Fuller, J. C. Severiens, *Physical Review* **1954**, *96*, 21–24.
- [9] J. Graetz, C. C. Ahn, R. Yazami, B. Fultz, *Journal of the Electrochemical Society* **2004**, *151*, 698–702.
- [10] T. Noritake, M. Aoki, S. I. Towata, T. Takeuchi, U. Mizutani, *Acta Cryst.* **2007**, *26*, 726–234.
- [11] H. Okamoto, *J. Phase Equilib.* **2017**, *38*, 70–81.
- [12] L. Arnberg, S. Westman, *Acta Chem. Scand.* **1972**, *26*, 1748–1750.
- [13] A. J. Bradley, J. Thewlis, *Proc. R. Soc. London Ser. A* **1926**, *112*, 678–692.
- [14] W. B. Pearson, *A handbook of lattice spacings and structures of metals and alloys*, **1958**, p. 284.
- [15] P. Ramachandrarao, T. Anantharaman, *Transactions of the Metallurgical Society of AIME* **1969**, *245*, 886–887.
- [16] G. J. Miller, *European Journal of Inorganic Chemistry* **1998**, 523–536.
- [17] A. Anani, R. A. Huggins, *J. Power Sources* **1992**, *38*, 351–362.
- [18] A. Anani, R. A. Huggins, *J. Power Sources* **1992**, *38*, 363–372.
- [19] J. W. Kim, J. H. Ryu, K. T. Lee, S. M. Oh, *J. Power Sources* **2005**, *147*, 227.
- [20] S. M. Hwang, H. Y. Lee, S. W. Jang, S. M. Lee, S. J. Lee, H. K. Baik, J. Y. Lee, *Electrochemical and Solid-State Letters* **2001**, *4*, 97–100.
- [21] R. Pöttgen, T. Dinges, H. Eckert, P. Sreeraj, H.-D. Wiemhöfer, *Z. Phys. Chem.* **2010**, *224*, 1475–1507.
- [22] F. Winter, S. Dupke, H. Eckert, U. C. Rodewald, R. Pöttgen, *Zeitschrift für Anorganische und Allgemeine Chemie* **2013**, *639*, 2790–2795.
- [23] Z. Wu, B. D. Mosel, H. Eckert, R.-D. Hoffmann, R. Pöttgen, *Chem. Eur. J.* **2004**, *10*, 1558.
- [24] P. Sreeraj, N. A. Kaskhedikar, H.-D. Wiemhöfer, J. Maier, R. Pöttgen, *Solid State Ionics* **2010**, *181*, 59.

- [25] Z. Wu, R.-D. Hoffmann, D. Johrendt, B. D. Mosel, H. Eckert, R. Pöttgen, *J. Mater. Chem.* **2003**, *13*, 2561.
- [26] P. Sreeraj, H.-D. Wiemhöfer, R.-D. Hoffmann, J. Walter, A. Kirfel, R. Pöttgen, *Solid State Sci.* **2006**, *8*, 843.
- [27] A. Henze, V. Hlukhyy, T. F. Fässler, *Inorg. Chem.* **2015**, *54*, 1152–1158.
- [28] A. Henze, T. F. Fässler, *Inorg. Chem.* **2016**, *55*, 822–827.
- [29] F. Kiefer, T. F. Fässler, *Solid State Sciences* **2011**, *13*, 636–640.
- [30] E. Menges, V. Hopf, H. Schäfer, A. Weiss, **1969**, *21*, 1351–1352.
- [31] J. Evers, G. Oehlinger, G. Sextl, H. â. Becker, *Angew. Chem. Int. Ed.* **1987**, *26*, 76–78.
- [32] J. Evers, G. Oehlinger, *Angew. Chem. Int. Ed.* **2001**, *40*, 1050–1053.
- [33] H. G. von Schnering, R. Nesper, J. Curda, K.-F. Tebbe, *Angew. Chem.* **1980**, *92*, 1070–1070.
- [34] V. Hopf, H. Schäfer, A. Weiss, *Z. Naturforsch. B* **1970**, *25*, 653.
- [35] A. Grüttner, R. Nesper, H. G. von Schnering, *Acta Cryst.* **1981**, *A37*, C161.
- [36] R. Nesper, Habilitation, Universität Stuttgart, **1988**.
- [37] Q. Johnson, G. S. Smith, D. Wood, *Acta Cryst.* **1965**, *18*, 131.
- [38] G. R. Goward, N. J. Taylor, D. C. S. Souza, L. F. Nazar, *J. Alloys Compd.* **2001**, *329*, 82.
- [39] D. G. Kevorkov, V. V. Pavlyuk, O. I. Bodak, *Polish J. Chem.* **1997**, *71*, 712–715.
- [40] L. Lacroix-Orio, M. Tillard, C. Belin, *Solid State Sciences* **2008**, *10*, 5–11.
- [41] U. Müller, *Anorganische Strukturchemie, Vol. 6. Auflage*, **2008**.
- [42] V. Markiv, E. Gladyshevskii, T. Fedoruk, *Izv. Akad. Nauk SSSR* **1966**, *1966*, 118–121.
- [43] H. Pauly, A. Weiss, H. Witte, *Z. Metallkd.* **1968**, *59*, 414–418.
- [44] E. Zintl, W. Dullenkopf, *Z. Phys. Chem. B-Chem E* **1932**, *16*, 195–205.
- [45] H. Pauly, A. Weiss, H. Witte, *Z. Metallkd.* **1968**, *59*, 47–58.
- [46] H. Pauly, A. Weiss, H. Witte, *Z. Metallkd.* **1968**, *59*, 554–558.
- [47] H. Schoenemann, H. Schuster, *Rev. Chim. Miner.* **1976**, *13*, 32–40.
- [48] H. Schuster, *Z. Anorg. Allg. Chem.* **1969**, *370*, 149.
- [49] A. Mewis, S. H-U., *Z. Naturforsch. B* **1971**, *26*, 62.

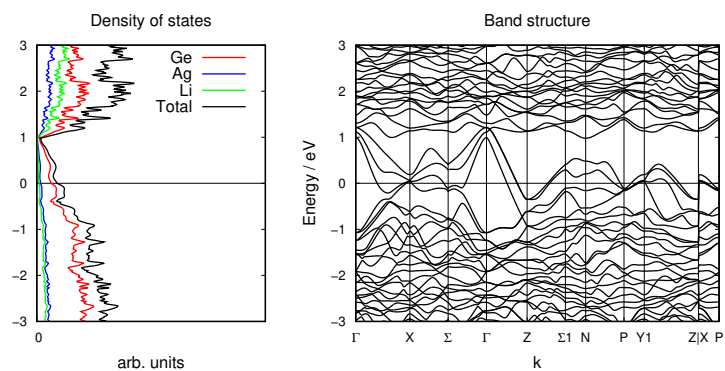
- [50] F. Wang, G. J. Miller, *Eur. J. Inorg. Chem.* **2011**, *924*, 3989–3998.
- [51] O. Heusler, *Ann. Phys.* **1934**, *411*, 155–201.
- [52] H. Nowotny, W. Sibert, *Z. Metallkd.* **1941**, *33*, 391–394.
- [53] R. Matthes, H. Schuster, *Z. Naturforsch. B* **1980**, *35*, 778–780.
- [54] H. Schuster, G. Schroeder, *Z. Naturforsch. B* **1972**, *27*, 81–82.
- [55] G. Schroeder, H. Schuster, *Z. Anorg. Allg. Chem.* **1977**, *431*, 217–220.
- [56] E. Zintl, G. Brauer, *Z. Elektrochem. Angew. P.* **1935**, *41*, 297–202.
- [57] T. Yamanaka, S. Morimoto, *Acta Crystallogr. B.* **1996**, *52*, 232–238.
- [58] V. Ganesan, K. S. Girirajan, *J. Phys.* **1986**, *27*, 475–478.
- [59] H. E. Swanson, E. Tatge, *Phys. Rev.* **1955**, *99*, 1737–1743.
- [60] L. Pauling, *The Nature of the Chemical Bond*, Ithaca, NY, **1960**.
- [61] N. M. Trease, L. Zhou, H. J. Chang, B. Y. Zhu, C. P. Grey, *Solid State Nucl. Mag.* **2012**, *42*, 62–70.



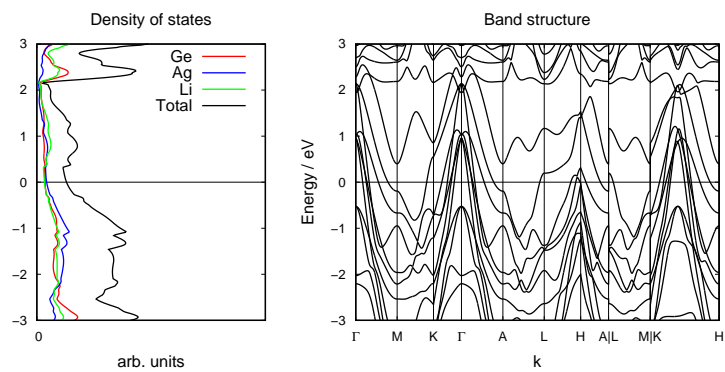
(a)



(b)



(c)



(d)

Figure 6.21: Band structure and density of states of a) **Cub1**, b) **Tet2**, c) **Tet5** and d) **Tri3**.

Substitutional Effects in the Li-Si Binary System by Ag

7.1 Introduction

Like in chapter 6, now the lighter homologous Si instead of Ge was used to synthesize new ZINTL-phases, which can meet the requirements for new battery materials. In the following sections the binary systems are discussed, but the Li-Ag system, which is already discussed in chapter 6.1.2.

7.1.1 The binary system Li-Si

In the group of Prof. T. F. Fässler, Dr. M. H. Zeilinger investigated the binary phase diagram of Li-Si thoroughly in 2013. In his work he discovered three new Li-Si phases: $\text{Li}_{17}\text{Ge}_4$, $\text{Li}_{4.1}\text{Si}$, $\text{Li}_{13}\text{Si}_4$ and established the single crystal structure determination of $\text{Li}_{15}\text{Si}_4$. Therefore he revised the Li-Si phase diagram (Figure 13.21). A graphical overview of all Li-Si phases is given in Figure 7.1 and listed in Table 7.1. With the structure of $\text{Li}_{17}\text{Ge}_4$ a theoretical specific capacity of $4200 \frac{\text{mA}\cdot\text{h}}{\text{g}}$ would be possible. This outmatches a conventional Li-C anode material almost by times of ten ($372 \frac{\text{mA}\cdot\text{h}}{\text{g}}$ for LiC_6). Additionally, the natural abundance, low weight and low price makes those materials a promising anode material for Li-ion batteries.

But, the very high volume change during charging and discharging process due to the structural change the material undergoes during lithiation is about 300 %. This leads to contact loss and active material pulverization and ends in quick capacity fading.

To overcome this cycle stability problem of Li-Si compounds for example composite materials stabilizing the micro structure of the anode or the integration of a transition metal (*TM*) leading to ternary phases like discussed in chapter 6.1.4 for $TM = \text{Ag}$ and $Tt = \text{Ge}$. Here in chapter 7.1.3 the integration of Ag in Li-Si phases is reviewed.

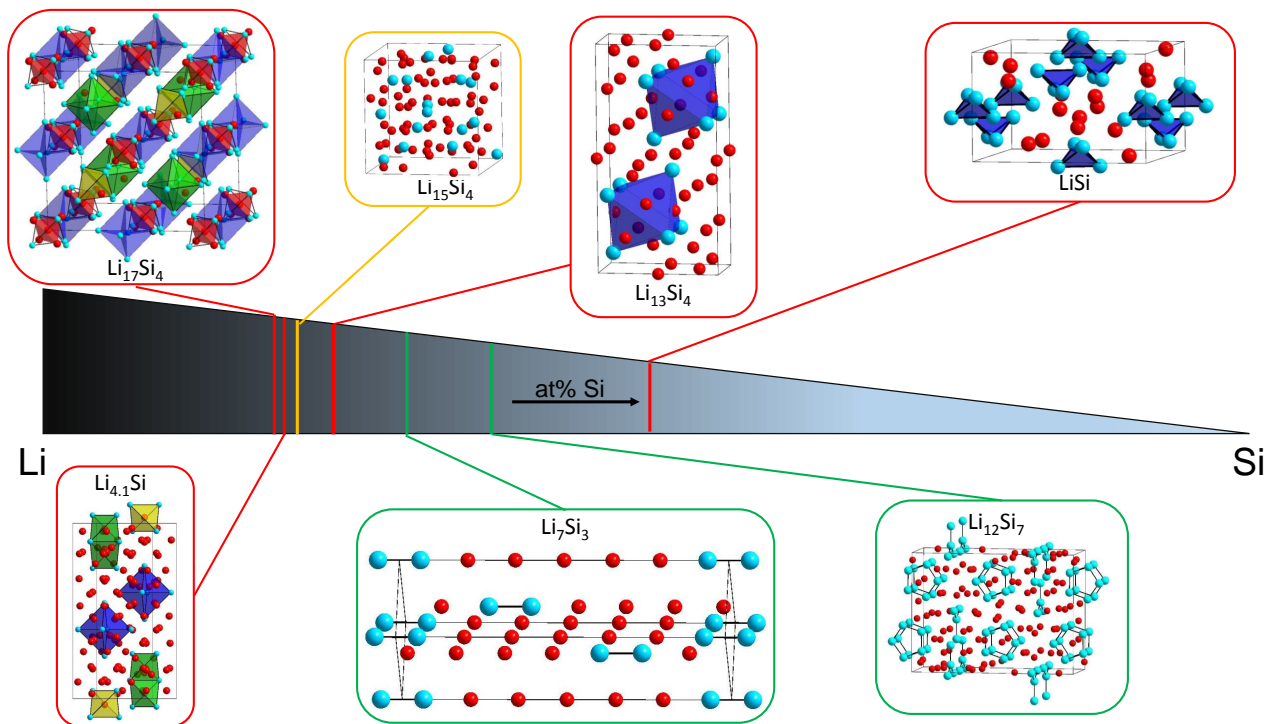


Figure 7.1: Fragments of the crystal structures of binary Li-Si phases. The phases are color-coded according to the dimensionality of the anionic Si framework: Si octa- or tetrahedrons (red), isolated Si atoms (yellow) and two-dimensional molecular units like dimer, triangles or rings (green). For clarity most of the Li atoms were removed in the structure $\text{Li}_{17}\text{Si}_4$.

7.1.2 The binary system Ag-Si

In the Ag-Si phase system only two metastable structures are known. The first one has a phase width from 75-95 at.-% Ag and crystallizes in a hexagonal space group.^[1,2] The other one is Ag_2Si crystallizing in an orthorhombic system.^[3]

7.1.3 Substitution of Ag in the binary system Li-Si

In chapter 7.1.1 the problem of active material pulverization is mentioned and therefore quick capacity fading. The integration of a *TM* can help to build more stable two- or three-dimensional anionic networks to prohibit the high volume change during lithiation and delithiation process of the material.^[4,5] In chapter 6.1.4 the advantages and examples are given for the integration of a *TM* like a higher complexity and number of possible structures, formation of networks and also first studies showing better cycling stability.^[6,7]

In this thesis in particular $TM = Ag$ was investigated. In the Li-Ag-Si phase system already several compounds do exist listed in Table 7.1. The ternary phase diagram is given in Figure 7.3.

The first structure published in this phase diagram was Li_2AgSi 1968 by Pauly.^[8] He published several compounds with the general formula Li_2TMX ($TM = Cu, Ag, Au; X = Al, Ga, In, Tl, Si, Ge, Sn, Pb, Sb, Bi$), but in the case of Li_2AgSi the compound was a doubtful case and no structural details were published. Seven years later another compound $Li_8Ag_3Si_5$ was published in this phase system, but the structure was later identified by Kevorkov as $Li_3Ag_2Si_3$.^[9,10] In this publication also two further compounds $LiAg_2Si$ and Li_2AgSi_2 are mentioned. The next compound $Li_{13}Ag_5Si_6$ was published over 10 years later and exhibits the same diamond-like structure motif as the Ge-compounds investigated in chapter 6.^[11] Since all those phases in the Li-Ag-Ge system showed high-temperature phase, the thermal behavior of $Li_{13}Ag_5Si_6$ was investigated and a high-temperature phase was found. In the next section the structure of the low-temperature phase $\alpha-Li_{13}Ag_5Si_6$ is described. The last known compound in this phase system is $Li_{12}Ag_{0.85}Si_4$, which has the same structure motif as the heavier homologous compound $Li_{12}AgGe_4$.

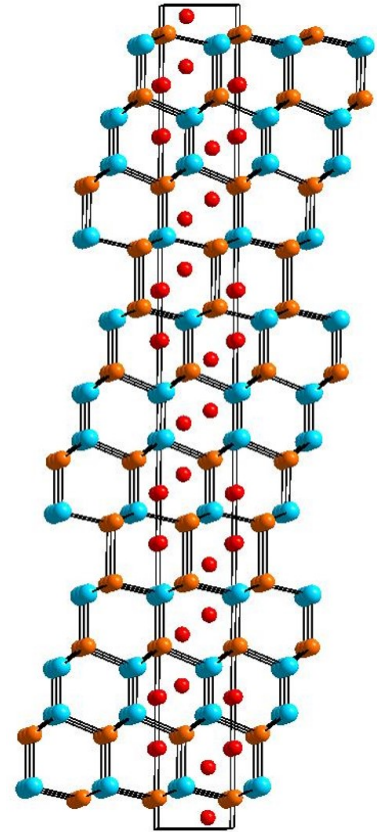


Figure 7.2: Excerpt of the crystal structure of $\alpha-Li_{13}Ag_5Si_6$ showing the diamond-like anionic Ag/Si-substructure stuffed with Li-ions. Li, Ag and Si are shown in red, grey and light blue, respectively.

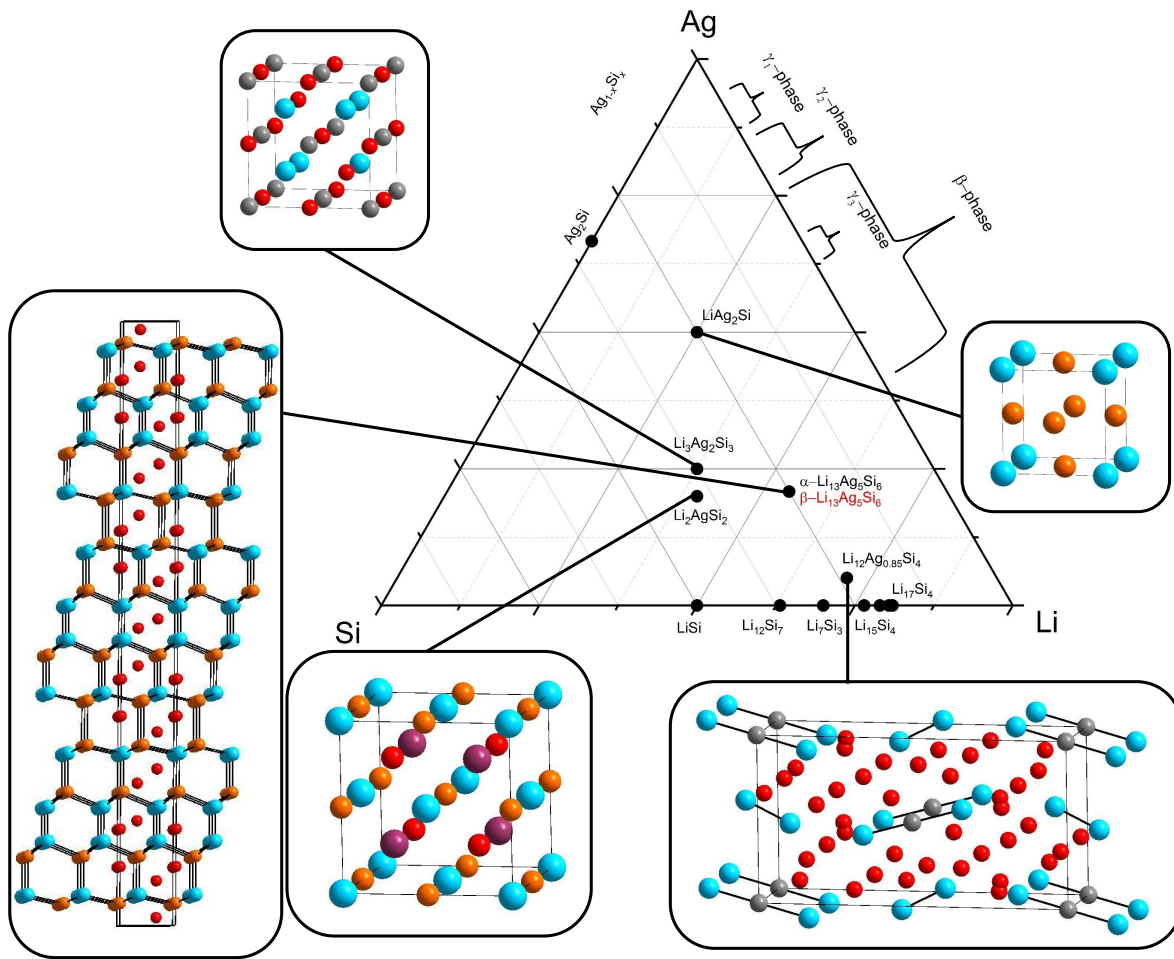


Figure 7.3: Ternary composition diagram of the phase system Li-Ag-Si including all known binaries. For clarity not all Li-Si-compounds were assigned. A full list of all compounds is given in Table 7.1. At the corners the pure elements Li, Ag and Si are located. Compounds investigated in this thesis are given in red and an excerpt of the crystal structure of all known ternary compounds is given. Li, Ag, Si, Li/Si and Li/Ag positions are shown in red, grey, light blue, purple and light orange, respectively.

Table 7.1: All known binary and ternary compounds in the Li-Ag-Si phase diagram

Compound	Space Group	Ref.
LiSi	$I4_1/a$	[12,13]
$Li_{12}Si_7$	$Pnma$	[14]
Li_7Si_3	$R\bar{3}m$	[14]
$Li_{13}Si_4$	$Pbam$	[15]
$Li_{15}Si_4$	$I\bar{4}3d$	[16]
$Li_{4.1}Si$	$Cmcm$	[17]
$Li_{17}Si_4$	$F\bar{4}3m$	[18]
Ag_2Si	n.a. ^[a]	[3]
$Ag_{1-x}Si_x$ $x = 0.75-0.95$		[1,2]
Ag-Li (β -phase)	$Pm\bar{3}m$	[19]
Ag-Li (γ_1 -phase)	$I\bar{4}3m$	[19]
Ag-Li (γ_2 -phase)	$I\bar{4}3m$	[19]
Ag-Li (γ_3 -phase)	$I\bar{4}3m$	[19]
$Li_{12}Ag_{0.85}Si_4$	$Pbam$	[20]
Li_2AgSi	[a]	[8]
$Li_8Ag_3Si_5$ ^[c]	$P4_2/nnm$	[9]
$Li_3Ag_2Si_3$	$P4_2/nnm$	[10]
Li_2AgSi_2	$F\bar{4}3m$	[10]
$LiAg_2Si$	$Pm\bar{3}m$	[10]
α - $Li_{13}Ag_5Si_6$	$R\bar{3}m$	[11]
β - $Li_{13}Ag_5Si_6$	$I4_1/amd$	[b]

^[a] no crystal structure was published

^[b] this thesis

^[c] later identified as $Li_3Ag_2Si_3$

7.1.4 The Compound α - $Li_{13}Ag_5Si_6$

α - $Li_{13}Ag_5Si_6$ published by Belin *et al.* crystallizes in space group $R\bar{3}m$ and is isostructural to the Li_2AgGe (Figure 7.2). α - $Li_{13}Ag_5Si_6$ has mixed Li/Ag positions, whereas α - Li_2AgGe has only ordered positions. The [AgSi] polyanionic network forms a pseudo diamond-like motif like the structures investigated in the Li-Ag-Ge phase system. The Ag sites are partial occupied by about 19% Li. The interatomic distances for Si-Si (2.405 Å) and Ag-Ag (3.103 Å) are in accordance with α -Si and Ag elements for metallic radii. The Ag-Si distance of 2.694 Å matches the distances found in $LiAg_2Si$ (2.8602 Å) and $Li_3Ag_2Si_3$ (2.6377 Å), although the Ag-Si interatomic distance of $LiAg_2Si$ is a bit longer. Band structure calculations has been car-

ried out and the material shows anisotropic metallic behavior. The group of Belin also found a reversible specific capacity around $800 \frac{\text{mA}\cdot\text{h}}{\text{g}}$. In the following $\alpha\text{Li}_{13}\text{Ag}_5\text{Si}_6$ was investigated due to its thermal behavior leading to a new high-temperature phase.

7.2 The Compound $\beta\text{-Li}_{13}\text{Ag}_5\text{Si}_6$

7.2.1 Synthesis of $\beta\text{-Li}_{13}\text{Ag}_5\text{Si}_6$

$\beta\text{-Li}_{13}\text{Ag}_5\text{Si}_6$ was synthesized by a high temperature route described in chapter 2.6.2. 150 mg of the low-temperature phase $\alpha\text{-Li}_{13}\text{Ag}_5\text{Si}_6$ was grinded, transferred to a tantalum ampule and the ampule was sealed (chapter 2.5). The ampule was placed in a corundum tube, which was equipped with an attached balloon for pressure compensation. The corundum tube was evacuated, filled with Ar, heated to 575°C and held for 24 h. Subsequently it was rapidly cooled down by transferring the ampule directly to an iced water bath.

After opening the ampule, the product appeared as metallic lustrous silver powder, which was sensitive to air and moisture. SC- and P-XRD-measurement were performed.

$\alpha\text{-Li}_{13}\text{Ag}_5\text{Si}_6$ was synthesized analogue to $\alpha\text{-Li}_2\text{Ag}_{0.8}\text{Ge}_{1.2}$ described in chapter 6.3.1.

7.2.2 Characterization of $\beta\text{-Li}_{13}\text{Ag}_5\text{Si}_6$

The compound was characterized by SC-XRD measurements. The preparation was performed analogous to the procedure described in chapter 3.1 and a 0.1 mm diameter capillary was used for the measurement. A face-centered cubic cell was found exhibiting a NaTi-like structure motif. Selected crystallographic data is given in Table 7.2 and 7.3. Additional crystallographic data is given in the appendix (Table 13.27 and 13.28)

Table 7.2: Single crystal data and structure refinement of β -Li₁₃Ag₆Si₆

Formula	β-Li₁₃Ag₅Si₆
Formula weight/ $\frac{g}{mol}$	798.1
Space group	$Fd\bar{3}m$ (no. 227)
Z	0.33
Unit cell parameters/ \AA	$a = 6.0686(17)$
Volume/ \AA^3	223.49(11)
$\rho_{calc}/\frac{g}{cm^3}$	1.113
abs. coeff./ mm^{-1}	2.271
F(000)	67
Crystal shape/color	block/grey silver
Temperature (K)	293
Θ range/deg	5.82-46.81
Index Range in hkl	$-12 \leq h \leq 4$ $-7 \leq k \leq 11$ $-14 \leq l \leq 5$
Reflections collected	330
Unique reflections	69
reflections with $I > 2\sigma(I)$	64
Data/restraints/parameter	69/0/5
GOF on F^2	1.206
$R_1, wR_2 (I \geq 2\sigma(I))$	0.0762, 0.1450
R_1, wR_2 (all data)	0.0792, 0.1462
Largest diff. peak and hole	3.382, -2.826

Table 7.3: Atomic coordinates and equivalent isotropic displacement parameters of β -Li₁₃Ag₆Si₆

Atom	Wyck.	x	y	z	S.O.F.	$U_{eg}/\text{\AA}^2$
Si1	8a	0.1250	0.1250	0.1250	0.4(2)	0.0229(8)
Ag1	8a	0.1250	0.1250	0.1250	0.6(2)	0.0229(8)
Li1	8b	0.3750	0.3750	0.3750	1	0.016(8)

7.2.3 Structure Description of β -Li₁₃Ag₅Si₆

The compound β -Li₁₃Ag₅Si₆ crystallizes in space group $Fd\bar{3}m$ (no. 227) of the NaTl structure type. It is the same structure type as for compounds β -Li₂Ag_{0.8}Ge_{1.2} and γ - β -Li_{2.53}AgGe₂ in the Li-Ag-Ge phase system.

It shows a mixed occupation for the 8a Si/Ag position of a ratio of 0.4(2):0.6(2). Since only Si and Ag was refined on this position and not Li as well, which should also partial occupy this

position due to the stoichiometry, the actual ratio should be different, but in the range of the errors.

The Si/Ag positions build a diamond-like network stuffed with Li-atoms in the channels. The Li atoms are also arranged in a diamond-like fashion. The structure is shown in Figure 7.4. In general the same structural derivation given in chapter 6.2.3 for β -Li₂Ag_{0.8}Ge_{1.2} apply here as well giving a not electron-precise ZINTL-phase.

The Ag/Si-Ag/Si inter atomic distance is 2.6278(7) Å. Compared to the structures of β -Li₂Ag_{0.8}Ge_{1.2} and γ - β -Li_{2.53}AgGe₂ it is slightly shorter, which makes sense due to the smaller atom Si instead of Ge. The low temperature phase α -Li₁₃Ag₅Si₆ shows all three types of bonds (Table 7.4) and matches the heteroatomic bond Ag-Si (2.694 Å). The fact that it is slightly shorter than the Ag-Si bonds shows the higher contribution of Si-Si bonds due to the totally mixed positions, which is expected due to the stoichiometry.

The Li-Li distance of 2.6278(7) Å is mainly caused by symmetry since no bonds are considered. The distance is fixed by the Ag-Si network.

Compound	X1-X2	Distance / Å
β -Li ₂ Ag _{0.8} Ge _{1.2}	Ag/Ge-Ag/Ge	2.6876(3)
γ -Li _{2.53} AgGe ₂	Ag/Ge-Ag/Ge	2.6789(3)
α -Li ₁₃ Ag ₅ Si ₆	Si-Si	2.405
α -Li ₁₃ Ag ₅ Si ₆	Ag-Ag	3.103
α -Li ₁₃ Ag ₅ Si ₆	Ag-Si	2.694
LiAg ₂ Si	Ag-Si	2.860
Li ₃ Ag ₂ Si ₃	Ag-Si	2.638

7.2.4 Thermal Analysis

α -Li₁₃Ag₅Si₆ was investigated by DSC experiments. The sample was handled according to chapter 3.3. The thermograms are shown in Figure 7.5.

The sample shows a phase transition at 497 °C and the melting point at about 650 °C. This information was used to synthesize the high temperature compound above 500 °C.

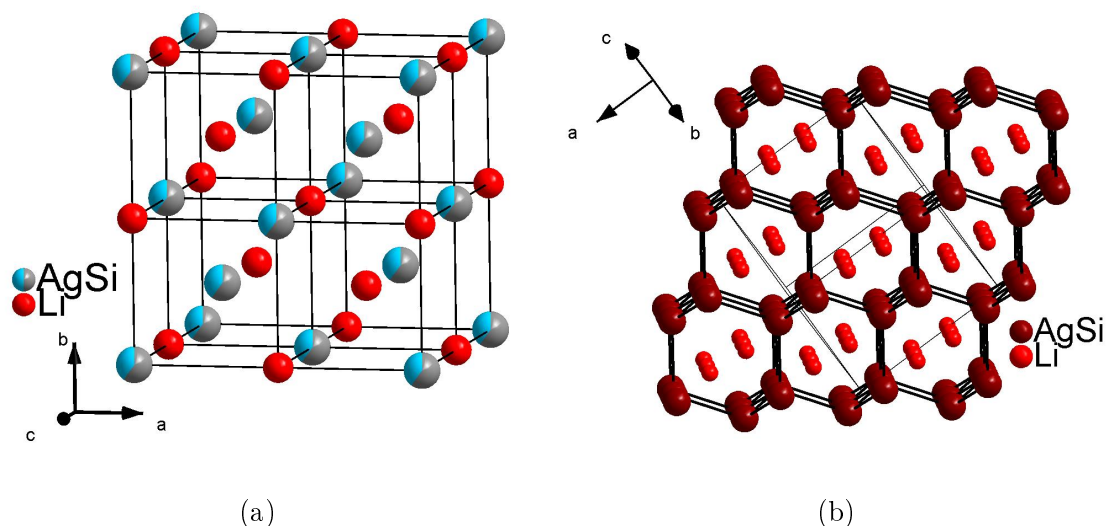


Figure 7.4: (a) A unit cell of $\beta\text{-Li}_{13}\text{Ag}_5\text{Si}_6$. Li is shown in red according and Ag/Si in grey/light blue according to site occupation at a 90% probability level. The thinner lines show the CsCl-like substructure. (b) Structure of $\beta\text{-Li}_{13}\text{Ag}_5\text{Si}_6$ showing the diamond-like network of Ag/Si. Li is shown in red and Ag/Ge in dark red. The thinner lines show the unit cell borders.

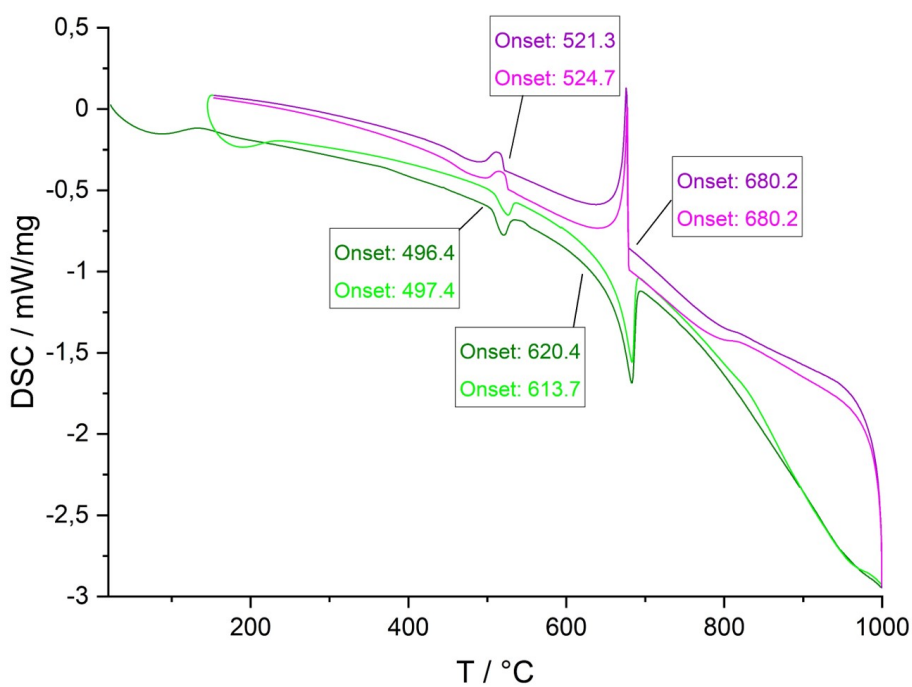


Figure 7.5: DSC thermogram of $\beta\text{-Li}_{13}\text{Ag}_5\text{Si}_6$. Lines and numbers indicate the onset temperatures of the corresponding thermal effects. The 1st and 2nd heating circle is shown in green and light green, respectively. The 1st and 2nd cooling circle is shown in violet and light violet, respectively.

References

- [1] H. L. Luo, W. Klement, T. R. Anantharaman, *Trans. Indian Inst. Met.* **1965**, *355*, 214–218.
- [2] T. Anantharaman, H. L. Luo, W. Klement, *Nature* **1966**, *210*, 1040–1041.
- [3] Suryanarayana, *J. Less-Common Met.* **1974**, *35*, 347–352.
- [4] A. Anani, R. A. Huggins, *J. Power Sources* **1992**, *38*, 351–362.
- [5] A. Anani, R. A. Huggins, *J. Power Sources* **1992**, *38*, 363–372.
- [6] J. W. Kim, J. H. Ryu, K. T. Lee, S. M. Oh, *J. Power Sources* **2005**, *147*, 227.
- [7] S. M. Hwang, H. Y. Lee, S. W. Jang, S. M. Lee, S. J. Lee, H. K. Baik, J. Y. Lee, *Electrochemical and Solid-State Letters* **2001**, *4*, 97–100.
- [8] H. Pauly, A. Weiss, H. Witte, *Z. Metallkd.* **1968**, *59*, 58.
- [9] H. Schuster, W. Seelentag, *Z. Naturforsch. B* **1975**, *30B*, 804.
- [10] D. G. Kevorkov, V. V. Pavlyuk, O. I. Bodak, *Polish J. Chem.* **1997**, *71*, 712–715.
- [11] L. Lacroix-Orio, M. Tillard, C. Belin, *Solid State Sciences* **2008**, *10*, 5–11.
- [12] J. Evers, G. Oehlinger, G. Sextl, *Angew. Chem. Int. Ed.* **1993**, *32*, 1442.
- [13] W. S. Tang, J.-N. Chotard, R. Janotz, *J. Electrochem. Soc.* **2013**, *160*, A1232.
- [14] H. G. von Schnering, R. Nesper, J. Curda, K.-F. Tebbe, *Angew. Chem.* **1980**, *92*, 1070–1070.
- [15] M. Zeilinger, T. F. Fässler, *Acta Cryst.* **2013**, *E69*, i81.
- [16] M. Zeilinger, V. Baran, L. van Wüllen, U. Häussermann, T. F. Fässler, Stabilizing the Phase Li₁₅Si₄, **2013**.
- [17] M. Zeilinger, I. M. Kurylyshyn, U. Häussermann, T. F. Fässler, *Chem. Mater.* **2013**, *25*, 4623.
- [18] M. Zeilinger, D. Benson, U. Häussermann, T. F. Fässler, *Chem. Mater.* **2013**, *25*, 1960–1967.
- [19] T. Noritake, M. Aoki, S. I. Towata, T. Takeuchi, U. Mizutani, *Acta Cryst.* **2007**, *26*, 726–234.
- [20] A. Slabon, S. Budnyk, E. Cuervo-Reyes, M. Wörle, R. Verel, R. Nesper, *Chemistry - A European Journal* **2013**, *19*, 16528–16531.

The Framework Compound $\text{Li}_6\text{B}_{18}(\text{Li}_3\text{N})_x$ hosting Li_3N and chemi-inspired B_4C_2 structures

8.1 Introduction

To cover the demand of our everyday electric energy consumption improved battery materials are inevitable and Li-ion batteries have many advantages like high gravimetric and volumetric capacities compared to other charge carriers (see chapter 1.1).^[1] Additional to develop new anode or cathode materials improving the electrolyte for fast ion conducting is crucial. Conventional Li-ion batteries use liquid electrolytes and due to their state of matter the volumetric capacity is limited.^[2,3] This means by changing the electrolyte also the capacity can be improved. Additionally, going from liquid to solid electrolyte the formation of dendrites, which leads to quick capacity fading and safety issues of metallic Li anodes, could be prohibited. Therefore, another advantage of solid electrolytes is to allow the usage of metallic Li as anode material, which would highly improve the energy density of Li-ion batteries.^[4]

All-solid state Li-ion batteries (ASSLIBs) are already known. The lithium-iodine battery uses LiI as solid electrolyte, but is limited to low energy devices due to the lack in specific power.^[5] Also ASSLIBs using Li-metal as anode materials are already known. Additionally, those ASSLIBs were stacked bi-polar for usage in electric cars. This offers a less complex thermal management systems.^[6]

Suitable material classes for solid electrolyte can be borides, phosphides, oxides, sulfides, and organic polymers. The demands of those materials are high. the material is supposed to be either thermodynamically stable or kinetically inert to Li-metal and cathode materials. the stability can be achieved by formation of stable solid electrolyte interface (SEI) like in conventional LIBs. Additionally, the usage of a combination of electrolytes differ for anode or cathode contact side can

be an option.^[7] Nevertheless, not only high stability is requested, also high ion-conductivity is necessary to keep up with conventional LIBs. Therefore, the specific ionic conductivity should be higher than $1 \cdot 10^{-3} \text{ Scm}^{-1}$ to compete. On the other hand, electronic conductivity is needed to be very low. Mechanical properties are also important to achieve withstand volume change during cycling and handling of the battery and reduce grain-boundary resistances by current constriction effects without the need of high temperature sintering. Therefore, the material should be soft.

Structure-property relationships show certain structural feature, which can be associated with high ion conductivity. Diffusion through a solid can be improved by vacancies of the charge carrier.^[8] This concludes also in a crucial low activation energy E_a of the mobility, because the next position to hop on is free and no repulsion does occur. This process seems to be favored through faces compared to edges of its respective coordination polyhedron.^[9] One of the lowest activation energies in sulfide-based materials are expected for Li between face-sharing tetrahedra in a body centered cubic sulfur packing.^[10] Tetragonal $\text{Li}_{10}\text{GeP}_2\text{S}_{12}$ is one of the fastest ion conductors crystallizing in a distorted variant.^[11] This compound and $\text{Li}_{11}\text{Si}_2\text{PS}_{12}$,^[12] which can even compete with liquid electrolytes ($\sigma_{RT} = 1 \cdot 10^{-2} \text{ Scm}^{-1}$), belongs to the well-known LGPS-type superionic conductor. The activation energies for Li diffusion in LGPS-type compounds are about 20 kJmol^{-1} . The LISICON family is another class of superionic conductors. $\text{Li}_{2+2x}\text{ZnGeO}_4$ is one of the representatives found 1078 exhibiting a ion conductivity of $1 \cdot 10^{-6} \text{ Scm}^{-1}$.^[13,14] Improvements were achieved by using sulfide compounds (thio-LISICONs).^[15,16]

A compound, which has already been synthesized in the 1970s, is Li_3N . This compound showed excellent ion conductivity of $6 \cdot 10^{-3} \text{ Scm}^{-1}$ at room temperature, but lacks electrochemical stability.^[17-19] Therefore, this compound is not suitable as solid electrolyte.

Not only crystalline materials can be considered as solid electrolyte. Glassy/amorphous compounds were investigated as well. Various combinations of binary sulfides might be potential candidates. For instance, the mixture of Li_2S with $\text{B}_2\text{S}_3/\text{LiI}$, SiS_2/LiBr , and $\text{P}_2\text{S}_5/\text{LiI}$ show ion conductivities of up to 10^{-3} Scm^{-1} .^[20-24] In particular boron is a promising candidate due to its very light molecular mass thinking of gravimetric capacities. The compound LiBSi_2 exhibits a tetrahedral open framework structure showing large open channels, which are stuffed with Li-ions. The compounds can be synthesized by a combination of high-temperature and high pressure synthesis.^[25] Due to synthesis problem no ion conductivity was measured so far, but structure-property relationships promise Li-ion mobility.

Such large open channel frameworks are in general a promising structure class of materials for solid electrolytes. Another example is the template structure $\text{Li}_6\text{B}_{18}(\text{Tp})_x$.

The boron network provides a large network-structure, which can host Li-ions and other greater guest structures or templates (Tp) like Li_2O and LiBH_4 . The network is built of a $3^24^86^2$ network of interconnected B_6 octahedra. In former works impedance measurements were carried out showing an activation energy of 38.5 kJmol^{-1} above $150 \text{ }^\circ\text{C}$.^[26]

Without the presence of a template tetragonal Li_2B_6 is formed. The structure is related to $\text{Li}_6\text{B}_{18}(Tp)_x$.^[27] The compound builds also a pore structure of a 4^{12} framework of interconnected B_6 octahedra. The formed cubic voids are filled by Li. Those cubic $M\text{B}_6$ structures are usually very stable and exhibit monovalent, divalent and trivalent variants ($M = \text{K, Mg, Ca, La, Y, } \dots$).^[28-31] This shows a huge structural and electronic flexibility of the framework, but only the divalent version should be semiconducting since the structure is electron-precise, whereas the others either have a electron-deficiency or excess.^[32,33] Therefore those are not suitable as solid electrolyte.

In this work experimental data of a new phase using Li_3N as guest structure was taken and computational analysis was carried out to confirm experimental achieved data. Additionally, possible Li paths for Li-ion mobility were investigated. At last, other electron neutral framework structure without guests were derived and compared.

8.2 The Compound $\text{Li}_6\text{B}_{18}(\text{Li}_3\text{N})_x$

In the following section the compound $\text{Li}_6\text{B}_{18}(\text{Li}_3\text{N})_x$ synthesized and characterized by **L. M. Scherf** and **T. Restle** is discussed. All experimental work was carried out by **L. M. Scherf** and **T. Restle**, whereas the computational analysis was performed by **J. Dums**. A brief summary of synthesis, characterization and structure description based on L. M. Scherfs and T. Restles work is given in the beginning.^[34,35]

8.2.1 Experimental Part

This part was carried out and evaluated by L. M. Scherf and T. Restle.

Synthesis and Characterization

$\text{Li}_6\text{B}_{18}(\text{Li}_3\text{N})_x$ was synthesized from 39.2 mg Li, 136.5 mg B, and the template species 60.8 mg Li_3N . An excess of Li was used to promote the formation of the crystalline template phase.^[36] The compounds were transferred to a stainless steel ampules. The ampule was enclosed in a quartz reaction container under vacuum and heated up to $900 \text{ }^\circ\text{C}$, which was hold for 24 h. Subsequently the compounds were cooled down slowly to room temperature.

The compound was characterized by P-XRD experiments with Rietveld refinement. Brief crystallographic data is given in Table 8.1 and 8.2. For more information see thesis of L. M. Scherf.^[34]

Table 8.1: Structure data of $\text{Li}_6\text{B}_{18}(\text{Li}_3\text{N})_x$ from P-XRD experiments

Formula	$\text{Li}_{6.35(7)}\text{B}_{18}\text{N}_{0.94(1)}$
Formula weight/ $\frac{g}{mol}$	251.8
Space group	$P6/mmm$ (no. 191)
Z	1
Unit cell parameters	$a = 8.2736 \text{ \AA}$ $c = 4.1846 \text{ \AA}$
Volume/ \AA^3	248.06
color	dark red

Table 8.2: Atomic coordinates of $\text{Li}_6\text{B}_{18}(\text{Li}_3\text{N})_x$ from P-XRD experiments

Atom	Wyck.	x	y	z
B1	$12q$	0.4478	0.1152	0.5
B2	$6i$	0.5	0	0.798
$Tp1$	$1a$	0	0	0
Li1	$2c$	$\frac{1}{3}$	$\frac{2}{3}$	0
Li2	$6l$	0.1527	0.3055	0
Li3	$1b$	0	0	0.5

Structure Description

The structure crystallizes in space group $P6/mmm$ (No. 191) with a boride network. The sub-lattice or host-structure is built of B_6 octahedra, which are connected to a $3^24^86^2$ network. Along the c -axis two kinds of channels are build. In the smaller channel isolated Li-ions a stuffed, whereas in the bigger channel the template Li_3N is located. The substructure on the channel is equivalent to the compound Li_3N . The structure is illustrated in Figure 8.1.

8.2.2 Computational Analysis

This section describes the computational analysis carried out to support the experimental data. The calculations were carried out with crystal14 on a DFT-HSE06/TZVP level of theory. The starting geometry was taken from experimental

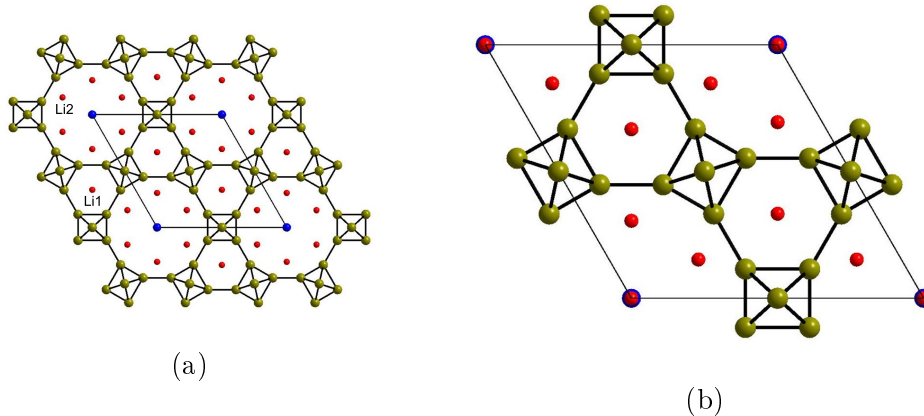


Figure 8.1: Structure of $\text{Li}_6\text{B}_{18}(\text{Li}_3\text{N})_x$. B, N and Li atoms are shown in dark yellow, blue and red, respectively. The $3^24^86^2$ boron network built of B_6 octahedra is shown with black bonds. (a) View along c -axis with a enlarged cell showing two kinds of channel stuffed with either Li or Li_3N . (b) View along c -axis showing only the unit cell.

data shown in chapter 8.2.1. Additional computational detail are given in chapter 4. The structures were optimized assuming full occupation of all atomic positions in $\text{Li}_6\text{B}_{18}(\text{Li}_3\text{N})$ within the constraints imposed by the space group symmetry. Band structures, density of states (DOS) and Mulliken population analysis were performed. Three models of Li_6B_{18} were built in order to simulate a guest-removed host-network and singlepoint calculations were carried out. Additionally, Raman calculations at a DFT-PBE0/SVP level of theory were performed after a structure optimization of the same level. PBE0 was chosen, because HSE06 is not implemented for Raman calculations in CRYSTAL14. Since the structure shows channels stuffed with Li or Li_3N Li-mobility was simulated and energy barriers were calculated. This was done by several single point calculations scanning the motion of the Li atom at several steps.

Geometry Optimization

The obtained structure parameters of the optimized structure $\text{Li}_6\text{B}_{18}(\text{Li}_3\text{N})$ show less than 1.8 % derivation from the experimental data, confirming the applied level of theory (Table 8.3). The nature of a stationary point on the potential energy surface could not be confirmed by a frequency calculation, because the frequencies show one slightly imaginary (-82 cm^{-2}). This can be explained by the full occupation instead of a partial one in the experimental structure. Symmetry reductions were carried out in order to reach a true local energy minimum, but they distorted the original structure too much to be reasonable.

Table 8.3: Atomic distances d and cell parameters a , and c for $\text{Li}_6\text{B}_{18}(\text{Li}_3\text{N})$, as well as, deviation Δd from experimental data in percentages

Parameter	$\text{Li}_6\text{B}_{18}(\text{Li}_3\text{N})$ calc \AA	Deviation / %
a	8.2164	0.69
c	4.1093	1.80

Band Structure and Density of States (DOS)

Density of states and band structure of $\text{Li}_6\text{B}_{18}(\text{Li}_3\text{N})$ are depicted in Figure 8.2. The band structure reveals a direct bandgap of 1.9 eV at the Γ point, rendering the structure type an interesting candidate for optoelectronic applications. The size of the band gap corresponds to the reddish color of the compound.

Path of Brillouin zone is given in Figure 13.32 in the appendix. Interestingly, the top

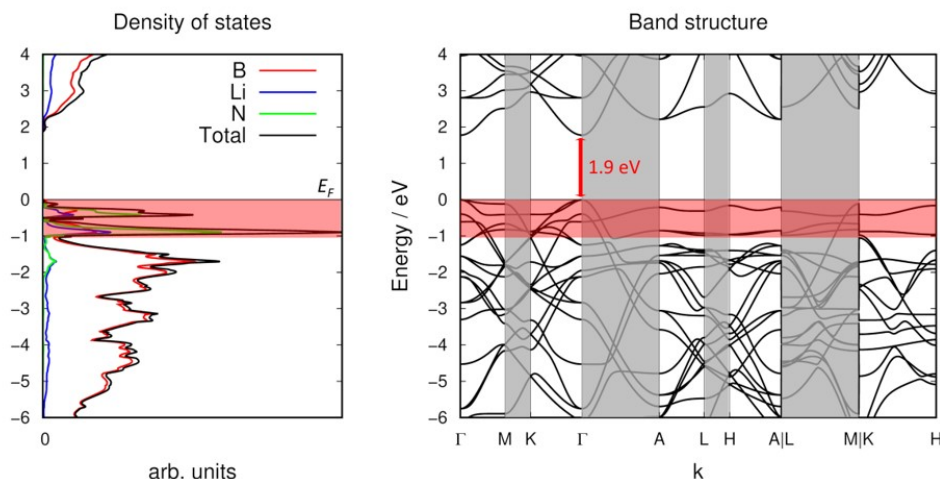


Figure 8.2: Total and partial DOS curves in the range of -6 eV to 4 eV for $\text{Li}_6\text{B}_{18}(\text{Li}_3\text{N})$. Band structure of $\text{Li}_6\text{B}_{18}(\text{Li}_3\text{N})$ in the range of -6 eV to 4 eV, the bands marked in red mainly correspond to states of the atoms situated in the large pores of the structure.

conducting bands situated between 0 and about -1.1 eV correspond mainly to atoms located inside the large pores of the open framework structure, as shown by the DOS curves. N has the largest contribution to the total DOS in this part, whereas it has almost no contribution at lower eV. This is expected for a true host-guest compound.

Raman spectroscopy

Experimental and calculated Raman spectra are depicted in Figure 8.3 and are in good agreement. The signals $1A_{1g}$, $2A_{1g}$ and $3A_{1g}$ correspond to the known A_{1g} , E_g and T_{2g} modes in cubic MB_6 . Due to the more complex structure of $Li_6B_{18}(Li_3N)$ compared to cubic MB_6 more signals occur. For each mode the unit cell contains three instead of one octahedral B_6 units, which can exhibit different vibrations at the same time and end up in a higher variation of modes. All modes are given in the appendix (Figure 13.22-13.31).

Template-free Li_6B_{18}

Since extraction experiments have shown that the template species can be at least partially removed by reaction with ethanol, we determined a variety of hexagonal, template-free structures. Several single-point calculations were carried to determine their electronic structures. The boron framework was kept intact. In addition, atomic positions Li1 and Li3 were maintained because, according to Rietveld refinement, they remain fully occupied even in the extracted $Li_{6-\gamma}B_{18}(Tp)_x$. Additionally, the atom projected DOS (Figure 8.2) shows, that only Li situated inside the large pores contribute to the states between 0 and -1.1 eV, with Li3 contributing less than Li2. Therefore, Li2 can be assigned to the guest species. For the template-free structures, position $Tp1$ was removed completely and the overall symmetry was reduced in order to split Li2 into a fully occupied and an empty position, yielding a sum formula of Li_6B_{18} .

Three different symmetry reduction methods were selected to construct three different Li atom configurations inside the large pore of the structure (Figure 13.35): Symmetry reduction to $P\bar{6}m2-Li_6B_{18}$ affords a stacked configuration in which every other Li2 position is occupied, whereas doubling of the c axis in $P6_3/mmc$ constructs a staggered Li2 configuration. Additionally, a $P\bar{6}2m$ configuration was considered, in which every other Li2b position is occupied in a stacked fashion. The starting configurations for these electronic structure calculations are given in the appendix.

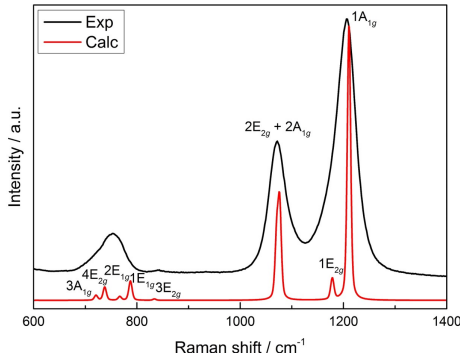


Figure 8.3: Raman spectra of $Li_6B_{18}(Li_3N)_x$ (experimental) in black and of $Li_6B_{18}(Li_3N)$ (calculated) in red with assigned modes. The Raman shifts of the calculated Raman spectra were multiplied by a factor of 0.95 due to the systematic overestimation of Raman frequencies by the functional PBE0.^[37]

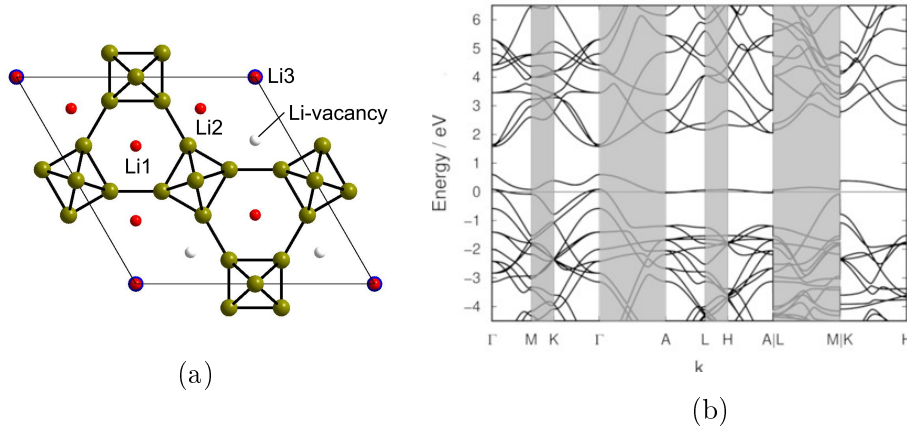


Figure 8.4: (a) Structure of template-free Li_6B_{18} in $P\bar{6}2m$, white globes represent the void Li2 positions. b) Band structure of $P\bar{6}2m\text{-Li}_6\text{B}_{18}$ in the range of -4.5 to 6.5 eV.

Single-point calculations revealed $P6_3/mmc$ as the lowest in energy almost equal to $P\bar{6}m2$, which is only 0.7 kJmol^{-1} per unit higher. $P\bar{6}2m$, however, is 71.9 kJmol^{-1} per unit higher than $P\bar{6}m2$. The band structures calculated for the different Li_6B_{18} structures show that removal of the template species does not result in true semiconductors (Figures 8.4). Thus, the pores must be completely free of any host species to obtain a true semiconductor without any gap states.

Li-Ion Diffusion Paths

In order to evaluate the applicability as solid electrolyte several possible diffusion paths were investigated by computational methods. In general five different paths were derived **P1-5**. A first evaluation of Li-atoms, which can be mobile is the Li removal energy:^[38]

$$\Delta E_{\text{Li}}(\text{Li}_6\text{B}_{18}\text{Li}_3\text{N}) = E_{\text{tot}}(\text{Li}_5\text{B}_{18}\text{Li}_3\text{N}) + E_{\text{tot}}(\beta - \text{Li}) - E_{\text{tot}}(\text{Li}_6\text{B}_{18}\text{Li}_3\text{N}) \quad (8.1)$$

The removal energy was calculated for all three Lithium positions Li1-3 listed in Table 8.4 considering only neutral compounds. This shows, that Li2 is the Lithium to remove most easily, whereas Li3 seems not fit to be moved. Li1 is only slightly higher in energy to be removed.

Along the c -axis are two different channels shown in Figure 8.5, where **A** is the larger one hosting Li_3N and **B** is the smaller one only stuffed by Li1. Additionally, there is another option for Li-ion mobility in ab -plane. The in-plane diffusion is similar to the

Table 8.4: Li removal energies for Li1-3

Li<i>x</i>	$\Delta E_{\text{Li}}(\text{Li}_6\text{B}_{18}\text{Li}_3\text{N})$
Li1	249 kJ/mol
Li2	230 kJ/mol
Li3	333 kJ/mol

one occurring in Li_3N , which is also happening in the Li-N-plane.

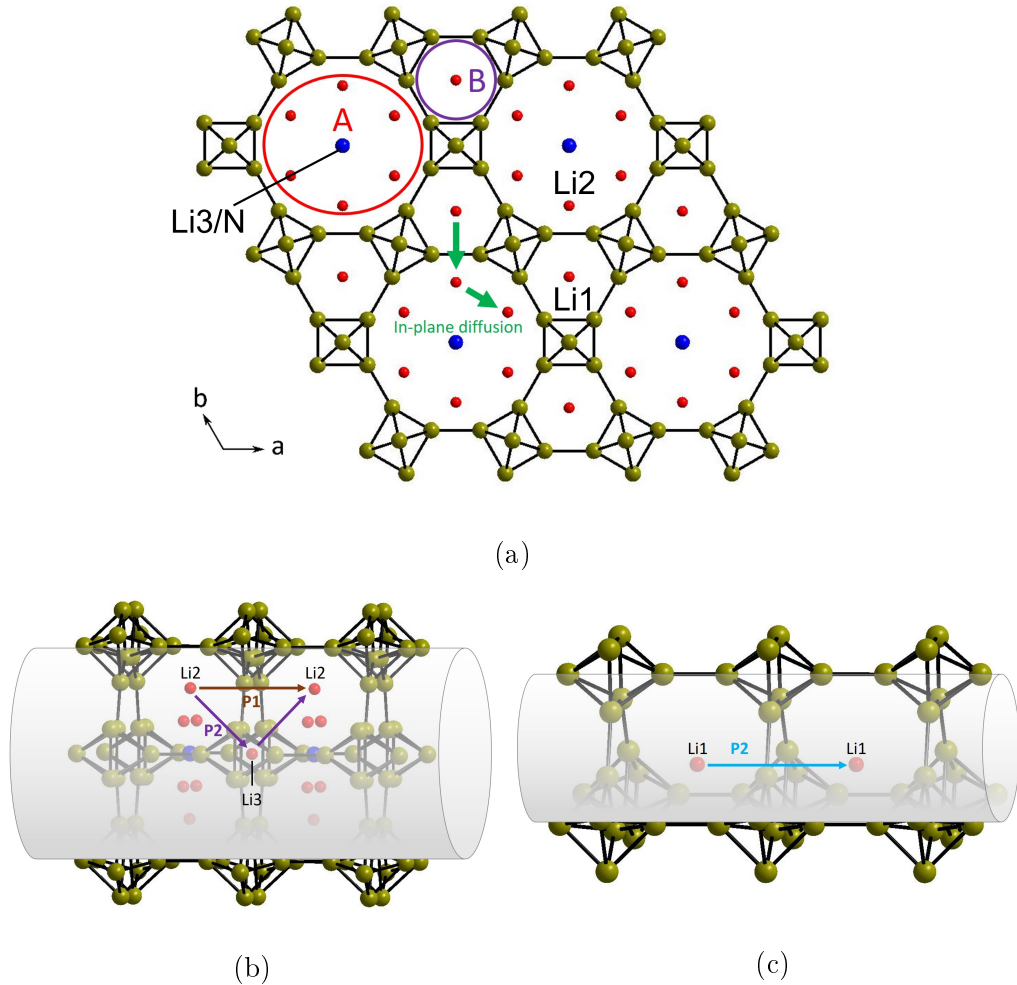


Figure 8.5: (a) Structure of $\text{Li}_6\text{B}_{18}(\text{Li}_3\text{N})$ showing channels **A** and **B** and in-plane diffusion path. (b) Channel **A** with diffusion paths **P1** and **P2**. (c) Channel **B** with diffusion paths **P3**.

For channel **A** there are two options for Li-ion mobility: **P1** and **P2**. **P1** is a motion from Li2 to Li2. This is basically a very simple model, because no vacancies are needed for the Li to move on, since the next Li2 is already in the next unit cell and without building a superstructure the next Li2 is automatically moving as well. Nevertheless, two different calculations were performed:

- a) Single point calculations without supercell and vacancy
- b) Single point calculations with 1x1x4 supercell and Li_3N vacancy

To calculate the **P2** path a superstructure with a Li3 vacancy is required. Therefore, only one method was used with 1x1x4 supercell and Li_3N vacancy. The results are

shown in Figure 8.6.

In channel **B** only one possible Li-ion diffusion namely **P3** with Li1→Li1 motion is present. In this case the same procedure is done like for **P1**.

The last Li-diffusion is a two-step diffusion. The first step is **P4**, which is the motion of a Li1 in a **B** channel to Li2 in a **A** channel in the *ab*-plane, which is shown in green (Figure 8.5). To simulate this diffusion a 2x2x1 superstructure was build and a Li₃N vacancy was added. For the second step from Li2 to Li2 in *ab*-plane of the same **A** channel alao a 2x2x1 supercell with Li₃N vacancy was used. The results are shown in Figure 8.6.

One can clearly see, that Li-diffusion along the **A** or **B** channel needs to pass a huge energy barrier of about 350-500 *kJ/mol*. On the other hand, the in-plane diffusion is preferred with a very low energy barrier. For the first step **P4** a barrier of about 20 *kJ/mol* is present. This matches the results of NMR-measurements with 5-20 *kJ/mol*.^[34] The second steps does not show a barrier at all. This can be explained due to charge distribution. The model of the Li diffusion is not sufficient, because a Li vacancy is build in the **A** channel. Considering only 5 Li2 atoms coordinating the nitrogen a equivalent pentagonal distribution is favored and therefore a negative energy barrier is gained. Nevertheless, this shows in general that the motion from one to the next Li2 position is very low in energy although n value could be gained. Further calculations including both steps at the same time or a motion of all six Li2 atoms at the same time is needed to simulate the diffusion. Additionally, β -Li₃N was investigated as well for the same kind of diffusion and shows also a negative energy barrier due to the same problem (see Figure 13.36).

8.2.3 Structure models of the type B₄C₂

Inspired by the structure of Li₆B₁₈(Li₃N) a neutral guest-free structure was derived hosting neither Li-ion, nor Li₃N. Since the boron network itself is charged some boron atoms were substituted by carbon to gain a charge neutral network. The four gained models have the formula B₄C₂ with space group *P6/mmm*, *P6/m*, *P6̄2m* and *P6̄m2*. Total energies and band structures were compared. A energy diagram showing the energies relative to the lowest one is shown in Figure 8.7. The energetically favored structure is *P6/m*, whereas *P6̄2m* and *P6/mmm* are very close to each other and

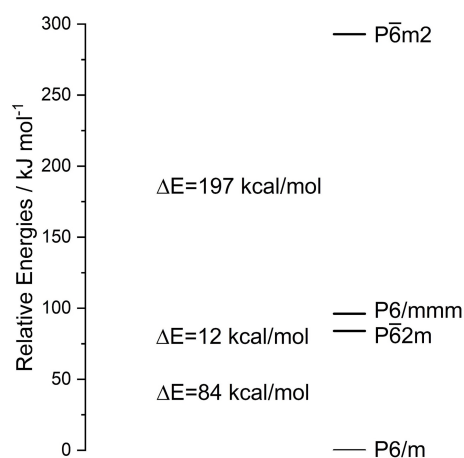


Figure 8.7: Relative energies of B₃C₂ structure models in space group *P6/mmm*, *P6/m*, *P6̄2m* and *P6̄m2*.

only differ in 12 kJ/mol. $P\bar{6}m2$ energetically very high with 293 kJ/mol above the lowest one $P6/m$.

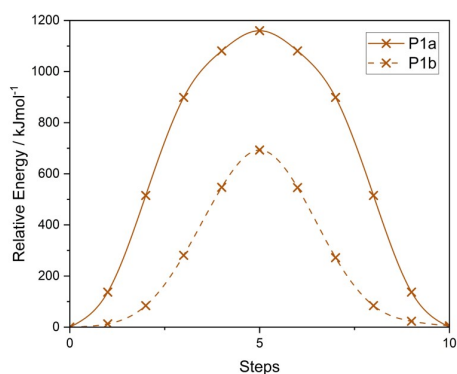
Band structure calculation show a semi-conducting behavior for all models with a band gap between 2.5 eV and 3.5 eV (see Figure 13.38-13.41).

References

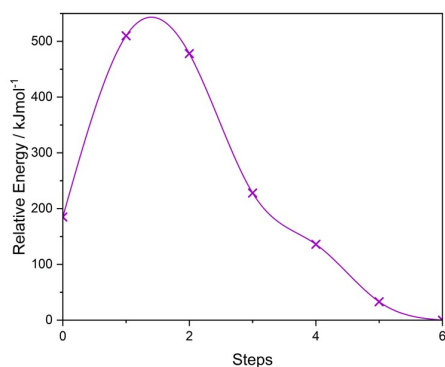
- [1] A. Patil, V. Patil, D. Wook Shin, J.-W. Choi, D.-S. Paik, S.-J. Yoon, *Mater. Res. Bull.* **2008**, *43*, 1913–1942.
- [2] J. Janek, W. G. Zeier, *Nat. Energy* **2016**, 16141.
- [3] J. G. Kim, B. Son, S. Mukherjee, N. Schuppert, A. Bates, O. Kwon, M. J. Choi, H. Y. Chung, S. Park, *J. Power Sources* **2015**, *282*, 299–322.
- [4] A. L. Robinson, J. Janek, *MRS Bulletin* **2014**, *39*, 1046–1047.
- [5] T. R. Crompton, *Small Batteries: Lithium - Iodine Batteries*, Palgrave, London, **1982**, pp. 196–197.
- [6] W. ZY, C. SJ, W. JY, W. ZH, Z. ZH, Y. XY, D. YH, X. XX, *J. Power Sources* **2018**, *394*, 57–66.
- [7] S. P. Culver, R. Koerver, W. G. Zeier, J. Janek, *Adv. Energy Mater.* **2019**, *9*, 1900626.
- [8] N. A. Anurova, V. A. Blatov, G. D. Ilyushin, O. A. Blatova, A. K. Ivanov-Schitz, L. N. Dem'yanets, *Solid State Ionics* **2008**, *179*, 2248–2254.
- [9] A. R. West, P. G. Bruce, *Acta Crystallogr. A.* **1982**, *38*, 1891–1896.
- [10] Y. Wang, W. D. Richards, S. P. Ong, L. J. Miara, J. C. Kim, Y. Mo, G. Ceder, *Nat. Mater.* **2015**, *14*, 1026–1031.
- [11] N. Kamaya, K. Homma, Y. Yamakawa, M. Hirayama, R. Kanno, M. Yone-mura, T. Kamiyama, Y. Kato, S. Hama, K. Kawamoto, A. Mitsui, A lithium superionic conductor. *eng*, **2011**.
- [12] A. Kuhn, O. Gerbig, C. Zhu, F. Falkenberg, J. Maier, B. V. Lotsch, *Phys. Chem. Chem. Phys.* **2014**, *16*, 14669–14674.
- [13] P. G. Bruce, A. R. West, *J. Electrochem. Soc.* **1983**, *130*, 662–669.
- [14] H.-P. Hong, *Mater. Res. Bull.* **1978**, *13*, 117–124.
- [15] R. Kanno, M. Murayama, *J. Electrochem. Soc.* **2001**, *148*, A742.
- [16] M. Murayama, R. Kanno, M. Irie, S. Ito, T. Hata, N. Sonoyama, Y. Kawamoto, *J. Solid. State. Chem.* **2002**, *168*, 140–148.

- [17] U. v. Alpen, A. Rabenau, G. H. Talat, *Appl. Phys. Lett.* **1977**, *30*, 621–623.
- [18] T. Lapp, S. Skaarup, A. Hooper, *Solid State Ionics* **1983**, *11*, 97–103.
- [19] S. PE, F. JJ, W. MC, S. CD, I. JJ, G. SG, G. AS, *J. Power Sources* **1999**, *81-82*, 739–747.
- [20] H. Wada, M. Menetrier, A. Levasseur, P. Hagenmuller, *MATCH Commun. Math. Comput. Chem.* **1983**, *18*, 189–193.
- [21] M. Menetrier, A. Hojjaji, C. Estournes, A. Levasseur, *Solid State Ionics* **1991**, *48*, 325–330.
- [22] M. Ménétrier, C. Estournès, A. Levasseur, K. J. Rao, *Solid State Ionics* **1992**, *53-56*, 1208–1213.
- [23] S. Sahami, S. W. Shea, J. H. Kennedy, *J. Electrochem. Soc.* **1985**, *132*, 985–986.
- [24] J. P. Malugani, G. Robert, *Solid State Ionics* **1980**, *1*, 519–523.
- [25] M. Zeilinger, L. van Wüllen, D. Benson, V. F. Kranak, S. Konar, T. F. Fässler, U. Häussermann, *Angew. Chem. Int. Ed.* **2013**, *52*, 5978–5982.
- [26] M. Panda, PhD thesis, University Hamburg, **2006**.
- [27] G. Mair, H. G. von Schnering, M. Wörle, R. Nesper, *Z. Anorg. Allg. Chem.* **1999**, *625*, 1207–1211.
- [28] M. von Stackelberg, F. Neumann, *Z. Phys. Chem. Abt. B* **1932**, *19*, 314–320.
- [29] R. Naslain, J. Étourneau, *C. R. Seances Acad. Sci. Ser. C* **1966**, *263*, 484–487.
- [30] H. Moissan, P. Williams, *Comptes Rendus Hebdomadaires Des Séances De L'Académie Des Sciences* **1897**, *125*, 629–634.
- [31] T. Kasuya, *Europhys. Lett.* **1994**, *26*, 283–287.
- [32] P. G. Perkins, D. R. Armstrong, A. Breeze, *J. Phys. C: Solid State Phys.* **1975**, *8*, 3558–3570.
- [33] P. G. Perkins, A. V. J. Sweeney, *J. Less-Common Met.* **1976**, *47*, 165–173.
- [34] L. M. Scherf, PhD thesis, TU Munich, **2017**.
- [35] T. Restle, PhD thesis, TU Munich, **2020**.
- [36] M. Wörle, R. Nesper, G. Mair, H. G. von Schnering, *Solid State Sci.* **2007**, *9*, 459–464.
- [37] M. L. Laury, M. J. Carlson, A. K. Wilson, *Journal of Computational Chemistry* **2012**, *33*, 2380–2387.

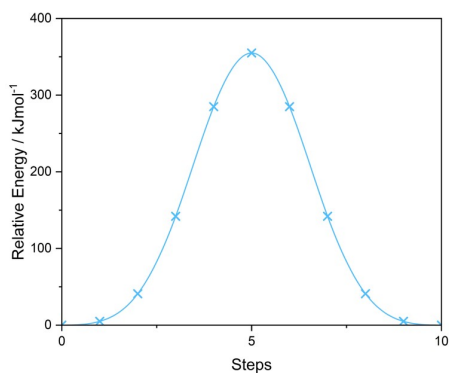
- [38] W. Li, G. Wu, C. M. Araujo, R. H. Scheicher, A. Blomqvist, R. Ahuja, Z. Xiong, Y. Fengb, P. Chen, *Energy Environ. Sci.* **2010**, *3*, 1524–1530.



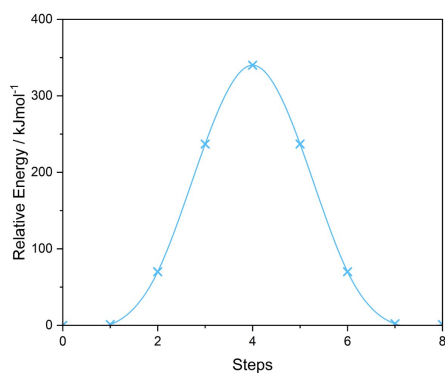
(a)



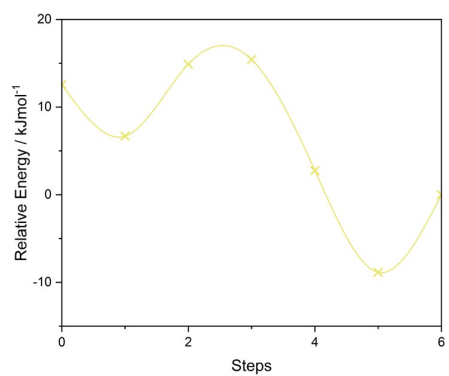
(b)



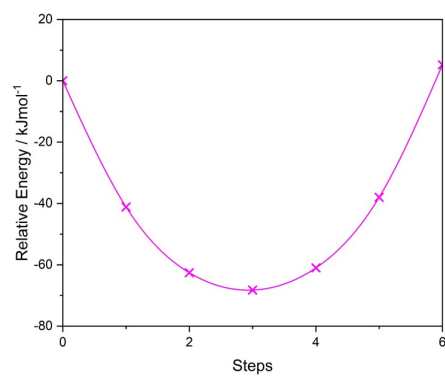
(c)



(d)



(e)



(f)

Figure 8.6: (a) Relative energies of **P1**. (b) Relative energies of **P2**. (c) Relative energies of **P3a**. (d) Relative energies of **P3b**. (e) Relative energies of **P4**. (f) Relative energies of **P5**.

Computational Analysis of Low Dimensional Structures

9.1 Introduction

ZINTL and KLEMM introduced the pseudo-element concept, which is a method to describe the tendency of bond localization in intermetallic compounds by assuming salt-like structures, that are electron-precise.^[1] This concept was originally only applied for semiconductors, but was expanded also to other systems. In the borderline case to typical metals the concept is still hard to apply.^[2-5] More detailed information about ZINTL concept is given in chapter 1.2.1.

An example for a typical low dimensional ZINTL phase is CaSi, where "Si²⁻" is isoelectronic to sulfur. Sulfur shows helical chain, whereas Si builds a polyanionic zig-zag chain. This planarity is explained due to effects of the Ca orbitals.^[6] In the ZINTL concept the role of the counter ion is neglected and therefore the motif of the polyanion can change slightly.^[6,7] The transformation from helical to planar conformation is responsible for the metallic character. In comparison the semiconductor KBi, where "Bi⁻" is also isoelectronic to group 16 Bi, builds helical polyanionic chains analogue to grey selenium and tellurium (Figure 9.6).^[8]

In chapter 9.4.2 KBi·NH₃ is described, which builds the same zig-zag chains as CaSi and metallic character due to the zig-zag chain-formation. The in chapter 9.4.2 investigated compound involves the heavy element Bismuth, which shows a huge variety of modifications. It occurs in nature, for example, as native element or as simple cations in minerals.^[9] Whereas, it can form complex polycations in molten salt. Examples for those polycations are [Bi₉]⁵⁺,^[10] [Bi₈]²⁺,^[11] and [Bi₅]³⁺,^[12] which are following Wade's rule. The in chapter 9.4.2 mentioned compound KBi and KBi·NH₃ are also examples for the variety of polyanionic structures formed by Bi, even though they are not electron-precise according to the ZINTL concept, the Bi atoms in these intermetallic compounds are connected by localized bonds.^[13] In K₃Bi₂ and K₅Bi₄ Bi polyanionics occur as well. The smallest anion is a Bi-dumbbell

$[\text{Bi}_2]^{2-}$ with formally double-bonded Bi atoms.^[14]

By adding different solvents to compounds like K_5Bi_4 and K_3Bi_2 some Bi-containing polyanions can be obtained. Dissolving K_5Bi_4 in ethylenediamine $[\text{Bi}_4]^{2-}$ anion a square-planar ring is formed after the addition of [2.2.2]-cryptant.^[15,16]

In this work the polyanionic system of Bi was extended to intermetalloid species^[17] by the reactions of bismuthides with low-valent tin anions. Representatives of the Sn-Bi system are the cluster species $[\text{Sn}_3\text{Bi}_3]^{5-}$, $[\text{Sn}_3\text{Bi}_3]^{3-}$ ^[18] and $[\text{Sn}_4\text{Bi}_4]^{4-}$.^[19] These compounds are obtained by extraction of ternary and quaternary phases.

Herein the polyanion $[\text{SnBi}_3]^{5-}$ analogue of the carbonate ion is discussed with respect to the electronic configuration (chapter 9.5).

Another field of interest of low dimensional ZINTL phases are all solid-state batteries, which have been investigated thoroughly in the recent year (see also chapter 1.1).^[20-22] Group 14 phosphides published in the chair of Prof. Fässler already show nice ionic conductivity up to $1 \frac{\text{mS}}{\text{cm}}$ ($\text{Li}_{14}\text{SiP}_6$, Li_8SiP_4 and $\alpha/\beta\text{-Li}_8\text{GeP}_4$).^[23-25] A noticeable structure motif of those structures and other in this phase systems are the typical $[\text{TpP}_4]^{8-}$ tetrahedra. Dependent on the Li-content different connectivities of those tetrahedra are found. They can be isolated (Li_8SiP_4) or form dimers ($\text{Li}_{10}\text{Si}_2\text{P}_6$ ^[26]), slabs ($\text{Li}_3\text{Si}_3\text{P}_7$ ^[26]) and three-dimensional networks (Li_2SiP_2 ^[23]). The advantage of phosphorus-based electrolytes compared to sulfur-based is the higher charge of the tetrahedra due to a formal charged "S²⁻" and "P³⁻". This lead to a higher Li-content in order to achieve charge compensation.

In chapter 9.2, Al and Ga instead of Ge/Si was used as central metal. Using a group 13 metal the charge of the tetrahedra is again increased by one ending up at the general formula $[\text{TrP}_4]^{9-}$. T. Restle already reported of the structure Li_8AlP_4 in 2019 showing high ionic conductivity of $3.0 \frac{\text{mS}}{\text{cm}}$ at room temperature.^[27] Also the compounds Li_3AlP_2 and Li_3GaP_2 were already mentioned, but without reliable crystallographic data.^[28,29]

As a alternative to Li-ion batteries, Na-ion batteries are also interesting for further investigations. Therefore the Na-Ta-P phase system was investigated (chapter 9.3). Sodium-based battery materials are less common compared to Li-based materials in recent researches, but still are worth to be investigated thoroughly.

9.2 The Compounds Li_3TrP_2 ($\text{Tr} = \text{Al}, \text{Ga}$)

In the following section the compounds Li_3AlP_2 and Li_3GaP_2 synthesized and characterized by **T. Restle** are discussed. All experimental work was carried out by **T. Restle**, whereas the computational analysis was performed by **J. Dums**. A brief summary of synthesis, characterization and structure description based on T.

Restles work is given in the beginning.^[30]

9.2.1 Experimental Part

This part was carried out and evaluated by T. Restle.

Synthesis and Characterization

Both compounds were synthesized from elements. The elements were loaded in a WC milling set and ball milled for 36 h at 350 rpm with resting periods for Li_3AlP_2 and 18 h at 350 rpm with resting periods for Li_3GaP_2 . Both achieved powders were each pressed into a pellet and transferred into a niobium ampule, which were sealed. The ampules were evacuated in silica reaction containers and heated in a tube furnace up to 700 °C, which was hold for 24 h. Subsequently the compounds were cooled down slowly to room temperature.

The compounds were characterized by P-XRD experiments with Rietveld refinement. Brief crystallographic data is given in Table 9.1 and 9.2. For more information see publications of T. Restle.^[30]

Table 9.1: Structure data of Li_3AlP_2 and Li_3GaP_2

Formula	Li_3AlP_2	Li_3GaP_2
Formula weight/ $\frac{g}{mol}$	109.75	152.49
Space group	<i>Cmce</i> (no. 64)	
Z	2	
Unit cell parameters/Å	$a = 11.5138$	$a = 11.5839$
	$b = 11.7634$	$b = 11.7809$
	$c = 5.8202$	$c = 5.8129$
Volume/Å ³	788.29	793.28
color	yellow ochre	brick red

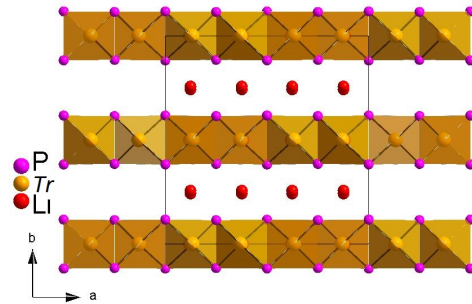
Structure Description

Both compounds Li_3AlP_2 and Li_3GaP_2 crystallize in the space group *Cmce* (no. 64). They can be described as a orthorhombic distorted cubic closed packing of P, where *Tr* occupies $\frac{1}{4}$ of the tetrahedral voids building TrP_4 tetrahedra. Edge-connected $\infty[\text{TrP}_2^{3-}]$ -layers of the tetrahedra are formed due to a occupation of the tetrahedral void by *Tr* of $\frac{1}{2}$ in every second layer. Dimers of tetrahedra are built by sharing P2-corners, which are connected with other dimers in the layer by P1 *via* edge. Li

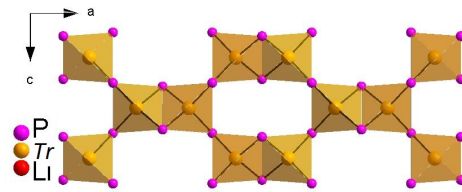
Table 9.2: Atomic coordinates of Li_3AlP_2 and Li_3GaP_2

Atom	Wyck.	Li_3AlP_2			Li_3GaP_2		
		x	y	z	x	y	z
P1	$8f$	0	0.1175	0.2138	0	0.1164	0.2117
P2	$8e$	$\frac{1}{4}$	0.3850	$\frac{1}{4}$	$\frac{1}{4}$	0.3826	$\frac{1}{4}$
$Tr1$	$8d$	0.1315	0	0	0.1333	0	0
Li1	$8d$	0.384	0	0	0.110	0	0
Li2	$16g$	0.123	0.2429	0.4805	0.117	0.2439	0.484

occupies the remaining tetrahedral voids, whereby Li1 is located within the layers and Li2 between the layers. The structure is illustrated in Figure 9.1.



(a)



(b)

Figure 9.1: Structure of Li_3TrP_2 ($Tr = \text{Al}, \text{Ga}$). P, Tr and Li atoms are shown in pink, orange and red, respectively. Tetrahedra are shown in transparent orange. (a) View along c -axis. Layers of tetrahedra are visible. Li are only shown in the unit cell represented by thin black lines. (b) View along b -axis. Top view of layer showing corner and edge-connection. Li are not shown.

9.2.2 Computational Analysis

This section describes the computational analysis carried out to support the experimental data. The calculations were carried out with crystal14 on a DFT-PBE0/TZVP level of theory. The starting geometry was taken from experimental data shown in chapter 9.2.1. Additional computational details are given in chapter 4. The structures were optimized within the constraints imposed by the space group symmetry.

Geometry Optimization

The optimized structures show a maximum deviation of parameters of 1.95 % for all parameters and average atomic distances. This shows a very good fit of the used level of theory. In Table 9.3 the atomic distances d and cell parameters a , b and c are given with percentage deviation compared to the experimental findings. All optimized parameters are given in the appendix (Table 13.37).

The nature of a stationary point on the potential energy surface was confirmed to be a minimum by a frequency calculation for each compound at Γ -point. Details are given in the appendix (Table 13.39).

Table 9.3: Atomic distances d and cell parameters a , b and c for Li_3AlP_2 and Li_3GaP_2 , as well as, deviation Δd from experimental data in percentages

	$d(\text{Li}_3\text{AlP}_2)$ / Å	$\Delta d(\text{Li}_3\text{AlP}_2)$ / %	$d(\text{Li}_3\text{GaP}_2)$ / Å	$\Delta d(\text{Li}_3\text{GaP}_2)$ / %
a	11.5388	0.22	11.5910	0.02
b	11.7560	0.06	11.7834	0.02
c	5.8267	0.11	5.8289	0.24
Average Tr -P	2.41	0	2.43	0.62
Tr - Tr	3.05	0.66	3.10	0
Li-Li	2.89	0.35	2.88	1.95
Tr -Li	2.92	1.85	2.92	0

Band Structure and Density of States (DOS)

Additionally, band structure and density of states were evaluated, which are illustrated in Figure 9.2. The calculations show a direct band gap of 3.1 eV and 2.8 eV for Li_3AlP_2 and Li_3GaP_2 , respectively. This is in good accordance with the observed color of the phases. Li_3AlP_2 appears yellowish and also shows the larger band gap, whereas Li_3GaP_2 is brick red. Due to the DOS phosphorus contributes the highest

share at the valence band maximum. In comparison for the conduction band minimum aluminum and gallium have the highest contributions. Path of Brillouin zone is given in Table 13.38 in the appendix.

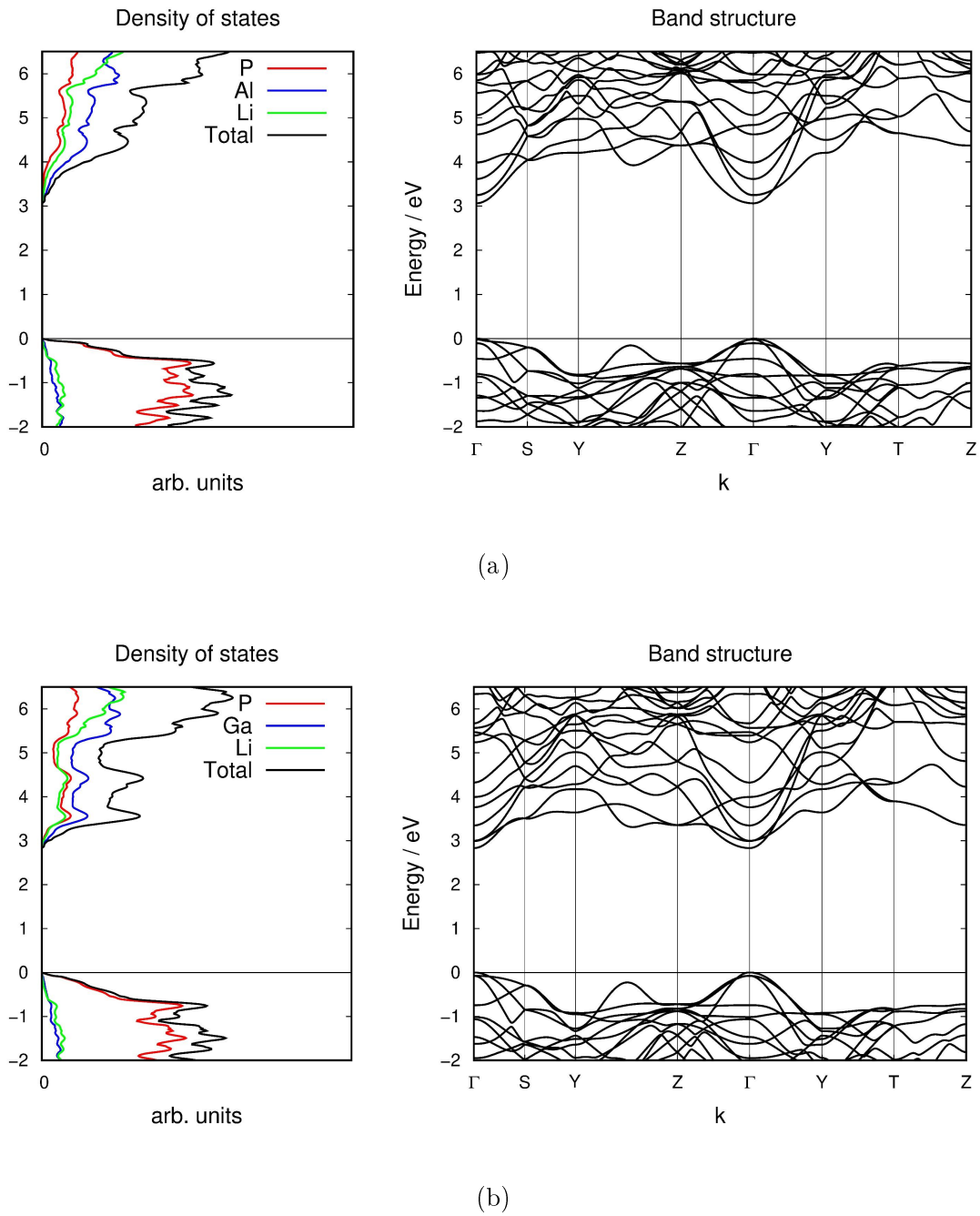


Figure 9.2: Density of states and band structure of (a) Li_3AlP_2 exhibiting a direct band gap of 3.1 eV and (b) Li_3GaP_2 exhibiting a direct band gap of 2.8 eV. The Fermi level is located at 0 eV.

9.3 The Compound Na_7TaP_4

In the following section the compound Na_7TaP_4 synthesized and characterized by **T. Restle** is discussed. All experimental work was carried out by **T. Restle**, whereas the computational analysis was performed by **J. Dums**. A brief summary of synthesis, characterization and structure description based on T. Restles work is given in the beginning.^[31]

9.3.1 Experimental Part

This part was carried out and evaluated by T. Restle.

Synthesis and Characterization

Na_7TaP_4 was synthesized from elements. Elements were stiochiometrical were ball-milled at 350 rpm with rest periods for 72 h using a ZrO_2 milling set. Subsequently, the obtained powder was pressed into a pellet and transferred to a niobium ampule, which was sealed. The ampule was enclosed in a quartz reaction container under vacuum and heated up to 700 °C, which was hold for 36 h. Subsequently the compounds were cooled down slowly to room temperature.

The compound was characterized by SC- and P-XRD experiments with Rietveld refinement. Brief crystallographic data is given in Table 9.4 and 9.5. For more information see publications of T. Restle.^[31]

Table 9.4: Structure data of Na_7TaP_4 from SC-XRD experiments

Formula	Na_7TaP_4
Formula weight/ $\frac{g}{mol}$	465.76
Space group	$P2_1/c$ (no. 14)
Z	4
Unit cell parameters	$a = 11.5604 \text{ \AA}$ $b = 8.1530 \text{ \AA}$ $c = 11.545 \text{ \AA}$ $\beta = 101.602^\circ$
Volume/ \AA^3	1065.91
color	vine red

Table 9.5: Atomic coordinates of Na₇TaP₄ from SC-XRD experiments

Atom	Wyck.	x	y	z
Na1	4e	0.1849	0.187	0.3408
Na2	4e	0.447	0.186	0.0723
Na3	4e	0.3079	0.8249	0.2054
Na4	4e	-0.0461	0.3383	0.0672
Na5	4e	0.5278	0.594	0.1407
Na6	4e	0.2604	0.582	0.4154
Na7	4e	0.0210	0.924	0.1402
Ta	4e	0.2499	0.4362	0.1347
P1	4e	0.1842	0.1585	0.0767
P2	4e	0.0998	0.5902	0.2001
P3	4e	0.3092	0.5829	-0.0295
P4	4e	0.4153	0.420	0.2970

Structure Description

The structure crystallizes in space group $P2_1/c$ (No. 14) with isolated TaP₄⁷⁻ tetrahedra. The structure is electrochemically balanced using the usual oxidation states Na⁺, Ta⁵⁺ and P³⁻.

P atoms arrange in a strongly distorted hexagonal closed packing. Ta occupies 1/8 of the tetrahedral voids, whereas Na occupies all octahedral void and additionally 3/8 of the tetrahedral voids. This end up in 50% unoccupied tetrahedral voids. The structure is illustrated in Figure 9.3.

9.3.2 Computational Analysis

This section describes the computational analysis carried out to support the experimental data. The calculations were carried out with crystal14 on a DFT-PBE0/TZVP level of theory. The starting geometry was taken from experimental data shown in chapter 9.3.1. Additional computational detail are given in chapter 4. The structures were optimized within the constraints imposed by the space group symmetry.

Geometry Optimization

The optimized structures show a maximum derivation of parameters of 0.6 % for all cell parameters and Ta-P interatomic distances. This reassures a very good fit of the used level of theory. In Table 9.6 the atomic distances d and cell parameters a , b , c

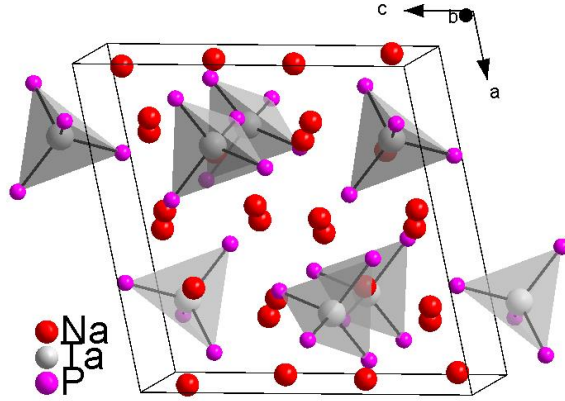


Figure 9.3: Structure of Na_7TaP_4 . P, Ta and Li atoms are shown in pink, light grey and red, respectively. Tetrahedra are shown in transparent grey.

and β are given with percentage deviation compared to the experimental findings. All optimized parameters are given in the appendix (Table 13.40).

The nature of a stationary point on the potential energy surface was confirmed to be a minimum by a frequency calculation for each compound at Γ -point. Details are given in the appendix (Table 13.42).

Table 9.6: Atomic distances d and cell parameters a , b , c and β for Na_7TaP_4 , as well as, deviation Δd from experimental data in percentages

Parameter	Calc.	Exp.	Deviation / %
a	11.516 Å	11.560 Å	0.38
b	8.133 Å	8.153 Å	0.25
c	11.495 Å	11.545 Å	0.43
β	101.4°	101.6°	0.19
Ta1-P1	2.449 Å	2.436 Å	-0.53
Ta1-P2	2.413 Å	2.403 Å	-0.36
Ta1-P3	2.420 Å	2.411 Å	-0.38
Ta1-P4	2.423 Å	2.410 Å	-0.53

Band Structure and Density of States (DOS)

Additionally, band structure and density of states were evaluated, which are illustrated in Figure 9.4. The calculations show a almost direct band gap of 2.9 eV. The

minimum of conduction band at Γ is slightly lower in energy than at X|Z. Due to the DOS phosphorus contributes the highest share at the valence band maximum, whereas tantalum has almost no contribution at all. In comparison for the conduction band minimum tantalum and sodium have a almost equal share, which is the highest and phosphorus has only a minor contribution.

Path of Brillouin zone is given in Table 13.41 in the appendix.

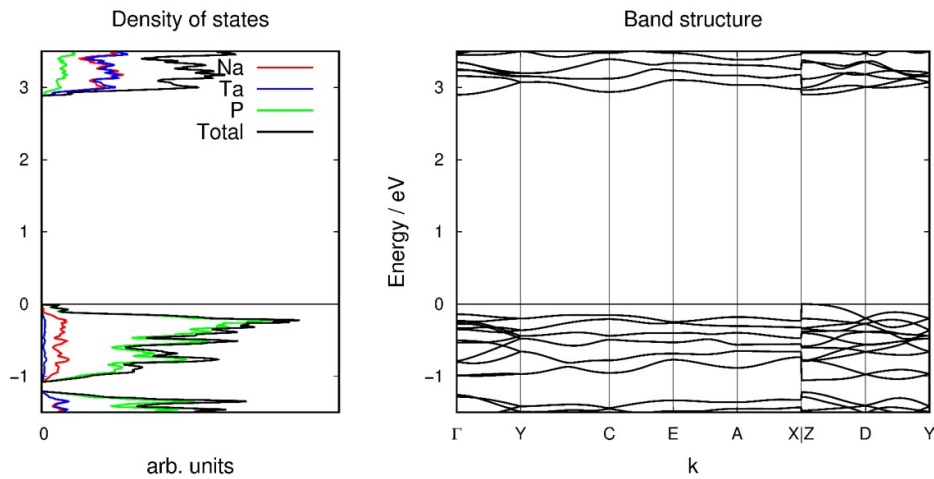


Figure 9.4: Density of states and band structure of Na_7TaP_4 exhibiting a almost direct band gap of 2.9 eV. The Fermi level is located at 0 eV.

Raman spectroscopy

The compound was investigated by raman spectroscopy and to confirm and assign the observed signals raman intensities were calculated. The experimental and calculated data is presented in Figure 9.5 and Table 9.7. Both spectra are in very good agreement and confirm the experimentally found structure with isolated TaP_4 tetrahedra. The most intense signal can be assigned to the symmetric stretching of the tetrahedra. In general vibrations between 300 cm^{-1} and 400 cm^{-1} are different modes of TaP_4 and below vibrations modes of Na also occur.

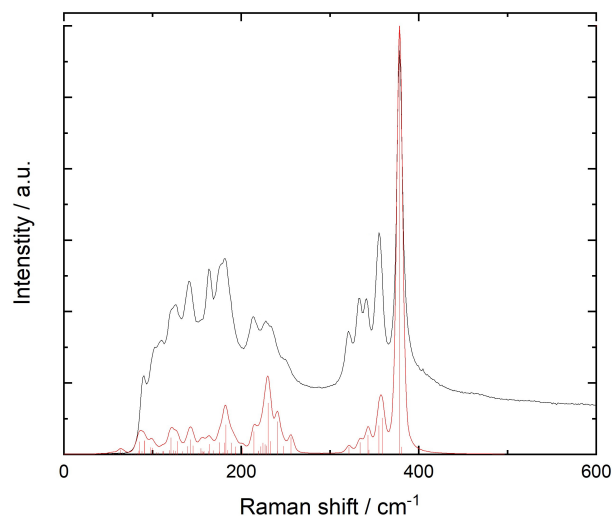


Figure 9.5: Experimental (black) and calculated (red) Raman spectrum for Na_7TaP_4 .

Table 9.7: Wavenumbers of the calculated and observed main vibration modes of the raman spectrum of Na_7TaP_4 . Additionally, associated assignment of the vibrational modes of the TaP_4 tetrahedra. All intensities are given in relative intensities a. u.

Exp. frequency / cm^{-1} (intensity / a.u.)	Calc. frequency / cm^{-1} (intensity / a.u.)	Mode symmetry	Vibration mode
378 (10)	378 (10)	A_g	symmetric stretch
355 (5.5)	355 (0.6) + 359 (0.8)	$B_g + A_g$	bending + asymmetric stretch
341 (3.9)	343 (0.5)	B_g	asymmetric stretch
333 (3.9)	334 (0.3)	A_g	asymmetric stretch
321 (3.0)	321 (0.2)	A_g	asymmetric stretch
228 (3.3)	230 (1.2)	A_g	wagging + bending
214 (3.4)	214 (0.5)	A_g	twisting
181 (4.9)	182 (0.7)	A_g	wagging + bending
164 (4.5)	164 (0.2)	A_g	rocking + wagging
141 (4.3)	143 (0.3)	A_g	twisting

9.4 The Compound $\text{KBi}\cdot\text{NH}_3$

In the following section the compound $\text{KBi}\cdot\text{NH}_3$ synthesized and characterized by **K. Mayer** are discussed. All experimental work was carried out by **K. Mayer**, whereas the computational analysis was performed by **J. Dums**. A brief summary of synthesis, characterization and structure description based on K. Mayers work is given in the beginning.^[32]

9.4.1 Experimental Part

This part was carried out and evaluated by K. Mayer.

Synthesis and Characterization

All reactions and manipulations were performed under a purified argon atmosphere using standard SCHLENK and glove box techniques. The compound $\text{KBi}\cdot\text{NH}_3$ was synthesized using K_5Bi_4 , Ph_2Zn and 18-crown-6 as starting materials. 2 mL of sodium-dried ammonia were added to the starting materials in a SCHLENK tube. The tube was subsequently stored at $-70\text{ }^\circ\text{C}$ for four months. The structure was characterized by SC-XRD-experiments and the structure data is given in Table 9.8 and 9.9. For more information see publications of K. Mayer.^[32]

Table 9.8: Structure data of $\text{KBi}\cdot\text{NH}_3$ from SC-XRD experiments

Formula	$\text{KBi}\cdot\text{NH}_3$
Formula weight/ $\frac{g}{mol}$	265.11
Space group	Cm (no. 8)
Z	4
Unit cell parameters	$a = 5.2192\text{ \AA}$ $b = 15.3308\text{ \AA}$ $c = 5.4311\text{ \AA}$ $\beta = 90.004\text{ }^\circ$
Volume/ \AA^3	434.57
color	silver

Structure Description

The compound crystallizes in space group Cm (No. 8) and consists of ${}^1_\infty[\text{Bi}]^-$ zigzag-chains. Each Bi atom is in the center of a trigonal prism formed by K atoms. This structure is similar to the structure of CaSi . The structure is illustrated in Figure 9.6

Table 9.9: Atomic coordinates of $\text{KBi}\cdot\text{NH}_3$ from SC-XRD experiments

Atom	Wyck.	x	y	z
Bi1	4b	0.0000	0.19690	0.0000
K1	4b	0.514	0.13731	0.495
N1	2a	0.508	0.0000	0.105
H1	4b	0.4041	0.0454	0.1241
H1	2a	0.5860	0.0000	-0.0407
N2	2a	0.892	0.0000	0.498
H3	2a	1.0266	0.0000	0.4084
H4	4b	0.8250	0.0485	0.4354

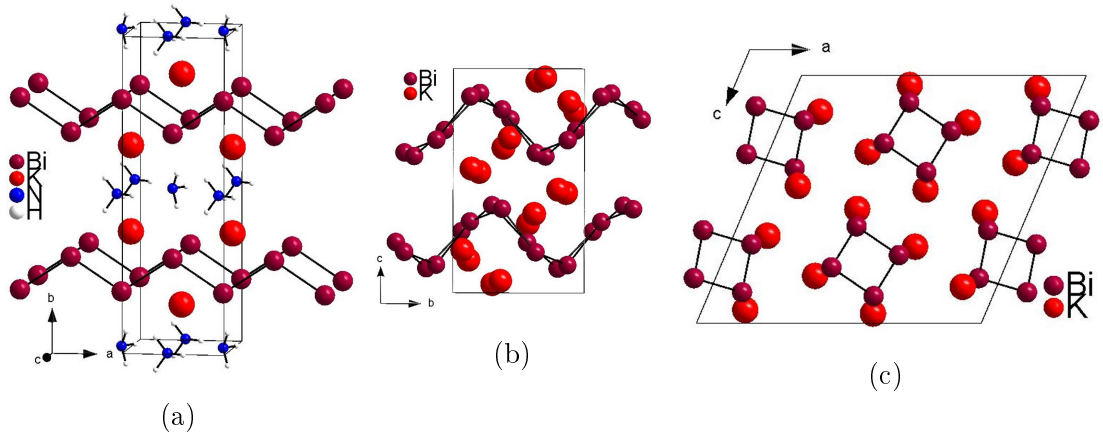


Figure 9.6: (a) Structure of $\text{KBi}\cdot\text{NH}_3$. (b) Structure of KBi along a axis. (c) Structure of KBi along b axis. Bi, K, N and H atoms are shown in ruby, red, blue and white, respectively.

9.4.2 Computational Analysis

This section describes the computational analysis carried out to support the experimental data. The calculations were carried out with crystal14 on a DFT-PBE0/TZVP and DFT-PBE/TZVP level of theory. The starting geometry was taken from experimental data shown in chapter 9.4.1. Additional computational detail are given in chapter 4. The structures were optimized within the constraints imposed by the space group symmetry.

Geometry Optimization

In this section the geometry optimization on a DFT-PBE0/TZVP level of theory are discussed.

The optimized structures show a maximum deviation of parameters of 3.63 % for

all parameters and atomic distances. In Table 9.10 the atomic distances d and cell parameters a , b and c are given with percentage deviation compared to the experimental findings. All optimized parameters are given in the appendix (Table 13.43-13.46). This shows a very good fit of the used level of theory.

The nature of a stationary point on the potential energy surface was investigated by a frequency calculation for each compound at Γ -point. Details are given in the appendix (Table 13.48 and 13.49). In case of KBi a local minimum is observed, whereas in case of $\text{KBi}\cdot\text{NH}_3$ a small imaginary frequency ($40i \text{ cm}^{-1}$) was found. A rotation of the hydrogen atoms around the nitrogen is causing this frequency and vanishes after symmetry reduction to $P1$ and subsequently optimization.

Table 9.10: Atomic distances d and cell parameters a , b and c for $\text{KBi}\cdot\text{NH}_3$ and KBi, as well as, deviation Δd from experimental data in percentages

	$d(\text{KBi}\cdot\text{NH}_3)$	$\Delta d(\text{KBi}\cdot\text{NH}_3) / \%$	$d(\text{KBi})$	$\Delta d(\text{KBi}) / \%$
a	5.1006 Å	2.27	14.0712 Å	1.07
b	15.8867 Å	3.63	7.3013 Å	0.74
c	5.3627 Å	1.26	13.3991 Å	0.16
β	88.14 °	2.07	112.15 °	0.78
Bi-Bi 1	3.10 Å	0.79	3.02 Å	1.18
Bi-Bi 2			3.03 Å	1.82
Bi-Bi 3			3.07 Å	0.17

Band Structure and Density of States (DOS)

Additionally, density of states were calculated showing a metallic character of the compound $\text{KBi}\cdot\text{NH}_3$ and a semi-conductor for KBi (Figure 9.8a and 9.8b). Two different functionals were used to confirm a metallic or semi-conducting character in a borderline case. PBE0 tends to overestimate the band gap, whereas PBE rather underestimates it. KBi exhibits a band gap of 1.5 eV (PBE0) and 0.5 eV (PBE).

The question arises, if the metal-

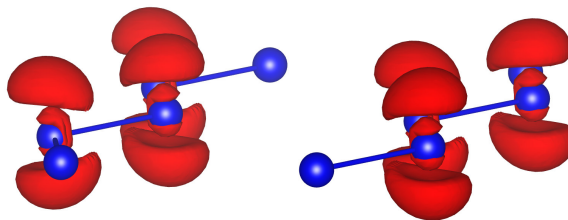


Figure 9.7: Band projected electron density of the energetically highest band located below the Fermi level of $\text{KBi}\cdot\text{NH}_3$ showing a p_z orbital type character. Bi is shown as blue spheres, the electron density with iso-value 0.006 is shown in red.

lic character only occurs due to the ${}^1_{\infty}[\text{Bi}]^-$ zigzag-chains. To investigate this case band structure along \vec{a} , \vec{b} and \vec{c} in real space were calculated (Figure 9.8c). The band structure shows metallic character along the direction of the chain and perpendicular to the chain along the c axis, whereas a band gap exists in direction of b perpendicular to the layers, turning this compound into an anisotropic metal. In the orbital projected density of states shown in the appendix (Figure 13.42 and 13.43) the major participation of the Bi p orbitals is shown at the fermi level. Specifically, the p_z orbital has a big impact at the fermi level, which is also confirmed by a band projected density matrix shown in Figure 9.7.

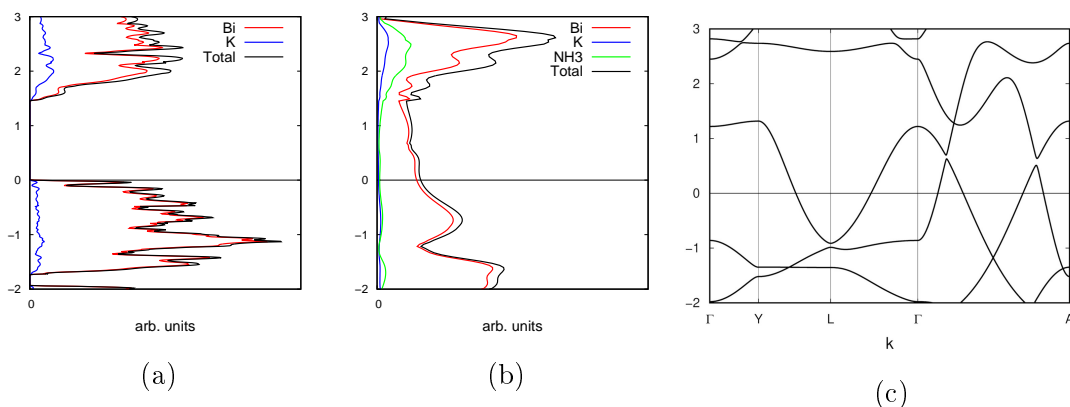


Figure 9.8: Density of States (DOS) and band structure in the energy range of 2 to 3 eV (0 eV is set for the Fermi level and marked by a horizontal line) based on the PBE0 functional. (a) DOS of KBi, atom projection is shown in red for Bi and blue for K. (b) DOS of KBi·NH₃. Atom projection is shown in red for Bi, blue for K, and green for NH₃. (c) Band structure of KBi·NH₃. The path $\Gamma \rightarrow A$ corresponds to the a direction along the Bi chain, the paths $\Gamma \rightarrow Y$ and $Y \rightarrow L$ to the b and c direction, respectively.

9.5 The Anion $[\text{SnBi}_3]^{5-}$

In the following section the molecule $[\text{SnBi}_3]^{5-}$ synthesized and characterized by **K. Mayer** is discussed. All experimental work was carried out by **K. Mayer**, whereas the computational analysis was performed by **J. Dums**. A brief summary of synthesis, characterization and structure description based on K. Mayers work is given in the beginning.^[33]

9.5.1 Experimental Part

This part was carried out and evaluated by K. Mayer.

Synthesis and Characterization

All reactions and manipulations were performed under a purified argon atmosphere using standard SCHLENK and glove box techniques. The molecule was found in two compounds.

$K_5[SnBi_3] \cdot 9NH_3$: K_3Bi_2 , K_4Sn_9 and [2.2.2]Cryptand were mixed in a SCHLENK vessel. Liquid ammonia was condensed into the vessel turning the suspension into purple red. The vessel was stored at $-70^\circ C$ for seven months.

$K_9[K_{18} - \text{corwn} - 6] [SnBi_3]_2 \cdot 15NH_3$: K_3Bi_2 , $K_{12}Sn_{17}$ and 18-crown-6 were mixed in a SCHLENK vessel. Liquid ammonia was condensed into the vessel turning the suspension into deep-brown red. The vessel was stored at $-70^\circ C$ for four months.

The structures were characterized by SC-XRD-experiments and the structure data is given in Table 9.11. For more information see publications of K. Mayer.^[33]

The molecule $[SnBi_3]^{5-}$ found in those two compounds shows the motif of a planar trigonal coordinated Sn atom surrounded by Bi^-/Bi^{2-} anions.

Table 9.11: Structure data of $K_5[SnBi_3] \cdot 9NH_3$ and $K_9[K_{18} - \text{corwn} - 6] [SnBi_3]_2 \cdot 15NH_3$ from SC-XRD experiments

Formula	$K_5[SnBi_3] \cdot 9NH_3$	$K_9[K_{18} - \text{corwn} - 6] [SnBi_3]_2 \cdot 15NH_3$
Formula	1094.43	4804.16
weight/ $\frac{g}{mol}$		
Space group	$Pna2_1$ (no. 33)	$P\bar{1}$ (no. 2)
Z	4	2
Unit cell parameters	$a = 38.5023 \text{ \AA}$ $b = 9.7164 \text{ \AA}$ $c = 6.8765 \text{ \AA}$ $\alpha = 90^\circ$ $\beta = 90^\circ$ $\gamma = 90^\circ$	$a = 14.2409 \text{ \AA}$ $b = 17.423 \text{ \AA}$ $c = 28.055 \text{ \AA}$ $\alpha = 82.65^\circ$ $\beta = 75.297^\circ$ $\gamma = 65.877^\circ$
Volume/ \AA^3	2572.5	6143

9.5.2 Computational Analysis

This section describes the computational analysis carried out to support the experimental data. The calculations were carried out with Turbomole V7.1 on a DFT-PBE0/def2-TZVPP level of theory. The starting geometry was taken from experimental data shown in chapter 9.5.1. Additional computational detail are given in chapter 4. The structures were optimized and a continuum solvation model COSMO was applied for charge compensation. The molecules $[\text{SnBi}_3^{5-}]$ and $[\text{CO}_3^{2-}]$ were investigated and their characters of the stationary points were confirmed to be a minimum for both cases.

Geometry Optimization

The optimized parameters for both structures are given in Table 9.12. Both molecules show the symmetry of point group D_{3h} . The HOMO-LUMO gap of 2.65 eV for $[\text{SnBi}_3^{5-}]$ reveals a kinetically stable anion for the true local energetic minimum stated by frequency analysis. The Sn-Bi bond lengths and Bi-Sn-Bi angles of the optimized structure are in good agreement with the experimental findings. Since the symmetry of the anion was not restricted to D_{3h} during the optimization, a considerable π -bonding contribution of the Sn-Bi due to equal bond lengths and angles.

Table 9.12: Optimized parameters for XY_3^{n-} with $X = \text{Sn}, \text{C}$ and $Y = \text{Bi}, \text{O}$

Bond length/angle	$[\text{SnBi}_3^{5-}]$	$[\text{CO}_3^{2-}]$
X-Y / Å	2.807	1.286
Y-X-Y / °	120	120

Molecular orbital diagram

For both molecules $[\text{SnBi}_3^{5-}]$ and $[\text{CO}_3^{2-}]$ a molecular orbital diagram was established and compared due to the bonding situation. In this section the focal point is on $[\text{SnBi}_3^{5-}]$ (Figure 9.9), whereas detailed information for $[\text{CO}_3^{2-}]$ is given in the appendix (Figure 13.44).

This analogy of $[\text{SnBi}_3^{5-}]$ and $[\text{CO}_3^{2-}]$ is also shown in the analysis of the bonding situations. *HOMO-11*, *HOMO-6* and *HOMO-7* represent the three Bi-Sn σ -bonds. *HOMO-5* reflects the bonding orbital of the delocalized π -system, whereas the degenerated orbitals *HOMO-1* and *HOMO-2* correspond to non-binding orbitals (p-type lone pairs at Bi atoms). At last, the *LUMO* shows the antibonding π^* orbital. All together this shows a full analogy to $[\text{CO}_3^{2-}]$.

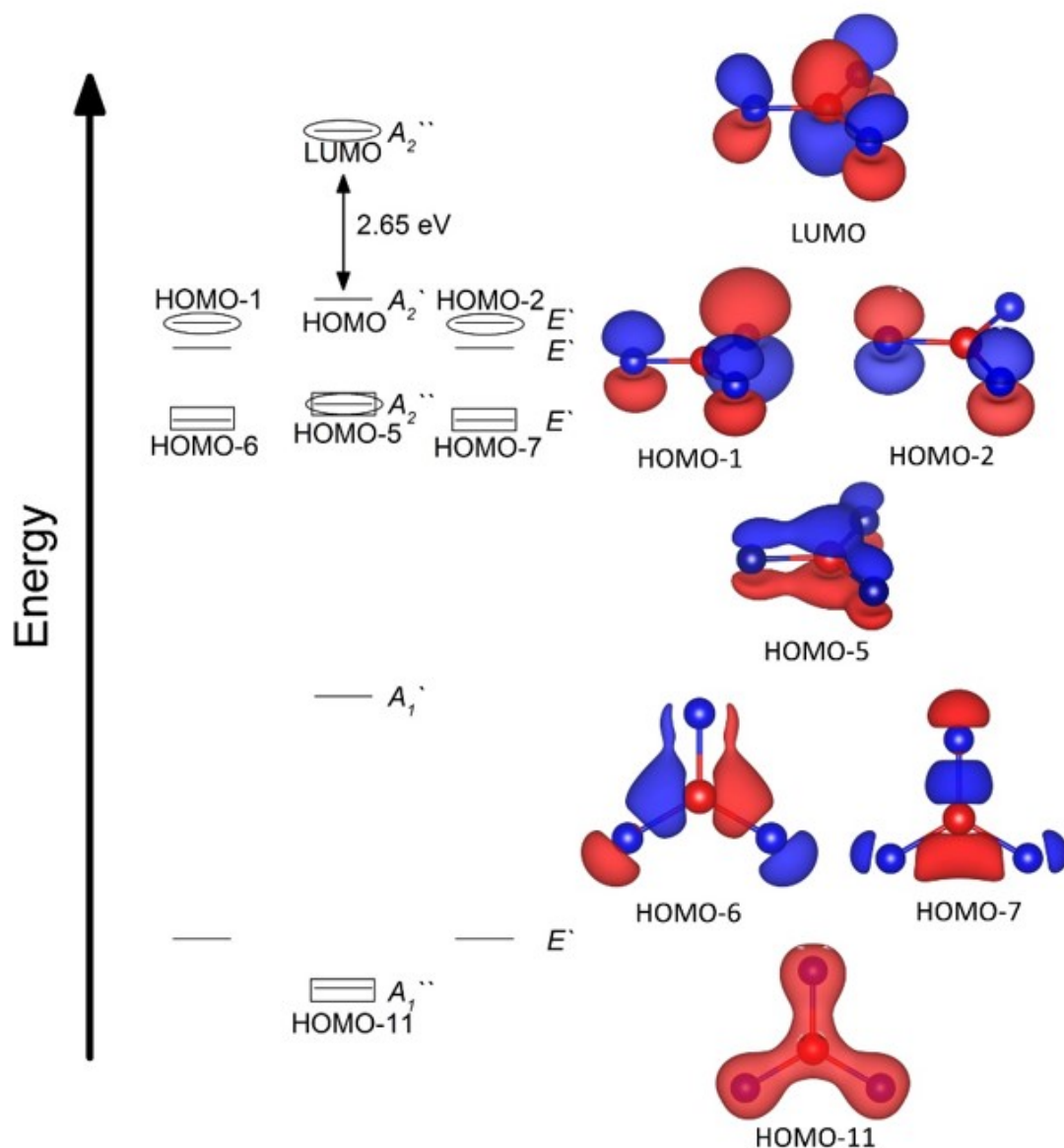


Figure 9.9: Molecular orbital diagram of $[\text{SnBi}_3]^{5-}$. The energy levels of the molecular orbitals of the π -system are marked by an ellipse and all Sn-Bi bonding-orbitals by rectangle. All highlighted molecular orbitals are shown on the right-hand side. Bi blue and Sn red spheres. The isovalue of the wave function is set to 0.04 a.u. for all orbitals.

Electron localization function (ELF) and charges

The bonding situation was also investigated by electron localization function (ELF) calculations.^[34] A single bond is characterized by a circular maximum, a double bond by two maxima above and below the molecular plane. Double bond contributions of delocalized double bonds, as in benzene, show an ellipsoidal cross section.^[35] ELF isovalue and the two-dimensional ELF cross section perpendicular to one Sn-

Bi bond vector (Figure 9.10) clearly show the typical ellipticity of a covalent bond with double-bond character. In addition, the ELF isosurface shows a monosynaptic basin of the Bi lone pairs. The AIM analysis reveals three bond critical points for the three Sn-Bi bonds with the Laplacian of the electron density ($\nabla^2\rho$) of all (3, -1) critical points being slightly negative which again is indicative of a covalent bonding. All of these critical points have the same ellipticity (ϵ) of 0.09, which corroborates the partial π -character.^[36,37] All Bi atoms are equally negatively charged according to Paboon and to the natural charges method, confirming the carbonate analogy ($-1.72 e^-$ for both methods). Sn appears with almost no charge no charge ($+0.15$ for both methods), which is in agreement with the resonance structure shown in Figure 9.11.

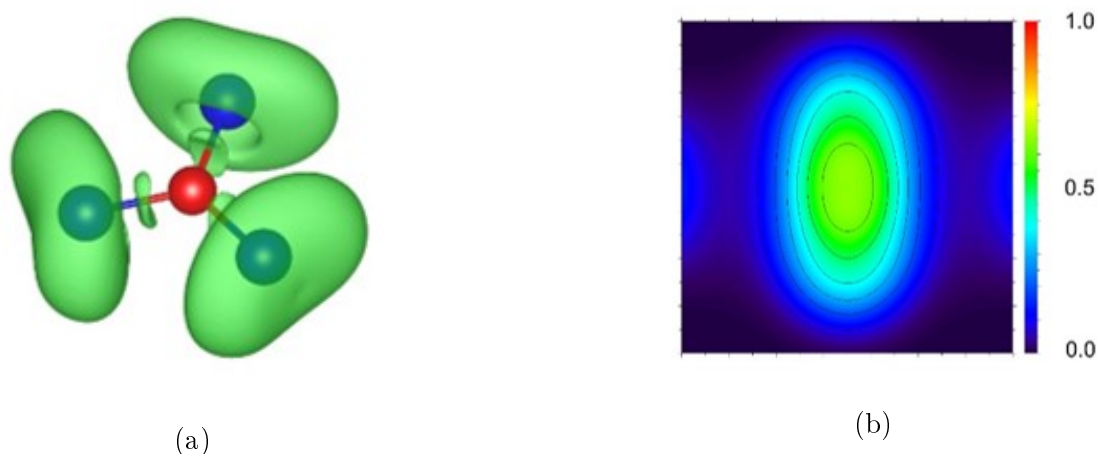


Figure 9.10: (a) 3D ELF isosurface (ELF = 0.6). The Bi atoms are blue and Sn atoms red. (b) ELF cross-section perpendicular to the Sn-Bi bond vector through the bond critical point. The elliptical shape indicates an intermediate between single and double bond as expected for a delocalized π -system. The increment of the ELF outlines is decreasing from ELF = 0.6 (inner line) with increment 0.1.

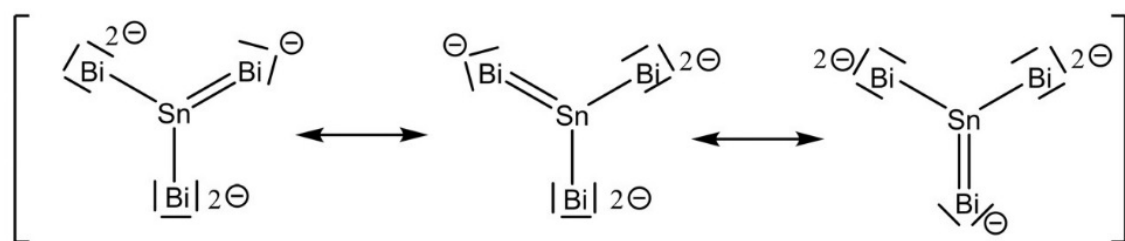


Figure 9.11: Resonance structures of the carbonate-like $[\text{SnBi}_3^{5-}]$.

References

- [1] R. Nesper, *Z. Anorg. Allg. Chem.* **2014**, *640*, 2639–2648.
- [2] R. Nesper, *Angew. Chem. Int. Ed.* **1991**, *30*, 789–817.
- [3] S. Stegmaier, T. F. Fässler, *J. Am. Chem. Soc.* **2011**, *133*, 19758–19768.
- [4] S. Stegmaier, T. F. Fässler, *Angew. Chem. Int. Ed.* **2012**, *51*, 2647–2650.
- [5] S. M. Kauzlarich, *Chemistry, Structure, and Bonding of Zintl Phases and Ions: Selected Topics and Recent Advances (Chemistry of Metal Clusters)*, Wiley-VCH Verlag, Weinheim, **1996**.
- [6] I. M. Kurylyshyn, T. F. Fässler, A. Fischer, C. Hauf, G. Eickerling, M. Presnitz, W. Scherer, *Angew. Chem. Int. Ed.* **2014**, *53*, 3029–3032.
- [7] A.-V. Mudring, J. D. Corbett, *Inorg. Chem.* **2005**, *44*, 5636–5640.
- [8] F. Emmerling, N. Längin, D. Petri, M. Kroeker, C. Röhr, *Z. Anorg. Allg. Chem.* **2004**, *630*, 171–178.
- [9] A. F. Holleman, N. Wiberg, *Lehrbuch der Anorganischen Chemie*, 102nd ed., Walter de Gruyter-Verlag, Berlin, **2007**.
- [10] A. Hershaft, J. D. Corbett, *Inorg. Chem.* **1963**, *2*, 979–985.
- [11] B. Krebs, M. Hucke, C. J. Brendel, *Angew. Chem. Int. Ed.* **1982**, *21*, 445–446.
- [12] B. Krebs, M. Mummert, C. Brendel, *J. Less-Common Met.* **1986**, *116*, 159–168.
- [13] F. Gascoin, S. C. Sevov, *Inorg. Chem.* **2001**, *40*.
- [14] N. Längin, D. Petri, M. Kroeker, C. Röhr, *Z. Anorg. Allg. Chem.* **2004**, *630*, 171–178.
- [15] A. Cisar, J. D. Corbett, *Inorg. Chem.* **1977**, *16*, 2482–2487.
- [16] A. N. Kuznetsov, T. F. Fässler, *Z. Anorg. Allg. Chem.* **2002**, *628*, 2537–2541.
- [17] C. Hoch, M. Wendorff, C. Röhr, *Acta Crystallogr. Sect. C* **2002**, *58*, i45–i46.
- [18] U. Friedrich, N. Korber, *ChemistryOpen* **2016**, *5*, 306–310.
- [19] U. Friedrich, M. Neumeier, C. Koch, N. Korber, *Chem. Commun.* **2012**, *48*, 10544–10546.
- [20] J. Janek, W. G. Zeier, *Nat. Energy* **2016**, *1*, 16141.
- [21] Y.-S. Hu, *Nat. Energy* **2016**, *1*, 16042.
- [22] Z. Gao, H. Sun, L. Fu, F. Ye, Y. Zhang, W. Luo, Y. Huang, *Adv. Mater.* **2018**, *30*, 1705702.

- [23] L. Toffoletti, H. Kirchhain, J. Landesfeind, W. Klein, L. van Wüllen, H. A. Gasteiger, T. F. Fässler, *Chem. Eur. J.* **2016**, *22*, 17635–17645.
- [24] H. Eickhoff, S. Strangmüller, W. Klein, H. Kirchhain, C. Dietrich, W. G. Zeier, L. van Wüllen, T. F. Fässler, *Chem. Mater.* **2018**, *30*, 6440–6448.
- [25] S. Strangmüller, H. Eickhoff, D. Müller, W. Klein, G. Raudaschl-Sieber, H. Kirchhain, C. Sedlmeier, V. Baran, A. Senyshyn, V. L. Deringer, L. van Wüllen, H. A. Gasteiger, T. F. Fässler, *J. Am. Chem. Soc.* **2019**, *141*, 14200–14209.
- [26] H. Eickhoff, L. Toffoletti, W. Klein, G. Raudaschl-Sieber, T. F. Fässler, *Inorg. Chem.* **2017**, *56*, 6688–6694.
- [27] T. M. F. Restle, C. Sedlmeier, H. Kirchhain, W. Klein, G. Raudaschl-Sieber, V. L. Deringer, L. van Wüllen, H. A. Gasteiger, T. F. Fässler, *Angew. Chem. Int. Ed.* **2019**, *n/a*, DOI 10.1002/ange.201914613.
- [28] R. Juza, W. Schulz, *Z. Anorg. Allg. Chem.* **1952**, *269*, 1–12.
- [29] R. Juza, W. Schulz, *Z. Anorg. Allg. Chem.* **1954**, *275*, 65–78.
- [30] T. M. F. Restle, J. V. Dums, G. Raudaschl-Sieber, T. F. Fässler, *Chem. Eur. J.* **2020**, *26*, 6737.
- [31] T. M. F. Restle, J. V. Dums, G. Raudaschl-Sieber, W. Klein, T. F. Fässler, *Inorganic Chemistry* **2020**, *59*, 18420–18426.
- [32] T. F. Fässler, K. Mayer, J. V. Dums, C. B. Benda, W. Klein, *Angew. Chem. Int. Ed.* **2020**, 1–7.
- [33] K. Mayer, J. V. Dums, W. Klein, T. F. Fässler, *Angew. Chem. Int. Ed.* **2017**, *56*, 15159–15163.
- [34] A. D. Becke, K. E. Edgecombe, *Chem. Phys.* **1990**, *92*, 5397–5403.
- [35] H. Grützmacher, T. F. Fässler, *Chem. Eur. J.* **2000**, *6*, 2317–2325.
- [36] R. F. W. Bader, T. S. Slee, D. Cremer, E. Kraka, *J. Am. Chem. Soc.* **1983**, *105*, 5061–5068.
- [37] S.-J. Kim, F. Kraus, T. F. Fässler, *J. Am. Chem. Soc.* **2009**, *131*, 14691478.

Computational Analysis of deltahedral Clusters

10.1 Introduction

Intermetallic phases enable a wide field of possible structures. To understand driving forces and the stability of such phases chemical concepts are used to describe the nature of those compounds. Specifically metal clusters, which represent the borderline between molecules and solid state chemistry showing the elements of a typical solid state compound as small units. A insight of the historical progress of this field is shown in chapter 5.2. In the following chapter several molecular units of intermetallic clusters with and without stabilizing ligands are investigated by computational methods.

The understanding of these clusters is challenging and several chemical concepts are trying to explain for example the bonding situation, such as valence, octet and (8- N) rules, LEWIS formula and their extension to the VSEP concept. Using this knowledge a lot of main-group element metal clusters could be explained and targeted synthesis were enabled. For typical solid state compounds like LAVES^[1,2] and FRANK-KASPAR^[3] phases, where atom size ratios are deciding, and HUME-ROTHERY^[4] phases, where valence electron concentration is the underlying rule, geometrical and electronical parameters are only considered. The introduction of molecular concepts to solid state chemistry was finally made by ZINTL and enhanced by LAVES and KLEMM.^[5,6] The concepts are closely described in chapter 1.2.1. In short this concepts uses a formal electron transfer and salt-like description. This enables the application of the (8- N) rule to describe oligo- or polymeric anionic subunits. Another extension of this concept was developed by including WADE's rule for polyhedral clusters.^[7,8]

As shown the description of such intermetallic clusters is challenging and a concept matching all structures of this wide field does not exist, yet. But a mighty tool helps to explain the stability and driving forces, as well as, helps to relate those clusters

to the above mentioned concepts. This tool is computational analysis, which is performed in this thesis.

10.1.1 ZINTL phases of the type A_4E_4 , A_4E_9 and $A_{12}E_{17}$

As mentioned above ZINTL phases describe a formal electron transfer and therefore salt-like structures. In solid state three general intermetaloid clusters are known and show a broad diversity of group 14 elements and alkali metal of the general type A_4E_4 ($A = \text{Na-Cs}$; $E = \text{Si, Ge, Sn, Pb}$),^[9-12] A_4E_9 ($A = \text{Na-Cs}$; $E = \text{Ge, Sn, Pb}$)^[12-20] and $A_{12}E_{17}$ ($A = \text{Na-Cs}$; $E = \text{Si, Ge, Sn}$).^[14,19,21] These by a high temperature route accessible phases already exhibit metal clusters of the type E_4^{4-} for A_4E_4 , E_9^{4-} for A_4E_9 and E_4^{4-} and E_9^{4-} for $A_{12}E_{17}$.

These clusters are the starting point of further synthesis for more complex structures stabilized by filling the cluster void (chapter 10.1.3) or by introducing ligands (chapter 10.1.4).

10.1.2 ZINTL phases in solution

Due to their very salt-like nature ZINTL phases are soluble in polar solvents. This method enables the isolation of a variety of ZINTL ions. During the solution process other reactions are possible such as oxidative coupling, filling of cluster cavities and organic or metal based substitution. By using diverse agents like [2.2.2]-cryptand or 18-crown-6 many ZINTL ions were synthesized.^[22-24] Diverse group 14 element clusters like E_4 ^[25-27] and E_9 ^[23,28-55] clusters are accessible through solution-based synthesis, but other clusters like E_5 , E_6 , E_7 and E_{10} ($E = \text{Ge, Sn, Pb}$) can be found.^[53,56-65]

10.1.3 Endohedral Clusters

Many of those ZINTL ions offer large shell-like structures possible for hosting atoms inside. Usually those atoms are transition metals, since the space usually is very small bigger guest molecules are unlikely. The smallest shell structure possible for hosting is the E_9 unit, since the tetrahedral E_4 is way too small for inserting atoms. Nevertheless, these core-shell structures offer a variety of additional shell units. Known possible structures are for E_x $x = 9, 10, 12, 16, 17, 18$.^[66,67] Additional larger units e.g. onion-like featuring multiple shells are known. In this thesis especially endohedral E_9 units were investigated (chapter 10.2). An overview of known $[TM@E_9]^{n-}$ is given in Table 10.1.

Table 10.1: Overview of known endohedral clusters of the type $[TM@E_9]^{n-}$

$E = \text{Ge}$	$E = \text{Sn}$	$E = \text{Pb}$
$[\text{Co}@E_9]^{5-}$ ^[68]	$[\text{Ru}@E_9]^{6-}$ ^[68]	$[\text{Cu}@E_9]^{3-}$ ^[69]
$[\text{Ni}@E_9]^{3-}$ ^[70]	$[\text{Co}@E_9]^{4.68-}$ ^[71]	
	$[\text{Co}@E_9]^{4.79-}$ ^[72]	
	$[\text{Ni}@E_9]^{4-}$ ^[72]	
	$[\text{Pt}@E_9]^{3-}$ ^[73]	
	$[\text{Cu}@E_9]^{3-}$ ^[69]	

10.1.4 Ligand-stabilized Clusters

Due to their very high anionic charge the discussed ZINTL ions are only soluble in very polar solvents. In order to lower the overall charge functionalization by organic ligands was carried out in several works. For example bis(trimethylsilyl)acetylene, yielding vinylated $[E_9(\text{CH}=\text{CH}_2)]^{3-}$ ($E = \text{Ge}, \text{Sn}$), $[\text{Ge}_9(\text{CH}=\text{CH}_2)_2]^{2-}$ or $[\text{CH}_2=\text{CH}-\text{Ge}_9-\text{Ge}_9-\text{CH}=\text{CH}_2]^{4-}$ clusters are known.^[74,75] Linking of two E_9 units *via* organic molecules was also already achieved ($[\text{R}-\text{Ge}_9-\text{CH}=\text{CH}-\text{CH}=\text{CH}-\text{Ge}_9-\text{R}]^{4-}$).^[76,77] But not only organic ligands were used to stabilize those ZINTL ions. Reaction with main group elements, especially Si, stabilize the cluster. The silylation reactions leads to very stable ZINTL ions compared to bare clusters. Additionally by lowering the total charge of the cluster the solubility in different solvents were raised and a wider field of possible solvents was achieved. A very prominent achieved silylated cluster is $[\text{Ge}_9(\text{Si}(\text{TMS})_3)_3]^-$.^[78] In chapter 10.3.1 and 10.3.2 two silylated clusters were investigated.

10.2 Bare Endohedral Clusters $TM@Tt_9$

In the following section several bare endohedral clusters synthesized and characterized by **B. Witzel** are discussed. All experimental work was carried out by **B. Witzel**, whereas the computational analysis was performed by **J. Dums**. A brief summary of synthesis and characterization based on B. Witzel work is given in the beginning.^[68]

10.2.1 $[\text{Co}@E_9]^{5-}$ and $[\text{Ru}@E_9]^{6-}$

Experimental Part

This part was carried out and evaluated by B. Witzel.

Synthesis and Characterization All reactions and manipulations were performed under a purified argon atmosphere using standard SCHLENK and glove box techniques.

$K_5Co_{0.2}Ge_9$: A binary phase of the nominal composition $CoGe$ was synthesized from elements by melting in an arc furnace. The obtained regulus consists of $CoGe$, Co_2Ge and $CoGe_2$ due to P-XRD-experiments. The sample was mixed with Ge and K yielding the stiochiometry $K_5Co_{0.2}Ge_9$ and subsequently heated in a sealed tantalum ampule up to 1000° for 8 h and afterwards lowered to 550° for another 24 h. The sample was quenched to room temperature.

$K_6[CoGe_9](OH)\cdot 16NH_3$: $K_5Co_{0.2}Ge_9$ and cryptand[2.2.2] were dissolved in liquid ammonia and stored at $-42^\circ C$ for six months.

$K_4Ru_3Sn_7$: A binary phase of the nominal composition Ru_3Sn_7 was synthesized from elements by melting in an arc furnace. The obtained regulus consists of Ru_3Sn_7 and Ru_2Sn_3 due to P-XRD-experiments. The sample was mixed with K yielding the stiochiometry $K_4Ru_3Sn_7$ and subsequently heated in a sealed tantalum ampule up to 1000° for 6 h and afterwards lowered to 600° for another 120 h. The sample was slowly cooled down to room temperature.

$[K_7(OH)]RuSn_9\cdot 10NH_3$: $K_5Co_{0.2}Ge_9$ and 18-crown-6 were dissolved in liquid ammonia and stored at $-42^\circ C$ for two months.

The structures were characterized by SC-XRD-experiments and the structure data is given in Table 10.2. For more information see publications of B. Witzel.^[68]

In the compounds bare endohedral clusters of the type $TM@Tt_9$ are found.

Table 10.2: Structure data of $K_6[CoGe_9](OH)\cdot 16NH_3$ and $[K_7(OH)]RuSn_9\cdot 10NH_3$ from SC-XRD experiments

Formula	$K_6[CoGe_9](OH)\cdot 16NH_3$	$[K_7(OH)]RuSn_9\cdot 10NH_3$
Formula weight/ $\frac{g}{mol}$	1236.39	3260.65
Space group	$Pnma$ (no. 62)	$Pnma$ (no. 62)
Z	4	4
Unit cell parameters	$a = 25.463 \text{ \AA}$ $b = 15.7469 \text{ \AA}$ $c = 10.0509 \text{ \AA}$	$a = 36.970 \text{ \AA}$ $b = 19.700 \text{ \AA}$ $c = 10.370 \text{ \AA}$
Volume/ \AA^3	4030.1	7553

Computational Analysis

This section describes the computational analysis performed to support the experimental data. The calculations were carried out with Gaussian09 program package

on a DFT-PBE0/def2-TZVPP level of theory. The starting geometry was taken from experimental data shown in chapter 10.2.1. Additional computational detail are given in chapter 4. The structures were optimized and a continuum solvation model PCM based on water was applied for charge compensation. The molecules $[\text{Co@Ge}_9]^{5-}$, $[\text{Ru@Sn}_9]^{6-}$, $[\text{Ge}_9]^{4-}$ and $[\text{Sn}_9]^{4-}$ were investigated and the nature of a stationary point on the potential energy surface could not be fully confirmed for $[\text{Co@Ge}_9]^{5-}$ and $[\text{Ru@Sn}_9]^{6-}$ by a frequency calculation, because every small imaginary frequency ($9.0i \text{ cm}^{-1}/17.8i \text{ cm}^{-1}$) is present in each case. This can be explained by the numerical error of the PCM method, as well as, the extraordinary high charge of the clusters. HIRSHFELD and natural charges were calculated for $[\text{Co@Ge}_9]^{5-}$ and $[\text{Ru@Sn}_9]^{6-}$. For a molecular orbital diagram single point calculations of $[\text{Ge}_9]^{4-}$ and $[\text{Sn}_9]^{4-}$ in D_{3h} symmetry were carried out. For Co^- and Ru^{2-} idealized orbitals were taken to construct the MO-scheme. Additionally, Raman intensities were calculated for all filled and empty clusters.

Geometry Optimization and Population Analysis The optimized parameters for all structures are given in Table 10.3 and 10.4. Detailed structure data is given in the appendix in Table 13.51 - 13.56. Both endohedral clusters show the symmetry of point group C_{4v} , which is in line with the experimental data. Whereas the empty clusters arrange in point group D_{3h} . The HOMO-LUMO gaps of 2.89 to 4.35 eV for reveal kinetically stable anions. Especially the cluster $[\text{Ge}_9]^{4-}$ shows a huge HOMO-LUMO gap with 4.35 eV. The bond lengths of the optimized structures are in good agreement with the experimental findings with a deviation of less than 0.6 Å or 2 %. Charge distribution based on population analyses according to HIRSHFELD and natural population analyses were carried out, and both methods account for negative charges for the endohedral *TM* atoms (Table 10.5).

Molecular orbital diagram A molecular orbital (MO) diagram was build, which is represented in Figure 10.1 for both clusters. To build a reasonable MO diagram a single point calculation for the empty clusters $[\text{Ge}_9]^{4-}$ and $[\text{Sn}_9]^{4-}$ was performed in D_{3h} symmetry resulting in slightly different HOMO-LUMO gaps of compared to the C_{4v} minimum structure.

The molecular orbitals allow for a classification according to the tensor surface harmonic theory in *S*, *P*, *D*, *F*, and *G* orbitals.^[79-81] The $1S^21P^61D^{10}2S^21F^{14}2P^6$ electronic configuration with an empty $1G$ orbital as the LUMO perfectly fits the superatom model of the 40 electron clusters $[\text{E}_9]^{4-}$. The *d* orbitals of the Co^- or Ru^{2-} interact with a *D* set of the cluster representing delocalized bonds, whereas the *F* and *G* type orbitals are mainly unaffected. The alternative analysis by intrinsic bond orbitals^[82] represented in Figure 13.50 and 13.51 shows that all interactions

Table 10.3: Comparison of observed and optimized parameters of $[\text{Ge}_9]^{4-}$ and $[\text{Co@Ge}_9]^{5-}$. The structures with D_{3h} symmetry are taken from the optimized structures of the filled clusters.

	$[\text{Ge}_9]^{4-}$ ^[68] (measured)	$[\text{Ge}_9]^{4-}$ (optimized)	$[\text{Ge}_9]^{4-}$ (single point)	$[\text{Co@Ge}_9]^{5-}$ (measured)	$[\text{Co@Ge}_9]^{5-}$ (optimized)
point group	C_{4v}	C_{4v}	D_{3h}	D_{3h}	D_{3h}
HOMO-LUMO gap / eV	/	4.35	3.66	/	3.73
d(Sn-Sn) / Å	2.5780- 2.8501	2.58-2.83	2.71-2.76	2.6826- 2.8105	2.71-2.76
d(Sn-Sn) / Å	/	/	/	2.3311- 2.3735	2.35-2.36

between the TM and the cluster atoms correspond to fully delocalized multicenter bonds. Additional details of the intrinsic bond orbitals are given in the appendix (Table 13.57 and 13.58).

Table 10.4: Comparison of observed and optimized parameters of $[\text{Sn}_9]^{4-}$ and $[\text{Ru}@\text{Sn}_9]^{6-}$. The structures with D_{3h} symmetry are taken from the optimized structures of the filled clusters.

	$[\text{Sn}_9]^{4-}$ ^[68] (measured)	$[\text{Sn}_9]^{4-}$ (optimized)	$[\text{Sn}_9]^{4-}$ (single point)	$[\text{Ru}@\text{Sn}_9]^{6-}$ (measured)	$[\text{Ru}@\text{Sn}_9]^{6-}$ (optimized)
point group	C_{4v}	C_{4v}	D_{3h}	D_{3h}	D_{3h}
HOMO-LUMO gap / eV	/	3.52	2.98	/	2.89
d(Sn-Sn) / Å	2.9346- 3.2245	2.96-3.22	3.09-3.14	3.0512- 3.1409	3.09-3.14
d(Sn-Sn) / Å	/	/	/	2.6120- 2.7173	2.66-2.69

Table 10.5: Hirshfeld, natural, and Mulliken charges of $[\text{Co}@\text{Ge}_9]^{5-}$ and $[\text{Ru}@\text{Sn}_9]^{6-}$

	$[\text{Co}@\text{Ge}_9]^{5-}$		
	HIRSHFELD	Natural charges	MULLIKEN
Average Ge	-0.50	-0.16	-0.67
Co	-0.53	-3.56	1.07
	$[\text{Ru}@\text{Sn}_9]^{6-}$		
	HIRSHFELD	Natural charges	MULLIKEN
Average Sn	-0.64	-0.3	-0.47
Ru	-0.25	-3.32	-1.73

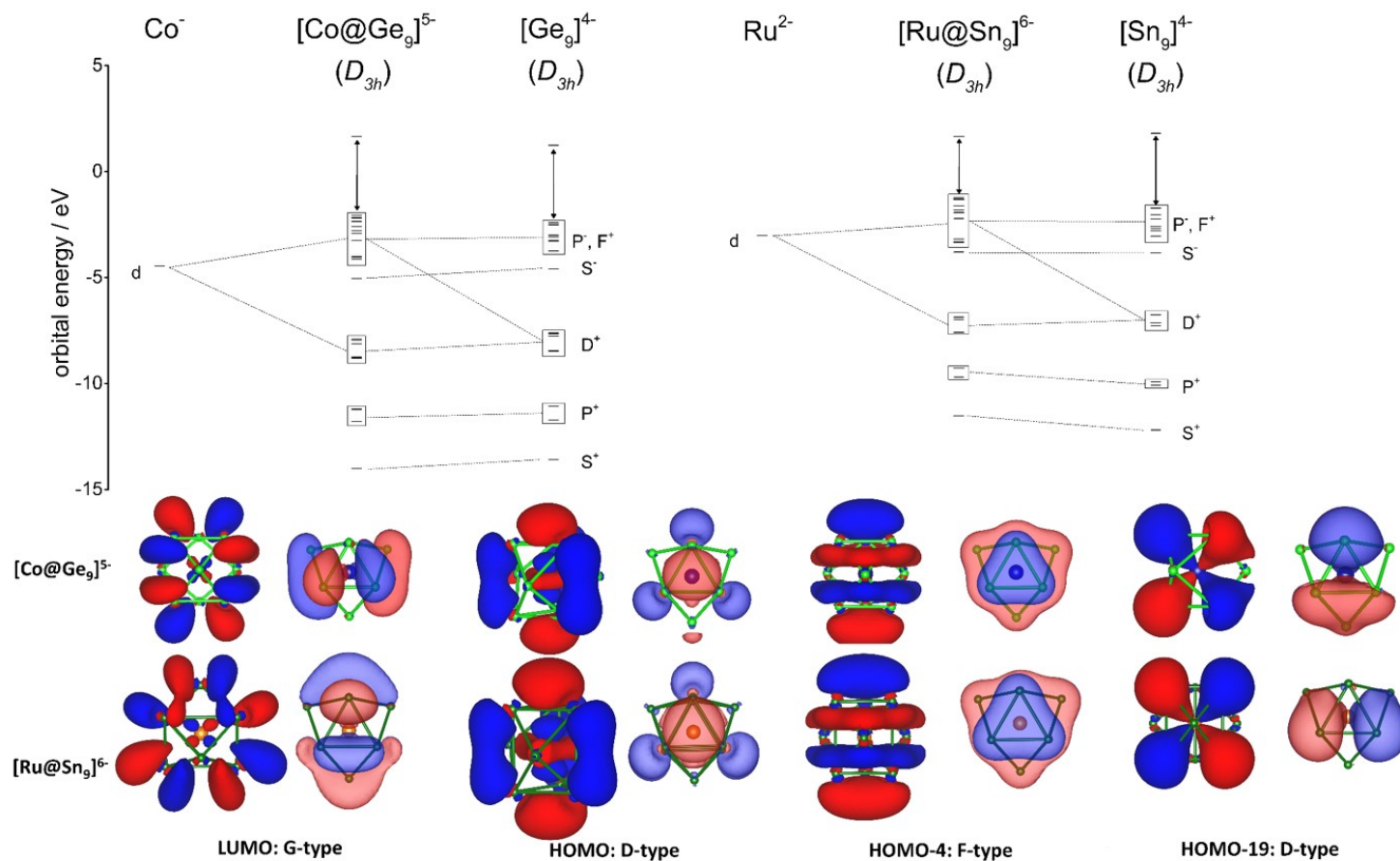


Figure 10.1: Molecular orbital interaction diagram of $[\text{Co@Ge}_9]^{5-}$ in fragments of Co^- and $[\text{Ge}_9]^{4-}$ (D_{3h} symmetry) and of $[\text{Ru@Sn}_9]^{6-}$ in fragments of Ru^{2-} and $[\text{Sn}_9]^{4-}$ (D_{3h} symmetry). Important contributions are indicated by dashed lines of both molecular orbital interaction diagrams. Relevant molecular orbitals of $[\text{Co@Ge}_9]^{5-}$ and $[\text{Ru@Sn}_9]^{6-}$ with iso-values 0.025 and 0.02, respectively. Each orbital shows a specific shape of D, F, and G orbital type.

Raman analysis The formation of such clusters is most intriguing, however, experimental data are scarcely reported.^[83–86] Generally two possible ways for the formation of such endohedral clusters have to be considered:

- during a solid-state reaction
- by an intermediate cluster opening step in solution

To investigate these two possibilities one has to find out, if those clusters already exist in the solid state phase. To detect such filled clusters in alloys, which are solely characterized by a crude phase assignment, we applied Raman spectroscopy for the first time. Owing to the absence of experimental data of such alloys, Raman frequencies calculated from the molecular anions $[\text{Co}@\text{Ge}_9]^{5-}$ and $[\text{Ru}@\text{Sn}_9]^{6-}$ were used as a reference. In case of the empty clusters, a close accordance with an acceptable error of 5 %^[87] is observed between the measured^[88,89] and the simulated data. Even though more complex phonon modes must be considered in the solid, the strongest modes match very well the experimental data for both binary ZINTL compounds K_4Ge_9 and K_4Sn_9 and may serve as a characteristic marker for the presence of empty $[E_9]$ clusters. The main mode of the $[E_9]$ cluster is a breathing motion, that is, inflating and deflating, which is observed at 220 cm^{-1} for $[\text{Ge}_9]$ and 146 cm^{-1} for $[\text{Sn}_9]$. According to DFT calculations these modes are shifted to higher wavenumbers by about 25 cm^{-1} for $[\text{Co}@\text{Ge}_9]^{5-}$ and 40 cm^{-1} for $[\text{Ru}@\text{Sn}_9]^{6-}$, if the endohedral species is present. The characteristic modes of filled clusters, however, are those which include the central atom. The vibrations of the discrete cluster anions correspond to the modes A and B in the regions 360 and 260 cm^{-1} , respectively. Fortunately these vibrations appear in a region where none of the related compounds shows any other modes,^[88,90,91] and thus it can be considered as an evidence for the presence of the filled clusters in the solid-state precursors.

10.2.2 Raman Studies of other Bare Endohedral Clusters of the type $TM@Tt_9$

Raman analysis by computational methods were carried out for other endohedral clusters of the type $TM@Tt_9$ ($TM = \text{Ni, Rh, Pd}$; $Tt = \text{Ge, Sn}$) with the same computational method. To sum up the data a shift of the main signal occurs by filling the clusters and new characteristic modes appear like shown in Figure 10.2 on the left bottom (A and B). This offers a technique to detect endohedral clusters in solid state phases. in Table 10.6 the results of main mode and characteristic modes compared to experimental data is summarized.

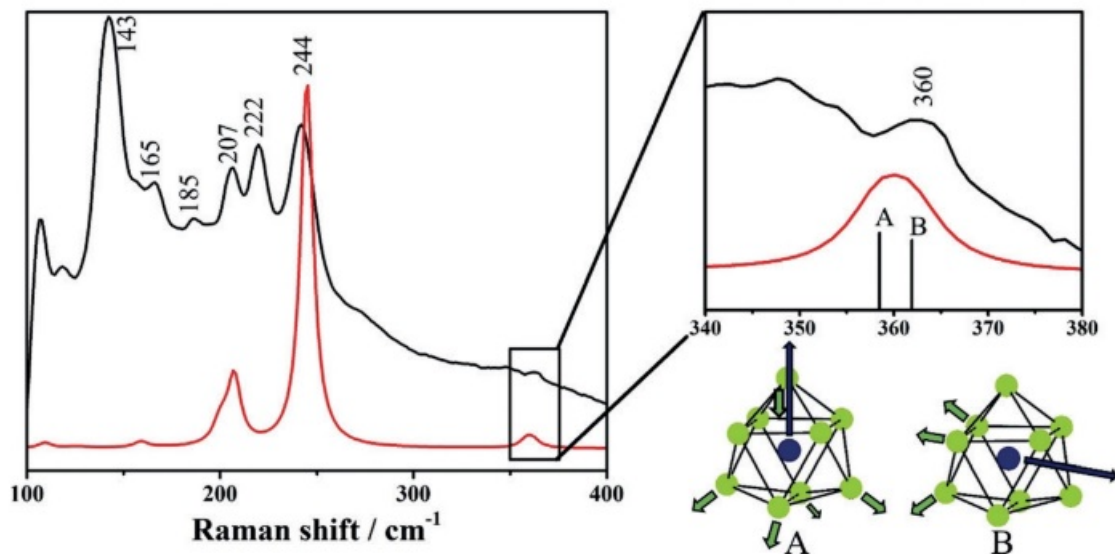


Figure 10.2: The Raman spectrum of the precursor $K_5Co_{1.2}Ge_9$ (black lines) and the calculated Raman spectrum of $[Co@Ge_9]^{5-}$ (red lines); the enlarged section shows the resonances of the vibration modes "A" and "B".

Table 10.6: Main signals and characteristic modes of endohedral cluster $TM@Tt_9$ ($TM = Ni, Rh, Pd$; $Tt = Ge, Sn$). Raman shifts of the $[Pd@Sn_9]^{4-}$ cluster are treated with a scale factor of 1.04

Endohedral Cluster	Main signal / cm^{-1} (calc.)	Main signal / cm^{-1} (exp.)	Characteristic signal / cm^{-1} (calc.)
$[Co@Ge_9]^{5-}$	245	242	358, 361, 398
$[Ni@Ge_9]^{4-}$	240	238	330, 334, 371
$[Ru@Sn_9]^{6-}$	175	181	265, 266, 286
$[Rh@Sn_9]^{5-}$	174	173	244, 245, 268
$[Pd@Sn_9]^{4-}$	173	175	228, 230, 255

10.3 Ligand-stabilized Ge/Si-Clusters

10.3.1 The Molecule $[(Ge_9\{Si(TMS)_3\}_2)^tBu_2P$

In the following section several bare endohedral clusters synthesized and characterized by **F. Geitner** are discussed. All experimental work was carried out by **F. Geitner**, whereas the computational analysis was performed by **J. Dums**. A brief summary of synthesis and characterization based on F. Geitner work is given in the beginning.^[92]

Experimental Part

This part was carried out and evaluated by F. Geitner.

Synthesis and Characterization All reactions and manipulations were performed under a purified argon atmosphere using standard SCHLENK and glove box techniques.

$[(\text{Ge}_9(\text{Si}(\text{TMS})_3)_2)^t\text{Bu}_2\text{P}]\text{Cu}(\text{NHC}^{\text{Dipp}})$: $\text{K}_2[\text{Ge}_9(\text{Si}(\text{TMS})_3)_2]$ was mixed with a solution of ${}^t\text{Bu}_2\text{PCl}$ in MeCN. After 30 min a solution of $\text{NHC}^{\text{Dipp}}\text{CuCl}$ in MeCN was added. The supernatant solution was filtered off, and the solid was washed with MeCN. Afterwards the solid was dissolved in toluene and filtered. Toluene was removed and the remaining solid was washed with hexane.

The structures were characterized by SC-XRD-experiments and the structure data is given in Table 10.7. For more information see publications of F. Geitner.^[92]

Table 10.7: Structure data of $[(\text{Ge}_9(\text{Si}(\text{TMS})_3)_2)^t\text{Bu}_2\text{P}]\text{Cu}(\text{NHC}^{\text{Dipp}})$ from SC-XRD experiments

Formula	$[(\text{Ge}_9(\text{Si}(\text{TMS})_3)_2)^t\text{Bu}_2\text{P}]\text{Cu}(\text{NHC}^{\text{Dipp}})$
Formula weight/ $\frac{g}{mol}$	1745.95
Space group	$P\bar{1}$ (no. 2)
Z	2
Unit cell parameters	$a = 13.961 \text{ \AA}$ $b = 15.006 \text{ \AA}$ $c = 23.068 \text{ \AA}$ $\alpha = 73.93^\circ$ $\beta = 84.92^\circ$ $\gamma = 62.67^\circ$
Volume/ \AA^3	4121.3

Computational Analysis

This section describes the computational analysis carried out to support the experimental data. The calculations were carried out with Gaussian09 program package on a DFT-PBE0/def2-TZVPP level of theory. The starting geometry was taken from experimental data shown in chapter 10.3.1 for $[(\text{Ge}_9(\text{Si}(\text{TMS})_3)_2)^t\text{Bu}_2\text{P}]\text{Cu}(\text{NHC}^{\text{Dipp}})$ and from literature for $[{}^t\text{Bu}_3\text{PCu}(\text{NHC}^{\text{Dipp}})]^+$.^[93] Additional computational detail are given in chapter 4. The structures were investigated by single point calculations and a continuum solvation model PCM based on water was applied for charge

compensation. HIRSHFELD and natural charges were calculated for both molecules. Additionally, both compounds were analyzed by ELF.

The single point calculation of $[(\text{Ge}_9(\text{Si}(\text{TMS})_3)_2)^t\text{Bu}_2\text{P}]\text{Cu}(\text{NHC}^{\text{Dipp}})$ shows a significant HOMO-LUMO gap of 3.26 eV, proving its kinetic stability. The calculation of HIRSHFELD and natural charges reveals, that the positive charge situated at the Cu^+ center in $[(\text{Ge}_9(\text{Si}(\text{TMS})_3)_2)^t\text{Bu}_2\text{P}]\text{Cu}(\text{NHC}^{\text{Dipp}})$ is similar as in cationic compound $[^t\text{Bu}_3\text{PCu}(\text{NHC}^{\text{Dipp}})]^+$. Furthermore, a significantly negative overall charge of the $[\text{Ge}_9]$ cluster is found, manifesting the zwitterionic nature of $[(\text{Ge}_9(\text{Si}(\text{TMS})_3)_2)^t\text{Bu}_2\text{P}]\text{Cu}(\text{NHC}^{\text{Dipp}})$ (Table 10.8). Moreover, the calculations reveal a decrease of the positive charge situated at P upon formal replacement of an alkyl group in $[^t\text{Bu}_3\text{PCu}(\text{NHC}^{\text{Dipp}})]^+$ by the $[\text{Ge}_9]$ unit, which can also be rationalized by the lower Pauling electronegativity of Ge (2.0) compared to C (2.5).^[94]

Table 10.8: Selected charges from Hirshfeld and Natural Population Analysis for $[(\text{Ge}_9(\text{Si}(\text{TMS})_3)_2)^t\text{Bu}_2\text{P}]\text{Cu}(\text{NHC}^{\text{Dipp}})$ and $[^t\text{Bu}_3\text{PCu}(\text{NHC}^{\text{Dipp}})]^+$.

Atom	$[(\text{Ge}_9(\text{Si}(\text{TMS})_3)_2)^t\text{Bu}_2\text{P}]\text{Cu}(\text{NHC}^{\text{Dipp}})$		$[^t\text{Bu}_3\text{PCu}(\text{NHC}^{\text{Dipp}})]^+$	
	HIRSHFELD	NPA	HIRSHFELD	NPA
P1	0.08	0.41	0.16	0.85
Cu1	0.16	0.42	0.20	0.41
$[\text{Ge}_9]$ (Ge1- Ge9)	-0.33	-0.91	-	-

The ELF of compound $[(\text{Ge}_9(\text{Si}(\text{TMS})_3)_2)^t\text{Bu}_2\text{P}]\text{Cu}(\text{NHC}^{\text{Dipp}})$ and cationic complex $[^t\text{Bu}_3\text{PCu}(\text{NHC}^{\text{Dipp}})]^+$ reveals for both cases strong covalent bonds between Cu^+ and P as well as P and Ge or C, respectively (Figure 10.3).

10.3.2 The Molecule $[(\text{Si}/\text{Ge})_9\{\text{Si}(\text{TMS})_3\}_3]^-$

In the following section the molecule $[(\text{Si}/\text{Ge})_9\{\text{Si}(\text{TMS})_3\}_3]^-$ synthesized and characterized by **M. Giebel** is discussed. All experimental work was carried out by **M. Giebel**, whereas the computational analysis was performed by **J. Dums**. A brief summary of synthesis and characterization based on M. Giebel work is given in the beginning.^[95]

Experimental Part

This part was carried out and evaluated by M. Giebel.

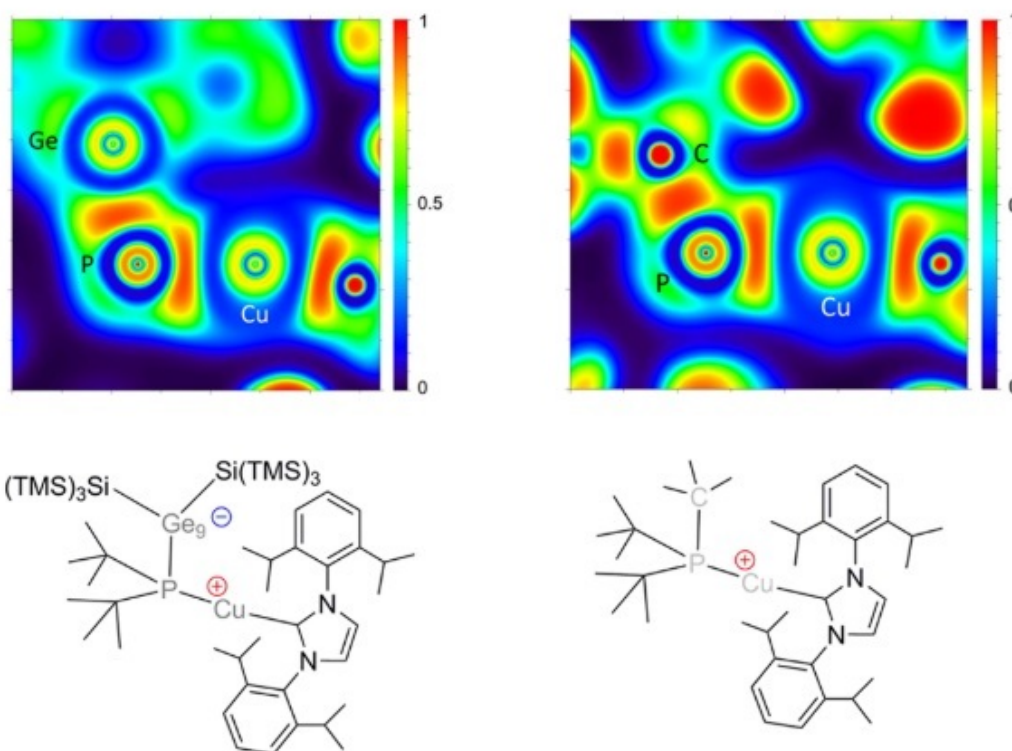


Figure 10.3: Color-filled maps of ELF representations and corresponding Lewis structures of zwitterion $[(\text{Ge}_9(\text{Si}(\text{TMS})_3)_2)^t\text{Bu}_2\text{P}]\text{Cu}(\text{NHC}^{\text{Dipp}})$ and $[^t\text{Bu}_3\text{PCu}(\text{NHC}^{\text{Dipp}})]^+$ below, respectively. ELF through the plane of Ge, P, and Cu atoms of $[(\text{Ge}_9(\text{Si}(\text{TMS})_3)_2)^t\text{Bu}_2\text{P}]\text{Cu}(\text{NHC}^{\text{Dipp}})$ as indicated by gray atoms below. ELF of $[^t\text{Bu}_3\text{PCu}(\text{NHC}^{\text{Dipp}})]^+$ through the plane of C, P, and Cu atoms as indicated by gray atoms below.

Synthesis and Characterization All reactions and manipulations were performed under a purified argon atmosphere using standard SCHLENK and glove box techniques.

$\text{K}[(\text{Si}/\text{Ge})_9(\text{Si}(\text{TMS})_3)_3]$: $\text{Si}(\text{TMS})_3\text{Cl}$ and acetonitrile were added to $\text{K}_{12}\text{Si}_{17-x}\text{Ge}_x$ ($x = 5, 9, 12, 17$). The mixture was stirred for three days and subsequently filtrated. The reaction residue was extracted with additional acetonitrile. The solvent was removed from the filtrate *in vacuo* and the residue re-dissolved in toluene. Afterwards 2.2.2-crypt was added and the solution was stored at $-32\text{ }^\circ\text{C}$ for two days.

The structures were characterized by SC-XRD-experiments and the structure data is given in Table 10.9.

Table 10.9: Structure data of $\text{K}(2.2.2\text{-crypt})[(\text{Si}_{1.68}\text{Ge}_{7.32})(\text{Si}(\text{TMS})_3)_3]$ from SC-XRD experiments

Formula	$\text{K}(2.2.2\text{-crypt})[(\text{Si}_{1.68}\text{Ge}_{7.32})(\text{Si}(\text{TMS})_3)_3]$
Space group	$P2_1/c$ (no. 14)
Z	8
Unit cell parameters	$a = 26.7403 \text{ \AA}$ $b = 24.0116 \text{ \AA}$ $c = 29.2996 \text{ \AA}$ $\beta = 113.356^\circ$
Volume/ \AA^3	17271.1

Computational Analysis

This section describes the computational analysis carried out to support the experimental data. The calculations were carried out with Turbomol V7.3 program package on a DFT-PBE0/def2-TZVP level of theory. The starting geometry was taken from experimental data shown in chapter 10.3.2 for $[(\text{Si}/\text{Ge})_9\{\text{Si}(\text{TMS})_3\}_3]^-$ and the ligand $(\text{Si}(\text{TMS})_3)$ was shortened due to computational resources. Therefore, $(\text{Si}(\text{SiH}_3)_3)$ was used as ligand instead of $(\text{Si}(\text{TMS})_3)$ and additionally the ratio of Si to Ge was set to 2:7 in the cluster resulting in a $[\text{Si}_2\text{Ge}_7(\text{Si}(\text{SiH}_3)_3)_3]^-$ cluster anion (Figure 10.4). Multipole-accelerated resolution-of-the-identity technique was used to speed up the calculations and a continuum solvation model (conductor-like screening model, COSMO) was applied for compensation of the negative charge. The structure was optimized and the character of a stationary point was investigated with harmonic frequency calculations. No imaginary frequency was found.

A HOMO-LUMO gap of 3.84 eV obtained and the optimized structure shows only minor deviations from the experimental findings, which reassures the applied method. Raman intensities were calculated for a wave length of $\lambda = 532 \text{ nm}$. The wave numbers obtained were shifted by of factor of 1.04 due to numerical deviation.^[87]

With the use of the theoretical Raman spectrum the measured spectrum was in-

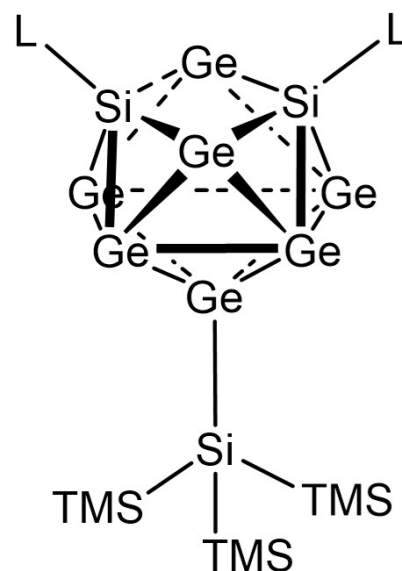


Figure 10.4: Structure of $[\text{Si}_2\text{Ge}_7(\text{Si}(\text{SiH}_3)_3)_3]^-$.

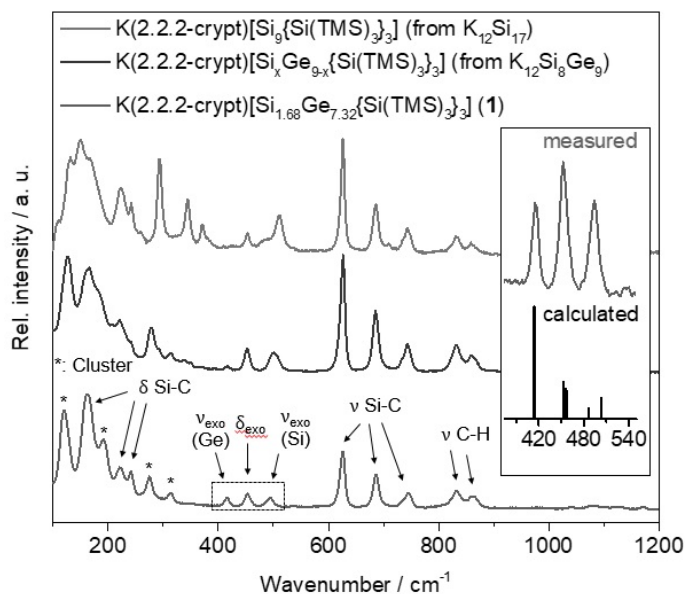


Figure 10.5: Measured and calculated Raman spectra ($\lambda = 532$ nm for $[(\text{Si}/\text{Ge})_9\{\text{Si}(\text{TMS})_3\}_3]^-$ and $[\text{Si}_2\text{Ge}_7\{\text{Si}(\text{SiH}_3)_3\}_3]^-$, respectively.

terpreted. The measured spectrum shows at various characteristic Si-C and C-H vibrations in the TMS groups of the silyl groups.^[96] Notable are the vibrations at 415 cm^{-1} , 453 cm^{-1} and 494 cm^{-1} , which are caused by the cluster. They can be assigned to bending (δ_{exo}) and stretching (ν_{exo}) modes of the cluster exo bonds towards the silyl groups. For ν_{exo} the frequencies differ slightly depending on Si (494 cm^{-1}) or Ge (415 cm^{-1}) at the cluster. This is also state by experimental work, where different ratios of Si:Ge show that for higher Si content the signal at 415 cm^{-1} is reduced and otherwise. The experimental and computational spectra are shown in Figure 10.5.

10.3.3 The Molecule $[\text{Ge}_4\text{HZn}(\text{Ph})_2]^{3-}$

In the following section the molecule $[\text{Ge}_4\text{HZn}(\text{Ph})_2]^{3-}$ synthesized and characterized by **T. Henneberger** is discussed. All experimental work was carried out by **T. Henneberger**, whereas the computational analysis was performed by **J. Dums**. A brief summary of synthesis and characterization based on T. Henneberger work is given in the beginning.^[97]

Experimental Part

This part was carried out and evaluated by T. Henneberger.

Synthesis and Characterization All reactions and manipulations were performed under a purified argon atmosphere using standard SCHLENK and glove box techniques.

$[\text{K}([\text{18}] \text{crown}-6)]_2[\text{Rb}([\text{18}] \text{crown}-6)]_2[\text{HGe}_4\text{ZnPh}_2] \cdot \text{NH}_3$ was synthesized by dissolving $\text{K}_6\text{Rb}_6\text{Ge}_{17}$, ZnPh_2 and $[\text{18}] \text{crown}-6$ in ammonia. The solution was stored at -70° for 30 months.

The structures were characterized by SC-XRD-experiments and the structure data is given in Table 10.10. Molecular units of $[\text{Ge}_4\text{HZn}(\text{Ph})_2]^{3-}$ were found in the structure.

Table 10.10: Structure data of $[\text{K}([\text{18}] \text{crown}-6)]_2[\text{Rb}([\text{18}] \text{crown}-6)]_2[\text{HGe}_4\text{ZnPh}_2] \cdot \text{NH}_3$ from SC-XRD experiments

Formula	$[\text{K}([\text{18}] \text{crown}-6)]_2[\text{Rb}([\text{18}] \text{crown}-6)]_2[\text{HGe}_4\text{ZnPh}_2] \cdot \text{NH}_3$
Space group	<i>Pbcn</i> (no. 60)
Z	4
Unit cell parameters	$a = 12.8668 \text{ \AA}$
	$b = 28.2571 \text{ \AA}$
	$c = 20.0883 \text{ \AA}$
Volume/ \AA^3	7303.7

Computational Analysis

This section describes the computational analysis carried out to support the experimental data. The calculations were carried out with Gaussian09 program package on a DFT-PBE0/def2-TZVP level of theory. The starting geometry was taken from experimental data shown in chapter 10.3.3 for the molecules $[\text{Ge}_4\text{HZn}(\text{Ph})_2]^{3-}$ and $[\text{Ge}_4\text{Zn}(\text{Ph})_2]^{4-}$. Additional computational detail are given in chapter 4. The structures were investigated by geometry optimization and a continuum solvation model PCM based on water was applied for charge compensation. The nature of a stationary point on the potential energy surface could be confirmed by a frequency calculation to be a minimum. Additionally an optimization was carried out for an apex-protonation of $[\text{Ge}_4\text{HZn}(\text{Ph})_2]^{3-}$. The problem, which had to be solved by computational chemistry, is the existence of the proton along the Ge-Ge bond and how this affects the bonding situation.

Both molecules $[\text{Ge}_4\text{HZn}(\text{Ph})_2]^{3-}$ and $[\text{Ge}_4\text{Zn}(\text{Ph})_2]^{4-}$ reveal local minimum structures and exhibit large HOMO-LUMO gaps of 4.1 eV and 3.3 eV, respectively, show-

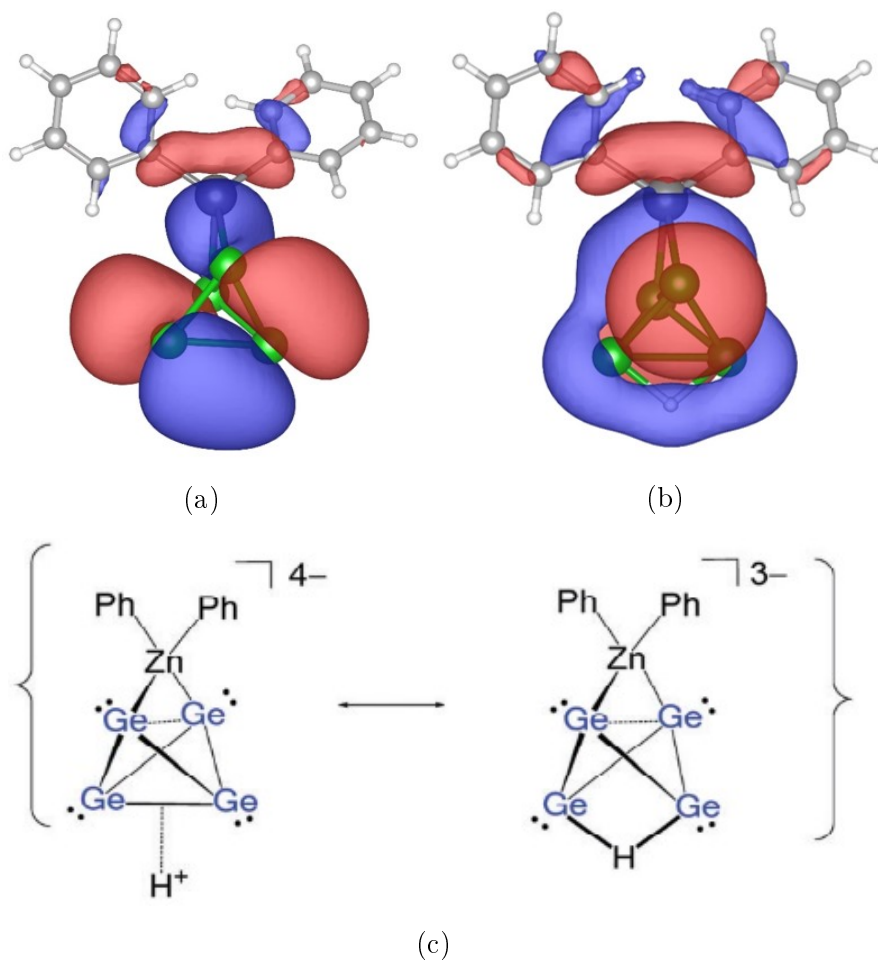


Figure 10.6: (a) Representation of the HOMO of $[\text{Ge}_4\text{Zn}(\text{Ph})_2]^{4-}$; (b) HOMO-2 of $[\text{Ge}_4\text{HZn}(\text{Ph})_2]^{3-}$; (c) resonance structure between the deprotonated $[\text{Ge}_4\text{Zn}(\text{Ph})_2]^{4-}$ and a $3c-2e$ Ge-H-Ge bond.

ing kinetically stable structures. Both minimum structures adopt C_2 symmetry, and for the protonated structure the structural parameters are in good agreement with the experimental data. The theoretical and experimental bond length Ge1-Ge1^i are in good agreement for $[\text{Ge}_4\text{HZn}(\text{Ph})_2]^{3-}$ with a deviation of only 0.7 % (exp.: 2.82 Å; comp.: 2.80 Å), whereas the calculations for the structure without a proton gives a value of 2.64 Å for the relevant Ge-Ge distance which is 6.4 % shorter than the experimental value. This argues for the existence of the proton at this position. Molecular orbitals reveal more information about the bonding situation. The HOMO of $[\text{Ge}_4\text{Zn}(\text{Ph})_2]^{4-}$ is located along the Ge-Ge edge opposing the edge coordinating the ZnPh_2 unit and allows for an interaction with an empty s orbital of a proton. As a result of the interaction with a bridging H atom the corresponding HOMO-2 of $[\text{Ge}_4\text{HZn}(\text{Ph})_2]^{3-}$ is lower in energy (0.35 eV with respect to the HOMO) and establishes the formation of a $3c-2e$ bond (Figure 10.6). A computed structure for the protonation at an apex of the Ge_4 unit in $[\text{Ge}_4\text{Zn}(\text{Ph})_2]^{4-}$ does not

lead to a local minimum as observed for P_4H^+ ,^[98,99] but transfers to the bridging position.

References

- [1] F. Stein, M. Palm, G. Stauthoff, *Intermetallics* **2004**, *12*, 713.
- [2] F. Stein, M. Palm, G. Stauthoff, *Intermetallics2* **2005**, *13*, 1056.
- [3] F. C. Frank, J. S. Kasper, *Acta Crystallogr.* **1958**, *11*, 184.
- [4] M. Ruhnow, *Cryst. Res. Technol.* **2013**, *48*, 294.
- [5] E. Zintl, *Angew. Chem.* **1939**, *52*, 1–6.
- [6] W. Klemm, *Proc. Chem. Soc.* **1959**, 329.
- [7] K. Wade, *J. Chem. Soc.* **1971**, 792–793.
- [8] R. Nesper, *Angew. Chem. Int. Ed.* **1991**, *30*, 789–817.
- [9] H. G. von Schnering, J. Llanos, J. H. Chang, K. Peters, E. M. Peters, R. Nesper, *Z. Kristallogr. - New Cryst. Struct.* **2005**, *220*, 324.
- [10] H. G. von Schnering, M. Schwarzl, J.-H. Chang, K. Peters, E.-M. Peters, R. Nesper, *Z. Kristallogr. - New Cryst. Struct.* **2005**, *220*, 525.
- [11] Y. Grin, M. Baitinger, R. Kniep, H. G. von Schnering, *Z. Kristallogr. - New Cryst. Struct.* **1999**, *214*, 453.
- [12] S. Bobev, S. C. Sevov, *Polyhedron* **2002**, *21*, 641.
- [13] A. M. Guloy, R. Ramlau, Z. Tang, W. Schnelle, M. Baitinger, Y. Grin, *Nature* **2006**, *443*, 320–323.
- [14] H. G. Von Schnering, M. Baitinger, U. Bolle, W. Carrillo-Cabrera, J. Curda, Y. Grin, F. Heinemann, J. Llanos, K. Peters, A. Schmeding, M. Somer, *Z. Anorg. Allg. Chem.* **1997** **0623**.
- [15] S. Ponou, T. F. Fässler, *Z. Anorg. Allg. Chem.* **2007**, *633*, 393–397.
- [16] V. Queneau, S. C. Sevov, *Angew. Chem. Int. Ed.* **1997**, *36*, 1754–1756.
- [17] C. Hoch, M. Wendorff, C. Röhr, *Acta Crystallogr. Sect. C* **2002**, *58*, i45–i46.
- [18] V. Queneau, S. C. Sevov, *Inorg. Chem.* **1998**, *37*, 1358–1360.
- [19] C. Hoch, M. Wendorff, C. Röhr, *J. Alloy. Compd.* **2003**, *361*, 206–221.
- [20] E. Todorov, S. C. Sevov, *Inorg. Chem.* **1998**, *37*, 3889–3891.
- [21] V. Queneau, E. Todorov, S. C. Sevov, *J. Am. Chem. Soc.* **1998**, *120*, 3263.

- [22] S. J. Gomez, D. Cheikh, T. Vo, P. Von Allmen, K. Lee, M. Wood, G. J. Snyder, B. S. Dunn, J.-P. Fleurial, S. K. Bux, *Chem. Mater.* **2019**, *31*, 4460–4468.
- [23] C. H. E. Belin, J. D. Corbett, A. Cisar, *J. Am. Chem. Soc.* **1977**, *99*, 7163–7169.
- [24] T. F. Fässler, R. Hoffmann, *Angew. Chem. Int. Ed.* **1999**, *38*, 543–546.
- [25] C. Lorenz, S. Gärtner, N. Korber, *Crystals* **2018**, *8*, 276.
- [26] K. Wiesler, K. Brandl, A. Fleischmann, N. Korber, *Z. Anorg. Allg. Chem.* **2009**, *635*, 508.
- [27] M. Waibel, T. F. Fässler, *Z. Naturforsch. B: Chem. Sci.* **2013**, 732.
- [28] S. Joseph, C. Suchentrunk, N. Korber, *Z. Naturforsch. B: Chem. Sci.* **2010**.
- [29] C. B. Benda, T. Henneberger, W. Klein, T. F. Fässler, *Z. Anorg. Allg. Chem.* **2016**, *643*, 146.
- [30] S. Joseph, C. Suchentrunk, F. Kraus, N. Korber, *Eur. J. Inorg. Chem.* **2009**, *2009*, 4641.
- [31] C. Suchentrunk, J. Daniels, M. Somer, W. Carrillo-Cabrera, N. Korber, *Z. Naturforsch. B: Chem. Sci.* **2005**, *60b*, 277.
- [32] C. Downie, J.-G. Mao, A. M. Guloy, *Inorg. Chem.* **2001**, *40*, 4721–4725.
- [33] W. Carrillo-Cabrera, U. Aydemir, M. Somer, A. Kircali, T. F. Fässler, S. D. Hoffmann, *Z. Anorg. Allg. Chem.* **2007** **0633**.
- [34] M. Somer, W. Carrillo-Cabrera, E. M. Peters, K. Peters, H. G. von Schnering, *Z. Anorg. Allg. Chem.* **1998**, *624*, 1915.
- [35] L. Diehl, K. Khodadadeh, D. Kummer, J. Strähle, *Z. Naturforsch.* **1976**, *31*, 522.
- [36] L. Diehl, K. Khodadadeh, D. Kummer, J. Strähle, *Chem. Ber.* **1976**, *109*, 3404–3418.
- [37] J. D. Corbett, P. A. Edwards, *J. Am. Chem. Soc.* **1977**, *99*, 3313–3317.
- [38] R. Hauptmann, R. Hoffmann, T. F. Fässler, *Z. Anorg. Allg. Chem.* **2001**, *627*, 2220–2224.
- [39] C. B. Benda, M. Waibel, T. Köchner, T. F. Fässler, *Chemistry* **2014**, *20*, 16738–16746.
- [40] R. Hauptmann, T. F. Fässler, *Z. Anorg. Allg. Chem.* **2002**, *628*, 1500–1504.
- [41] L. Yong, S. D. Hoffmann, T. F. Fässler, *Inorg. Chim. Acta* **2006**, *359*, 4774.
- [42] T. F. Fässler, R. Hoffmann, *J. Chem. Soc. Dalton Trans.* **1999**, 3339.

- [43] J. Campbell, D. A. Dixon, H. P. A. Mercier, G. J. Schrobilgen, *Inorg. Chem.* **1995**, *34*, 5798–5809.
- [44] V. Angilella, C. Belin, *Faraday Trans.* **1991**, *87*, 203.
- [45] R. Hauptmann, T. F. Fässler, *Z. Kristallogr. - New Cryst. Struct.* **2003**, *218*, 461–463.
- [46] T. F. Fässler, M. Hunziker, *Z. Anorg. Allg. Chem.* **1996**, *622*, 837–844.
- [47] T. F. Fässler, R. Hoffmann, *Z. Kristallogr. - New Cryst. Struct.* **2000**, *215*, 139–142.
- [48] L. Yong, S. D. Hoffmann, T. F. Fässler, *Z. Kristallogr. - New Cryst. Struct.* **2005**, *220*, 49–52.
- [49] J. M. Goicoechea, S. C. Sevov, *Inorg. Chem.* **2005**, *44*, 2654–2658.
- [50] T. F. Fässler, U. Schütz, *Inorg. Chem.* **1999**, *38*, 1866–1870.
- [51] T. F. Faessler, M. Hunziker, *Inorg. Chem.* **1994**, *33*, 5380–5381.
- [52] S. C. Critchlow, J. D. Corbett, *J. Am. Chem. Soc.* **1983**, *105*, 5715–5716.
- [53] J. M. Goicoechea, S. C. Sevov, *J. Am. Chem. Soc.* **2004**, *126*, 6860–6861.
- [54] C. Suchentrunk, N. Korber, *Inorg. Chim. Acta* **2006**, *30*, 1737–1739.
- [55] J. D. Corbett, P. A. Edwards, *J. Chem. Soc. Chem. Commun.* **1975**, 984–985.
- [56] J. Campbell, G. J. Schrobilgen, *Inorg. Chem.* **1997**, *36*, 4078–4081.
- [57] M. Somer, W. Carrillo-Cabrera, E.-M. Peters, K. Peters, M. Kaupp, H. G. von Schnering, *Z. Anorg. Allg. Chem.* **1999**, *625*, 37.
- [58] F. Hastreiter, C. Lorenz, J. Hioe, S. Gärtner, L. Nanjundappa, N. Korber, R. M. Gschwind, *Angew. Chem. Int. Ed.* **2019**, *58*, 3133.
- [59] Y. Gholiee, S. Salehzadeh, S. Khodaveisi, *New J. Chem.* **2019**, *43*, 7797.
- [60] Q. Zhang, G. Armatas, M. G. Kanatzidis, *Inorg. Chem.* **2009**, *48*, 8665–8667.
- [61] P. A. Edwards, J. D. Corbett, *Inorg. Chem.* **1977**, *16*, 903–907.
- [62] C. Liu, L.-J. Li, Q.-J. Pan, Z.-M. Sun, *Chem. Ber.* **2017**, *53*, 6315–6318.
- [63] P. Kircher, G. Huttner, K. Heinze, G. Renner, *Angew. Chem. Int. Ed.* **1998**, *37*, 1664–1666.
- [64] P. Kircher, G. Huttner, K. Heinze, G. Renner, *Angew. Chem. Int. Ed.* **1998**, *37*, 1664–1666.
- [65] A. Spiekermann, S. D. Hoffmann, T. F. Fässler, *Angew. Chem. Int. Ed.* **2006**, *45*, 3459–3462.
- [66] T. F. Fässler, S. D. Hoffmann, *Angew. Chem. Int. Ed.* **2004**, *43*, 6242–6247.

- [67] R. J. Wilson, N. Lichtenberger, B. Weinert, S. Dehnen, *Chem. Rev.* **2019**, *119*, 8506–8554.
- [68] B. J. Witzel, W. Klein, J. V. Dums, M. Boyko, T. F. Fässler, *Angew. Chem. Int. Ed.* **2019**, *58*, 12908–12913.
- [69] S. Scharfe, T. F. Fässler, S. Stegmaier, S. D. Hoffmann, K. Ruhland, *Chemistry* **2008**, *14*, 4479–4483.
- [70] J. M. Goicoechea, S. C. Sevov, *Angew. Chem. Int. Ed.* **2005**, *44*, 4026.
- [71] H. He, W. Klein, L.-A. Jantke, T. F. Fässler, *Z. Anorg. Allg. Chem.* **2014**, *640*, 2864–2870.
- [72] V. Hlukhyy, H. He, L.-A. Jantke, T. F. Fässler, *Chem. Eur. J.* **2012**, *18*, 12000.
- [73] B. Kesanli, J. E. Halsig, P. Zavalij, J. C. Fettingner, Y.-F. Lam, B. W. Eichhorn, *J. Am. Chem. Soc.* **2007**, *129*, 4567–4574.
- [74] C. B. Benda, J.-Q. Wang, B. Wahl, T. F. Fässler, *Eur. J. Inorg. Chem.* **2011**, *2011*, 4262–4269.
- [75] M. W. Hull, A. Ugrinov, I. Petrov, S. C. Sevov, *Inorg. Chem.* **2007**, *46*, 2704–2708.
- [76] M. M. Bentlohner, W. Klein, Z. H. Fard, L.-A. Jantke, T. F. Fässler, *Angew. Chem. Int. Ed.* **2015**, *54*, 3748.
- [77] S. Frischhut, M. M. Bentlohner, W. Klein, T. F. Fässler, *Inorg. Chem.* **2017**, *56*, 10691–10698.
- [78] A. Schnepf, *Angew. Chem. Int. Ed.* **2003**, *42*, 2624–2625.
- [79] A. J. Stone, *Inorg. Chem.* **1981**, *20*, 563–571.
- [80] A. J. Stone, M. J. Alderton, *Inorg. Chem.* **1982**, *21*, 2297–2302.
- [81] W. A. de Heer, *Rev. Mod. Phys.* **1993**, *65*, 611–676.
- [82] G. Knizia, *J. Chem. Theory Comput.* **2013**, *9*, 4834–4843.
- [83] S. Mitzinger, L. Broeckaert, W. Massa, F. Weigend, S. Dehnen, *Nat. Commun.* **2016**, *7*, 10480.
- [84] J.-Q. Wang, S. Stegmaier, B. Wahl, T. F. Fässler, *Chem. Eur. J.* **2010**, *16*, 1793–1798.
- [85] C. B. Benda, M. Waibel, T. F. Fässler, *Angew. Chem. Int. Ed.* **2015**, *54*, 365.
- [86] N. Lichtenberger, Y. J. Franzke, W. Massa, F. Weigend, S. Dehnen, *Chem. Eur. J.* **2018**, *24*, 12022–12030.

- [87] M. L. Laury, M. J. Carlson, A. K. Wilson, *Journal of Computational Chemistry* **2012**, *33*, 2380–2387.
- [88] H. G. Von Schnering, M. Baitinger, U. Bolle, W. Carrillo-Cabrera, J. Curda, Y. Grin, F. Heinemann, J. Llanos, K. Peters, A. Schmeding, M. Somer, *Z. Anorg. Allg. Chem.* **1997**, *623*, 1037–1039.
- [89] J. Campbell, H. P. A. Mercier, H. Franke, D. P. Santry, D. A. Dixon, G. J. Schrobilgen, *Inorg. Chem.* **2002**, *41*, 86–107.
- [90] J. Dong, O. F. Sankey, *J. Phys. Condens. Matter* **1999**, *11*, 6129–6145.
- [91] C. W. Myles, J. Dong, O. F. Sankey, C. A. Kendziora, G. S. Nolas, *Phys. Rev. B* **2002**, *65*, 235208.
- [92] F. S. Geitner, J. V. Dums, T. F. Fässler, *J. Am. Chem. Soc.* **2017**, *139*, 11933–11940.
- [93] F. Lazreg, A. M. Z. Slawin, C. S. Cazin, *J. Organometallics* **2012**, *31*, 7969.
- [94] L. Pauling, *J. Am. Chem. Soc.* **1932**, *54*, 3570.
- [95] M. Giebel, PhD thesis, **2019**.
- [96] R. E. Wochele, *Der Hypersilylrest, -Si(Si(CH₃)₃)₃, als Ligand in metallorganischen Verbindungen von Elementen der 13. und 14. Gruppe*, University Stuttgart, **2001**.
- [97] T. Henneberger, W. Klein, J. V. Dums, T. F. Fässler, *Chem. Commun.* **2018**, *54*, 12381–12384.
- [98] J.-L. M. Abboud, M. Herreros, R. Notario, M. Esseffar, O. Mo, M. Yanez, *J. Am. Chem. Soc.* **1996**, *118*, 1126.
- [99] A. Wiesner, S. Steinhauer, H. Beckers, C. Müller, S. Riefel, *Chem. Sci.* **2018**, *9*, 7169.

Part IV
Conclusion

In this thesis polar intermetallic phases were investigated by computational and experimental methods. The variety of different compounds discussed, which different physical properties, shows the versatility of these compounds. A main part of the focus was on ternary systems Li-Ge-Ni, Li-Ge-Ag and Li-Si-Ag. In these systems compounds were found showing an interesting lattice by adding Lithium and lead to promising candidates for Lithium-ion-batteries. In the system Li-Ge-Ni a layered structure was found, which intercalated Lithium. These might offer Li-mobility between the layers. In the systems Li-Ge-Ag and Li-Si-Ag a 3-D network could be observed with channels stuffed by Li. Again offering potential Li-mobility.

Additionally, further topics were investigated only by computational methods like the system Li-B. In this system the Li mobility paths in compound $\text{Li}_6\text{B}_{18}(\text{Li}_3\text{N})_x$ were investigated. Furthermore, from $\text{Li}_6\text{B}_{18}(\text{Li}_3\text{N})_x$ the theoretical compound Li_6B_{18} was derived, which is a electron-precise ZINTL-phase containing well-known $[\text{B}_6]^{2-}$ -octahedra. This means, that Li_2B_6 is a stable sublattice. Further models were derived from this structure coming up with a B-C-network B_4C_2 .

Also other solid-state-compounds were investigated due to their potential as electrolyte material. In the systems Al-P and Ga-P band structure calculations were carried out. Not only compounds containing Li were investigated. For example for Na_7TaP_4 Raman spectra were successfully simulated.

The last part of the thesis describes the transition from typical intermetallic phases through ZINTL phases towards molecular ionic clusters. For this reason KBi was compared to the solvate $\text{KBi}\cdot\text{NH}_3$, which was synthesized by a solution based route. Going further towards cluster ions $[\text{SnBi}_3]^{5-}$ could be described as an analogues to $[\text{CO}_3]^{2-}$ as an electron-precise ion only by using partial multiple bonds.

In the end typical polyanionic clusters of transition metals were studied. These clusters show a completely delocalized electronic structure, which can be described by a super atom model. Further the electronic structure of germanium clusters were calculated showing, that the charge can be decreased by adding organic ligands or hydrogen atoms.

In the following parts a brief summary of all investigated structures is given.

Substitutional Effects

11.1 Substitutional Effects in the Li-Ge Binary System by Ni

This chapter shows investigations of the phase system Li-Ni-Ge, where a new compound $\text{Li}_{14}\text{Ni}_{8+x}\text{Ge}_{9-x}$ representing the third compound in this system was synthesized. The compound features Ge-bridged rhombic dodecahedra of eight Ni atoms arranged as a cube with six capped Ge atoms. The single clusters are filled by either Ni or Ge. This cluster is the first of its kind synthesized by solid state reaction. The compound was investigated by periodic and molecular calculations. The Ni atom located at some of the cluster center positions is responsible for the metallic behavior, whereas the Ge atom the the same position stabilized the cluster shown by a large HOMO-LUMO gap. This indicated a kinetically stable cluster, but molecular calculations show, that in this configuration the cluster would like to distort the O_h -symmetry, but is prohibited by the surrounding.

Additionally, this chapter shows investigations of another phase in the phase system Li-Ni-Ge, namely $\text{LiNi}_{1+x}\text{Ge}$ ($x = 0.17$) representing the fourth compound in this system was synthesized. The compound features a Ni filled Ge-Ni double layers with intercalated Li. The compound was investigated by periodic calculations, clearly suggesting Ni to be located at the central position in the double layer. This layered structure might be interesting for electrode materials due to the layered structure, therefore, electrochemical investigations should be performed.

11.2 Substitutional Effects in the Li-Ge Binary System by Ag

Three new compounds could be synthesized and were identified by XRD-experiments: $\beta\text{-Li}_2\text{Ag}_{1-x}\text{Ge}_{1+x}$, $\alpha\text{-Li}_2\text{Ag}_{0.8}\text{Ge}_{1.2}$ and $\gamma\text{-Li}_{2.53}\text{AgGe}_2$. The compounds show the same NaTl-like structure motif. Additionally, the already known compounds α -

$\text{Li}_{2.53}\text{AgGe}_2$ and $\alpha\text{-Li}_2\text{AgGe}$, which exhibit the same motif were linked using the Bärnighausen family tree. The structures were compared to several HEUSLER- and ZINTL-phases, which led to the assumption of a not electron-precise ZINTL-phases. By using quantum chemical methods, the metallic character of all compounds could be confirmed. The driving force of building this structure could be simplified as trend to ordered structures with many heteroatomic bond combined with stabilizing Ge-subunits, like dumbbells and zig-zag-chains.

11.3 Substitutional Effects in the Li-Si Binary System by Ag

A new phase $\beta\text{-Li}_{13}\text{Ag}_5\text{Ge}_6$ could be found investigating the thermal behavior of $\alpha\text{-Li}_{13}\text{Ag}_5\text{Ge}_6$. The DSC measurement showed a possible phase transition at 497 °C. By quenching the sample at appropriate temperature the new phase was obtained and the structure was solved and refined by XRD-techniques. It shows the same structural behavior and motif as the heavier homologous in the Li-Ag-Ge phase system discussed in chapter 6.

Computational Analysis of ZINTL phases and ions

12.1 The Framework Compound $\text{Li}_6\text{B}_{18}(\text{Li}_3\text{N})_x$ hosting Li_3N and chemi-inspired B_4C_2 structures

Computational analysis reveal a semi-conducting compound $\text{Li}_6\text{B}_{18}(\text{Li}_3\text{N})$ with a band gap of 1.9 eV. The structure shows a typical host-guest behavior due to the band structure calculations. Raman calculations confirm the experimental data.

Li-Ion diffusion was simulated and showed the highest mobility in *ab* plane (**P4**; energy barrier: 20 kJ/mol), which matched NMR-measurements. Diffusion in *c* direction along the channels **A** and **B** is not favored with a high energy barrier of 350-500 kJ/mol.

Three models were derived simulating a completely guest-free structure Li_6B_{18} in space groups $P6_3/mmc$, $P\bar{6}m2$ and $P\bar{6}2m$, where $P6_3/mmc$ is the most suitable due to the total energy.

Additionally, four models in space group $P6/mmm$, $P6/m$, $P\bar{6}2m$ and $P\bar{6}m2$ were derived without containing Li at all. For charge compensation boron was substituted with carbon. All models show semiconducting behavior and the model in space group $P6/m$ is the energetically favored.

12.2 Computational Analysis of Low Dimensional Structures

Computational analysis was performed for four novel compounds and one molecule found in several compounds. For the periodic calculations band structures were evaluated after the used level of theory was stated to be appropriate by structural comparison. All structure show minor deviations compared to the optimized structures. The band gaps showed semi-conducting behavior for Li_3AlP_2 , Li_3GaP_2 and

Na_7TaP_4 contemplate as solid electrolytes. Comparing the structural related compounds Li_3AlP_2 and Li_3GaP_2 the band gap is slightly smaller for Li_3GaP_2 . In the case of Na_7TaP_4 Raman calculations were carried out, which allowed to assign the measured vibrations. Both spectra, measured and calculated, are in good accordance.

In the case of $\text{KBi}\cdot\text{NH}_3$ the band gap showed metallic behavior. The compound was compared to the semiconductor KBi , which posses the same composition despite the additional solvent molecule. Due to the solvent molecules the Bi chains form flat zigzag chains, which are related to the isovalenceelectronic compound CaSi revealing also metallic properties. The band structure shows, that the metallic properties arise along the chains and perpendicular to the chains in c direction turning the compound into an anisotropic metal.

For the molecule $[\text{SnBi}_3]^{5-}$ a molecular orbital diagram was established showing very high similarities compared to $[\text{CO}_3]^{2-}$. Additionally, ELF and AIM analysis show a double bond contributions of delocalized double bond for each Bi-Sn bond. All together this shows a full analogy to $[\text{CO}_3]^{2-}$.

12.3 Computational Analysis of deltahedral Clusters

First part of this chapter was analyzing the endohedrally filled clusters of the type $TM@Tt_9$. The two anions $[\text{Co}@Ge_9]^{5-}$ and $[\text{Ru}@Sn_9]^{6-}$ were analyzed by establish an molecular orbital diagram. The structures fit the consideration of the superatom model. Additionally, Raman calculations were carried out, which revealed two vibrations affected by the central atom. This method can due to those results be used to assure the presence of endohedrally filled clusters in general of the type $TM@Tt_9$. Secondly, three different ligand stabilized deltahedral clusters were investigated $[(\text{Ge}_9\{\text{Si}(\text{TMS})_3\}_2)^t\text{Bu}_2\text{P}, (\text{Si}/\text{Ge})_9\{\text{Si}(\text{TMS})_3\}_3]^-$ and $[\text{Ge}_4\text{HZn}(\text{Ph})_2]^{3-}$. For the first molecule the zwitterionic nature of the neutral compound was confirmed. In case of $(\text{Si}/\text{Ge})_9\{\text{Si}(\text{TMS})_3\}_3]^-$ Raman analysis were used to assign cluster exo bonds vibrations towards silyl groups clearly showing a mixed $(\text{Si}/\text{Ge})_9$ cluster. Last, a $3c - 2e$ Ge-H-Ge bond was confirmed for $[\text{Ge}_4\text{HZn}(\text{Ph})_2]^{3-}$

Appendix

13.1 Substitutional Effects in the Li-Ge Binary System by Ni

Table 13.1: Atomic coordinates and equivalent isotropic displacement parameters for $\text{Li}_{14}\text{Ni}_{8.3}\text{Ge}_{8.7}$

Atom	Wyck.	x	y	z	S.O.F.	$U_{eg}/\text{\AA}^2$
Ge1	24e	0	0.22368	0.52957	1	0.007(1)
Ge2	4a	0	0	0	0.69(9)	0.005(1)
Ni2	4a	0	0	0	0.31(9)	0.005(1)
Ge3	8c	$\frac{1}{4}$	$\frac{1}{4}$	$\frac{1}{4}$	1	0.007(1)
Ni1	32f	0.12721	0.12721	0.12721	1	0.006(1)
Li1	32f	0.37845	0.12155	0.12155	1	0.020(3)
Li2	24d	$\frac{1}{4}$	$\frac{1}{4}$	0	1	0.020(4)

Table 13.2: Interatomic distances for $\text{Li}_{14}\text{Ni}_{8.3}\text{Ge}_{8.7}$

Atom1	Atom2	Distance / \AA
Ge1	Ni1	2.4034(6)
	Ni1	2.4034(6)
	Ni1	2.4034(6)
	Ni1	2.4034(6)
	Ge2	2.6336(9)
	Li1	2.723(4)
	Li1	2.723(4)
	Li1	2.723(4)
	Li1	2.723(4)

Continued on next page

Continued from table 13.2

Atom1	Atom2	Distance / Å	
Ge2	Li2	2.95960(10)	
	Li2	2.95960(10)	
	Ni1	2.5940(9)	
	Ni1	2.5940(9)	
	Ni1	2.5940(9)	
	Ni1	2.5940(9)	
	Ni1	2.5940(9)	
	Ni1	2.5940(9)	
	Ni1	2.5940(9)	
	Ni1	2.5940(9)	
	Ni1	2.5940(9)	
	Ge3	Ge1	2.6336(9)
		Ge1	2.6336(9)
Ge1		2.6336(9)	
Ni1		2.5040(9)	
Ni1		2.5041(9)	
Ni1		2.5041(9)	
Ni1		2.5041(9)	
Li1		2.619(16)	
Li1		2.619(16)	
Li1		2.619(16)	
Ni1	Li2	2.94335(3)	
	Li2	2.94335(3)	
	Li2	2.94335(3)	
	Li2	2.94335(3)	
	Ge1	2.4034(6)	
	Ge1	2.4034(6)	
	Li2	2.5344(3)	
	Li2	2.5344(3)	
	Li2	2.5344(3)	
	Li1	2.959(10)	
	Li1	2.959(10)	
	Li1	2.959(10)	
	Li1	Li2	2.573(6)
Li2		2.573(6)	

Continued on next page

Continued from table 13.2

Atom1	Atom2	Distance / Å
Li2	Li2	2.573(6)
	Ge1	2.723(4)
	Ge1	2.723(4)
	Ge1	2.723(4)
	Li1	2.862(19)
	Li1	2.862(18)
	Li1	2.862(18)
	Ni1	2.959(10)
	Ni1	2.5344(3)
	Ni1	2.5344(3)
	Ni1	2.5344(3)
	Li1	2.573(6)
	Li1	2.573(6)
	Li1	2.573(6)
	Ge3	2.94335(3)
	Ge1	2.95960(10)
Ge1	2.95960(10)	

Table 13.3: Optimized parameters of $\text{Li}_{14}\text{Ni}_8\text{Ge}_9$ (**A**) with $a = 11.67939218$ Å

Atom	x / a	y / b	z / c
GE	0.000000000000E+00	2.351000372222E-01	-2.012943533250E-17
GE	0.000000000000E+00	0.000000000000E+00	0.000000000000E+00
GE	2.500000000000E-01	-2.500000000000E-01	-2.500000000000E-01
NI	1.220347321054E-01	1.220347321054E-01	1.220347321054E-01
LI	-1.232048588337E-01	1.232048588337E-01	-3.767951411663E-01
LI	2.500000000000E-01	2.500000000000E-01	0.000000000000E+00

Table 13.4: Optimized parameters of $\text{Li}_{14}\text{Ni}_9\text{Ge}_8$ (**B**) with $a = 11.68067171 \text{ \AA}$

Atom	x / a	y / b	z / c
GE	0.000000000000E+00	2.199656710367E-01	-1.135005288895E-20
NI	0.000000000000E+00	0.000000000000E+00	0.000000000000E+00
GE	2.500000000000E-01	-2.500000000000E-01	-2.500000000000E-01
NI	1.290489472063E-01	1.290489472063E-01	1.290489472063E-01
LI	-1.216940058753E-01	1.216940058753E-01	-3.783059941247E-01
LI	2.500000000000E-01	2.500000000000E-01	0.000000000000E+00

Table 13.5: Optimized parameters of $\text{Li}_{14}\text{Ni}_{8.25}\text{Ge}_{8.75}$ (**C**) with $a = 11.68100660 \text{ \AA}$

Atom	x / a	y / b	z / c
GE	0.000000000000E+00	2.110276771135E-01	0.000000000000E+00
GE	-5.000000000000E-01	-2.635596639708E-01	0.000000000000E+00
GE	-5.000000000000E-01	2.363702555495E-01	-5.000000000000E-01
NI	0.000000000000E+00	0.000000000000E+00	0.000000000000E+00
GE	-5.000000000000E-01	-5.000000000000E-01	0.000000000000E+00
GE	2.504832929671E-01	-2.504832929671E-01	-2.504832929671E-01
NI	1.321697751283E-01	1.321697751283E-01	1.321697751283E-01
NI	-3.794515556462E-01	-3.794515556462E-01	1.218867981298E-01
LI	-1.199445094519E-01	1.199445094519E-01	-3.739427762328E-01
LI	3.761176824077E-01	-3.761176824077E-01	-3.761176824077E-01
LI	-2.528431571447E-01	-2.528431571447E-01	0.000000000000E+00
LI	2.479751018895E-01	-2.479751018895E-01	-5.000000000000E-01

Table 13.6: Optimized parameters of $\text{Li}_{14}\text{Ni}_8\text{Ge}_8$ (**D**) with $a = 11.66728744 \text{ \AA}$

Atom	x / a	y / b	z / c
GE	-1.808467562830E-17	2.147197499238E-01	-3.610714756956E-17
GE	2.500000000000E-01	-2.500000000000E-01	-2.500000000000E-01
NI	1.297159988149E-01	1.297159988149E-01	1.297159988149E-01
LI	-1.205723843175E-01	1.205723843175E-01	-3.794276156825E-01
LI	2.500000000000E-01	2.500000000000E-01	1.169743567627E-18

Table 13.7: Optimized parameters of $\text{Li}_{14}\text{Ni}_{8.75}\text{Ge}_8$ (**E**) with $a = 11.67743928 \text{ \AA}$

Atom	x / a	y / b	z / c
GE	-9.229431722389E-56	2.150364568799E-01	0.000000000000E+00
GE	-5.000000000000E-01	-2.801005996545E-01	0.000000000000E+00
GE	-5.000000000000E-01	2.192939678406E-01	-5.000000000000E-01
NI	-5.000000000000E-01	-5.000000000000E-01	0.000000000000E+00
GE	2.501278740749E-01	-2.501278740749E-01	-2.501278740749E-01
NI	1.290316635757E-01	1.290316635757E-01	1.290316635757E-01
NI	-3.708963769148E-01	-3.708963769148E-01	1.288190958588E-01
LI	-1.211316743090E-01	1.211316743090E-01	-3.774612721192E-01
LI	3.782695986042E-01	-3.782695986042E-01	-3.782695986042E-01
LI	-2.493914513852E-01	-2.493914513852E-01	0.000000000000E+00
LI	2.496973325681E-01	-2.496973325681E-01	-5.000000000000E-01

Table 13.8: Optimized parameters of $\text{Li}_{14}\text{Zn}_8\text{Ge}_9$ (**F**) with $a = 12.44436295 \text{ \AA}$

Atom	x / a	y / b	z / c
GE	0.000000000000E+00	2.457670914564E-01	-2.012943533250E-17
GE	0.000000000000E+00	0.000000000000E+00	0.000000000000E+00
GE	2.500000000000E-01	-2.500000000000E-01	-2.500000000000E-01
ZN	1.286132220543E-01	1.286132220543E-01	1.286132220543E-01
LI	-1.179633828613E-01	1.179633828613E-01	-3.820366171387E-01
LI	2.500000000000E-01	2.500000000000E-01	0.000000000000E+00

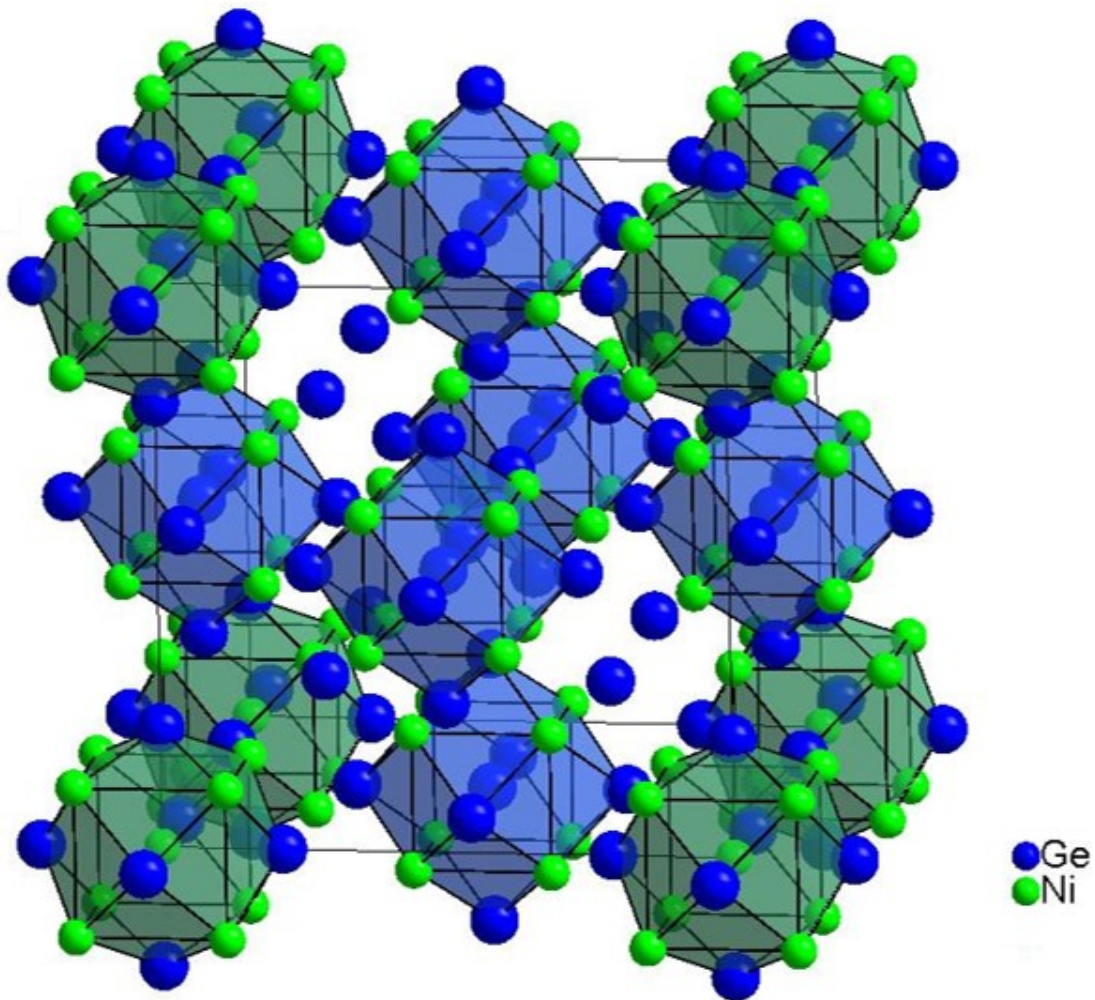


Figure 13.2: Unit cell of the $\text{Li}_{14}\text{Ni}_{8.25}\text{Ge}_{8.75}$ structural model (symmetry decreased to $Pm\bar{3}m$), Lithium atoms omitted for clarity. The blue polyhedra show the cluster unit with Ge located at the center and the green polyhedra shows the cluster unit with Ni located at the center. Ni and Ge are represented as spheres in green and blue, respectively.

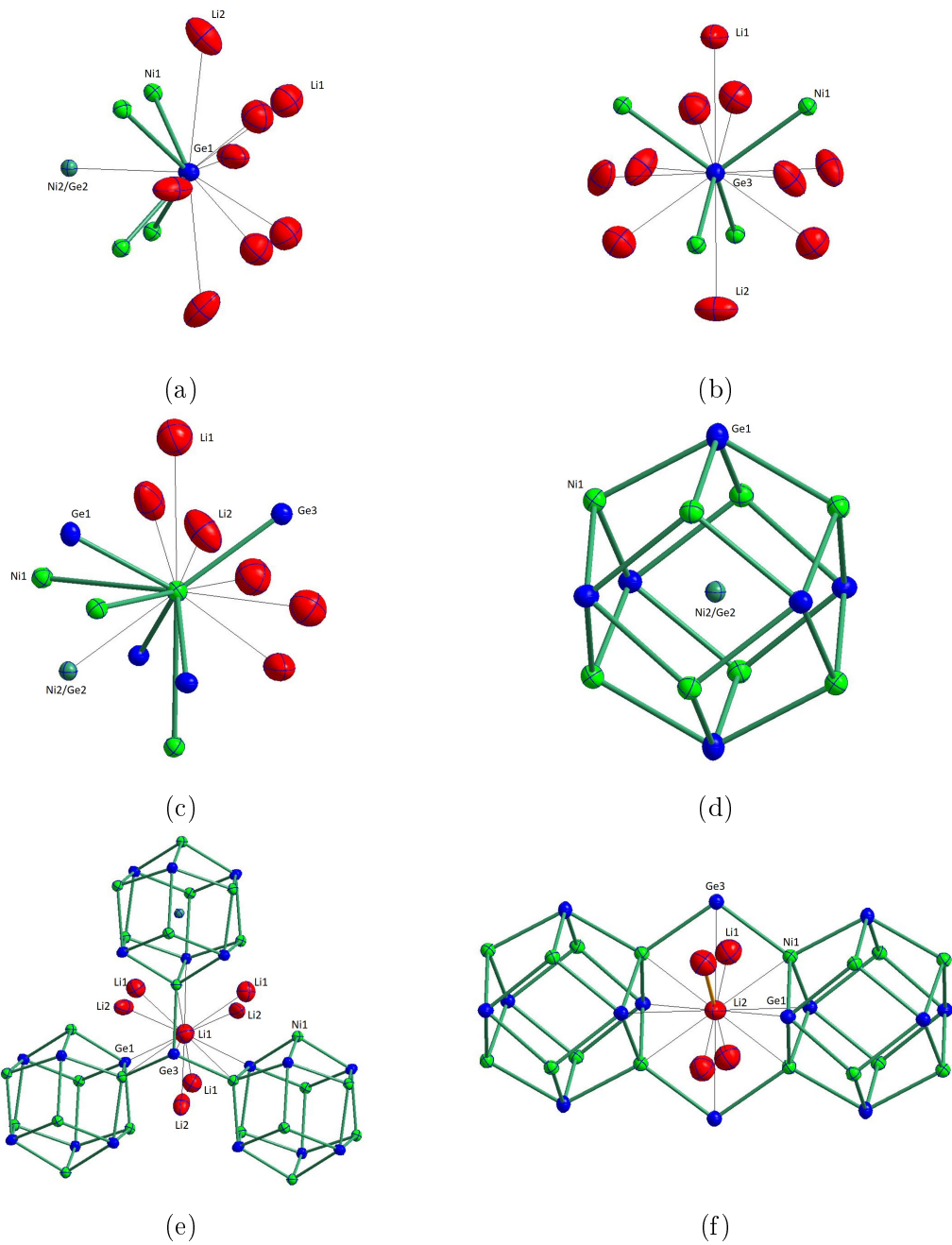


Figure 13.1: Coordination polyhedra of (a) - (b) Ge atoms (c) - (d) Ni containing atomic positions and (e) - (f) Li atoms. Li, Ni, Ni/Ge and Ge positions are shown as ellipsoids at the 90 % probability level in red, green, teal and blue respectively. Covalent bonds are marked with thick lines. Thin lines represent the coordination of Li atoms.

Table 13.9: Atomic distances (d) and cell parameter a for $\text{Li}_{14}\text{Ni}_8\text{Ge}_9$ (Ge at $X2$), $\text{Li}_{14}\text{Ni}_9\text{Ge}_8$ (Ni at $X2$) and $\text{Li}_{14}\text{Ni}_8\text{Ge}_8$ (empty $X2$), as well as, experimental data are shown in Å and as deviation (Δd) from experimental data in percentages

	$\text{Li}_{14}\text{Ni}_8\text{Ge}_9$		$\text{Li}_{14}\text{Ni}_9\text{Ge}_8$		$\text{Li}_{14}\text{Ni}_8\text{Ge}_8$		Experimental Data
	$d / \text{Å}$	$\Delta d / \%$	$d / \text{Å}$	$\Delta d / \%$	$d / \text{Å}$	$\Delta d / \%$	$d / \text{Å}$
a	11.68	-0.8	11.68	-0.8	11.67	-0.9	11.773
Ni1-Ni1	2.85	-5.0	3.01	0.3	3.03	1.0	3.00
Ni1-Ge1	2.41	0.4	2.38	-0.8	2.36	-1.7	2.40
Ni1- $X2$	2.47	-4.6	2.61	0.8	-	-	2.59
Ni1-Li2	2.55	0.8	2.5	-1.2	2.5	-1.2	2.53
Ni1-Li1	2.98	0.7	2.91	-1.7	2.92	-1.4	2.96
Li1-Li1	2.87	0.4	2.84	-0.7	2.81	-1.7	2.86
Ni1-Ge3	2.59	3.6	2.45	-2.0	2.43	-2.8	2.50

Table 13.10: Atomic distances (d) and cell parameter a for $\text{Li}_{14}\text{Ni}_{8.25}\text{Ge}_{8.75}$ and $\text{Li}_{14}\text{Ni}_{8.75}\text{Ge}_8$. One has to distinguish the different polyhedra in the structures, if Ni, Ge or no atom is located at the $X2$ position. For this reason there are two distances listed for each case related to which atom is located at the center of the Ni-cube. The data is shown in Å and as deviation (Δd) from experimental data in percentages

	$\text{Li}_{14}\text{Ni}_{8.25}\text{Ge}_{8.75}$ ($X2 = \text{Ge}$)		$\text{Li}_{14}\text{Ni}_{8.25}\text{Ge}_{8.75}$ ($X2 = \text{Ni}$)		$\text{Li}_{14}\text{Ni}_{8.75}\text{Ge}_8$ ($X2 = \text{empty}$)		$\text{Li}_{14}\text{Ni}_{8.75}\text{Ge}_8$ ($X2 = \text{Ni}$)	
	$d / \text{Å}$	$\Delta d / \%$	$d / \text{Å}$	$\Delta d / \%$	$d / \text{Å}$	$\Delta d / \%$	$d / \text{Å}$	$\Delta d / \%$
a	11.68	-0.8	11.68	-0.8	11.68	-0.8	11.68	-0.8
Ni1-Ni1	2.85	-5.0	3.09	3.0	3.01	0.3	3.01	0.3
Ni1-Ge1	2.42	0.8	2.37	-1.3	2.36	-1.7	2.38	-0.8
Ni1- $X2$	2.45	-5.4	2.67	3.1	-	-	2.61	0.8
Ni1-Li2	2.53	0.0	2.52	-0.4	2.49	-1.6	2.50	-1.2
Ni1-Li1	3.03	2.4	2.83	-4.4	2.90	-2.0	2.92	-1.4
Li1-Li1	2.80	-2.1	2.80	-2.1	2.83	-1.0	2.84	-0.7
Ni1-Ge3	2.61	4.4	2.39	-4.4	2.45	-2.0	2.45	-2.0

Table 13.11: Mulliken partial charges (e^-) of $\text{Li}_{14}\text{Ni}_8\text{Ge}_9$, $\text{Li}_{14}\text{Ni}_9\text{Ge}_8$, $\text{Li}_{14}\text{Ni}_8\text{Ge}_8$ and $\text{Li}_{14}\text{Zn}_8\text{Ge}_9$

Atom	$\text{Li}_{14}\text{Ni}_8\text{Ge}_9$	$\text{Li}_{14}\text{Ni}_9\text{Ge}_8$	$\text{Li}_{14}\text{Ni}_8\text{Ge}_8$	$\text{Li}_{14}\text{Zn}_8\text{Ge}_9$
Ge1	-0.79	-0.76	-0.58	-1.19
X2	-0.47	0.12	-	-0.19
Ge3	-0.84	-0.74	-0.75	-1.15
Ni1/Zn1	0.17	0.11	0.25	0.41
Li1	0.41	0.38	0.35	0.47
Li2	0.37	0.37	0.33	0.44

Table 13.12: Mulliken bond overlaps (e^-) of $\text{Li}_{14}\text{Ni}_8\text{Ge}_9$, $\text{Li}_{14}\text{Ni}_9\text{Ge}_8$, $\text{Li}_{14}\text{Ni}_8\text{Ge}_8$ and $\text{Li}_{14}\text{Zn}_8\text{Ge}_9$

Bond	$\text{Li}_{14}\text{Ni}_8\text{Ge}_9$	$\text{Li}_{14}\text{Ni}_9\text{Ge}_8$	$\text{Li}_{14}\text{Ni}_8\text{Ge}_8$	$\text{Li}_{14}\text{Zn}_8\text{Ge}_9$
Ni1/Zn1-Ge1	0.13	0.13	0.17	0.17
Ni1/Zn1-Ge3	0.18	0.18	0.16	0.22
Ni1/Zn1- Ni1/Zn1	0.02	0.02	0.04	0.02
X2-Ge1	0.28	-0.01	-	-0.07
X2-Ni1/Zn1	0.08	0.11	-	0.00

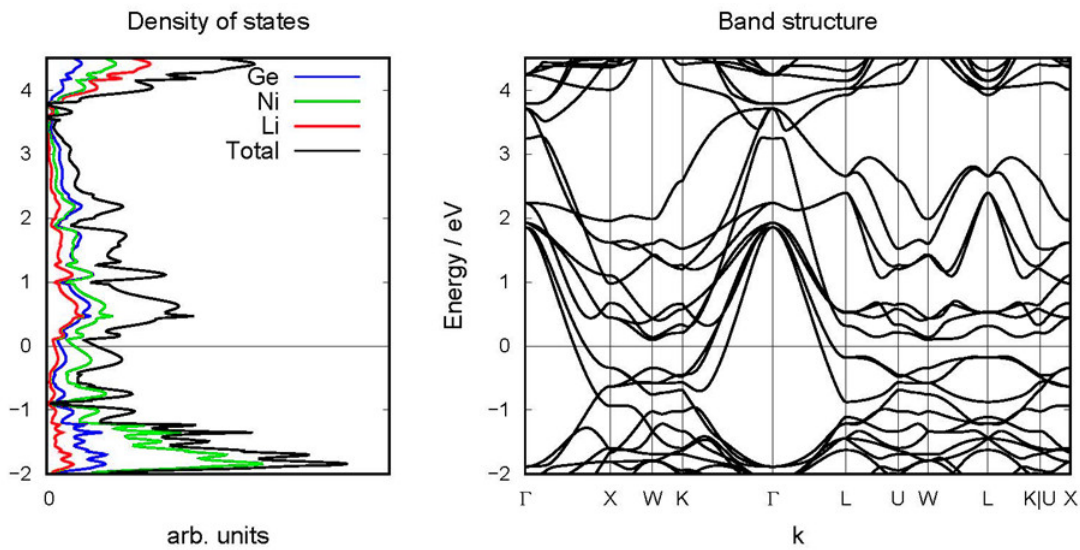


Figure 13.3: Density of States (DOS, left) and band structure (right) of $\text{Li}_{14}\text{Ni}_9\text{Ge}_8$. The Fermi level is at zero energy.

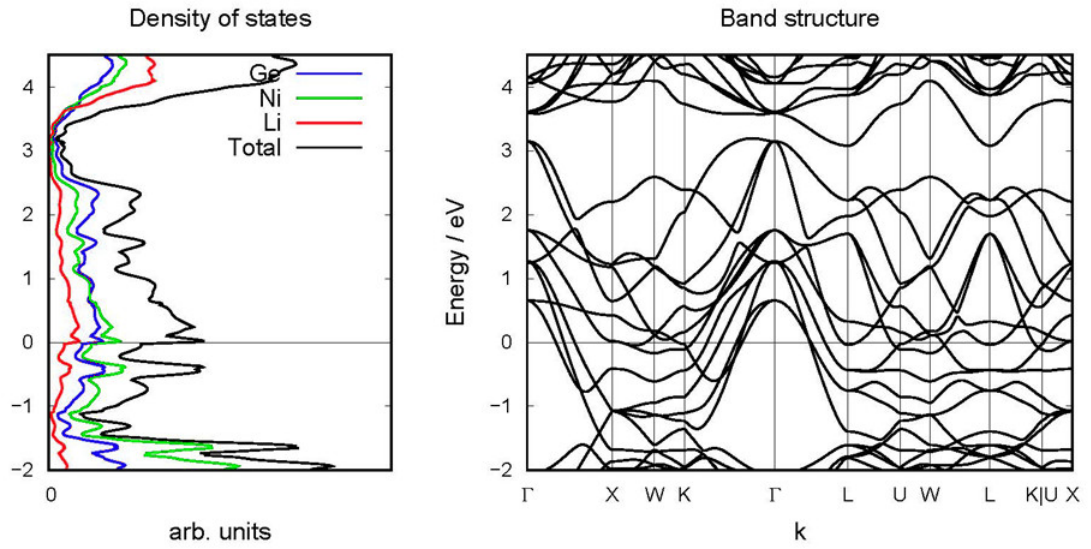


Figure 13.4: Density of States (DOS, left) and band structure (right) of $\text{Li}_{14}\text{Ni}_8\text{Ge}_9$. The Fermi level is at zero energy.

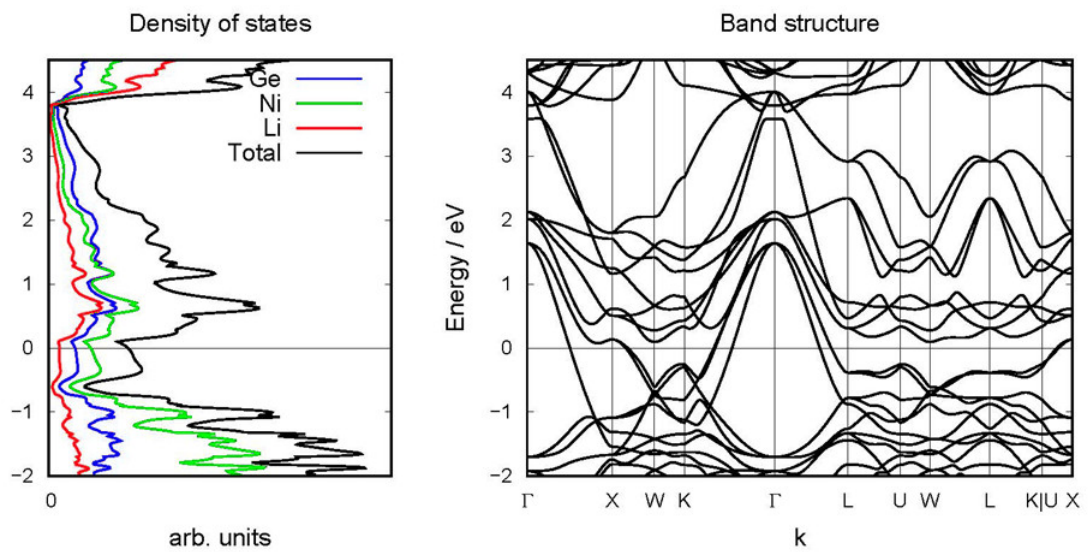


Figure 13.5: Density of States (DOS, left) and band structure (right) of $\text{Li}_{14}\text{Ni}_8\text{Ge}_8$. The Fermi level is at zero energy.

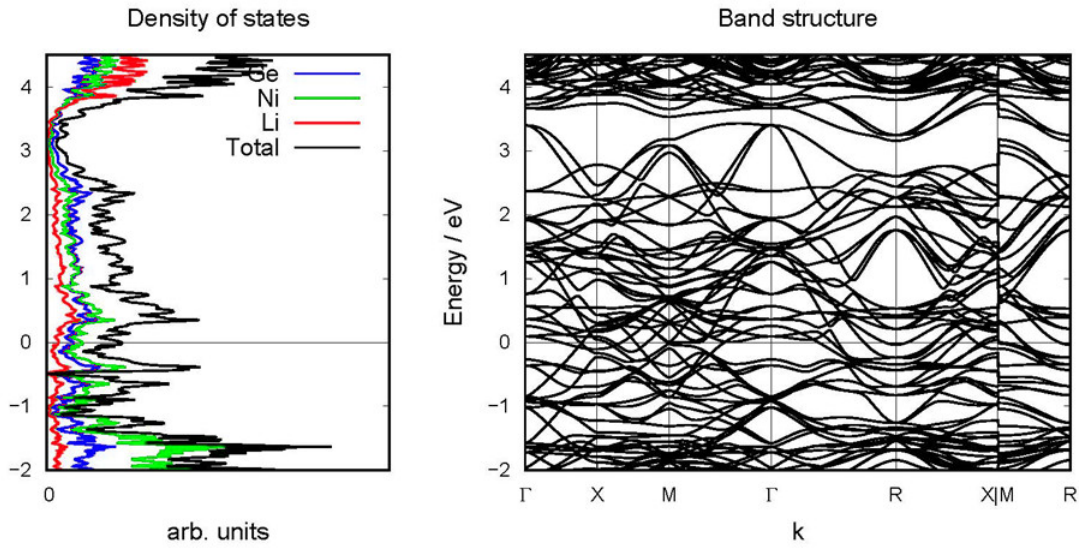


Figure 13.6: Density of States (DOS, left) and band structure (right) of $\text{Li}_{14}\text{Ni}_{8.25}\text{Ge}_{8.75}$. The Fermi level is at zero energy.

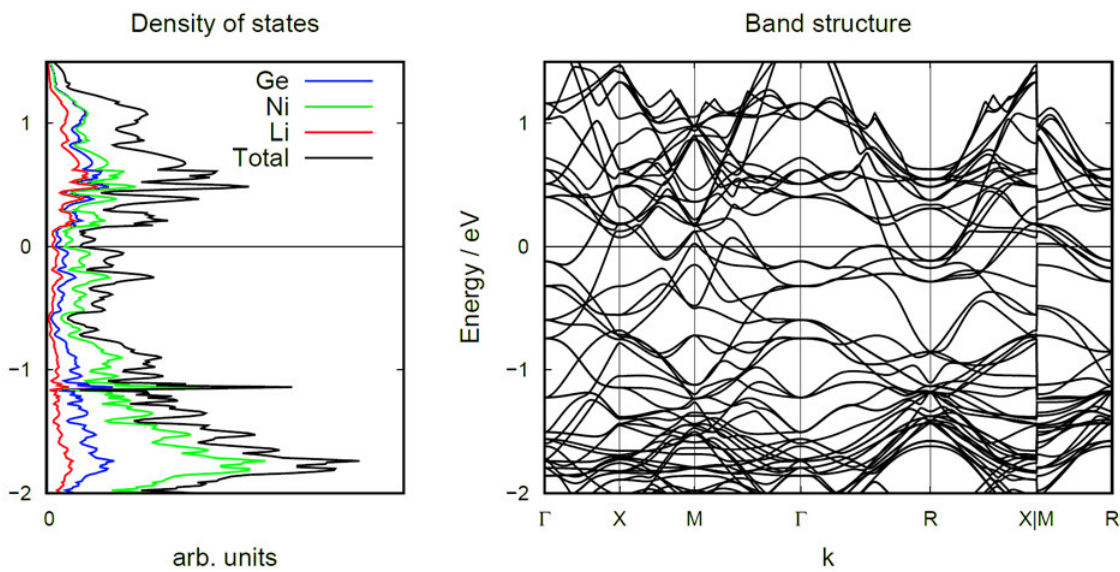


Figure 13.7: Density of States (DOS, left) and band structure (right) of $\text{Li}_{14}\text{Ni}_{8.75}\text{Ge}_8$. The Fermi level is at zero energy.

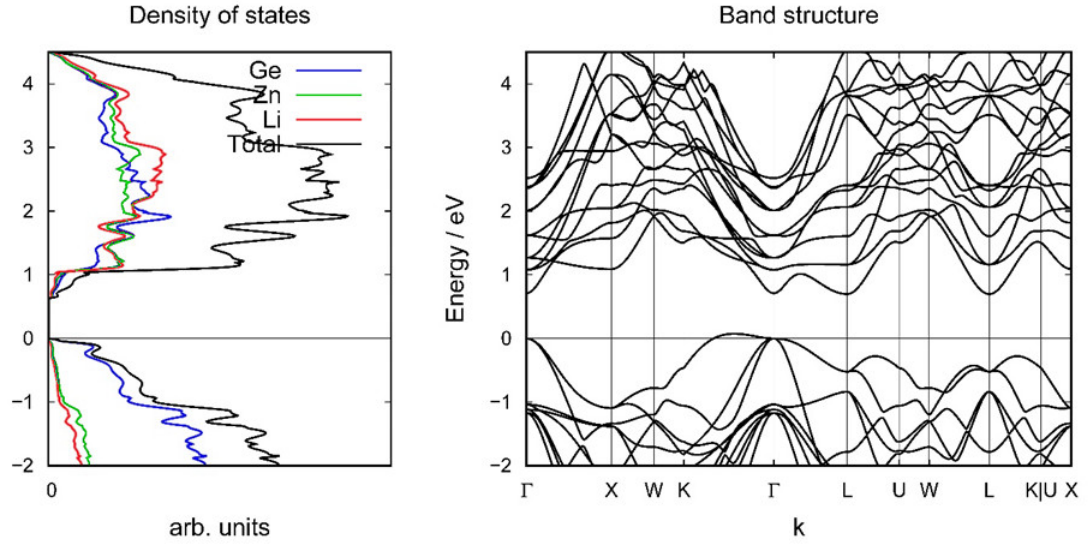
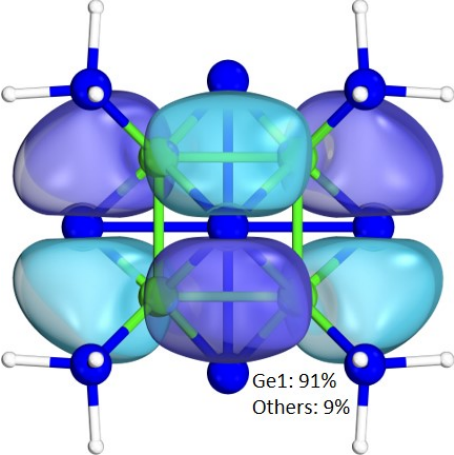
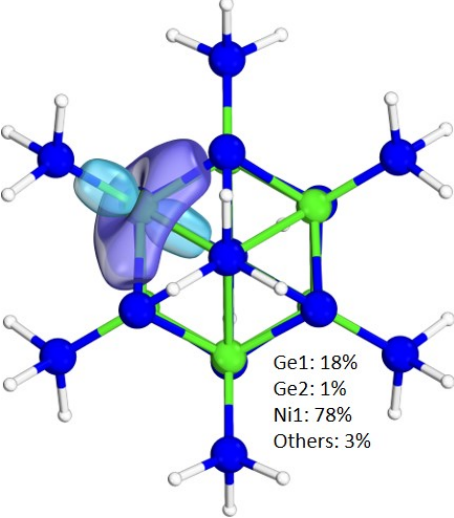
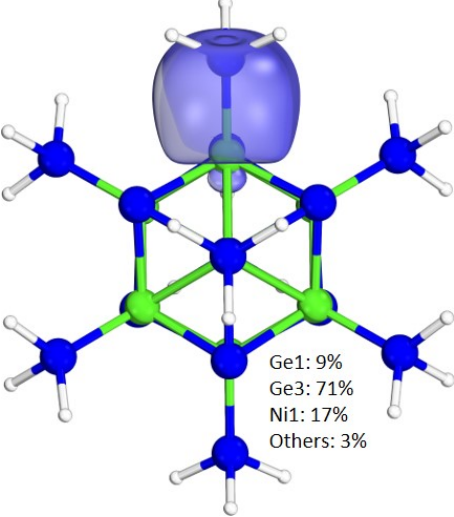


Figure 13.8: Density of States (DOS, left) and band structure (right) of $\text{Li}_{14}\text{Zn}_8\text{Ge}_9$. The Fermi level is at zero energy.

Table 13.13: Atomic distances (d) for **G** and **H** as well as, experimental data are shown in Å and as deviation (Δd) from experimental data in percentages

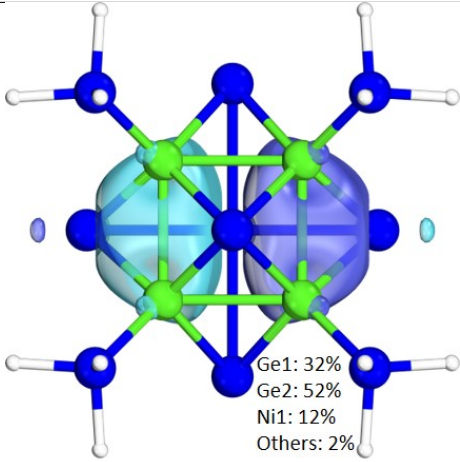
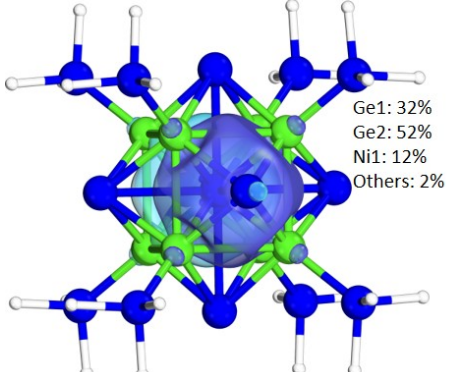
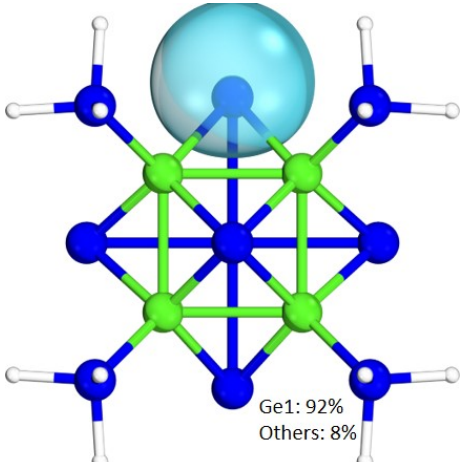
	G		H		Exp. Data
	$d / \text{Å}$	$\Delta d / \%$	$d / \text{Å}$	$\Delta d / \%$	$d / \text{Å}$
Ni1-Ni1	2.84	-5.2	2.7	-9.8	3.00
Ni1-Ge1	2.32	-3.5	2.42	-9.8	2.40
Ni1-X2	2.46	-5.2	2.34	-0.7	2.59

Table 13.14: Relevant IBOs with atom contribution of $[\text{Ge}@Ni_8\text{Ge}_6]^{6-}$. Ge and Ni is colored blue and green, respectively.

IBO #	Example Figure
365-367	 <p>Ge1: 91% Others: 9%</p>
325-332	 <p>Ge1: 18% Ge2: 1% Ni1: 78% Others: 3%</p>
293-300	 <p>Ge1: 9% Ge3: 71% Ni1: 17% Others: 3%</p>

Continued on next page

Continued from table 13.14

IBO #	Example Figure
292	 <p>Ge1: 32% Ge2: 52% Ni1: 12% Others: 2%</p>
291	 <p>Ge1: 32% Ge2: 52% Ni1: 12% Others: 2%</p>
285-290	 <p>Ge1: 92% Others: 8%</p>

Continued on next page

Continued from table 13.14

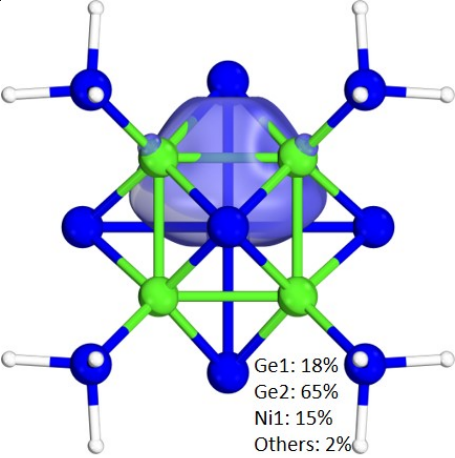
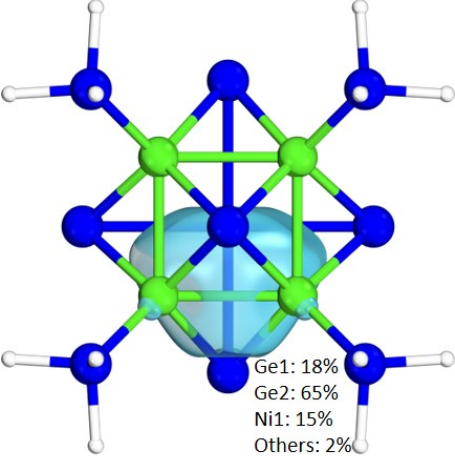
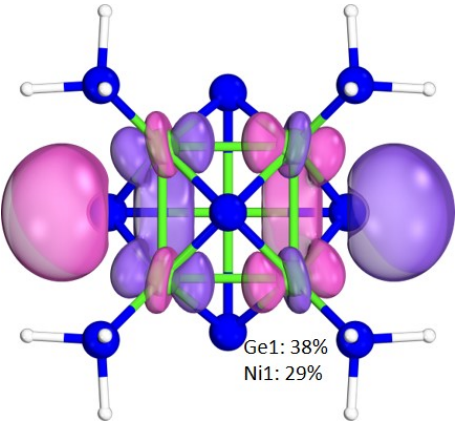
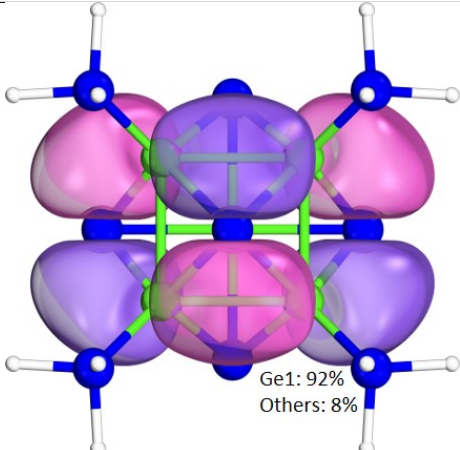
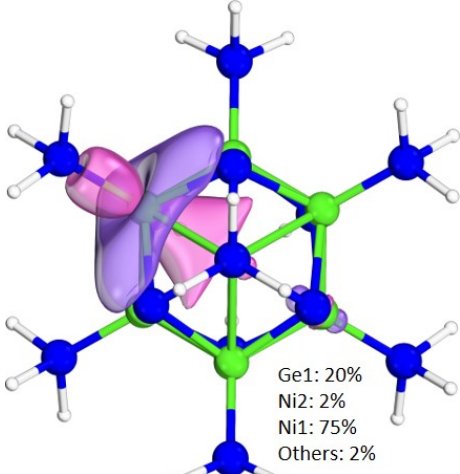
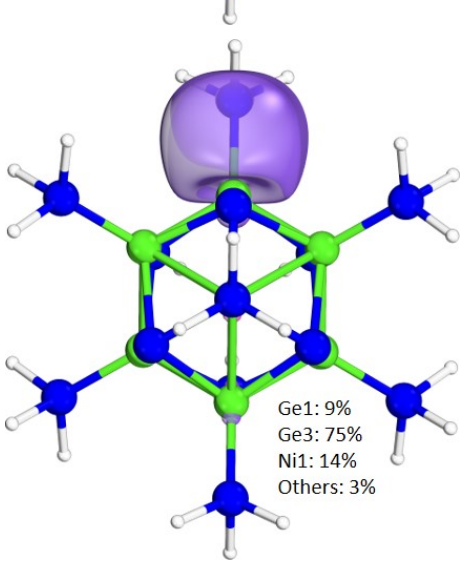
IBO #	Example Figure
284	 <p data-bbox="869 645 981 748">Ge1: 18% Ge2: 65% Ni1: 15% Others: 2%</p>
283	 <p data-bbox="869 1126 981 1229">Ge1: 18% Ge2: 65% Ni1: 15% Others: 2%</p>

Table 13.15: Relevant IBOs with atom contribution of $[\text{Ni}@\text{Ni}_8\text{Ge}_6]^{6-}$. Ge and Ni is colored blue and green, respectively.

IBO #	Example Figure
364-366	 <p data-bbox="869 1877 981 1933">Ge1: 38% Ni1: 29%</p>

Continued on next page

Continued from table 13.15

IBO #	Example Figure
361-363	 <p>Ge1: 92% Others: 8%</p>
337-344	 <p>Ge1: 20% Ni2: 2% Ni1: 75% Others: 2%</p>
284-291	 <p>Ge1: 9% Ge3: 75% Ni1: 14% Others: 3%</p>

Continued on next page

Continued from table 13.15

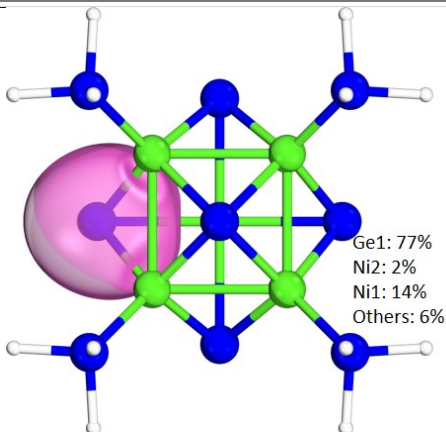
IBO #	Example Figure
278-283	 <p>Ge1: 77% Ni2: 2% Ni1: 14% Others: 6%</p>

Table 13.16: Atomic coordinates and equivalent isotropic displacement parameters for $\text{LiNi}_{1+x}\text{Ge}$

Atom	Wyck.	x	y	z	S.O.F.	$U_{eg}/\text{\AA}^2$
Ge1	24e	0	0.22368	0.52957	1	0.007(1)
Ge2	4a	0	0	0	0.69(9)	0.005(1)
Ni2	4a	0	0	0	0.31(9)	0.005(1)
Ge3	8c	$\frac{1}{4}$	$\frac{1}{4}$	$\frac{1}{4}$	1	0.007(1)
Ni1	32f	0.12721	0.12721	0.12721	1	0.006(1)
Li1	32f	0.37845	0.12155	0.12155	1	0.020(3)
Li2	24d	$\frac{1}{4}$	$\frac{1}{4}$	0	1	0.020(4)

Table 13.17: Interatomic distances for $\text{Li}_{14}\text{Ni}_{8.3}\text{Ge}_{8.7}$

Atom1	Atom2	Distance / \AA
Ge1	Ni1	2.4034(6)
	Ni1	2.4034(6)
	Ni1	2.4034(6)
	Ni1	2.4034(6)
	Ge2	2.6336(9)
	Li1	2.723(4)
	Li1	2.723(4)
	Li1	2.723(4)
	Li1	2.723(4)
	Li2	2.95960(10)

Continued on next page

Continued from table 13.17

Atom1	Atom2	Distance / Å
Ge2	Li2	2.95960(10)
	Ni1	2.5940(9)
	Ni1	2.5940(9)
	Ni1	2.5940(9)
	Ni1	2.5940(9)
	Ni1	2.5940(9)
	Ni1	2.5940(9)
	Ni1	2.5940(9)
	Ni1	2.5940(9)
	Ge1	2.6336(9)
	Ge1	2.6336(9)
Ge3	Ge1	2.6336(9)
	Ni1	2.5040(9)
	Ni1	2.5041(9)
	Ni1	2.5041(9)
	Ni1	2.5041(9)
	Li1	2.619(16)
	Li1	2.619(16)
	Li1	2.619(16)
	Li1	2.619(16)
	Li2	2.94335(3)
	Li2	2.94335(3)
Ni1	Li2	2.94335(3)
	Li2	2.94335(3)
	Ge1	2.4034(6)
	Ge1	2.4034(6)
	Li2	2.5344(3)
	Li2	2.5344(3)
	Li2	2.5344(3)
	Li1	2.959(10)
	Li1	2.959(10)
	Li1	2.959(10)
	Li1	Li2
Li2		2.573(6)
Li2		2.573(6)

Continued on next page

Continued from table 13.17

Atom1	Atom2	Distance / Å
	Ge1	2.723(4)
	Ge1	2.723(4)
	Ge1	2.723(4)
	Li1	2.862(19)
	Li1	2.862(18)
	Li1	2.862(18)
	Ni1	2.959(10)
Li2	Ni1	2.5344(3)
	Ni1	2.5344(3)
	Ni1	2.5344(3)
	Li1	2.573(6)
	Li1	2.573(6)
	Li1	2.573(6)
	Ge3	2.94335(3)
	Ge1	2.95960(10)
	Ge1	2.95960(10)

13.2 Substitutional Effects in the Li-Ge Binary System by Ag

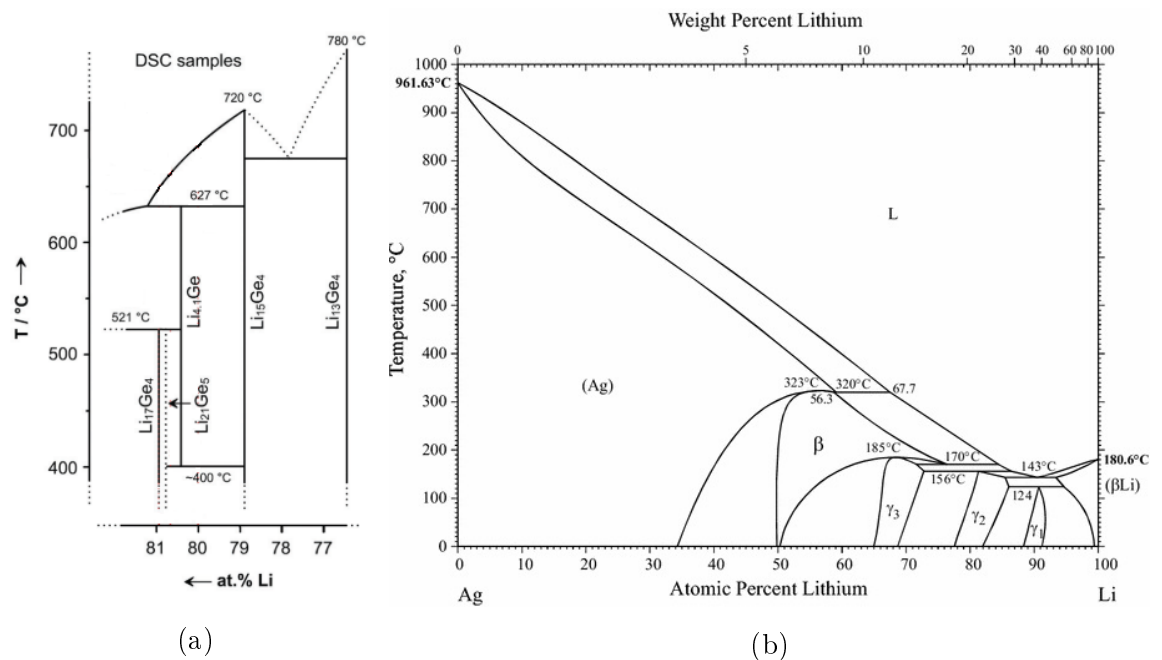


Figure 13.9: (a) Excerpt of the Li-rich Li-Ge phase diagram based on DSC investigations by Fässler *et al.*. The graph was taken from the publication of M. Zeilinger.^[1] (b) Phase diagram of the Li-Ag system. The graph was taken from the publication of H. Okamoto.^[2]

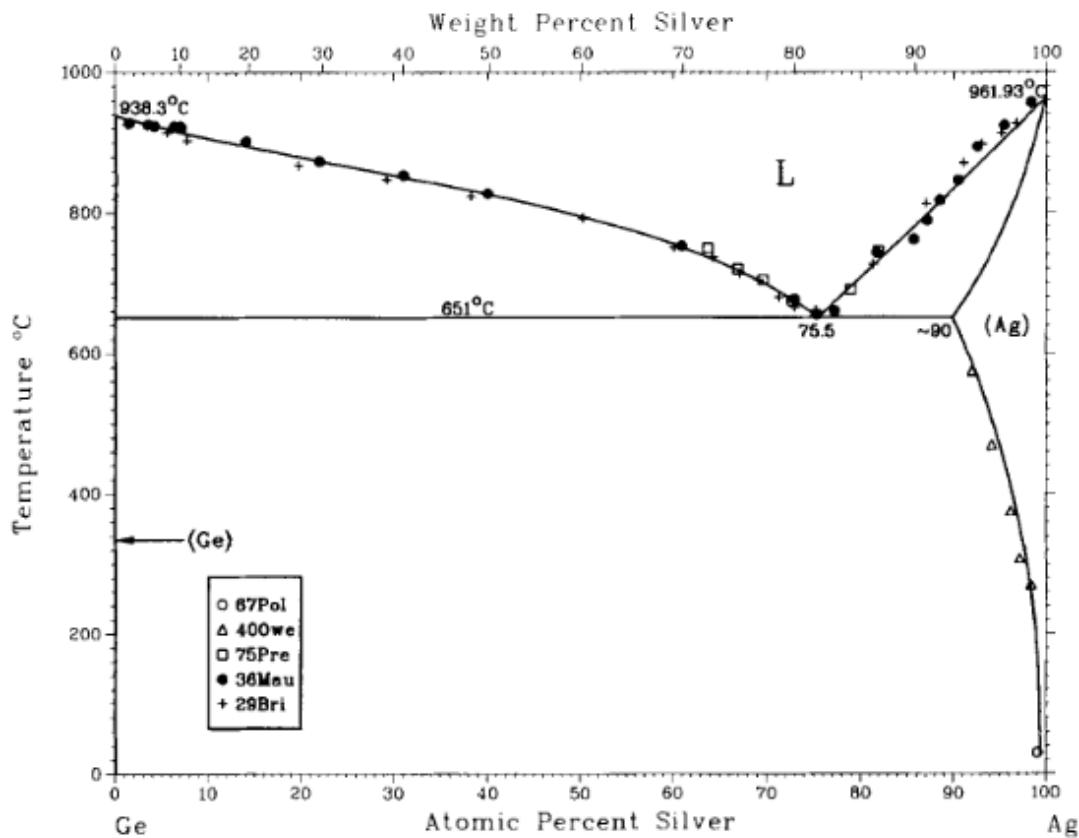


Figure 13.10: Phase diagram of the Li-Ag system without Ag_4Ge due to not reliable data. The graph was taken from the publication of R.W. Olesinski and G. J. Abbaschian.^[3]

Table 13.18: Atomic coordinates and isotropic displacement parameters for $\beta\text{-Li}_2\text{Ag}_{0.8}\text{Ge}_{1.2}$

Atom	Wyckoff	x / a	y / b	z / c	S.O.F.	$U_{iso} / \text{\AA}^2$
Ge1	8a	0.1250	0.1250	0.1250	0.49(12)	0.0136(3)
Ag1	8a	0.1250	0.1250	0.1250	0.49(12)	0.0136(3)
Li1	8b	0.3750	0.3750	0.3750	1	0.030(6)

Table 13.19: Interatomic distances for β -Li₂Ag_{0.8}Ge_{1.2}

Atom 1	Atom 2	Distance / Å
Ge1	Ag1	2.6876(3)
	Li1	2.6876(3)
	Ge1	2.6876(3)
Li1	Li1	2.6876(3)
	Ag1	2.6876(3)
	Ge1	2.6876(3)

Table 13.20: Atomic coordinates and isotropic displacement parameters for γ -Li_{2.53}AgGe₂

Atom	Wyckoff	x / a	y / b	z / c	S.O.F.	U _{iso} / Å ²
Ge1	8a	0.1250	0.1250	0.1250	0.67	0.0105(3)
Ag1	8a	0.1250	0.1250	0.1250	0.33	0.0105(3)
Li1	8b	0.3750	0.3750	0.3750	0.8(3)	0.011(14)

Table 13.21: Interatomic distances for γ -Li_{2.53}AgGe₂

Atom 1	Atom 2	Distance / Å
Ge1	Ag1	2.6789(3)
	Li1	2.6789(3)
	Ge1	2.6789(3)
Li1	Li1	2.6789(3)
	Ag1	2.6789(3)
	Ge1	2.6789(3)

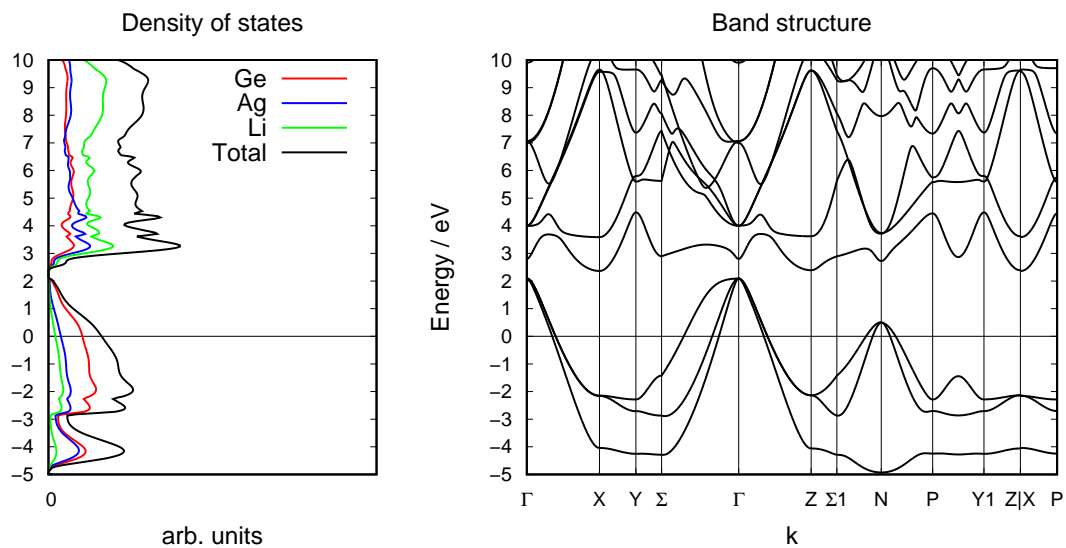


Figure 13.11: Band structure and density of states of **Tet1**.

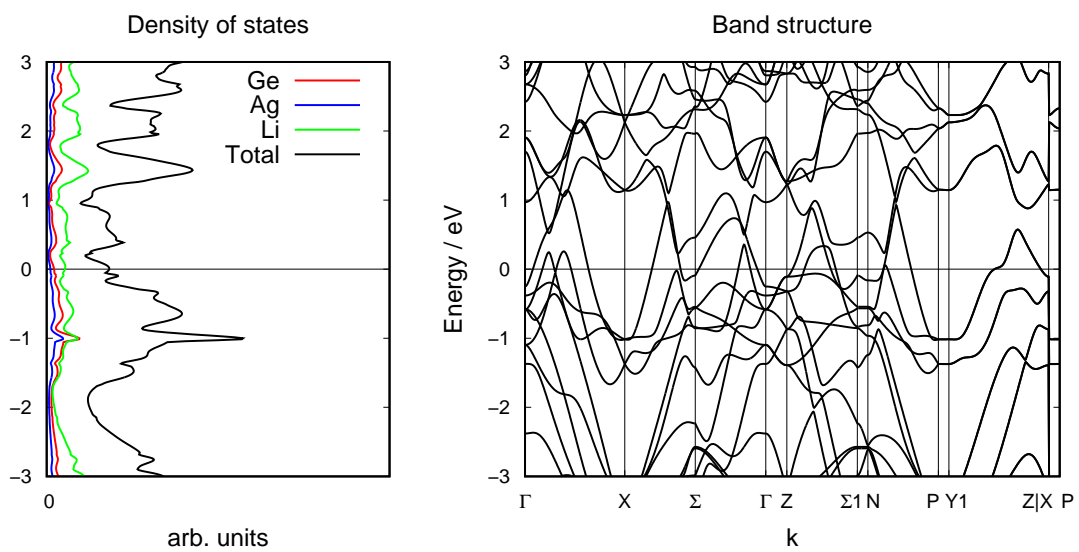


Figure 13.12: Band structure and density of states of **Tet3**.

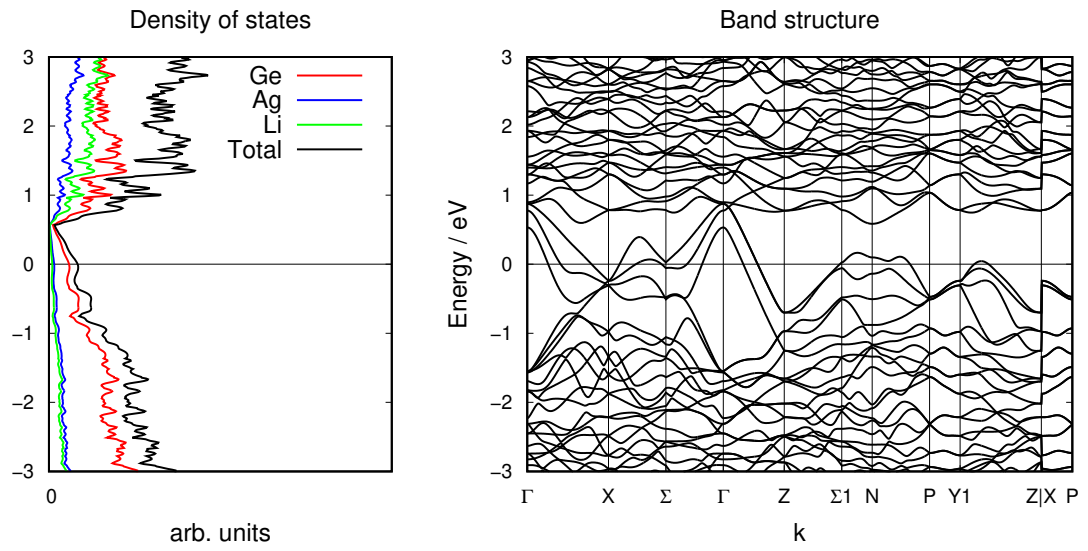


Figure 13.13: Band structure and density of states of **Tet4**.

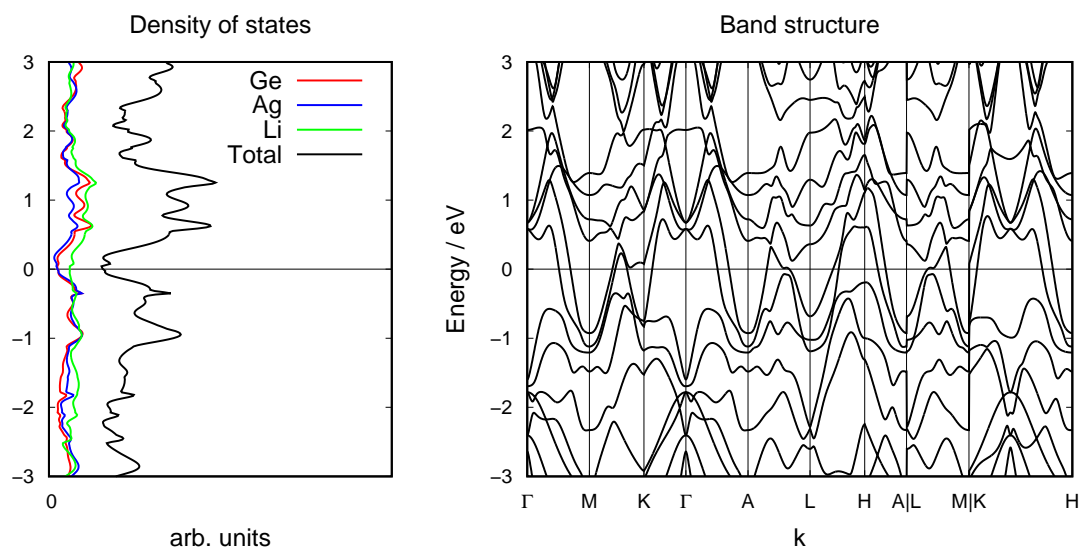


Figure 13.14: Band structure and density of states of **Tri1**.

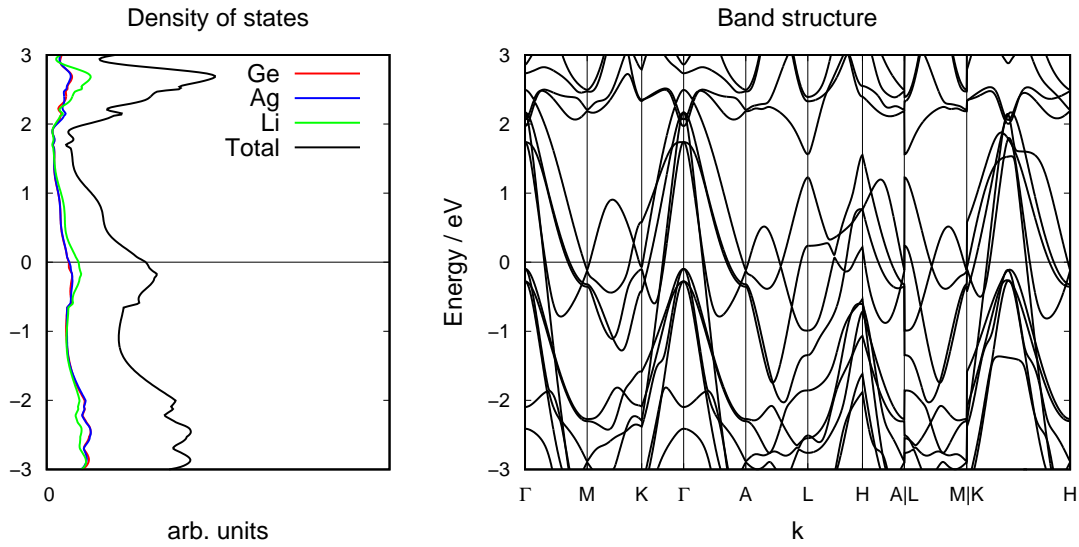


Figure 13.15: Band structure and density of states of **Tri2**.

Table 13.22: Atom positions of optimized structure **Cub1** with $a = 6.28598257 \text{ \AA}$

Cub1	x/a	y/b	z/c
Ag1	$\frac{1}{2}$	$\frac{1}{2}$	$\frac{1}{2}$
Ge1	$\frac{3}{4}$	$\frac{3}{4}$	$\frac{3}{4}$
Li1	0	0	0
Li2	$\frac{1}{4}$	$\frac{1}{4}$	$\frac{1}{4}$

Table 13.23: Atom positions of optimized structure **Tet1** with $a = 4.42896886 \text{ \AA}$ and $b = 6.27645206 \text{ \AA}$

Tet1	x/a	y/b	z/c
Ag1	0	$\frac{1}{2}$	$\frac{1}{4}$
Ge1	0	0	0
Li1	0	0	$\frac{1}{2}$
Li2	0	$\frac{1}{2}$	$\frac{3}{4}$

Table 13.24: Atom positions of optimized structure **Tet2** ($a = 4.48666292 \text{ \AA}$ and $b = 30.60807151 \text{ \AA}$) and **Tet3** ($a = 4.55062470 \text{ \AA}$ and $b = 30.48655642 \text{ \AA}$)

Tet2	\mathbf{x}/a	\mathbf{y}/b	\mathbf{z}/c
Ge1	0	$\frac{1}{4}$	0.77345
Ge2	0	$\frac{1}{4}$	$\frac{3}{8}$
Ag1	0	$\frac{1}{4}$	0.17493
Li1	0	$\frac{1}{4}$	0.07658
Li2	0	$\frac{1}{4}$	0.27627
Li3	0	$\frac{3}{4}$	$\frac{1}{8}$
Tet3	\mathbf{x}/a	\mathbf{y}/b	\mathbf{z}/c
Ag1	0	$\frac{1}{4}$	0.77926
Ge1	0	$\frac{1}{4}$	$\frac{3}{8}$
Ge2	0	$\frac{1}{4}$	0.17357
Li1	0	$\frac{1}{4}$	0.07353
Li2	0	$\frac{1}{4}$	0.27190
Li3	0	$\frac{3}{4}$	$\frac{1}{8}$

Table 13.25: Atom positions of optimized structure **Tet4** ($a = 9.90727791 \text{ \AA}$ and $b = 18.66196260 \text{ \AA}$) and **Tet5** ($a = 9.84999635 \text{ \AA}$ and $b = 18.56971458 \text{ \AA}$)

Tet4	x/a	y/b	z/c
Ge1	0	$\frac{1}{4}$	0.79701
Ge2	0.59734	0.43970	0.12928
Ge3	0.59480	0.45498	0.45676
Ag1	0	$\frac{1}{4}$	$\frac{1}{8}$
Ag2	0.61465	-0.05314	0.21368
Li1	0	$\frac{1}{4}$	-0.03648
Li2	0.07810	-0.09112	0.44189
Li3	0.59942	0.45794	0.29063
Li4	0.79984	0.35936	0.37589
Tet5	x/a	y/b	z/c
Ge1	0	$\frac{1}{2}$	0.42136
Ge2	0.59389	0.18724	0.00545
Ge3	0.59082	0.19991	0.33553
Ge4	0	0	0.67284
Ge5	0.10535	0.18674	0.24562
Ge6	0.59979	0.70301	0.41989
Ag1	0	$\frac{1}{2}$	$\frac{3}{4}$
Ag2	0.61878	0.68895	0.08757
Ag3	0	0	0
Ag4	0.19710	0.38776	0.33714
Li1	0.07668	0.66233	0.31564
Li2	0.58635	0.18866	0.15822
Li3	0.79509	0.10824	0.25068
Li4	0	0	0.83800
Li5	0.66692	0.41489	0.06978
Li6	0.70932	0.40086	0.41639
Li7	0.60148	0.18586	0.49277

Table 13.26: Atom positions of optimized structure **Tri1** ($a = 4.57992683 \text{ \AA}$ and $b = 43.98534009 \text{ \AA}$), **Tri2** ($a = 4.45524956 \text{ \AA}$ and $b = 43.33687075 \text{ \AA}$) and **Tri3** ($a = 4.47047618 \text{ \AA}$ and $b = 42.85285361 \text{ \AA}$)

Tri1	\mathbf{x}/a	\mathbf{y}/b	\mathbf{z}/c
Ge1	0	0	0.03252
Ge2	0	0	0.28221
Ag1	0	0	0.53190
Ag2	0	0	0.77901
Li1	0	0	0.09575
Li2	0	0	0.34357
Li3	0	0	0.59230
Li4	0	0	0.84255
Tri2	\mathbf{x}/a	\mathbf{y}/b	\mathbf{z}/c
Ge1	0	0	0.02993
Ge2	0	0	0.53034
Ag1	0	0	0.28313
Ag2	0	0	0.78312
Li1	0	0	0.09406
Li2	0	0	0.34403
Li3	0	0	0.59438
Li4	0	0	0.84414
Tri3	\mathbf{x}/a	\mathbf{y}/b	\mathbf{z}/c
Ge1	0	0	0.02969
Ge2	0	0	0.78328
Ag1	0	0	0.28046
Ag2	0	0	0.53524
Li1	0	0	0.09282
Li2	0	0	0.34206
Li3	0	0	0.59664
Li4	0	0	0.84611

r5cm

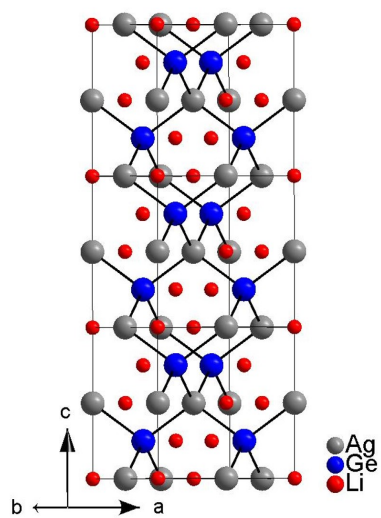


Figure 13.16: Structure of **Cub1**.

r4cm

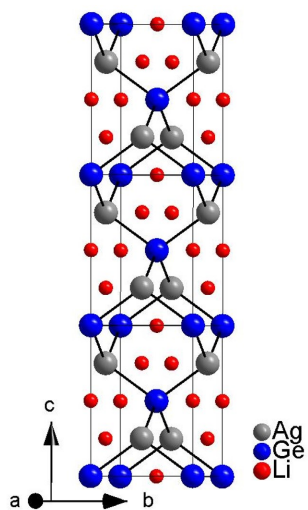


Figure 13.17: Structure of **Tet1**.

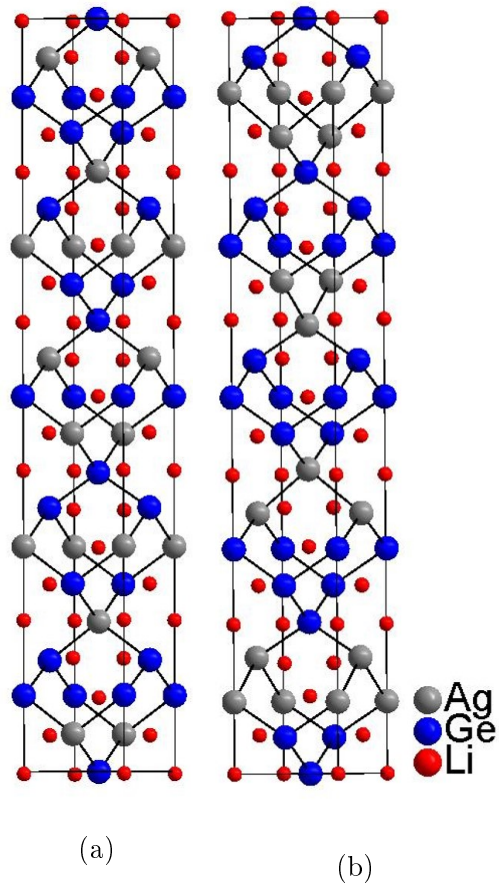


Figure 13.18: (a) Structure of **Tet2**. (b) Structure of **Tet3**.

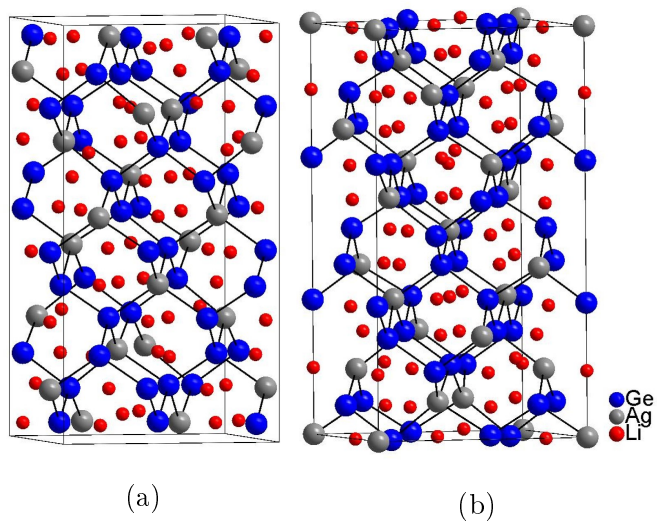


Figure 13.19: (a) Structure of **Tet4**. (b) Structure of **Tet5**.

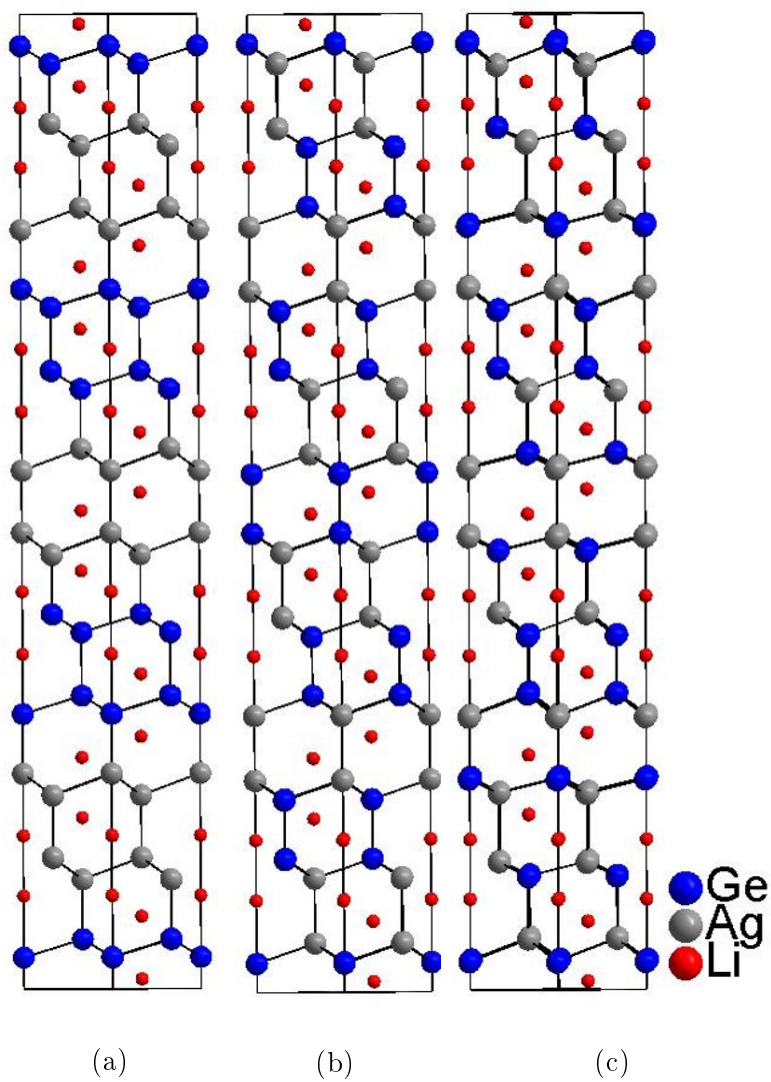


Figure 13.20: (a) Structure of **Tri1**. (b) Structure of **Tri2**. (c) Structure of **Tri3**

13.3 Substitutional Effects in the Li-Si Binary System by Ag

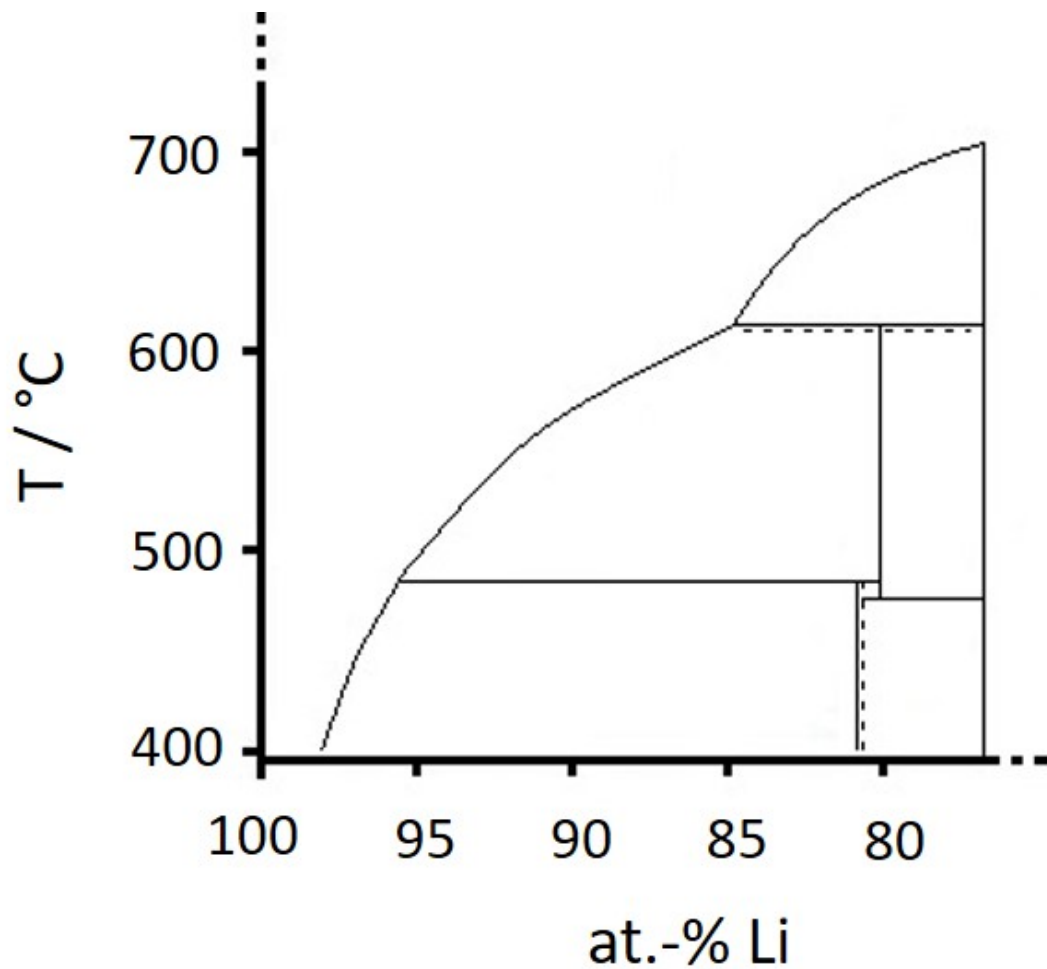


Figure 13.21: Phase diagram of the Li-Si system at Li at.-% above 75 %

Table 13.27: Atomic coordinates and isotropic displacement parameters for β - $\text{Li}_{13}\text{Ag}_5\text{Si}_6$

Atom	Wyckoff	x / a	y / b	z / c	S.O.F.	$U_{iso} / \text{\AA}^2$
Si1	$8a$	0.1250	0.1250	0.1250	0.6(2)	0.0229(8)
Ag1	$8a$	0.1250	0.1250	0.1250	0.4(2)	0.0229(8)
Li1	$8b$	0.3750	0.3750	0.3750	1	0.016(8)

Table 13.28: Interatomic distances for β -Li₁₃Ag₅Si₆

Atom 1	Atom 2	Distance / Å
Si1	Ag1	2.6876(3)
	Li1	2.6278(7)
	Si1	2.6278(7)
Li1	Li1	2.6278(7)
	Si1	2.6278(7)
	Si1	2.6278(7)

13.4 The Framework Compound Li₆B₁₈(Li₃N)_x

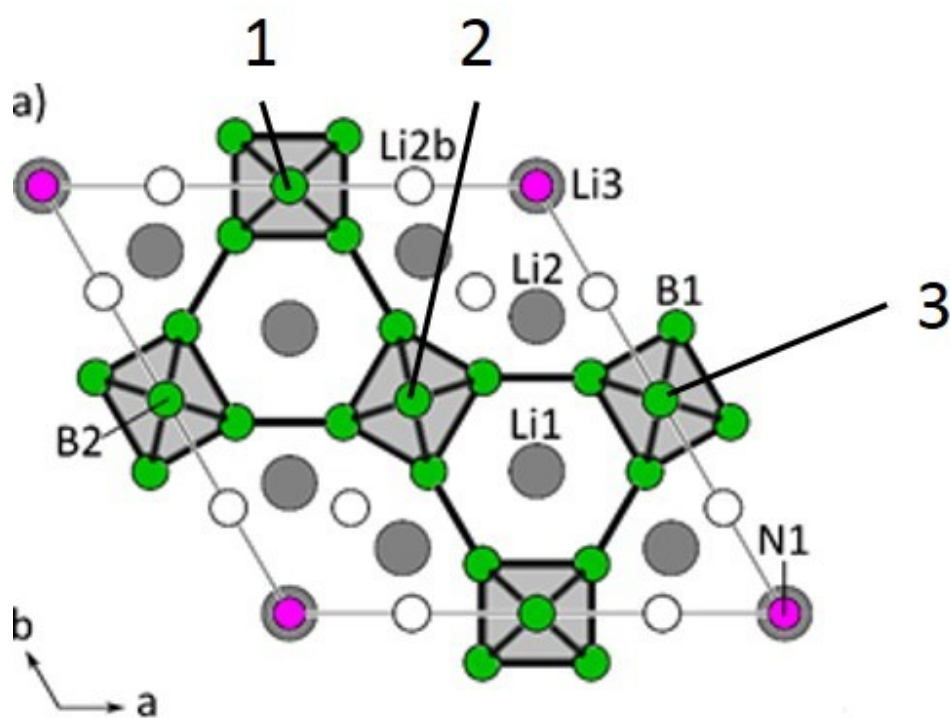


Figure 13.22: Structure of Li₆B₁₈(Li₃N). The three B₆ units for the Raman mode are labeled by 1, 2 and 3.

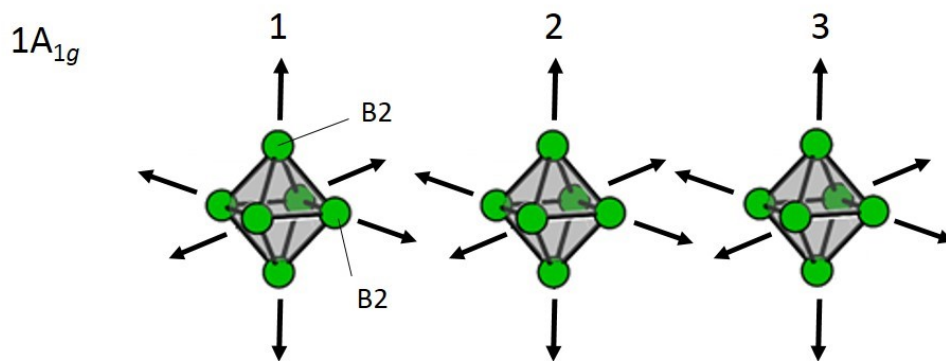


Figure 13.23: Raman mode $1A_{1g}$ for the three B_6 units 1, 2 and 3.

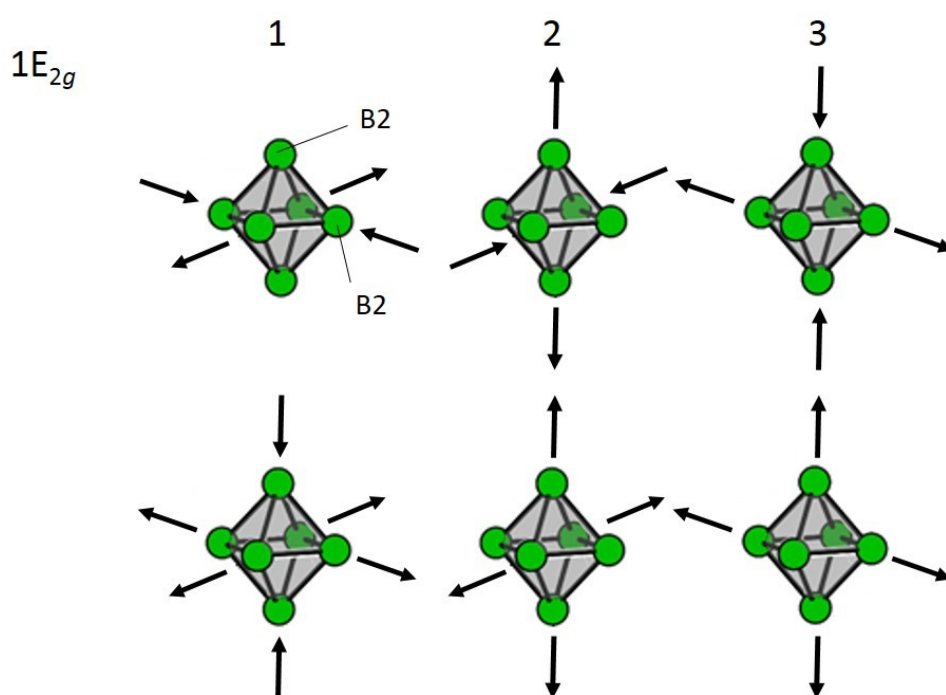


Figure 13.24: Raman mode $1E_{2g}$ for the three B_6 units 1, 2 and 3.

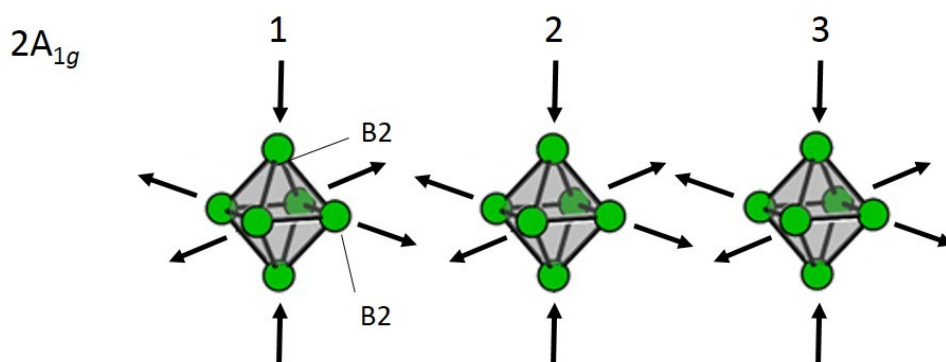


Figure 13.25: Raman mode $2A_{1g}$ for the three B_6 units 1, 2 and 3.

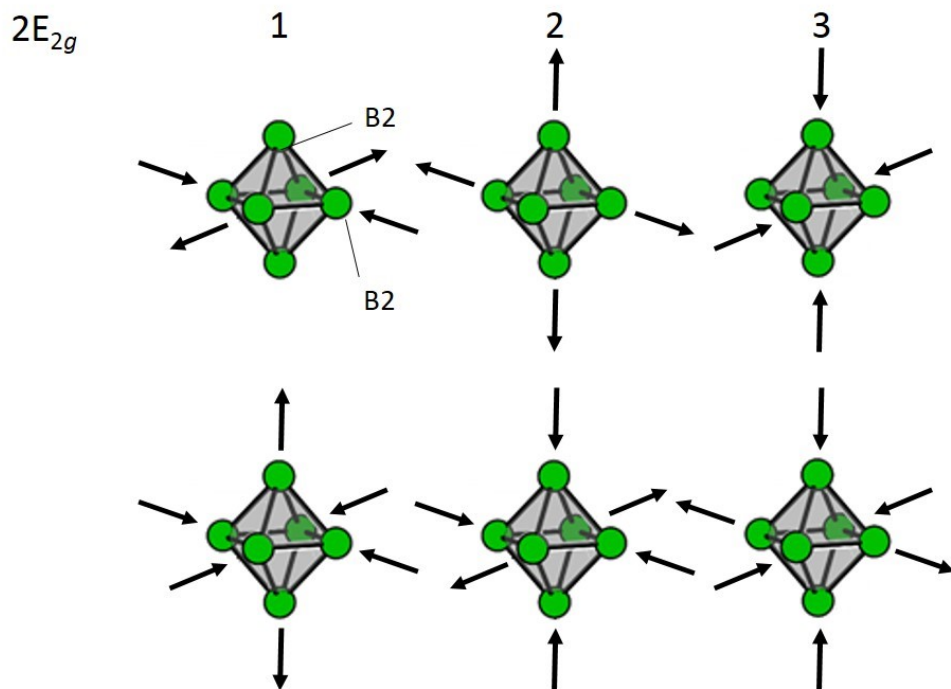


Figure 13.26: Raman mode $2E_{2g}$ for the three B_6 units 1, 2 and 3.

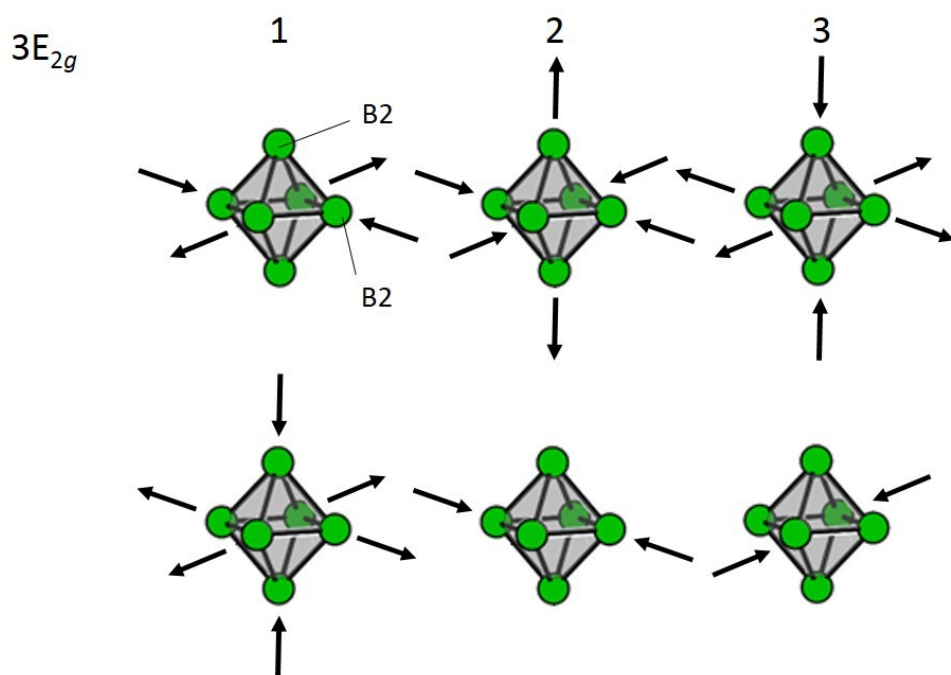


Figure 13.27: Raman mode $3E_{2g}$ for the three B_6 units 1, 2 and 3.

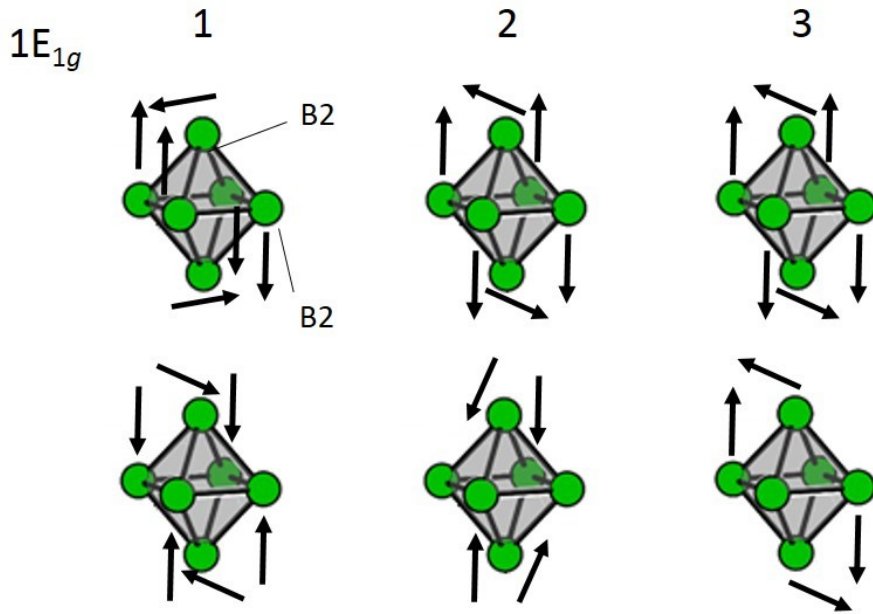


Figure 13.28: Raman mode $1E_{1g}$ for the three B_6 units 1, 2 and 3.

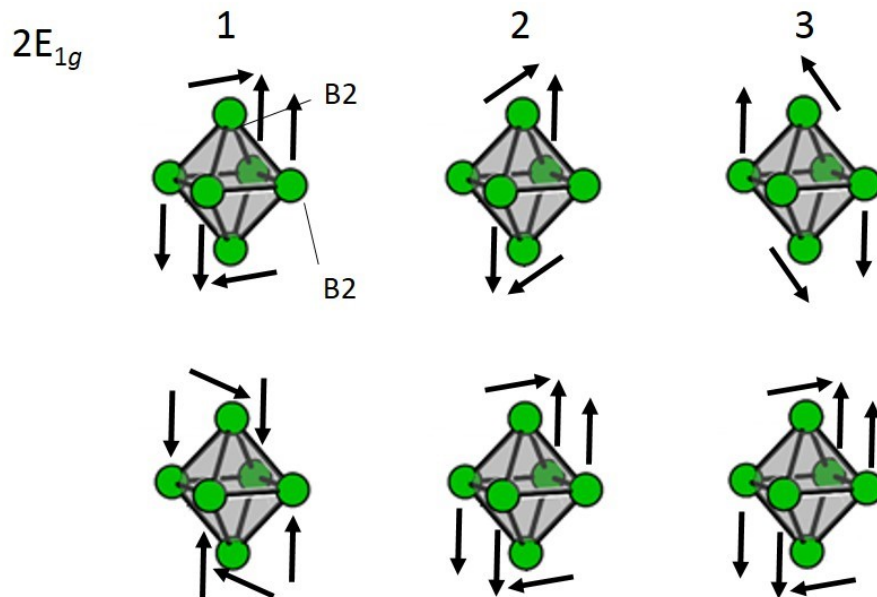


Figure 13.29: Raman mode $2E_{1g}$ for the three B_6 units 1, 2 and 3.

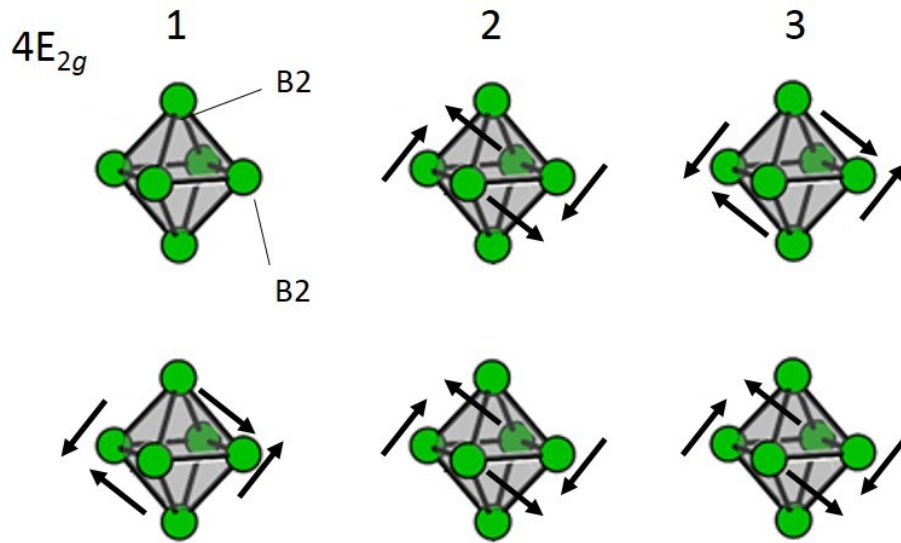


Figure 13.30: Raman mode $4E_{2g}$ for the three B_6 units 1, 2 and 3.

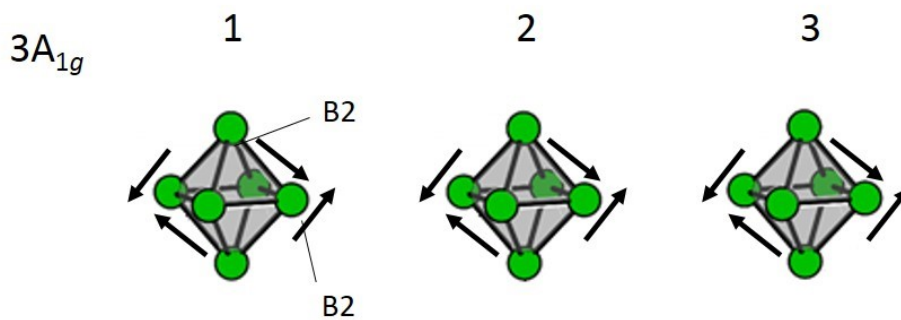


Figure 13.31: Raman mode $3A_{1g}$ for the three B_6 units 1, 2 and 3.

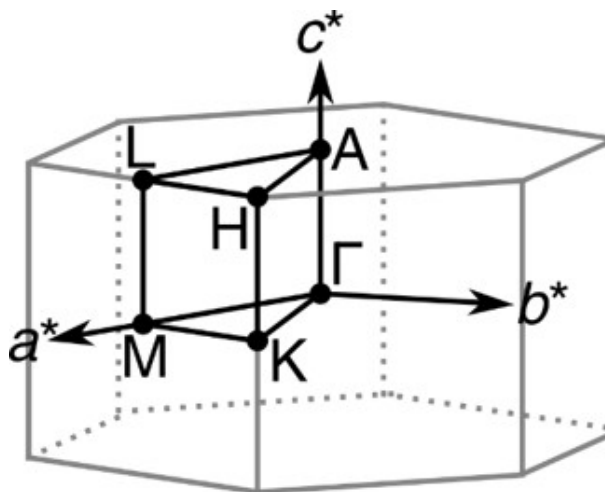


Figure 13.32: Brillouin zone for $\text{Li}_6\text{B}_{18}(\text{Li}_3\text{N})$ in $P6/mmm$ and related hexagonal space groups, showing symmetry points in the k space with respect to the reciprocal conventional vectors. $\Gamma - M - K - \Gamma - A - L - H - A \mid L - M \mid K - H$ was used as path for the band structure.^[4]

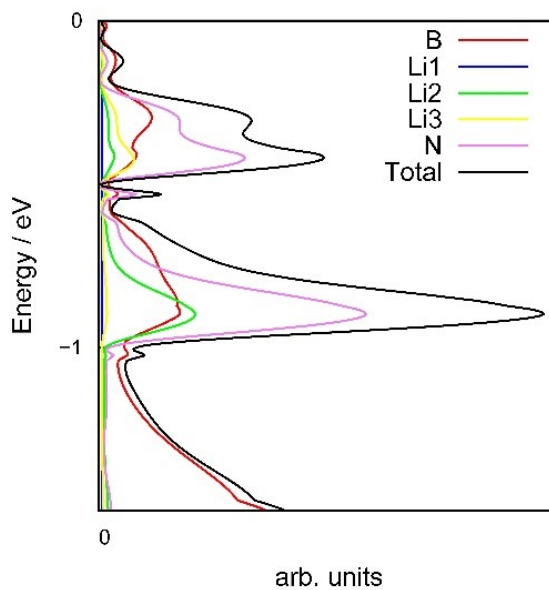


Figure 13.33: Atom-projected DOS of $\text{Li}_6\text{B}_{18}(\text{Li}_3\text{N})$. Only the Li atoms in large pores contribute to the states next to the Fermi level.

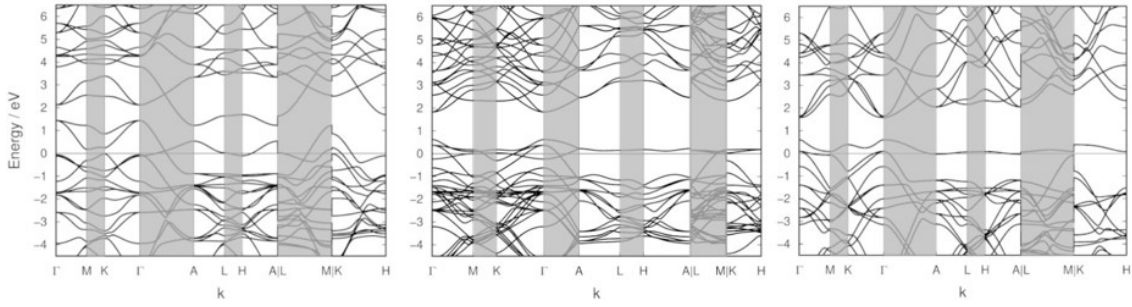


Figure 13.34: Band structures of Li_6B_{18} in $P\bar{6}2m$ (left), $P6_3/mmc$ (middle), and $P\bar{6}m2$ (right).

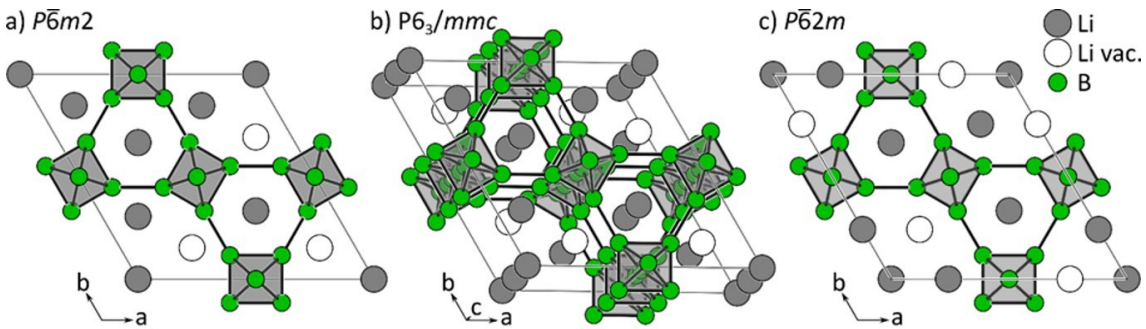


Figure 13.35: Structures of Li_6B_{18} in $P\bar{6}2m$ (left), $P6_3/mmc$ (middle), and $P\bar{6}m2$ (right).^[5]

Table 13.29: Atom positions of optimized structure $\text{Li}_6\text{B}_{18}(\text{Li}_3\text{N})$ with $a = 8.2164 \text{ \AA}$ and $b = 4.1093 \text{ \AA}$

Atom	x/a	y/b	z/c
B1	4.534645356746E-01	1.232629321489E-01	-5.000000000000E-01
B2	-5.000000000000E-01	-1.108710078925E-16	-2.040463155520E-01
Li1	3.333333333333E-01	-3.333333333333E-01	0.000000000000E+00
Li2	9.811800650871E-21	4.905900325436E-21	-5.000000000000E-01
Li3	1.502004693334E-01	3.004009386668E-01	0.000000000000E+00
N	9.811800650871E-21	4.905900325436E-21	0.000000000000E+00

Table 13.30: Atom positions of optimized structure Li_6B_{18} in $P\bar{6}2m$ with $a = 8.270 \text{ \AA}$ and $b = 4.1832 \text{ \AA}$

Atom	x/a	y/b	z/c
B1 1	0.4478	0.1152	0.5
B1 2	0.4478	0.3326	0.5
B2	0.5	0	0.7981
Li1	$\frac{1}{3}$	$\frac{2}{3}$	0
Li2	0.2420	0	0
Li3	0	0	0.5

Table 13.31: Atom positions of optimized structure Li_6B_{18} in $P6_3/mmc$ with $a = 8.2709 \text{ \AA}$ and $b = 8.3664 \text{ \AA}$

Atom	x/a	y/b	z/c
B1	0.4478	0.1152	0
B2	0.5	0	0.1491
Li1 1	$\frac{1}{3}$	$\frac{2}{3}$	0.75
Li1 2	$\frac{1}{3}$	$\frac{2}{3}$	0.25
Li2	0.1527	0.3055	0.75
Li3	0	0	0

Table 13.32: Atom positions of optimized structure Li_6B_{18} in $P\bar{6}m2$ with $a = 8.2709 \text{ \AA}$ and $b = 4.1832 \text{ \AA}$

Atom	x/a	y/b	z/c
B1 1	0.4478	0.1152	0
B1 2	-0.4478	-0.1152	0
B2	0.5	0	0.2981
Li1 1	$\frac{1}{3}$	$\frac{2}{3}$	-0.5
Li1 2	$\frac{2}{3}$	$-\frac{2}{3}$	0.5
Li2	0.1527	0.3055	-0.5
Li3	0	0	0

Table 13.33: Atom positions of optimized structure B_4C_2 in $P6/mmm$ with $a = \text{XXXX \AA}$ and $b = \text{XXX \AA}$

Atom	x/a	y/b	z/c
------	-------	-------	-------

Table 13.34: Atom positions of optimized structure B_4C_2 in $P6/m$ with $a = 7.53777332 \text{ \AA}$ and $b = 4.09640289 \text{ \AA}$

Atom	x/a	y/b	z/c
B1	4.522884430117E-01	1.296776252196E-01	5.000000000000E-01
B2	5.000000000000E-01	-9.900239236267E-17	-2.025518116725E-01
C	4.528224500429E-01	3.355783419639E-01	5.000000000000E-01

Table 13.35: Atom positions of optimized structure B_4C_2 in $P\bar{6}m2$ with $a = 7.57828533 \text{ \AA}$ and $b = 4.11149348 \text{ \AA}$

Atom	x/a	y/b	z/c
B1	4.415433056523E-01	1.112135753170E-01	-5.000000000000E-01
B2	4.893993356974E-01	-2.120132860512E-02	-2.019480588140E-01
C	1.359488060812E-01	4.647914037406E-01	-5.000000000000E-01

Table 13.36: Atom positions of optimized structure B_4C_2 in $P\bar{6}2m$ with $a = XXXX \text{ \AA}$ and $b = XXX \text{ \AA}$

Atom	x/a	y/b	z/c
B1	4.398492034086E-01	1.292196768795E-01	-5.000000000000E-01
B2	4.951559830784E-01	-5.837411134902E-17	-2.018670406888E-01
C	4.643965577832E-01	3.466345621204E-01	-5.000000000000E-01

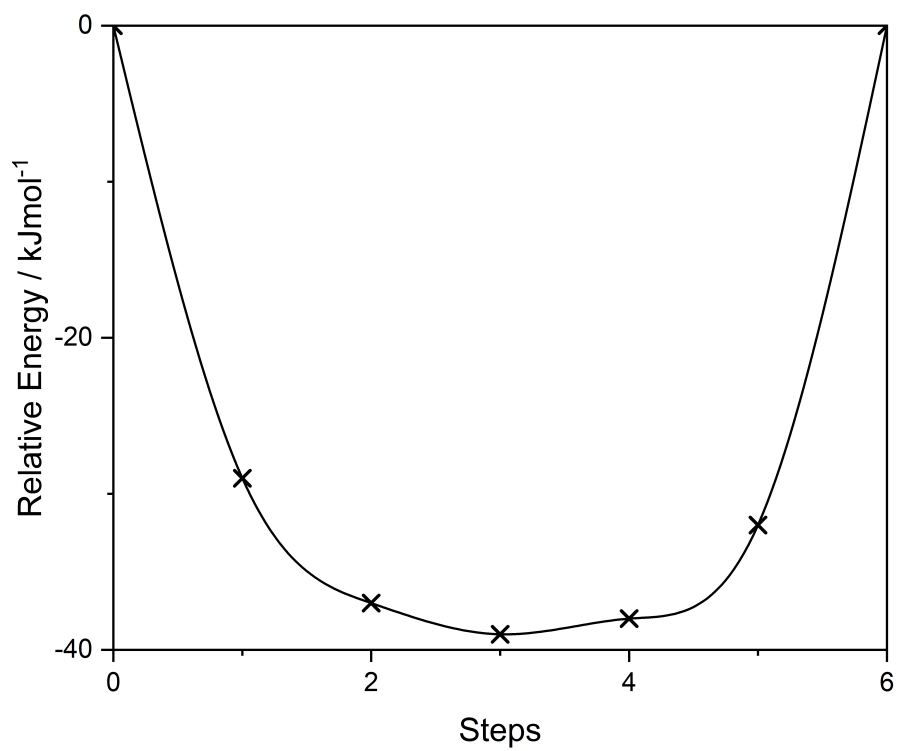


Figure 13.36: Relative energies of Li diffusion path in Li_3N

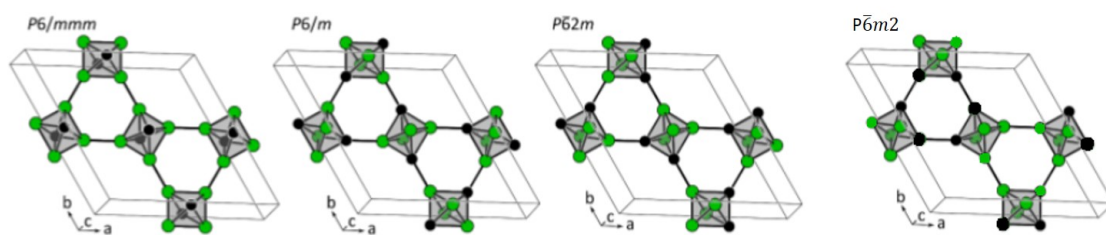


Figure 13.37: Structure models of B_4C_2

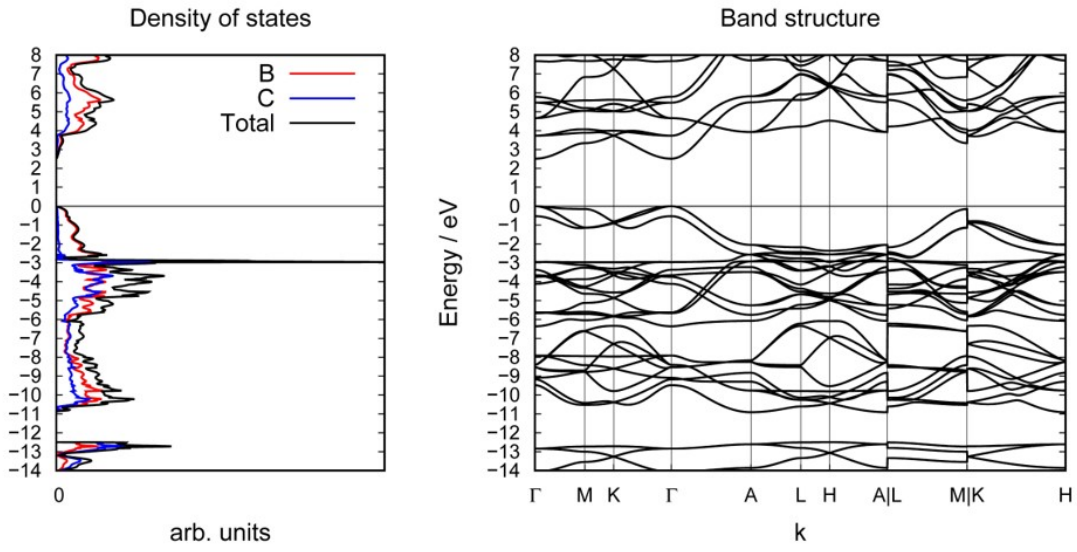


Figure 13.38: Band structure of $P6/m-B_4C_2$

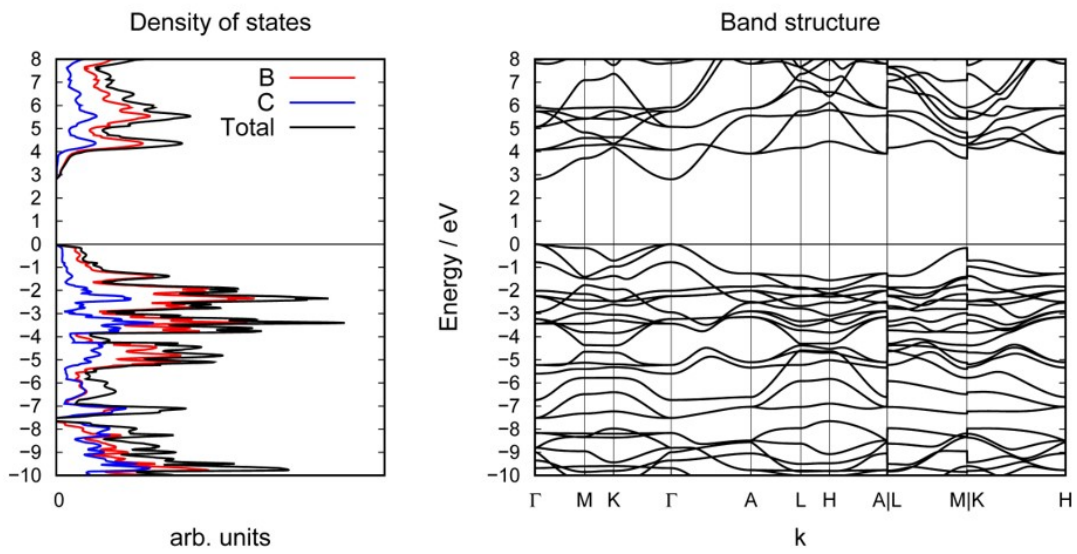


Figure 13.39: Band structure of $P\bar{6}m2-B_4C_2$

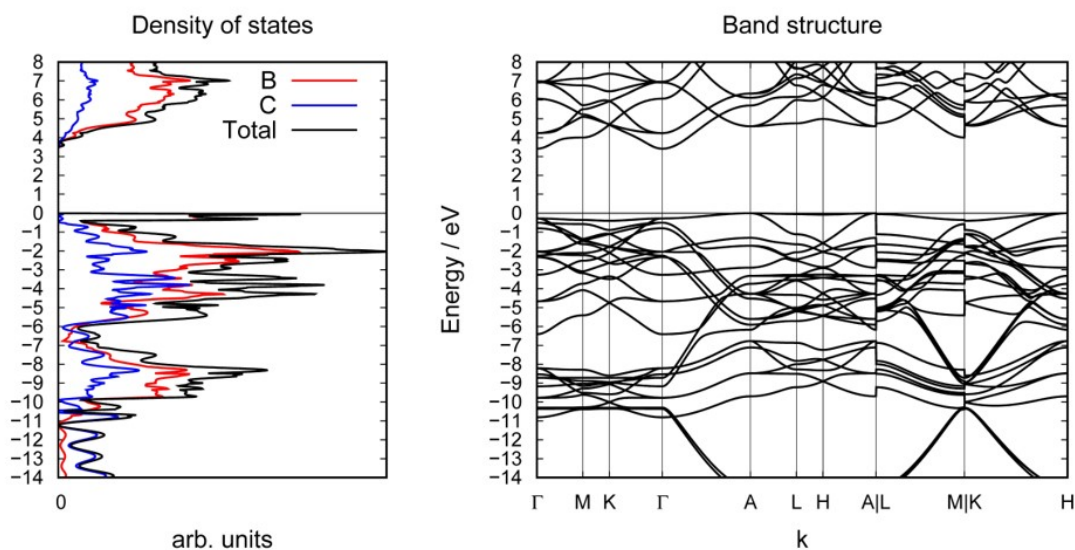


Figure 13.40: Band structure of $P6/mmm-B_4C_2$

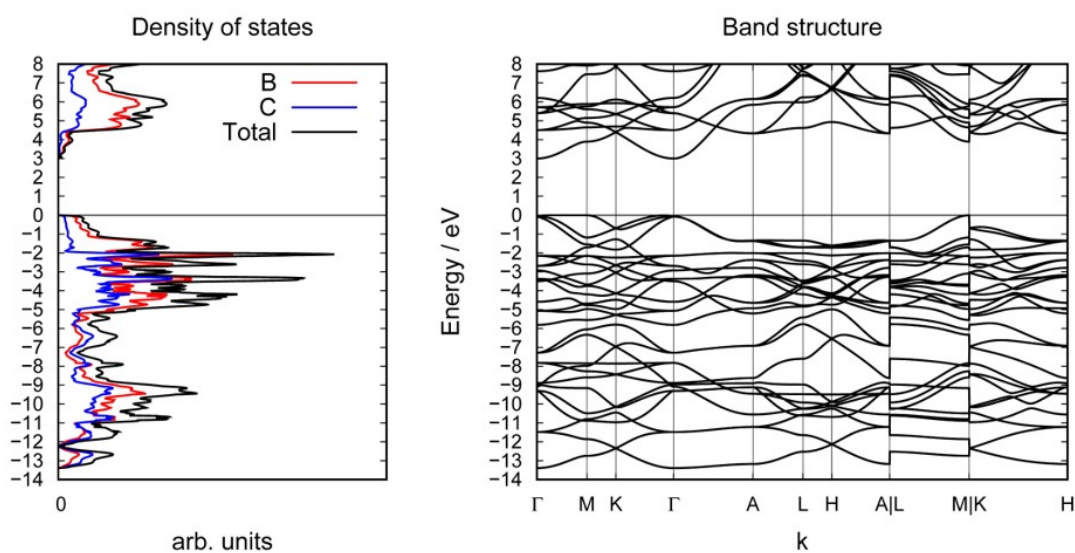


Figure 13.41: Band structure of $P\bar{6}2m-B_4C_2$

13.5 The Compounds Li_2TrP_2 ($Tr = Al, Ga$)

Table 13.39: Frequencies of Li_3AlP_2 and Li_3GaP_2 from frequencies analysis at Γ -point

Li_3AlP_2 Frequencies / cm^{-1}	Li_3GaP_2 Frequencies / cm^{-1}
0.00	0.00

Continued on next page

Continued from table 13.39

Li ₃ AlP ₂ Frequencies / cm ⁻¹	Li ₃ GaP ₂ Frequencies / cm ⁻¹
0.00	0.00
0.00	0.00
142.07	109.16
147.88	109.30
149.67	113.22
174.80	126.55
177.90	131.73
178.65	133.36
186.85	139.05
189.89	157.38
196.59	169.06
197.45	172.94
206.75	177.02
214.79	183.49
219.36	187.28
228.38	192.42
228.89	195.82
235.23	195.90
240.91	215.50
241.00	222.37
245.10	235.56
246.71	237.65
262.03	243.12
267.50	243.83
272.17	250.57
273.53	251.52
274.77	257.00
276.02	266.26
287.53	276.04
296.69	276.49
298.20	277.14
302.17	279.40
314.26	283.18
316.07	292.24
317.99	299.59

Continued on next page

Continued from table 13.39

Li ₃ AlP ₂ Frequencies / cm ⁻¹	Li ₃ GaP ₂ Frequencies / cm ⁻¹
320.20	301.44
324.37	304.38
338.11	313.93
339.37	314.05
341.05	316.64
348.10	318.27
350.36	320.13
352.72	326.17
355.45	332.75
356.73	334.18
359.79	335.67
364.06	346.39
373.24	347.85
373.90	352.01
374.26	352.86
377.77	353.81
380.12	356.83
387.30	359.15
387.63	363.91
389.88	366.22
396.10	372.45
396.64	385.32
404.85	389.29
404.86	389.49
409.69	393.34
410.97	399.52
417.90	403.68
420.42	406.89
434.37	411.06
443.13	420.88
458.53	422.46
463.46	428.41
471.47	445.39
490.72	447.45
502.44	454.71

Continued on next page

Continued from table 13.39

Li ₃ AlP ₂ Frequencies / cm ⁻¹	Li ₃ GaP ₂ Frequencies / cm ⁻¹
504.92	466.22

13.6 The Compound Na₇TaP₄

Table 13.40: Atomic coordinates of optimized Na₇TaP₄

Atom	Wyck.	x	y	z
Na1	4e	1.856E-01	1.861E-01	3.381E-01
Na2	4e	4.474E-01	1.848E-01	7.635E-02
Na3	4e	3.071E-01	-1.728E-01	2.044E-01
Na4	4e	-4.703E-02	3.410E-01	6.902E-02
Na5	4e	-4.739E-01	-4.061E-01	1.360E-01
Na6	4e	2.624E-01	-4.239E-01	4.171E-01
Na7	4e	1.765E-02	-7.583E-02	1.370E-01
Ta	4e	2.491E-01	4.370E-01	1.329E-01
P1	4e	1.839E-01	1.565E-01	7.630E-02
P2	4e	9.630E-02	-4.060E-01	1.986E-01
P3	4e	3.067E-01	-4.157E-01	-2.957E-02
P4	4e	4.192E-01	4.179E-01	2.944E-01

Table 13.41: Symmetry k-points for orthorhombic lattice for compounds Na₇TaP₄. Brillouin zone path Γ -Y-C-E-A-X|Z-D-Y is derived from the paths of Curtarolo et al.^[4]

	$\times b_1$	$\times b_2$	$\times b_3$
Γ	0	0	0
Y	0	0	$\frac{1}{2}$
C	0	$\frac{1}{2}$	$\frac{1}{2}$
E	$-\frac{1}{2}$	$\frac{1}{2}$	$\frac{1}{2}$
A	$-\frac{1}{2}$	$\frac{1}{2}$	0
X	0	$\frac{1}{2}$	0
Z	$-\frac{1}{2}$	0	0
D	$\frac{1}{2}$	0	$\frac{1}{2}$
Y	0	0	$\frac{1}{2}$

Table 13.37: Atomic coordinates of optimized Li_3AlP_2 and Li_3GaP_2

Atom	Wyck.	Li_3AlP_2			Li_3GaP_2		
		x	y	z	x	y	z
P1	$8f$	0	0.38201	0.21016	0	0.38217	0.21212
P2	$8e$	$\frac{1}{4}$	0.11603	$\frac{1}{4}$	$\frac{1}{4}$	0.11833	$\frac{1}{4}$
Tr1	$8d$	0.36774	0	0	0.36647	0	0
Li1	$8d$	0.11487	0	0	0.11557	0	0
Li2	$16g$	0.62386	0.25874	0.02222	0.87746	0.24166	- 0.01907

 Table 13.38: Symmetry k-points for orthorhombic lattice for compounds Li_3AlP_2 and Li_3GaP_2 . Brillouin zone path Γ -S-Y-Z- Γ -Y-T-Z is derived from the paths of Curtarolo et al.^[4]

	$\times b_1$	$\times b_2$	$\times b_3$
Γ	0	0	0
S	0	$\frac{1}{2}$	0
Y	$-\frac{1}{2}$	$\frac{1}{2}$	0
Z	0	0	$\frac{1}{2}$
Γ	0	0	0
Y	$-\frac{1}{2}$	$\frac{1}{2}$	0
T	$-\frac{1}{2}$	$\frac{1}{2}$	$\frac{1}{2}$
Z	0	0	$\frac{1}{2}$

 Table 13.42: Frequencies of Na_7TaP_4 from frequencies analysis at Γ -point

Na_7TaP_4 Frequencies / cm^{-1}	Na_7TaP_4 Frequencies / cm^{-1}
0	170.4201
0	171.5448
0	172.3799
43.0861	173.538
53.6225	176.5436
57.2908	177.1229
57.4521	177.3755
65.8415	180.8453
68.3744	180.9166
68.5624	181.3077

Continued on next page

Continued from table 13.42

Na ₇ TaP ₄ Frequencies / cm ⁻¹	Na ₇ TaP ₄ Frequencies / cm ⁻¹
72.69	185.0681
78.3795	186.3188
78.81	186.373
78.898	187.3002
82.7107	188.1311
85.774	190.1326
87.1993	190.4072
87.6668	194.0816
88.2168	194.6855
90.7892	198.0714
91.6458	199.32
93.1425	199.4148
93.6394	199.6877
95.9029	199.7898
96.6097	205.2785
98.316	207.4946
99.3765	210.7946
101.039	211.8564
102.6302	212.9179
103.164	214.4276
105.1641	214.6299
107.3235	220.8981
107.9909	222.5782
109.5272	225.9306
114.8919	226.1165
115.9942	226.2734
118.6668	228.7475
118.6916	229.7135
120.4982	231.2837
122.7916	233.7302
122.9023	233.8295
123.7836	234.357
124.4265	235.3434
127.5288	236.1884
128.7198	237.2365

Continued on next page

Continued from table 13.42

Na ₇ TaP ₄ Frequencies / cm ⁻¹	Na ₇ TaP ₄ Frequencies / cm ⁻¹
130.0859	237.293
131.4268	240.1887
131.5696	244.9794
131.8237	245.755
137.7293	248.1592
138.9227	248.263
143.8694	248.6313
145.3472	255.0179
146.8699	262.8701
146.9943	262.9893
147.1306	264.0101
150.2366	328.8653
151.1657	331.2992
154.9636	335.3318
156.8435	344.0892
157.6619	344.7515
158.8975	352.57
159.157	353.3366
160.515	353.3903
161.4022	354.507
161.9972	365.9695
162.206	368.423
162.8075	369.8906
162.8939	390.1121
166.6761	391.3843
168.1589	392.4149
168.8261	393.0782

Table 13.43: Atomic coordinates of optimized KBi·NH₃ (DFT-PBE0/TZVP)

Atom	Wyck.	x	y	z
Bi1	4 <i>b</i>	0.49628	0.30300	0.01918
K1	4 <i>b</i>	-0.00052	0.36382	0.52048
N1	2 <i>a</i>	0.43019	0.00000	-0.08381
H1	4 <i>b</i>	0.82356	0.44898	-0.03101
H2	2 <i>a</i>	0.59999	0.00000	0.02094
N2	2 <i>a</i>	-0.09864	0.00000	0.48043
H3	2 <i>a</i>	0.00365	0.00000	0.32116
H4	4 <i>b</i>	0.46249	0.44897	0.58214

Table 13.44: Atomic coordinates of optimized KBi·NH₃ (DFT-PBEXC/TZVP). Atomic parameters are $a = 5.26408108 \text{ \AA}$, $b = 15.88009753 \text{ \AA}$, $c = 5.33503938 \text{ \AA}$ and $\beta = 87.776869^\circ$

Atom	Wyck.	x	y	z
Bi1	4 <i>b</i>	0.50257	0.30159	0.01700
K1	4 <i>b</i>	0.00386	0.36589	0.51924
N1	2 <i>a</i>	0.42547	0.00000	-0.08313
H1	4 <i>b</i>	0.82053	0.44846	-0.02987
H2	2 <i>a</i>	0.59081	0.00000	0.02560
N2	2 <i>a</i>	-0.09926	0.00000	0.48070
H3	2 <i>a</i>	-0.00127	0.00000	0.31820
H4	4 <i>b</i>	0.46457	0.44854	0.58310

13.7 The Compound KBi·NH₃

Table 13.47: Symmetry k-points for orthorhombic lattice for compounds KBi·NH₃.

Point label (starting point)	$\times b_1 \times b_2 \times b_2$	Point label (final point)	$\times b_1 \times b_2 \times b_2$	Direction in real space
Γ	0 0 0	Y	$\frac{1}{2} \frac{1}{2} 0$	\vec{b}
Y	$\frac{1}{2} \frac{1}{2} 0$	L	$\frac{1}{2} \frac{1}{2} \frac{1}{2}$	\vec{c}
L	$\frac{1}{2} \frac{1}{2} \frac{1}{2}$	Γ	0 0 0	n. a.
Γ	0 0 0	A	$\frac{1}{2} -\frac{1}{2} 0$	\vec{a}

Table 13.45: Atomic coordinates of optimized KBi (DFT-PBE0/TZVP). Atomic parameters are $a = 14.07124071 \text{ \AA}$, $b = 7.30134576 \text{ \AA}$, $c = 13.39905252 \text{ \AA}$ and $\beta = 112.150986^\circ$

Atom	Wyck.	x	y	z
Bi1	$4e$	0.07203	0.13524	0.67671
Bi2	$4e$	0.11284	0.87835	0.86621
Bi3	$4e$	0.38825	0.55278	0.77320
Bi4	$4e$	0.57579	0.78924	0.88701
K1	$4e$	0.11448	0.62568	0.63720
K2	$4e$	0.39887	0.79342	0.54194
K3	$4e$	0.65632	0.56122	0.69468
K4	$4e$	0.84187	0.86854	0.56276

Table 13.46: Atomic coordinates of optimized KBi (DFT-PBEXC/TZVP). Atomic parameters are $a = 14.0352994 \text{ \AA}$, $b = 7.42247064 \text{ \AA}$, $c = 13.40923965 \text{ \AA}$ and $\beta = 111.682852^\circ$

Atom	Wyck.	x	y	z
Bi1	$4e$	0.06859	0.14263	0.66903
Bi2	$4e$	0.11633	0.88665	0.86317
Bi3	$4e$	0.38461	0.54701	0.77356
Bi4	$4e$	0.57471	0.78479	0.88921
K1	$4e$	0.11090	0.63246	0.63161
K2	$4e$	0.39983	0.78866	0.54439
K3	$4e$	0.65722	0.55650	0.69827
K4	$4e$	0.83696	0.87501	0.57061

Table 13.48: Frequencies of KBi·NH₃ from frequencies analysis at Γ -point (DFT-PBE0/TZVP)

KBi·NH ₃ Frequencies / cm ⁻¹	KBi·NH ₃ Frequencies / cm ⁻¹
-39.5283	186.0853
0	197.0654
0	371.0131
0	445.248
51.5934	515.9681
72.8262	536.5161

Continued on next page

Continued from table 13.48

KBi·NH ₃ Frequencies / cm ⁻¹	KBi·NH ₃ Frequencies / cm ⁻¹
78.7536	1144.6288
79.7572	1197.884
84.2184	1624.1075
97.9295	1641.9928
99.295	1647.403
109.1477	1669.724
112.311	3368.4981
115.317	3387.1741
125.4786	3461.8101
132.9517	3482.231
145.2012	3551.0222
157.1522	3568.9537

Table 13.49: Frequencies of KBi from frequencies analysis at Γ -point (DFT-PBE0/TZVP)

KBi Frequencies / cm ⁻¹	KBi Frequencies / cm ⁻¹
0.0000	92.2207
0.0000	92.4814
0.0000	94.4975
15.4240	94.9243
16.2750	95.8001
18.7053	96.3243
22.4390	96.5504
26.0406	97.3923
28.6581	98.6232
31.9797	99.1107
32.9930	101.0322
36.7883	101.9658
37.0923	102.6993
39.6889	105.1367
40.3961	105.7322
42.7001	106.7443
45.2567	107.0610
47.0007	110.3889

Continued on next page

Continued from table 13.49

KBi Frequencies / cm^{-1}	KBi Frequencies / cm^{-1}
48.0694	110.8177
48.8313	111.2962
50.7894	111.9893
51.5267	112.2181
51.9909	112.5223
52.8015	115.2705
53.0079	116.9385
54.4306	117.1548
55.8212	118.2220
56.7383	118.7145
57.0495	119.9295
58.7552	120.4016
59.0725	121.2720
59.1479	121.3391
61.7347	122.3859
66.0372	124.3031
67.2048	125.2030
71.4879	125.8857
71.5489	125.9674
75.0526	127.0276
75.8555	127.1853
76.2107	128.8211
82.5997	129.8492
85.1691	130.6971
87.1403	130.9361
87.4348	130.9877
88.8482	132.3319
89.2896	133.1510
90.5514	135.1789
90.6036	136.2338

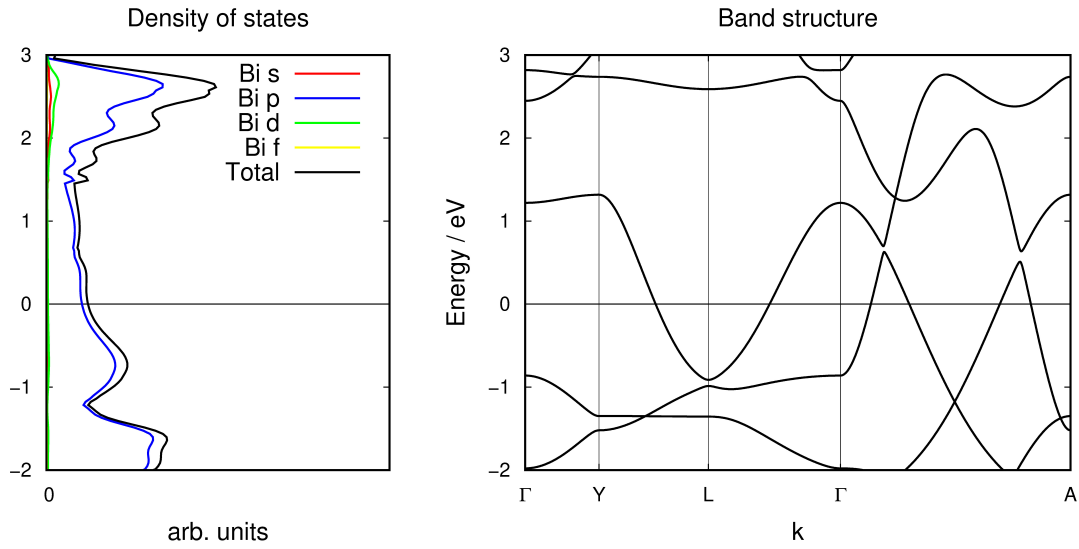


Figure 13.42: Orbital projected DOS and band structure of $\text{KBi}\cdot\text{NH}_3$ showing a major precipitation of Bi p orbitals at the fermi level.

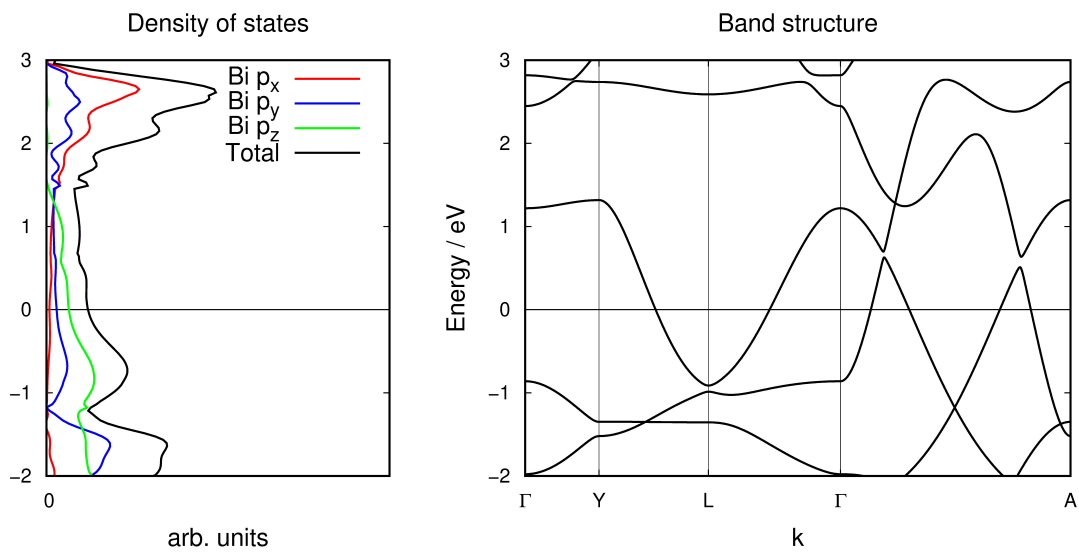


Figure 13.43: Orbital projected DOS and band structure of $\text{KBi}\cdot\text{NH}_3$ showing a major precipitation of Bi p_z orbitals at the fermi level.

13.8 The Anion $[\text{SnBi}_3^{5-}]$

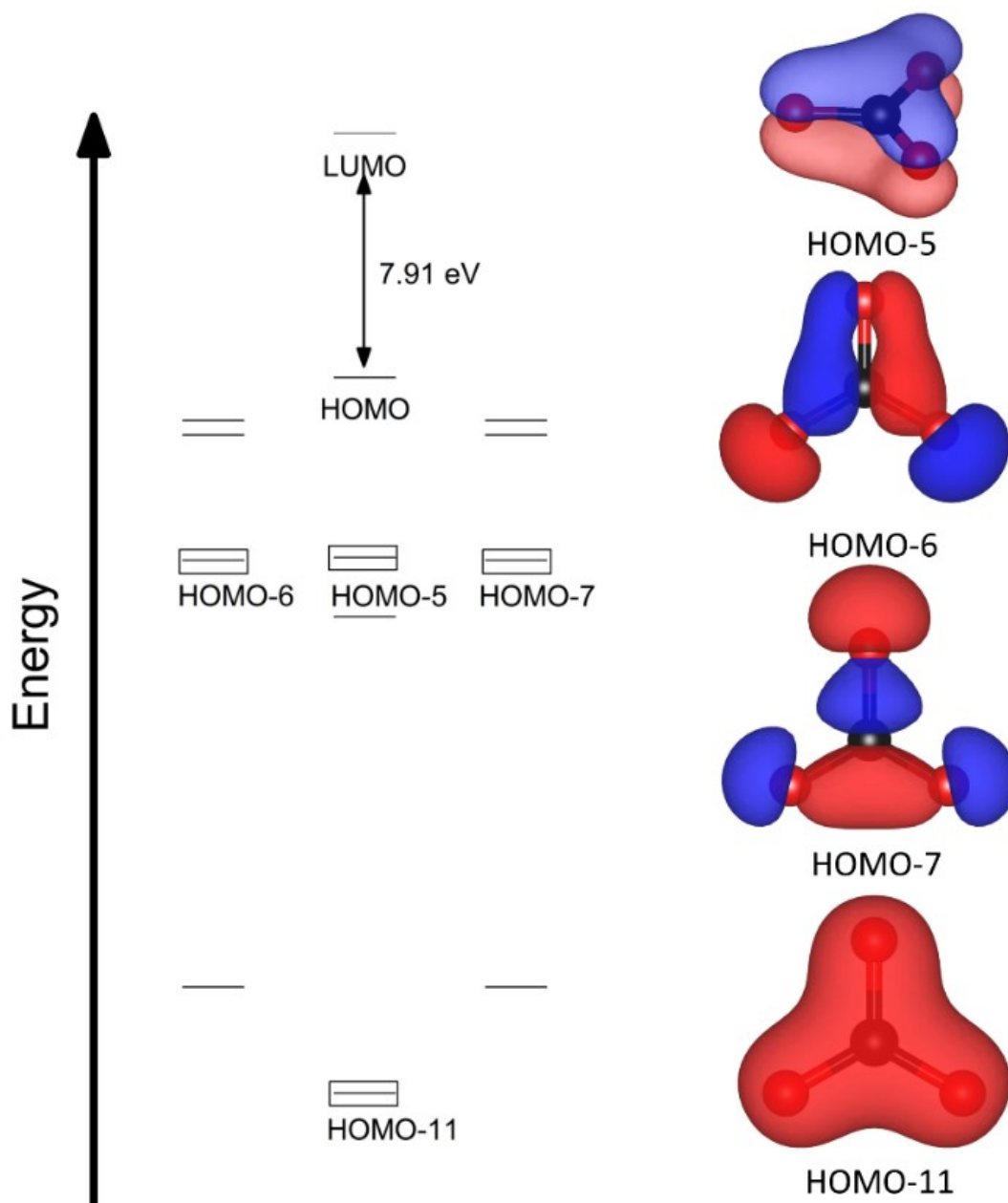


Figure 13.44: Molecular orbital diagram of $[\text{CO}_3]^{2-}$. Bonding orbitals are marked by a rectangle and shown on the right side. The C atoms are shown in black and O atoms in red, respectively. The isovalue is set to 0.4 for all orbitals.

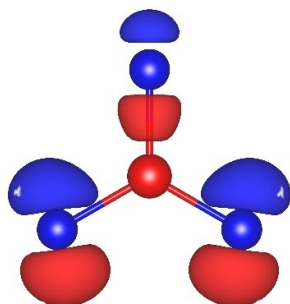


Figure 13.45: Molecular orbital *HOMO-3* of $[\text{SnBi}_3]^{5-}$. The Bi atoms are shown in blue and Sn atoms in red, respectively. The isovalue is 0.04.

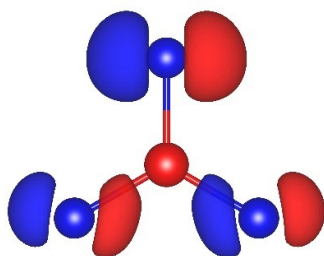


Figure 13.46: Molecular orbital *HOMO-4* of $[\text{SnBi}_3]^{5-}$. The Bi atoms are shown in blue and Sn atoms in red, respectively. The isovalue is 0.04.

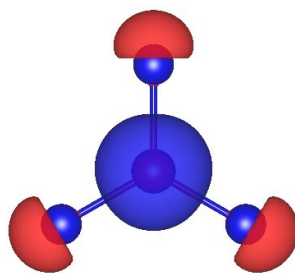


Figure 13.47: Molecular orbital *HOMO-8* of $[\text{SnBi}_3]^{5-}$. The Bi atoms are shown in blue and Sn atoms in red, respectively. The isovalue is 0.04.

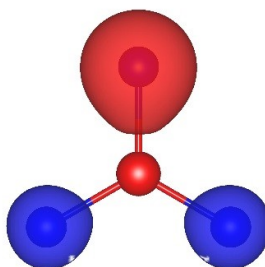


Figure 13.48: Molecular orbital *HOMO-9* of $[\text{SnBi}_3]^{5-}$. The Bi atoms are shown in blue and Sn atoms in red, respectively. The isovalue is 0.04.

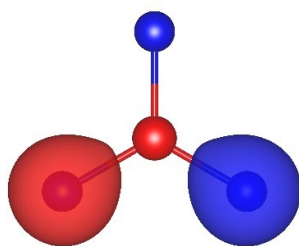


Figure 13.49: Molecular orbital *HOMO-10* of $[\text{SnBi}_3]^{5-}$. The Bi atoms are shown in blue and Sn atoms in red, respectively. The isovalue is 0.04.

Table 13.50: Calculated Paboon and NPA charges for $[\text{SnBi}_3]^{5-}$ and $[\text{CO}_3]^{2-}$

Element	Paboon	NPA
Sn	0.15	0.15
Bi	-1.72	-1.72
C	0.64	0.64
O	-0.88	-0.88

13.9 Bare Endohedral Clusters $TM@Tt_9$

Table 13.51: Structural data of optimized cluster $[Co@Ge_9]^{5-}$

Element	x	y	z
Ge	1.754429	-0.025411	-1.568484
Ge	1.727585	-1.368275	0.809898
Ge	1.723820	1.391664	0.774161
Ge	-0.002806	-2.050651	-1.160395
Ge	0.002843	2.014362	-1.221688
Sn	-0.000022	-0.000475	-0.003702
Ge	-0.000145	0.027470	2.353174
Ge	-1.755337	-0.021188	-1.568311
Ge	-1.731230	-1.364584	0.810952
Ge	-1.719140	1.397013	0.773817

Table 13.52: Structural data of optimized cluster $[Ru@Sn_9]^{6-}$

Element	x	y	z
Sn	-0.883530	0.984447	2.313091
Sn	-0.883530	0.984447	-2.313091
Sn	2.091891	0.662152	1.559871
Sn	2.091891	0.662152	-1.559871
Sn	1.778932	-1.986201	0.000000
Sn	-0.883530	-2.007967	1.561354
Sn	-0.883530	-2.007967	-1.561354
Sn	-2.689441	0.032670	-0.000000
Sn	0.260110	2.677284	0.000000
Ru	0.000838	-0.001157	0.000000

Table 13.53: Structural data of optimized cluster $[\text{Ge}_9]^{4-}$ (C_{4v})

Element	x	y	z
Ge	1.365402	1.827951	0.251689
Ge	-0.764857	1.206380	1.593993
Ge	-0.767294	1.592558	-1.207136
Ge	1.368290	-0.252739	1.824677
Ge	1.365012	0.252677	-1.826781
Ge	-2.399291	0.000113	0.002215
Ge	1.365504	-1.827285	-0.253963
Ge	-0.765148	-1.592779	1.208041
Ge	-0.767619	-1.206875	-1.592734

Table 13.54: Structural data of optimized cluster $[\text{Ge}_9]^{4-}$ (D_{3h})

Element	x	y	z
Ge	5.874090	3.936240	6.257360
Ge	3.946590	2.558600	7.616600
Ge	3.934890	5.318730	7.608360
Ge	4.545070	1.899040	5.057550
Ge	4.541400	5.964510	5.049450
Ge	1.665610	3.925480	7.122990
Ge	3.824590	3.928050	3.408160
Ge	1.926120	2.550050	4.809280
Ge	1.924790	5.311920	4.813100

Table 13.55: Structural data of optimized cluster $[\text{Sn}_9]^{4-}$ (C_{4v})

Element	x	y	z
Sn	-1.576001	-0.119022	2.104121
Sn	0.884056	1.698038	-1.516464
Sn	-1.570441	0.120436	-2.107902
Sn	0.879498	1.517300	1.698803
Sn	0.878251	-1.698782	1.518545
Sn	-1.572577	2.108080	0.118104
Sn	0.882597	-1.517686	-1.697210
Sn	-1.574568	-2.106696	-0.121802
Sn	2.769185	-0.001669	0.003805

Table 13.56: Structural data of optimized cluster $[\text{Sn}_9]^{4-}$ (D_{3h})

Element	x	y	z
Sn	26.232200	12.461910	7.815670
Sn	26.232200	17.088090	7.815670
Sn	26.920830	13.215130	4.903150
Sn	26.920830	16.334870	4.903150
Sn	24.319750	14.775000	4.314820
Sn	23.411160	13.213650	6.817550
Sn	23.411160	16.336350	6.817550
Sn	24.732570	14.775000	9.200690
Sn	28.209560	14.775000	7.302180

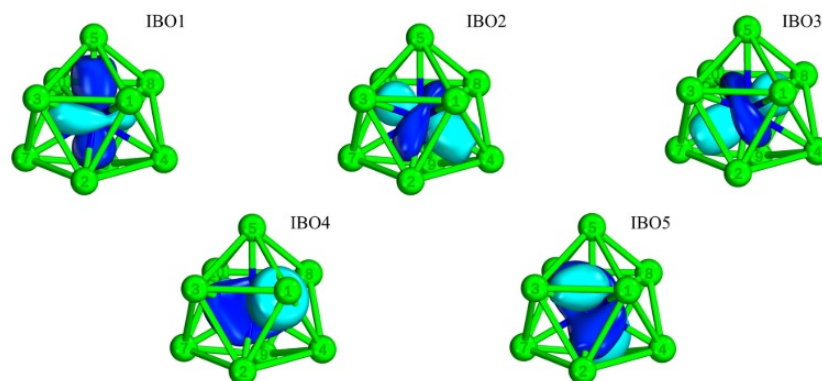


Figure 13.50: IBOs concerning the central atom of $[\text{Co}@\text{Ge}_9]^{5-}$. Co and Ge is shown in blue and light green, respectively.

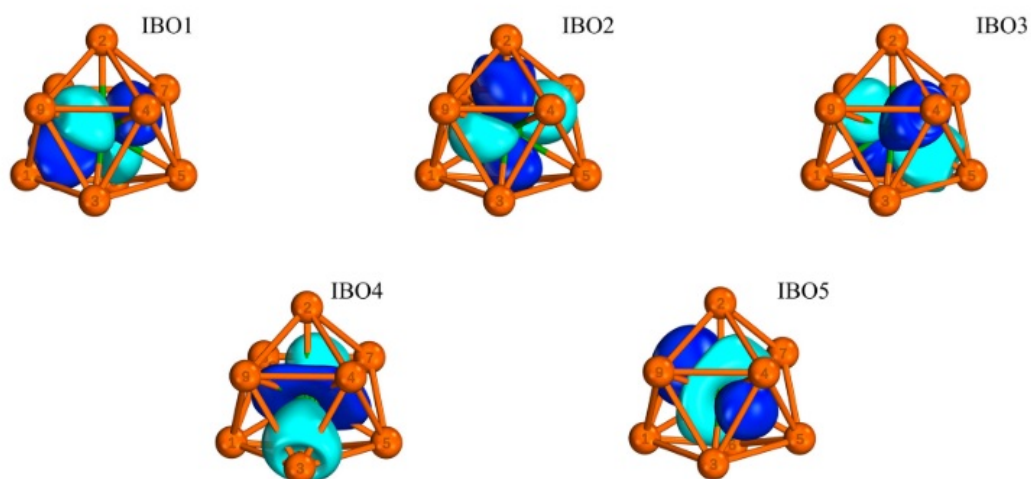


Figure 13.51: IBOs concerning the central atom of $[\text{Ru}@\text{Sn}_9]^{6-}$. Ru and Sn is shown in green and orange, respectively.

Table 13.57: Atom contribution for IBOs per 2 electrons and in percentage for $[\text{Co}@\text{Ge}_9]^{5-}$

	Co6	Ge1	Ge2	Ge3	Ge4	Ge5	Ge7	Ge8	Ge9	Ge10	other
IBO1	1.732	0	0.024	0.063	0	0.116	0	0.043	0	0	0.022
IBO2	1.736	0	0.056	0	0.117	0	0	0.048	0	0	0.043
IBO3	1.745	0	0.032	0	0	0	0.111	0.021	0	0.065	0.026
IBO4	1.561	0.228	0	0.047	0	0	0	0.06	0	0.065	0.038
IBO5	1.559	0	0.058	0.056	0	0	0	0	0.218	0.082	0.027
Overall	1.33	0.228	0.17	0.166	0.117	0.116	0.111	0.172	0.218	0.212	0.156
Overall	1.33	2.28	1.7	1.66	1.17	1.16	1.11	1.72	2.18	2.12	1.56
/											
%											

Table 13.58: Atom contribution for IBOs per 2 electrons and in percentage for $[\text{Ru}@\text{Sn}_9]^{6-}$

	Ru	Sn1	Sn2	Sn3	Sn4	Sn5	Sn6	Sn7	Sn8	Sn9	other
IBO1	1.605	0.175	0	0	0	0	0.105	0	0	0.087	0.027
IBO2	1.583	0	0.149	0	0	0	0.028	0.173	0	0.052	0
IBO3	1.569	0	0	0	0.198	0.136	0.044	0	0	0.035	0
IBO4	1.492	0	0	0.371	0.03	0	0	0.031	0	0.02	0.055
IBO5	1.485	0	0	0	0.026	0	0	0.031	0.386	0	0.072
Overall	1.734	0.175	0.149	0.371	0.254	0.136	0.177	0.235	0.386	0.194	0.154
Overall	1.34	1.75	1.49	3.71	2.54	1.36	1.77	2.35	3.86	1.94	1.54
/											
%											

Table 13.59: Calculated Raman intensities for $[\text{Co@Ge}_9]^{5-}$

Frequency / cm^{-1}	Raman activity / a.u.
47.94	4.12
68.36	6.63
72.55	5.61
104.89	0.32
109.45	14.10
110.47	0.87
120.57	0.73
123.98	2.01
124.14	0.06
127.38	1.39
129.20	1.54
158.96	8.59
159.39	8.55
167.69	0.05
199.00	29.02
200.86	32.31
203.43	15.11
207.06	97.26
207.64	94.97
244.90	1057.90
358.48	23.23
361.93	21.02
398.39	0.01

Table 13.60: Calculated Raman intensities for $[\text{Ge}_9]^{4-}$

Frequency / cm^{-1}	Raman activity / a.u.
10.44	0.00
84.23	3.59
84.51	3.54
132.22	0.18
133.48	44.93
142.85	38.29
149.75	14.53
149.92	14.79
153.79	18.41
157.98	18.06
161.69	27.41
161.81	27.27
177.24	20.07
194.09	0.05
194.25	0.04
197.79	0.40
217.98	2.59
225.35	677.48
228.44	4.39
228.49	4.39
241.49	16.21

Table 13.61: Calculated Raman intensities for $[\text{Ru}@\text{Sn}_9]^{6-}$

Frequency / cm^{-1}	Raman activity / a.u.
62.21	20.24
84.85	16.40
87.27	20.67
88.76	18.69
89.18	14.74
107.02	25.61
113.60	22.65
139.33	119.39
139.73	103.86
140.95	330.42
144.1402	79.65
147.30	300.39
174.56	4370.53
265.63	109.01
266.95	104.17

Table 13.62: Calculated Raman intensities for $[\text{Sn}_9]^{4-}$

Frequency / cm^{-1}	Raman activity / a.u.
84.44	14.20
89.19	10.92
92.14	14.63
99.53	26.06
99.59	26.18
105.85	42.94
118.90	36.39
148.63	1961.46
153.71	13.16
153.77	12.91
164.0781	28.09

13.10 Basis Sets for periodic calculations

H: The def-TZVP basis set was modified by fixing the exponent of the outermost s function to 0.13 and reoptimizing the exponents of the other s functions in the valence space. The resulting energy loss w.r.t the unmodified basis set is 0.15 mH.

1 4		
0 0 3 1.0 1.0		
45.351741106	0.60251978000E-02	
6.8233001522	0.45021094000E-01	
1.5944879907	0.20189726000	
0 0 1 0.0 1.0		
0.44546978735	1.00000000000	
0 0 1 0.0 1.0		
0.13000000000	1.00000000000	
0 2 1 0.0 1.0		
0.80	1.00000000000	

Li: The diffuse outermost s-exponents in def-SVP were increased from 0.021 and 0.053 to 0.18 and 0.36, respectively. The (2*p*)/[1*p*] polarization function with exponents of 0.45 and 0.1 was replaced by one primitive *p*-type polarization function with an exponent of 0.18 (which is close to the exponent of 0.17 in the "Pold" polarization function of TURBOMOLE library. The outermost *s* and *p* functions were finally combined into a single *sp*-type function.

3 3		
0 0 5 2.0 1.0		
266.27785516	0.64920150325E-02	
40.069783447	0.47747863215E-01	
9.0559944389	0.20268796111	
2.4503009051	0.48606574817	
0.72209571855	0.43626977955	
0 0 1 1.0 1.0		
0.36	1.0000000000	
0 1 1 0.0 1.0		
0.18	1.0 1.0	

Na: The diffuse outermost s-exponents in the molecular def2-TZVP basis set were increased from 0.019 and 0.050 to 0.10 and 0.20, respectively.^[bla] The diffuse outermost *p*-exponents were increased from 0.03 and 0.09 to 0.1 and 0.2, respectively. The outermost *s* and *p* functions were combined into two *sp*-type functions. The *d*-polarization functions with exponents of 0.43 and 0.1 were replaced with one polarization function whose exponent is the geometric mean of the original exponents (0.207).

11 9	
0 0 7 2.0 1.0	
26041.109927	0.61806342811E-03
3906.1268548	0.47748604414E-02
888.97454993	0.24471684829E-01
251.45497961	0.94755394977E-01
81.650143512	0.26867496920
28.904158401	0.47925475440
10.625782932	0.33248591469
0 0 3 2.0 1.0	
53.769410179	0.19527731872E-01
16.308243025	0.92648010794E-01
2.3730384125	-0.39938670172
0 0 2 1.0 1.0	
0.95730772603	1.6428595391
0.40806460959	0.55692596966
0 1 1 0.0 1.0	
0.20	1.0 1.0
0 1 1 0.0 1.0	
0.10	1.0 1.0
0 2 5 6.0 1.0	
138.07979989	0.57951891929E-02
32.232700393	0.41620846251E-01
9.9816075360	0.16281916885
3.4822033928	0.36011784647
1.2299134620	0.44858979889
0 2 1 0.0 1.0	
0.41743959423	1.0
0 3 1 0.0 1.0	
2.609	1.0
0 3 1 0.0 1.0	
0.207	1.0

B: The def-TZVP basis set was modified as follows: The outermost *s*-function was removed, leaving still three *s*-functions in the valence space. The {411} *p* valence space was decontracted to {3111} and the outermost *p*-function was removed, leaving three *p*-functions in the valence space. The exponents of the outermost *s* and *p* functions were fixed to 0.17 and the exponents of the other *s* and *p* functions in the valence space were optimized for the boron atom in its ground state using

TURBOMOLE program package. Finally, the outermost *s* and *p* functions were combined into a single *sp*-type function to increase the efficiency of the CRYSTAL code. The resulting energy loss w.r.t the unmodified basis set is 15 mH.

0 0 6 2.0 1.0	
8564.8660687	0.22837198155E-03
1284.1516263	0.17682576447E-02
292.27871604	0.91407080516E-02
82.775469176	0.36342638989E-01
27.017939269	0.11063458441
9.8149619660	0.23367344321
0 0 2 2.0 1.0	
3.9295537119	0.41818777978
1.6980409139	0.22325473798
0 0 1 0.0 1.0	
0.57483069645	1.0000000000
0 1 1 0.0 1.0	
0.17000000000	1.0 1.0
0 2 3 1.0 1.0	
28.577505088	0.50265575179E-02
6.7104492541	0.32801738965E-01
2.0721954358	0.13151230768
0 2 1 0.0 1.0	
0.64922416350	1.0000000000
0 3 1 0.0 1.0	
0.50000000000	1.0000000000

C:

6 5	
0 0 5 2.0 1.0	
1238.4016938	0.54568832082E-02
186.29004992	0.40638409211E-01
42.251176346	0.18025593888
11.676557932	0.46315121755
3.5930506482	0.44087173314
0 0 1 2.0 1.0	
0.56046415662	1.00000000000
0 1 1 0.0 1.0	
0.23000000000	1.0 1.0
0 2 3 2.0 1.0	
11.852514432	0.38387871728E-01
2.5673213956	0.21117025112
0.79737433183	0.51328172114
0 3 1 0.0 1.0	
0.80000000000	1.00000000000

N: We modified the molecular def-TZVP basis by removing the outermost s -function, leaving still three s -functions in the valence space. The exponents of the outermost s and p functions were set fixed to 0.22 and the exponents of the other s and p functions were optimized as discussed above for the SVP basis set. The resulting energy loss w.r.t the unmodified basis set is 3 mH.

```

7 7
0 0 6 2.0 1.0
  19730.800647      0.21887984991E-03
  2957.8958745     0.16960708803E-02
  673.22133595     0.87954603538E-02
  190.68249494     0.35359382605E-01
  62.295441898     0.11095789217
  22.654161182     0.24982972552
0 0 2 2.0 1.0
  8.9809711129     0.40623896148
  3.6377863436     0.24338217176
0 0 1 0.0 1.0
  0.72643334701    1.00000000000
0 1 1 0.0 1.0
  0.22000000000    1.0 1.0
0 2 4 3.0 1.0
  63.222276180     0.55552416751E-02
  15.013291910     0.38052379723E-01
  4.6766636605     0.14953671029
  1.7814167689     0.34949305230
0 2 1 0.0 1.0
  0.68476710337    1.00000000000
0 3 1 0.0 1.0
  1.00000000000    1.00000000000

```

Al: The def-TZVP basis set was used as a starting point. We fixed the exponents of the outermost *s* and *p* functions to 0.10 and reoptimized the exponents of the other *s* and *p* functions in the valence space for the aluminum atom in its ground state. Finally, the outermost *s* and *p* functions were combined into *sp*-type functions. The resulting energy loss with respect to the original molecular basis set is 8.6 mH. The original *d*-polarization function with an exponent of 0.30 was applied.

```

13 9
0 0 7 2.0 1.0
  37792.550772      0.57047888709E-03
  5668.0682165     0.44093016538E-02
  1289.8582841     0.22630967411E-01
  364.86596028     0.88025644295E-01
  118.57631515     0.25223701612
  42.024867605     0.45960547169
  15.499501629     0.33277886014
0 0 3 2.0 1.0
  75.208026598     0.19250560190E-01
  23.031408972     0.87906743952E-01
  3.6348797649     -0.34246704535
0 0 2 2.0 1.0
  1.6020065437     1.5106266058
  0.78069416556     0.58071016470
0 0 1 0.0 1.0
  0.27777633704     1.0
0 1 1 0.0 1.0
  0.10000000000     1.0 1.0
0 2 6 6.0 1.0
  452.52303192     0.23110812466E-02
  107.08195049     0.18568641823E-01
  34.131021255     0.87216237035E-01
  12.587037428     0.26902101523
  4.9811919704     0.52128324272
  2.0070350900     0.60271687494
0 2 1 1.0 1.0
  0.82081434825     1.0
0 2 1 0.0 1.0
  0.39036158090     1.0
0 3 1 0.0 1.0
  0.300              1.0

```

P: For the triple-zeta-valence basis set, the def-TZVP basis set was used as a starting point. We fixed the exponents of the outermost s and p functions to 0.13 and reoptimized the exponents of the other s and p functions in the valence space for the phosphorus atom in its ground state. Finally, the outermost s and p functions were combined into sp -type functions. The resulting energy loss with respect to

the original molecular basis set is 2.9 mH. We applied the original *d*-polarization function with an exponent of 0.45.

```

15 8
0 0 7 2.0 1.0
52426.999233          0.55207164100E-03
7863.2660552         0.42678595308E-02
1789.5227333         0.21931529186E-01
506.27300165         0.85667168373E-01
164.60698546         0.24840686605
58.391918722         0.46336753971
21.643663201         0.35350558156
0 0 3 2.0 1.0
99.013837620         0.21895679958E-01
30.550439817         0.95650470295E-01
5.4537087661         -0.29454270186
0 0 2 2.0 1.0
2.6477257457         1.3294381200
1.2738231734         0.66109396473
0 1 1 0.0 1.0
0.35000000000         1.0 1.0
0 1 1 0.0 1.0
0.13000000000         1.0 1.0
0 2 6 6.0 1.0
472.27219248         0.25710623052E-02
111.58882756         0.20250297999E-01
35.445936418         0.91580716787E-01
12.990776875         0.25749454014
5.0486221658         0.42862899758
1.9934049566         0.34359817849
0 2 1 3.0 1.0
0.69644412108         1.00000000000
0 3 1 0.0 1.0
0.450                 1.0

```

K: The SVP basis set was derived from the molecular Karlsruhe def-SVP basis set. The most diffuse *s* exponent of 0.012 was removed. The remaining outermost *s*-exponent was increased from 0.029 to 0.14. The inner (*3s*) function was decontracted to (*2s1s*) and the exponent 0.282 was changed to 0.28. The most diffuse *p* exponent

of 0.04 was increased to 0.14. The ($3p$) function was decontracted to ($2p1p$) and the exponent of 0.208 was increased to 0.28. The two outermost s and p functions were finally combined into two sp -type functions.

```

19 8
0 0 6 2.0 1.0
31478.746764          0.39838653994E-02
4726.8876066         0.30501759762E-01
1075.4345353         0.15073752622
303.39811023         0.51912939801
98.327112831         1.0366957005
33.636222177         0.76398963199
0 0 3 2.0 1.0
65.639209962         -0.28242617106
7.3162592218         1.6914935860
2.8902580135         1.2965331953
0 0 2 2.0 1.0
4.5459748965         -0.76343555273E-02
.70404124062         0.25635718960E-01
0 1 1 1.0 1.0
0.28                  1.0 1.0
0 1 1 0.0 1.0
0.14                  1.0 1.0
0 2 5 6.0 1.0
361.22492154         0.20906479823E-01
84.670222166         0.15043641740
26.469088236         0.55440061077
9.2658077615         1.0409009991
3.3423388293         0.67825341194
0 2 2 6.0 1.0
1.5100876104         0.75248191146
0.56568375163         1.3708585031
0 3 1 0.0 1.0
0.353                 1.0

```

Ni: The diffuse outermost s -exponents in def-SVP were increased from 0.038 and 0.105 to 0.14 and 0.35, respectively. The exponent of the p -type polarization function was changed from 0.147 to 0.14 and the outermost s and p functions were then combined into a single sp -type function.

28 9	
0 0 6 2.0 1.0	
71074.803211	.14260386729E-02
10672.020941	.10928236994E-01
2428.1389007	.54212626938E-01
685.53595148	.18874768902
223.10072863	.38324616985
76.842014042	.29550637144
0 0 3 2.0 1.0	
148.71122016	-.11014443059
17.459154987	.64521426988
7.1625280665	.44797838103
0 0 3 2.0 1.0	
12.556137125	-.22645403224
2.0735740488	.72320959286
.85382640602	.44868026476
0 0 1 1.0 1.0	
0.35	1.0000000000
0 1 1 0.0 1.0	
0.14	1.0 1.0
0 2 5 6.0 1.0	
916.73608662	.93439635610E-02
216.06139913	.69737374902E-01
68.383914817	.27073495012
24.593843952	.53078301549
9.1392960204	.34410229438
0 2 3 6.0 1.0	
4.7193371746	.34076082016
1.8161849234	.56580169611
0.6784075072	.23616717361
0 3 4 9.0 1.0	
47.093832108	.28982316948E-01
13.146463975	.15494995950
4.4170548925	.37633115111
1.4771565078	.47365096014
0 3 1 0.0 1.0	
0.4373592179	.31247837833

Zn: The used basis set, derived from def-SVP, has been described in Tanskanen,

J. T.; HÅggglund, C.; Bent, S. F. Chem. Mater. 2014, 26, 2795-2802.

30 9

0 0 6 2.0 1.0

82000.711629 .14210764000E-02

12312.471777 .10891499487E-01

2801.3944193 .54057188059E-01

790.99424302 .18847463904

257.56551079 .38346549346

88.814933400 .29723794197

0 0 3 2.0 1.0

171.86353716 -.11051849523

20.302534785 .64607716984

8.3464123068 .44220117322

0 0 3 2.0 1.0

14.847536940 -.22705309278

2.4495029507 .72433217935

.99845821824 .44836495592

0 0 1 2.0 1.0

.40 1.0000000000

0 1 1 0.0 1.0

.16 1.0 1.0

0 2 5 6.0 1.0

1071.5185372 .92767797235E-02

252.69712152 .69541149434E-01

80.100829126 .27156772564

28.903393172 .53401355573

10.768899879 .34501323446

0 2 3 6.0 1.0

5.6446212530 .34129600164

2.1678291347 .56390521973

.80540898341 .23676109735

0 3 4 10.0 1.0

56.088939191 .29588869140E-01

15.751908917 .158725714045

5.3115812367 .379762291591

1.7737904917 .468989591719

0 3 1 0.0 1.0

.51975583665 .309071490776

Ga: The def-TZVP basis set was used as a starting point.[F. Weigend, R. Ahlrichs; Phys. Chem. Chem. Phys. 2005, 7, 3297.] We fixed the exponents of the outermost s and p functions to 0.09 and reoptimized the exponents of the other s and p functions in the valence space for the gallium atom in its ground state. Finally, the outermost s and p functions were combined into sp-type functions. At this point, the resulting energy loss with respect to the original molecular def-TZVP basis set was 3.0 mH. Next, we kept the outermost d-function fixed and optimized the exponents of the other d-functions in the valence space, analogously to the derivation of molecular def2-TZVP basis set for In-I and Tl-At.[F. Weigend, R. Ahlrichs; Phys. Chem. Chem. Phys. 2005, 7, 3297.] The energy was improved and the final energy was is 1.5 mH lower than in the molecular def-TZVP basis set.

31 14

0 0 8 2.0 1.0	
435548.66254	0.23646329650E-03
65289.589031	0.18335271776E-02
14858.784256	0.95371863081E-02
4205.9734729	0.38803412468E-01
1369.6416431	0.12661604848
492.30348905	0.30175310292
191.41923233	0.43543934218
75.840558665	0.23282363780
0 0 4 2.0 1.0	
474.30810613	-0.26743707958E-01
147.10297560	-0.12654657542
23.982599435	0.58840346839
10.298230094	0.56324271589
0 0 2 2.0 1.0	
16.050381430	-0.24516439508
2.6988468784	0.74578049593
0 0 1 2.0 1.0	
1.1452841362	1.0000000000
0 0 1 0.0 1.0	
0.25080935147	1.0000000000
0 1 1 0.0 1.0	
0.09000000000	1.0 1.0
0 2 6 6.0 1.0	
2432.0171070	0.22434065928E-02
576.12049582	0.18342265336E-01
185.11584354	0.87279697167E-01
69.246572556	0.25684868351
27.818107777	0.42398378107
11.420229938	0.25701340043
0 2 3 6.0 1.0	
42.819661530	-0.19326519119E-01
6.3885901000	0.31571386917
2.6698993326	0.57617792822
0 2 1 1.0 1.0	
1.0965804072	1.0000000000
0 2 1 0.0 1.0	
0.32984082243	1.0000000000
0 3 5 10.0 1.0	
107.38114308	0.11464613652E-01
31.543551222	0.73625747383E-01
11.422960020	0.23505107382

Ge: We modified the molecular def2-SVP basis set for periodic calculations by fixing the exponents of the outermost s and p functions to 0.11 and reoptimizing the exponents of the other s and p functions in the valence space for the Ge atom in its ground state. The basis set optimization was performed with the TURBOMOLE program package. The resulting energy loss w.r.t the unmodified basis set is 3 mH. We then further optimized the exponents of the d-functions while keeping the outermost exponent 0.246 fixed (analogously as done for elements In-Xe in the def2-SVP bases). This improved the energy by 11 mH.

32 11

0 0 6 2.0 1.0	
93889.836642	0.14233976060E-02
14097.497528	0.10910795654E-01
3207.5477309	0.54183705943E-01
905.76727269	0.18922820349
295.11014693	0.38612847001
101.84713141	0.30164050736
0 0 3 2.0 1.0	
196.56719662	-0.11118770940
23.405292522	0.64616007369
9.6839116702	0.44188904568
0 0 3 2.0 1.0	
17.269736544	-0.23027421375
2.8964622160	0.73017169398
1.2553621412	0.46197222255
0 0 1 2.0 1.0	
0.24193683152	1.00000000000
0 1 1 0.0 1.0	
0.11000000000	1.0 1.0
0 2 5 6.0 1.0	
1259.2085995	0.90115464252E-02
297.15626382	0.67986841689E-01
94.353387522	0.26853856488
34.176329677	0.53659649219
12.816139615	0.35633514961
0 2 3 6.0 1.0	
6.8471029784	0.33900693119
2.7717363939	0.56809365264
1.1458418175	0.27246539884
0 2 1 2.0 1.0	
0.36501515146	1.00000000000
0 3 4 10.0 1.0	
77.307034042	0.25755860205E-01
22.179982814	0.14536816132
7.7730468533	0.37134209859
2.8537306947	0.48002998436
0 3 1 0.0 1.0	
0.99741765223	1.00000000000
0 3 1 0.0 1.0	
0.24600000000	1.00000000000 ²⁸⁴

Ta: he diffuse outermost s-exponent of the molecular def2-TZVP basis set was removed (0.038) and the remaining outermost exponent of 0.103 was increased to 0.11. [1, 2] The two outermost p-exponents of 0.065 and 0.27 were replaced with one p-function (exponent 0.11). The outermost s and p functions were combined into one sp-type function. The outermost diffuse d-function with an exponent of 0.088 was removed. d-function with an exponent of 0.61 was decontracted out of the innermost contracted d-function, leaving a d-function with an exponent of 0.24 as the outermost d-function. The f-type polarization function was removed.

273 10

INPUT

13. 0 2 2 2 1 1

14.546408 1345.880647 0

7.273204 36.766806 0

9.935565 378.425301 0

4.967782 22.293091 0

6.347377 104.883956 0

3.173688 8.755848 0

2.017881 12.017961 0

3.040330 -11.728933 0

0 0 4 2.0 1.0

24.473650944 0.20590322488

18.721372549 -0.74670795514

11.500000000 3.4071363897

10.350000000 -2.8175487609

0 0 1 2.0 1.0

3.8436180089 1.0000000000

0 0 1 0.0 1.0

1.0202266016 1.0000000000

0 0 1 0.0 1.0

0.46774781869 1.0000000000

0 1 1 0.0 1.0

0.11 1.0 1.0

0 2 4 6.0 1.0

17.000000000 -0.32577305616E-01

12.008186536 0.10336287365

5.0278760583 -0.28526521696

1.1937124184 0.51790141155

0 2 1 0.0 1.0

0.57889707053 1.0000000000

0 3 2 3.0 1.0

3.9738796278 -0.52799310714E-01

1.4528884813 0.18558319471

0 3 1 0.0 1.0

0.61042908544 0.42959071631

0 3 1 0.0 1.0

0.24216276510 1.0000000000

Bi: We modified the molecular def2-TZVP basis set for periodic calculations by first removing the most diffuse p function with an exponent of 0.055, then fixing the exponents of the outermost s and p functions to 0.10, and finally reoptimizing the exponents of the other s and p functions in the valence space for the Bi atom in its ground state. The outermost s and p functions with an exponent of 0.1 were combined into one single sp-type function. The exponent of the outermost d-function was increased from 0.14 to 0.165 and the steep f function with an exponent of 1.05 was removed. The basis set optimization was performed with the TURBOMOLE program package. The resulting energy loss w.r.t the unmodified basis set is 3 mH.

283 13

INPUT

23. 0 2 4 4 2 2

13.043090 283.264227 0

8.221682 62.471959 0

10.467777 72.001499 0

9.118901 144.002277 0

6.754791 5.007945 0

6.252592 9.991550 0

8.081474 36.396259 0

7.890595 54.597664 0

4.955556 9.984294 0

4.704559 14.981485 0

4.214546 13.713383 0

4.133400 18.194308 0

6.205709 -10.247443 0

6.227782 -12.955710 0

0 0 4 2.0 1.0

716.41435310 0.31254307133E-03

83.806059047 0.17624768946E-02

21.116962853 -0.21910983437

15.491448187 0.40411224931

0 0 2 2.0 1.0

23.213322651 -0.68255758685E-01

6.6412776932 0.97888046471

0 0 1 0.0 1.0

1.7668753097 1.0000000000

0 0 1 0.0 1.0

0.87636753866 1.0000000000

0 0 1 0.0 1.0

0.26185055933 1.0000000000

0 1 1 0.0 1.0

0.10 1.0 1.0

0 2 3 6.0 1.0

15.249644669 0.74560356000

14.846176053 -0.85578637338

7.0636826784 0.40149159592

0 2 3 3.0 1.0

2.5802708340 0.35542729633

1.4990870077 0.63976991890

0.75411119473 0.32332773839

0 2 1 0.0 1.0

0.29617825843 1.0000000000

References

- [1] M. Zeilinger, T. F. Fassler, *Dalton Transactions* **2014**, *43*, 14959–14970.
- [2] H. Okamoto, *J. Phase Equilib.* **2017**, *38*, 70–81.
- [3] R. P. Elliott, F. A. Shunk, *Bull. alloy phase diagr.* **1980**, *1*, 47–51.
- [4] W. Setyawan, S. Curtarolo, *Comput. Mater. Sci.* **2010**, *49*, 299–312.
- [5] L. M. Scherf, PhD thesis, TU Munich, **2017**.

List of Figures

1.1	Scheme of conventional Li-ion battery cell. Cathode is made of Li_xCo_2 and anode of Li_xC with a liquid electrolyte such as LiPF_6	5
2.1	(a) Used silica tube showing all used parts next to each other and assembled silica tube. (b) Used disassembled aluminumoxid tube. . .	21
5.1	Ternary composition diagram of the phase system Li-Ni-Ge including all know binaries. For clarity not all Li-Ge-compounds were assigned. A full list if all compounds is given in Table. 5.1. At the corners the pure elements Li, Ni and Ge are located. Compounds investigated in this thesis are given in red and a excerpt of the crystal structure of all ternary compound is given. Li, Ni and Ge atoms are shown in red, green and blue, respectively. Structures written in red investigated in this work.	50
5.2	Excerpt of the CaNi_5Ge_3 crystal structure showing the rhombic dodecahedral surrounding of the endohedral Ni in green and Ge in blue. Ge, Ni and Ca atoms are represented as spheres in blue, green and red, respectively.	52
5.3	Structure of $[M@TM_8E_6]$ ($M = (\text{semi})\text{-metal}$, $TM = \text{transition metal}$, $E = \text{semi-metal or ligand}$).	53
5.4	Experimental P-XRD diffractogram (black) with the theoretical pattern of $\text{Li}_{14}\text{Ni}_{8.3}\text{Ge}_{8.7}$ (red). Minor unknown sidephases are marked with an asterisk.	57
5.5	Unit cell with highlighted Ni_8Ge_6 clusters of the compound $\text{Li}_{14}\text{Ni}_{8+x}\text{Ge}_{9-x}$. Li, Ni, Ge and Ni/Ge mixed positions are represented as as ellipsoids at the 90 % probability level in in red, green, blue and teal respectively. In chapter 13.1 further structure pictures are shown.	59

5.6	(a) Unit cell with highlighted Ni ₈ Ge ₆ clusters and Li ₈ cubes of the compound Li ₁₄ Ni _{8+x} Ge _{9-x} . (b) The cuboctahedral coordination sphere of Li2 atoms as well as the Li1 cubes in the octahedral voids are marked with red polyhedra. (c) (Ni/Ge@Ni ₈ Ge ₆) cluster with cuboctahedral surrounding of Li2 atoms (red polyhedron) and Ge3 atoms capping the triangular faces of the cuboctahedron in the compound Li ₁₄ Ni _{8+x} Ge _{9-x} . (d) Unit cell of Li ₁₄ Ni _{8+x} Ge _{9-x} in nearly bc-direction highlighting the Li filled channels in the structure. Covalent bonds are marked with thick teal lines. Thin lines represent the coordination of Li atoms. Li, Ni, Ge and Ni/Ge mixed positions are represented as ellipsoids at the 90 % probability level in red, green, blue and teal respectively.	61
5.7	Thermogramm of Li ₁₄ Ni _{8+x} Ge _{9-x} containing minor sidephases. The first and second heating traces are shown as black and purple lines, respectively. The first and second cooling traces are shown in red and blue, respectively.	62
5.8	Cluster unit showing atom labels and bond labels.	63
5.9	(a): IBO-325 of [Ge@Ni ₈ Ge ₆] ⁶⁻ showing a dz ² -like orbital at Ni1. Ge and Ni are colored blue and green, respectively. Contribution of each atom to the IBO: Ni1 78 %, Ge1 18 %, Ge2 1 %, Others 3 %. (b): IBO-300 of [Ge@Ni ₈ Ge ₆] ⁶⁻ showing a bonding orbital between Ge3 and Ni1. Contribution of each atom to the IBO: Ge3 71 %, Ni1 17 %, Ge1 9 %. (c): IBO-291 and (d) IBO-292 of [Ge@Ni ₈ Ge ₆] ⁶⁻ showing a p-like orbital at Ge2 bonding to Ge1 in x or y direction, respectively. Contribution of each atom to the IBO: Ge2 52 %, Ge1 32 %, Ni1 12 %. (e): IBO-283 and (f) IBO-284 of [Ge@Ni ₈ Ge ₆] ⁶⁻ showing a orbital at Ge1 in z direction. Contribution of each atom to the IBO: Ge2 54 %, Ge1 18 %, Ni1 15 %. Ge and Ni are colored blue and green, respectively.	66
5.10	Experimental P-XRD diffractogram (black) with the theoretical pattern of LiNi _{1+x} Ge (x = 0.17) (red). Minor sidephases are marked with an asterisk.	71

5.11	Structure of $\text{LiNi}_{1+x}\text{Ge}$. On the left side the unit cell is shown. The blue and red rectangles show close ups of layers and cluster units. And the top right pictures shows the top view of a cluster unit along c . The structure shows a ABC layered structure assigned in the illustration. Li, Ni1, Ni2 and Ge1 are represented as as ellipsoids at the 90 % probability level in in red, grey, black and green, respectively. The partial occupied position is shown in black. Thin black lines indicate polyhedra borders. For a better clarity Ni1 and Ni2 is marked by different colors.	72
5.12	Structure of $\text{LiNi}_{1+x}\text{Ge}$. (a): the dislocation of the layers ist shown in blue, yellow and red, which are respresenting the differend layers A, B and C. (b): Top view of (a). (c) and (d): tetrahedral coordination of the Li atom is shown. Li, Ni and Ge are represented as as ellipsoids at the 90 % probability level in in red, grey and green, respectively.	73
5.13	Structure of $\text{LiNi}_{1+x}\text{Ge}$ (left) and SrNi_3Ge_2 (right) showing different stacking of layers. Li, Sr, Ni and Ge are represented as as ellipsoids at the 90 % probability level for $\text{LiNi}_{1+x}\text{Ge}$ and spheres for SrNi_3Ge_2 in in red, yellow, grey and green, respectively.	74
5.14	(a) Thermogramm of $\text{LiNi}_{1+x}\text{Ge}$ containing minor sidephases. The first and second heating traces are shown in black and purple, respectively. The first and second cooling traces are shown in red and blue, respectively. (b) Experimental P-XRD diffractogram of sample after DSC measurement (black) and theoretical pattern of $\text{Li}_{15}\text{Ge}_4$ ^[11] and NbNiGe . ^[54]	75
6.1	Fragments of the crystal structures of binary Li-Ge phases. The phases are color-coded according to the dimensionality of the anionic Ge framework: Ge octa- or tetrahedra (red), isolated Ge atoms (yellow), no detailed structure available (black), two-dimensional molecular units like dimer, triangles or rings (green) and two-dimensional layers (light blue). For clarity most of the Li atoms were removed in the structure $\text{Li}_{17}\text{Ge}_4$	80
6.2	All known ternary compounds of the Li-Ag-Ge system according to their Li content. The structures are divided in three different categories: Molecular units of Ag and Ge (red), NaTl-like anionic substructure with channels for Li-ions (green) and three-dimensional structures without channels for Li-ions (light-blue).	82

6.3	Ternary composition diagram of the phase system Li-Ag-Ge including all know binaries. For clarity not all Li-Ge-compounds were assigned. A full list if all compounds is given in Table. 6.1. At the corners the pure elements Li, Ag and Ge are located. Compounds investigated in this thesis are given in red and a excerpt of the crystal structure of all known ternary compound is given. Li, Ag, Ge and a Li/Ag mixed position are shown in red, grey, blue and orange, respectively.	82
6.4	Excerpt of the crystal structure of α -Li ₂ AgGe showing the NaTl-like anionic Ag/Ge-substructure stuffed with Li-ions. Li, Ag and Ge are shown in red, grey and blue, respectively.	84
6.5	<i>(a)</i> Coordination environment of Li in α -Li ₂ AgGe. <i>(b)</i> Channel provided by the anionic Ag-Ge network for Li-ions. Li, Ag and Ge are shown in red, grey and blue, respectively.	85
6.6	Excerpt of the crystal structure of α -Li _{2.53} AgGe ₂ showing the NaTl-like anionic Ag/Ge-substructure stuffed with Li-ions. Li, Ag and Ge are shown in red, grey and blue, respectively.	85
6.7	<i>(a)</i> Coordination environment of Li-vacancy at <i>4b</i> postilion of α -Li _{2.53} AgGe ₂ . <i>(b)</i> Coordination environment of Li. <i>(c)</i> Channel provided by the anionic Ag-Ge network for Li-ions with Li-vacancies. Possible Li-mobility is shown with red arrows. Li, Ag, Ge and Li-vacancy are shown in red, grey, blue and white, respectively.	86
6.8	RIETVELD-refinement of β -Li ₂ Ag _{0.8} Ge _{1.2} from powder P-XRD diffraction data ($\lambda = 0.7107 \text{ \AA}$) at room temperature. Red circles show observed intensities Y_{obs} , the black line shows the calculated intensities Y_{calc} , blue line reveal the difference of observed and calculated intensities ($Y_{obs} - Y_{calc}$), and green marks indicate BRAGG positions of α -Li ₂ Ag _{0.8} Ge _{1.2} .The region from 17.1 to 17.55 ° has been excluded, because this peak belongs device issues and is not part of the measured powder.	91
6.10	Vergard-Plot of β -Li ₂ Ag _{1-x} Ge _{1+x} ($x = 0.1, 0.2, 0.25, \text{ and } 0.3$). Errors in a and x parameter is implied by vertical and horizontal lines. . . .	95

6.9	(a) Unit cell of a CsCl structure type showing the primitive cubic cell with filled cubic void. (b) Unit cell of an $ABCD$ structure derived from a CsCl structure by doubling all cell parameters a , b and c . (c) A_2CD structure of a typical HEUSLER phase. (d) AB_2C structure of a ZINTL phase like Li_2AuBi . (e) Unit cell of (1) . Li is shown in red and Ag/Ge in dark yellow. The thinner lines show the CsCl-like substructure. (f) Structure of (1) showing the diamond-like network of Ag/Ge. Li is shown in red and Ag/Ge in purple. The thinner lines show the unit cell borders.	96
6.11	P-XRD pattern of $\beta\text{-Li}_2\text{Ag}_{1-x}\text{Ge}_{1+x}$ with different stoichiometry ($x = 0.1, 0.2, 0.25$, and 0.3). Reflexes of $\beta\text{-Li}_2\text{Ag}_{0.8}\text{Ge}_{1.2}$ are shown by vertical lines. A clear trend is visible for larger 2Θ with higher Ag content. Side phase is marked by asterisk.	97
6.12	RIETVELD-refinement of $\alpha\text{-Li}_2\text{Ag}_{0.8}\text{Ge}_{1.2}$ from powder P-XRD diffraction data ($\lambda = 0.7107 \text{ \AA}$) at room temperature. Red circles show observed intensities Y_{obs} , the black line shows the calculated intensities Y_{calc} , blue line reveal the difference of observed and calculated intensities ($Y_{obs} - Y_{calc}$), and green marks indicate BRAGG positions of $\alpha\text{-Li}_2\text{Ag}_{0.8}\text{Ge}_{1.2}$	100
6.13	$\alpha\text{-Li}_2\text{Ag}_{0.8}\text{Ge}_{1.2}$ shown as a superstructure of the X_2YZ -structure in $XYZZ'Y'$ -layers. Li is always occupying the X position, whereas Ge and Ag switch within the X_2YZ -subunit between Y and Z position. Layers in a X_2YZ -subunit occupied by Ag and Ge is assigned as a and b , respectively. Li, Ag and Ge are shown in red, grey and blue spheres.	101
6.14	(a) The typical diamond-like structure is shown, which Li intercalated channels. (b) The Ge-Ge bonds are shown as thicker red lines to make the arrangement as $\frac{1}{\infty}[\text{Ge}_2]$ zig-zag chains along the a or b axis clear.	102
6.15	PXRD of $\alpha\text{-Li}_{2.53}\text{AgGe}_2$ (top) and $\gamma\text{-Li}_{2.53}\text{AgGe}_2$ (bottom). Peaks marked by asterisk are caused by the colimator	105
6.16	(a) A unit cell of (1) . Li is shown in red/white according to partial occupation and Ag/Ge in grey/blue according to site occupation at a 90% probability level. The thinner lines show the CsCl-derived substructure. (b) Structure of (1) showing the diamond-like network of Ag/Ge. Li is shown in red and Ag/Ge in purple. The thinner lines show the unit cell borders.	106

6.17	Group-subgroup relationships shown by the Bärnighausen family tree formalism. The aristotype in space group $Fd\bar{3}m$ is shown on top of the tree. By symmetry reduction described next to the arrows the hettotypes are derived. Synthesized compounds are labeled by numbers from (1) to (5) , whereas all theoretical models for quantum chemical calculations are labeled by a three letter code naming the crystal system and a number.	107
6.18	Addition to the Bärnighausen family tree this scheme is showing the Wyckoff position splitting. Li positions are shown in red, Ag in grey, Ge in green, mixed Ag/Ge in blue and vacancies in black. Most of the positions were calculated due to symmetry reductions rules, except structures with crystallographic data. In this case the experimental parameters were used in the tables.	108
6.19	DSC thermogram of (a) α -Li ₂ AgGe (5) (b) α -Li ₂ Ag _{0.8} Ge _{1.2} (3) and (c) α -Li _{2.53} AgGe ₂ (4). Lines and numbers indicate the onset temperatures of the corresponding thermal effects. The 1st and 2nd heating circle is shown in green and light green, respectively. The 1st and 2nd cooling circle is shown in violet and light violet, respectively.	111
6.20	⁶ Li MAS-NMR of five different phases of the Li-Ge-Ag phase system. Spectra were recorded at a spinning speed of 12.5 kHz (1-4) or 10 kHz (5).	113
6.22	Relative energies of Cub1 , Tet1-3 and Tri1-3 in kJ/mol per unit. Tet4-5 were not included due to different stoichiometry.	118
6.21	Band structure and density of states of a) Cub1 , b) Tet2 , c) Tet5 and d) Tri3	123
7.1	Fragments of the crystal structures of binary Li-Si phases. The phases are color-coded according to the dimensionality of the anionic Si framework: Si octa- or tetrahedrons (red), isolated Si atoms (yellow) and two-dimensional molecular units like dimer, triangles or rings (green). For clarity most of the Li atoms were removed in the structure Li ₁₇ Si ₄	126
7.2	Excerpt of the crystal structure of α -Li ₁₃ Ag ₅ Si ₆ showing the diamond-like anionic Ag/Si-substructure stuffed with Li-ions. Li, Ag and Si are shown in red, grey and light blue, respectively.	127

7.3	Ternary composition diagram of the phase system Li-Ag-Si including all known binaries. For clarity not all Li-Si-compounds were assigned. A full list of all compounds is given in Table. 7.1. At the corners the pure elements Li, Ag and Si are located. Compounds investigated in this thesis are given in red and an excerpt of the crystal structure of all known ternary compounds is given. Li, Ag, Si, Li/Si and Li/Ag positions are shown in red, grey, light blue, purple and light orange, respectively.	128
7.4	(a) A unit cell of β -Li ₁₃ Ag ₅ Si ₆ . Li is shown in red according and Ag/Si in grey/light blue according to site occupation at a 90% probability level. The thinner lines show the CsCl-like substructure. (b) Structure of β -Li ₁₃ Ag ₅ Si ₆ showing the diamond-like network of Ag/Si. Li is shown in red and Ag/Si in dark red. The thinner lines show the unit cell borders.	133
7.5	DSC thermogram of β -Li ₁₃ Ag ₅ Si ₆ . Lines and numbers indicate the onset temperatures of the corresponding thermal effects. The 1st and 2nd heating cycle is shown in green and light green, respectively. The 1st and 2nd cooling cycle is shown in violet and light violet, respectively.	133
8.1	Structure of Li ₆ B ₁₈ (Li ₃ N) _x . B, N and Li atoms are shown in dark yellow, blue and red, respectively. The 3 ² 4 ⁸ 6 ² boron network built of B ₆ octahedra is shown with black bonds. (a) View along <i>c</i> -axis with an enlarged cell showing two kinds of channels stuffed with either Li or Li ₃ N. (b) View along <i>c</i> -axis showing only the unit cell.	139
8.2	Total and partial DOS curves in the range of -6 eV to 4 eV for Li ₆ B ₁₈ (Li ₃ N). Band structure of Li ₆ B ₁₈ (Li ₃ N) in the range of -6 eV to 4 eV, the bands marked in red mainly correspond to states of the atoms situated in the large pores of the structure.	140
8.3	Raman spectra of Li ₆ B ₁₈ (Li ₃ N) _x (experimental) in black and of Li ₆ B ₁₈ (Li ₃ N) (calculated) in red with assigned modes. The Raman shifts of the calculated Raman spectra were multiplied by a factor of 0.95 due to the systematic overestimation of Raman frequencies by the functional PBE0. ^[37]	141
8.4	(a) Structure of template-free Li ₆ B ₁₈ in $P\bar{6}2m$, white globes represent the void Li ₂ positions. (b) Band structure of $P\bar{6}2m$ -Li ₆ B ₁₈ in the range of -4.5 to 6.5 eV.	142
8.5	(a) Structure of Li ₆ B ₁₈ (Li ₃ N) showing channels A and B and in-plane diffusion path. (b) Channel A with diffusion paths P1 and P2 . (c) Channel B with diffusion paths P3	143

8.7	Relative energies of B_3C_2 structure models in space group $P6/mmm$, $P6/m$, $P\bar{6}2m$ and $P\bar{6}m2$	144
8.6	(a) Relative energies of P1 . (b) Relative energies of P2 . (c) Relative energies of P3a . (d) Relative energies of P3b . (e) Relative energies of P4 . (f) Relative energies of P5	148
9.1	Structure of Li_3TrP_2 ($Tr = Al, Ga$). P, Tr and Li atoms are shown in pink, orange and red, respectively. Tetrahedra are shown in transparent orange. (a) View along c -axis. Layers of tetrahedra are visible. Li are only shown in the unit cell represented by thin black lines. (b) View along b -axis. Top view of layer showing corner and edge-connection. Li are not shown.	152
9.2	Density of states and band structure of (a) Li_3AlP_2 exhibiting a direct band gap of 3.1 eV and (b) Li_3GaP_2 exhibiting a direct band gap of 2.8 eV. The Fermi level is located at 0 eV.	154
9.3	Structure of Na_7TaP_4 . P, Ta and Li atoms are shown in pink, light grey and red, respectively. Tetrahedra are shown in transparent grey.	157
9.4	Density of states and band structure of Na_7TaP_4 exhibiting a almost direct band gap of 2.9 eV. The Fermi level is located at 0 eV.	158
9.5	Experimental (black) and calculated (red) Raman spectrum for Na_7TaP_4	159
9.6	(a) Structure of $KBi \cdot NH_3$. (b) Structure of KBi along a axis. (c) Structure of KBi along b axis. Bi, K, N and H atoms are shown in ruby, red, blue and white, respectively.	161
9.7	Band projected electron density of the energetically highest band located below the Fermi level of $KBi \cdot NH_3$ showing a p_z orbital type character. Bi is shown as blue spheres, the electron density with isovalue 0.006 is shown in red.	162
9.8	Density of States (DOS) and band structure in the energy range of 2 to 3 eV (0 eV is set for the Fermi level and marked by a horizontal line) based on the PBE0 functional. (a) DOS of KBi , atom projection is shown in red for Bi and blue for K. (b) DOS of $KBi \cdot NH_3$. Atom projection is shown in red for Bi, blue for K, and green for NH_3 . (c) Band structure of $KBi \cdot NH_3$. The path $\Gamma \rightarrow A$ corresponds to the a direction along the Bi chain, the paths $\Gamma \rightarrow Y$ and $Y \rightarrow L$ to the b and c direction, respectively.	163

9.9	Molecular orbital diagram of $[\text{SnBi}_3]^{5-}$. The energy levels of the molecular orbitals of the π -system are marked by an ellipse and all Sn-Bi bonding-orbitals by rectangle. All highlighted molecular orbitals are shown on the right-hand side. Bi blue and Sn red spheres. The iso-value of the wave function is set to 0.04 a.u. for all orbitals.	166
9.10	(a) 3D ELF isosurface (ELF = 0.6). The Bi atoms are blue and Sn atoms red. (b) ELF cross-section perpendicular to the Sn-Bi bond vector through the bond critical point. The elliptical shape indicates an intermediate between single and double bond as expected for a delocalized π -system. The increment of the ELF outlines is decreasing from ELF = 0.6 (inner line) with increment 0.1.	167
9.11	Resonance structures of the carbonate-like $[\text{SnBi}_3]^{5-}$	167
10.1	Molecular orbital interaction diagram of $[\text{Co@Ge}_9]^{5-}$ in fragments of Co^- and $[\text{Ge}_9]^{4-}$ (D_{3h} symmetry) and of $[\text{Ru@Sn}_9]^{6-}$ in fragments of Ru^{2-} and $[\text{Sn}_9]^{4-}$ (D_{3h} symmetry). Important contributions are indicated by dashed lines of both molecular orbital interaction diagrams. Relevant molecular orbitals of $[\text{Co@Ge}_9]^{5-}$ and $[\text{Ru@Sn}_9]^{6-}$ with iso-values 0.025 and 0.02, respectively. Each orbital shows a specific shape of D, F, and G orbital type.	179
10.2	The Raman spectrum of the precursor $\text{K}_5\text{Co}_{1.2}\text{Ge}_9$ (black lines) and the calculated Raman spectrum of $[\text{Co@Ge}_9]^{5-}$ (red lines); the enlarged section shows the resonances of the vibration modes "A" and "B".	181
10.3	Color-filled maps of ELF representations and corresponding Lewis structures of zwitterion $[(\text{Ge}_9(\text{Si}(\text{TMS})_3)_2)^t\text{Bu}_2\text{P}]\text{Cu}(\text{NHC}^{\text{DiPP}})$ and $[(^t\text{Bu}_3\text{PCu}(\text{NHC}^{\text{DiPP}}))]^+$ below, respectively. ELF through the plane of Ge, P, and Cu atoms of $[(\text{Ge}_9(\text{Si}(\text{TMS})_3)_2)^t\text{Bu}_2\text{P}]\text{Cu}(\text{NHC}^{\text{DiPP}})$ as indicated by gray atoms below. ELF of $[(^t\text{Bu}_3\text{PCu}(\text{NHC}^{\text{DiPP}}))]^+$ through the plane of C, P, and Cu atoms as indicated by gray atoms below.	184
10.4	Structure of $[\text{Si}_2\text{Ge}_7(\text{Si}(\text{SiH}_3)_3)_3]^-$	185
10.5	Measured and calculated Raman spectra ($\lambda = 532$ nm for $[(\text{Si}/\text{Ge})_9\{\text{Si}(\text{TMS})_3\}_3]^-$ and $[\text{Si}_2\text{Ge}_7(\text{Si}(\text{SiH}_3)_3)_3]^-$, respectively.	186
10.6	(a) Representation of the HOMO of $[\text{Ge}_4\text{Zn}(\text{Ph})_2]^{4-}$; (b) HOMO-2 of $[\text{Ge}_4\text{HZn}(\text{Ph})_2]^{3-}$; (c) resonance structure between the deprotonated $[[\text{Ge}_4\text{Zn}(\text{Ph})_2]^{4-}$ and a 3c-2e Ge-H-Ge bond.	188

13.2	Unit cell of the $\text{Li}_{14}\text{Ni}_{8.25}\text{Ge}_{8.75}$ structural model (symmetry decreased to $Pm\bar{3}m$), Lithium atoms omitted for clarity. The blue polyhedra show the cluster unit with Ge located at the center and the green polyhedra shows the cluster unit with Ni located at the center. Ni and Ge are represented as spheres in green and blue, respectively. . . .	208
13.1	Coordination polyhedra of (a) - (b) Ge atoms (c) - (d) Ni containing atomic positions and (e) - (f) Li atoms. Li, Ni, Ni/Ge and Ge positions are shown as ellipsoids at the 90 % probability level in red, green, teal and blue respectively. Covalent bonds are marked with thick lines. Thin lines represent the coordination of Li atoms.	209
13.3	Density of States (DOS, left) and band structure (right) of $\text{Li}_{14}\text{Ni}_9\text{Ge}_8$. The Fermi level is at zero energy.	212
13.4	Density of States (DOS, left) and band structure (right) of $\text{Li}_{14}\text{Ni}_8\text{Ge}_9$. The Fermi level is at zero energy.	213
13.5	Density of States (DOS, left) and band structure (right) of $\text{Li}_{14}\text{Ni}_8\text{Ge}_8$. The Fermi level is at zero energy.	213
13.6	Density of States (DOS, left) and band structure (right) of $\text{Li}_{14}\text{Ni}_{8.25}\text{Ge}_{8.75}$. The Fermi level is at zero energy.	214
13.7	Density of States (DOS, left) and band structure (right) of $\text{Li}_{14}\text{Ni}_{8.75}\text{Ge}_8$. The Fermi level is at zero energy.	214
13.8	Density of States (DOS, left) and band structure (right) of $\text{Li}_{14}\text{Zn}_8\text{Ge}_9$. The Fermi level is at zero energy.	215
13.9	(a) Excerpt of the Li-rich Li-Ge phase diagram based on DSC investigations by Fässler <i>et al.</i> . The graph was taken from the publication of M. Zeilinger. ^[1] (b) Phase diagram of the Li-Ag system. The graph was taken from the publication of H. Okamoto. ^[2]	223
13.10	Phase diagram of the Li-Ag system without Ag_4Ge due to not reliable data. The graph was taken from the publication of R.W. Olesinski and G. J. Abbaschlan. ^[3]	224
13.11	Band structure an density of states of Tet1	226
13.12	Band structure an density of states of Tet3	226
13.13	Band structure an density of states of Tet4	227
13.14	Band structure an density of states of Tri1	227
13.15	Band structure an density of states of Tri2	228
13.16	Structure of Cub1	232
13.17	Structure of Tet1	232
13.18	(a) Structure of Tet2 . (b) Structure of Tet3	233
13.19	(a) Structure of Tet4 . (b) Structure of Tet5	233
13.20	(a) Structure of Tri1 . (b) Structure of Tri2 . (c) Structure of Tri3 .	234

13.21	Phase diagram of the Li-Si system at Li at.-% above 75 %	235
13.22	Structure of $\text{Li}_6\text{B}_{18}(\text{Li}_3\text{N})$. The three B_6 units for the Raman mode are labeled by 1, 2 and 3.	236
13.23	Raman mode $1A_{1g}$ for the three B_6 units 1, 2 and 3.	237
13.24	Raman mode $1E_{2g}$ for the three B_6 units 1, 2 and 3.	237
13.25	Raman mode $2A_{1g}$ for the three B_6 units 1, 2 and 3.	237
13.26	Raman mode $2E_{2g}$ for the three B_6 units 1, 2 and 3.	238
13.27	Raman mode $3E_{2g}$ for the three B_6 units 1, 2 and 3.	238
13.28	Raman mode $1E_{1g}$ for the three B_6 units 1, 2 and 3.	239
13.29	Raman mode $1E_{1g}$ for the three B_6 units 1, 2 and 3.	239
13.30	Raman mode $4E_{2g}$ for the three B_6 units 1, 2 and 3.	240
13.31	Raman mode $3A_{1g}$ for the three B_6 units 1, 2 and 3.	240
13.32	Brillouin zone for $\text{Li}_6\text{B}_{18}(\text{Li}_3\text{N})$ in $P6/mmm$ and related hexagonal space groups, showing symmetry points in the k space with respect to the reciprocal conventional vectors. $\Gamma - M - K - \Gamma - A - L - H - A $ $L - M K - H$ was used as path for the band structure. ^[4]	241
13.33	Atom-projected DOS of $\text{Li}_6\text{B}_{18}(\text{Li}_3\text{N})$. Only the Li atoms in large pores contribute to the states next to the Fermi level.	241
13.34	Band structures of of Li_6B_{18} in $P\bar{6}2m$ (left), $P6_3/mmc$ (middle), and $P\bar{6}m2$ (right).	242
13.35	Structures of of Li_6B_{18} in $P\bar{6}2m$ (left), $P6_3/mmc$ (middle), and $P\bar{6}m2$ (right). ^[5]	242
13.36	Relative energies of Li diffusion path in Li_3N	245
13.37	Structure models of B_4C_2	245
13.38	Band structure of $P6/m\text{-B}_4\text{C}_2$	246
13.39	Band structure of $P\bar{6}m2\text{-B}_4\text{C}_2$	246
13.40	Band structure of $P6/mmm\text{-B}_4\text{C}_2$	247
13.41	Band structure of $P\bar{6}2m\text{-B}_4\text{C}_2$	247
13.42	Orbital projected DOS and band structure of $\text{KBi}\cdot\text{NH}_3$ showing a major precipitation of Bi p orbitals at the fermi level.	258
13.43	Orbital projected DOS and band structure of $\text{KBi}\cdot\text{NH}_3$ showing a major precipitation of Bi p_z orbitals at the fermi level.	258
13.44	Molecular orbital diagram of $[\text{CO}_3]^{2-}$. Bonding orbitals are marked by a rectangle and shown on the right side. The C atoms are shown in black and O atoms in red, respectively. The isovalue is set to 0.4 for all orbitals.	259
13.45	Molecular orbital $HOMO-3$ of $[\text{SnBi}_3]^{5-}$. The Bi atoms are shown in blue and Sn atoms in red, respectively. The isovalue is 0.04.	260

13.46	Molecular orbital <i>HOMO-4</i> of $[\text{SnBi}_3]^{5-}$. The Bi atoms are shown in blue and Sn atoms in red, respectively. The isovalue is 0.04.	260
13.47	Molecular orbital <i>HOMO-8</i> of $[\text{SnBi}_3]^{5-}$. The Bi atoms are shown in blue and Sn atoms in red, respectively. The isovalue is 0.04.	261
13.48	Molecular orbital <i>HOMO-9</i> of $[\text{SnBi}_3]^{5-}$. The Bi atoms are shown in blue and Sn atoms in red, respectively. The isovalue is 0.04.	261
13.49	Molecular orbital <i>HOMO-10</i> of $[\text{SnBi}_3]^{5-}$. The Bi atoms are shown in blue and Sn atoms in red, respectively. The isovalue is 0.04.	262
13.50	IBOs concerning the central atom of $[\text{Co@Ge}_9]^{5-}$. Co and Ge is shown in blue and light green, respectively.	265
13.51	IBOs concerning the central atom of $[\text{Ru@Sn}_9]^{6-}$. Ru and Sn is shown in green and orange, respectively.	266

List of Tables

2.1	Name, formula, shape, supplier and purity of starting materials	17
2.2	Compound, weighted materials, ampule material, kind of reaction tube and temperature program for all furnace syntheses	22
2.3	Experimental Contributions of other people for this thesis	23
4.1	Shrink usually used according to lattice constant a , b or c of primitive cell	39
5.1	All known binary and ternary compounds in the Li-Ni-Ge phase diagram	51
5.2	Non-centered rhombic dodecahedral clusters with $M = \text{Ni}$, their valence electron counts (CVE) and interatomic distances in the rhombic dodecahedra	54
5.3	Centered rhombic dodecahedral clusters with $M = \text{Ni}$, their valence electron counts (CVE) and interatomic distances in the rhombic dodecahedra	54
5.4	Masses and molar masses of the used chemicals, Mass loss by arc-welding was neglected	55
5.5	Crystal data and structure refinement	56
5.6	Atomic coordinates and equivalent isotropic displacement parameters for $\text{Li}_{14}\text{Ni}_{8.3}\text{Ge}_{8.7}$	56
5.7	All structure models for quantum chemical calculations with element at $X2$ position and deviation of distances between atoms with respect to experimental data. Position $X2$ is shown in Figure 5.8. The detailed structure comparison values and structure parameters are given in Tables 13.3-13.10	64
5.8	Summarized description of IBOs of structures G and H . All relevant IBOs are shown in the appendix (Table 13.14 and 13.15)	67
5.9	Masses and molar masses of the used chemicals	68
5.10	Single crystal data and structure refinement	69
5.11	Atomic coordinates and equivalent isotropic displacement parameters for $\text{LiNi}_{1.17}\text{Ge}$	70

5.12	Cell parameter a and b for $\text{LiNi}_{1.5}\text{Ge}$ (Ni at the central position), $\text{LiNiGe}_{1.5}$ (Ge at the central position) and LiNiGe (no central position), as well as, experimental data are shown in Å and as deviation (Δd) from experimental data in percentages	76
6.1	All known binary and ternary compounds in the Li-Ag-Ge phase diagram	83
6.2	Overview of all synthesized compounds and structure models	87
6.3	Masses and molar masses of the used chemicals for $\beta\text{-Li}_2\text{Ag}_{0.8}\text{Ge}_{1.2}$	88
6.4	Single crystal data and structure refinement of $\beta\text{-Li}_2\text{Ag}_{0.8}\text{Ge}_{1.2}$	89
6.5	Atomic coordinates and equivalent isotropic displacement parameters of $\beta\text{-Li}_2\text{Ag}_{0.8}\text{Ge}_{1.2}$	89
6.6	RIETVELD structure refinement details of $\beta\text{-Li}_2\text{Ag}_{0.8}\text{Ge}_{1.2}$ from P-XRD measurements at room temperature	90
6.7	Examples for structures derived from a ABCD-structure with given A , B , C and D occupation, assigned phase-type and reference	93
6.8	Interatomic distances for Ag-Ag, Ge-Ge and Ag-Ge of various compounds	94
6.9	Masses and molar masses of the used chemicals for $\alpha\text{-Li}_2\text{Ag}_{0.8}\text{Ge}_{1.2}$	98
6.10	RIETVELD structure refinement details of $\alpha\text{-Li}_2\text{Ag}_{0.8}\text{Ge}_{1.2}$ from P-XRD measurements at room temperature	99
6.11	Atomic coordinates and equivalent isotropic displacement parameters of $\alpha\text{-Li}_2\text{Ag}_{0.8}\text{Ge}_{1.2}$	99
6.12	Single crystal data and structure refinement of $\gamma\text{-Li}_{2.53}\text{AgGe}_2$	104
6.13	Atomic coordinates and equivalent isotropic displacement parameters of $\gamma\text{-Li}_{2.53}\text{AgGe}_2$	105
6.14	Possible atom distribution of Ag and Ge due to the coloring problem	106
6.15	Possible atom distribution of Ag and Ge due to the coloring problem of structure $\alpha\text{-Li}_2\text{AgGe}$	109
6.16	Ag:Ge ratio, average temperature of first and second phase transition, and melting point of 3-5	111
6.17	Model for computational analysis and their associated structure, as well as, deviations of cell parameters and interatomic distances from experimental data	115
6.18	Example compounds with network subunit, missing electron count to achieve isovalent structure to $\alpha\text{-Ge}$ and phase type	116
6.19	Average HIRSHFELD charges for selected models	117
6.20	Trend of number of bonds for Ag-Ge, Ag-Ag and Ge-Ge bonds with bond length and MULLIKEN overlap populations for Tet2-3	119

6.21	Trend of number of bonds for Ag-Ge, Ag-Ag and Ge-Ge bonds with bond length and MULLIKEN overlap populations for Tri1-3	119
7.1	All known binary and ternary compounds in the Li-Ag-Si phase diagram	129
7.2	Single crystal data and structure refinement of β -Li ₁₃ Ag ₆ Si ₆	131
7.3	Atomic coordinates and equivalent isotropic displacement parameters of β -Li ₁₃ Ag ₆ Si ₆	131
7.4	Interatomic distances of selected compound	132
8.1	Structure data of Li ₆ B ₁₈ (Li ₃ N) _x from P-XRD experiments	138
8.2	Atomic coordinates of Li ₆ B ₁₈ (Li ₃ N) _x from P-XRD experiments	138
8.3	Atomic distances <i>d</i> and cell parameters <i>a</i> , and <i>c</i> for Li ₆ B ₁₈ (Li ₃ N), as well as, deviation Δd from experimental data in percentages	140
8.4	Li removal energies for Li1-3	142
9.1	Structure data of Li ₃ AlP ₂ and Li ₃ GaP ₂	151
9.2	Atomic coordinates of Li ₃ AlP ₂ and Li ₃ GaP ₂	152
9.3	Atomic distances <i>d</i> and cell parameters <i>a</i> , <i>b</i> and <i>c</i> for Li ₃ AlP ₂ and Li ₃ GaP ₂ , as well as, deviation Δd from experimental data in percentages	153
9.4	Structure data of Na ₇ TaP ₄ from SC-XRD experiments	155
9.5	Atomic coordinates of Na ₇ TaP ₄ from SC-XRD experiments	156
9.6	Atomic distances <i>d</i> and cell parameters <i>a</i> , <i>b</i> , <i>c</i> and β for Na ₇ TaP ₄ , as well as, deviation Δd from experimental data in percentages	157
9.7	Wavenumbers of the calculated and observed main vibration modes of the raman spectrum of Na ₇ TaP ₄ . Additionally, associated assignment of the vibrational modes of the TaP ₄ tetrahedra. All intensities are given in relative intensities a. u.	159
9.8	Structure data of KBi·NH ₃ from SC-XRD experiments	160
9.9	Atomic coordinates of KBi·NH ₃ from SC-XRD experiments	161
9.10	Atomic distances <i>d</i> and cell parameters <i>a</i> , <i>b</i> and <i>c</i> for KBi·NH ₃ and KBi, as well as, deviation Δd from experimental data in percentages	162
9.11	Structure data of K ₅ [SnBi ₃]·9NH ₃ and K ₉ [K ₁₈ -corwn-6][[SnBi ₃] ₂ ·15NH ₃ from SC-XRD experiments	164
9.12	Optimized parameters for XY ³ⁿ⁻ with X = Sn, C and Y = Bi, O	165
10.1	Overview of known endohedral clusters of the type [TM@E ₉] ⁿ⁻	173
10.2	Structure data of K ₆ [CoGe ₉](OH)·16NH ₃ and [K ₇ (OH)]RuSn ₉ ·10NH ₃ from SC-XRD experiments	174

10.3	Comparison of observed and optimized parameters of $[\text{Ge}_9]^{4-}$ and $[\text{Co}@\text{Ge}_9]^{5-}$. The structures with D_{3h} symmetry are taken from the optimized structures of the filled clusters.	176
10.4	Comparison of observed and optimized parameters of $[\text{Sn}_9]^{4-}$ and $[\text{Ru}@\text{Sn}_9]^{6-}$. The structures with D_{3h} symmetry are taken from the optimized structures of the filled clusters.	177
10.5	Hirshfeld, natural, and Mulliken charges of $[\text{Co}@\text{Ge}_9]^{5-}$ and $[\text{Ru}@\text{Sn}_9]^{6-}$	177
10.6	Main signals and characteristic modes of endohedral cluster $TM@Tt_9$ ($TM = \text{Ni}, \text{Rh}, \text{Pd}; Tt = \text{Ge}, \text{Sn}$). Raman shifts of the $[\text{Pd}@\text{Sn}_9]^{4-}$ cluster are treated with a scale factor of 1.04	181
10.7	Structure data of $[(\text{Ge}_9(\text{Si}(\text{TMS})_3)_2)^t\text{Bu}_2\text{P}]\text{Cu}(\text{NHC}^{\text{Dipp}})$ from SC-XRD experiments	182
10.8	Selected charges from Hirshfeld and Natural Population Analysis for $[(\text{Ge}_9(\text{Si}(\text{TMS})_3)_2)^t\text{Bu}_2\text{P}]\text{Cu}(\text{NHC}^{\text{Dipp}})$ and $[^t\text{Bu}_3\text{PCu}(\text{NHC}^{\text{Dipp}})]^+$. . .	183
10.9	Structure data of $\text{K}(2.2.2\text{-crypt})[(\text{Si}_{1.68}\text{Ge}_{7.32})(\text{Si}(\text{TMS})_3)_3]$ from SC-XRD experiments	185
10.10	Structure data of $[\text{K}([18\text{ crown-6}])][\text{Rb}([18\text{ crown-6}])]_2[\text{HG}_{\text{e}_4}\text{ZnPh}_2]\cdot\text{NH}_3$ from SC-XRD experiments	187
13.1	Atomic coordinates and equivalent isotropic displacement parameters for $\text{Li}_{14}\text{Ni}_{8.3}\text{Ge}_{8.7}$	203
13.2	Interatomic distances for $\text{Li}_{14}\text{Ni}_{8.3}\text{Ge}_{8.7}$	203
13.3	Optimized parameters of $\text{Li}_{14}\text{Ni}_8\text{Ge}_9$ (A) with $a = 11.67939218 \text{ \AA}$. .	205
13.4	Optimized parameters of $\text{Li}_{14}\text{Ni}_9\text{Ge}_8$ (B) with $a = 11.68067171 \text{ \AA}$. .	206
13.5	Optimized parameters of $\text{Li}_{14}\text{Ni}_{8.25}\text{Ge}_{8.75}$ (C) with $a = 11.68100660 \text{ \AA}$	206
13.6	Optimized parameters of $\text{Li}_{14}\text{Ni}_8\text{Ge}_8$ (D) with $a = 11.66728744 \text{ \AA}$. .	206
13.7	Optimized parameters of $\text{Li}_{14}\text{Ni}_{8.75}\text{Ge}_8$ (E) with $a = 11.67743928 \text{ \AA}$.	207
13.8	Optimized parameters of $\text{Li}_{14}\text{Zn}_8\text{Ge}_9$ (F) with $a = 12.44436295 \text{ \AA}$. .	207
13.9	Atomic distances (d) and cell parameter a for $\text{Li}_{14}\text{Ni}_8\text{Ge}_9$ (Ge at $X2$), $\text{Li}_{14}\text{Ni}_9\text{Ge}_8$ (Ni at $X2$) and $\text{Li}_{14}\text{Ni}_8\text{Ge}_8$ (empty $X2$), as well as, experimental data are shown in \AA and as deviation (Δd) from experimental data in percentages	210
13.10	Atomic distances (d) and cell parameter a for $\text{Li}_{14}\text{Ni}_{8.25}\text{Ge}_{8.75}$ and $\text{Li}_{14}\text{Ni}_{8.75}\text{Ge}_8$. One has to distinguish the different polyhedra in the structures, if Ni, Ge or no atom is located at the $X2$ position. For this reason there are two distances listed for each case related to which atom is located at the center of the Ni-cube. The data is shown in \AA and as deviation (Δd) from experimental data in percentages . . .	211

13.11 Mulliken partial charges (e^-) of $\text{Li}_{14}\text{Ni}_8\text{Ge}_9$, $\text{Li}_{14}\text{Ni}_9\text{Ge}_8$, $\text{Li}_{14}\text{Ni}_8\text{Ge}_8$ and $\text{Li}_{14}\text{Zn}_8\text{Ge}_9$	212
13.12 Mulliken bond overlaps (e^-) of $\text{Li}_{14}\text{Ni}_8\text{Ge}_9$, $\text{Li}_{14}\text{Ni}_9\text{Ge}_8$, $\text{Li}_{14}\text{Ni}_8\text{Ge}_8$ and $\text{Li}_{14}\text{Zn}_8\text{Ge}_9$	212
13.13 Atomic distances (d) for G and H as well as, experimental data are shown in Å and as deviation (Δd) from experimental data in percentages	215
13.14 Relevant IBOs with atom contribution of $[\text{Ge}@Ni_8\text{Ge}_6]^{6-}$. Ge and Ni is colored blue and green, respectively.	216
13.15 Relevant IBOs with atom contribution of $[\text{Ni}@Ni_8\text{Ge}_6]^{6-}$. Ge and Ni is colored blue and green, respectively.	218
13.16 Atomic coordinates and equivalent isotropic displacement parameters for $\text{LiNi}_{1+x}\text{Ge}$	220
13.17 Interatomic distances for $\text{Li}_{14}\text{Ni}_{8.3}\text{Ge}_{8.7}$	220
13.18 Atomic coordinates and isotropic displacement parameters for $\beta\text{-Li}_2\text{Ag}_{0.8}\text{Ge}_{1.2}$	224
13.19 Interatomic distances for $\beta\text{-Li}_2\text{Ag}_{0.8}\text{Ge}_{1.2}$	225
13.20 Atomic coordinates and isotropic displacement parameters for $\gamma\text{-Li}_{2.53}\text{AgGe}_2$	225
13.21 Interatomic distances for $\gamma\text{-Li}_{2.53}\text{AgGe}_2$	225
13.22 Atom positions of optimized structure Cub1 with $a = 6.28598257$ Å	228
13.23 Atom positions of optimized structure Tet1 with $a = 4.42896886$ Å and $b = 6.27645206$ Å	228
13.24 Atom positions of optimized structure Tet2 ($a = 4.48666292$ Å and $b = 30.60807151$ Å) and Tet3 ($a = 4.55062470$ Å and $b = 30.48655642$ Å)	229
13.25 Atom positions of optimized structure Tet4 ($a = 9.90727791$ Å and $b = 18.66196260$ Å) and Tet5 ($a = 9.84999635$ Å and $b = 18.56971458$ Å)	230
13.26 Atom positions of optimized structure Tri1 ($a = 4.57992683$ Å and $b = 43.98534009$ Å), Tri2 ($a = 4.45524956$ Å and $b = 43.33687075$ Å) and Tri3 ($a = 4.47047618$ Å and $b = 42.85285361$ Å)	231
13.27 Atomic coordinates and isotropic displacement parameters for $\beta\text{-Li}_{13}\text{Ag}_5\text{Si}_6$	235
13.28 Interatomic distances for $\beta\text{-Li}_{13}\text{Ag}_5\text{Si}_6$	236
13.29 Atom positions of optimized structure $\text{Li}_6\text{B}_{18}(\text{Li}_3\text{N})$ with $a = 8.2164$ Å and $b = 4.1093$ Å	242
13.30 Atom positions of optimized structure Li_6B_{18} in $P\bar{6}2m$ with $a = 8.270$ Å and $b = 4.1832$ Å	243
13.31 Atom positions of optimized structure Li_6B_{18} in $P6_3/mmc$ with $a = 8.2709$ Å and $b = 8.3664$ Å	243
13.32 Atom positions of optimized structure Li_6B_{18} in $P\bar{6}m2$ with $a = 8.2709$ Å and $b = 4.1832$ Å	243
13.33 Atom positions of optimized structure B_4C_2 in $P6/mmm$ with $a = \text{XXXX}$ Å and $b = \text{XXX}$ Å	243

13.34	Atom positions of optimized structure B_4C_2 in $P6/m$ with $a = 7.53777332 \text{ \AA}$ and $b = 4.09640289 \text{ \AA}$	244
13.35	Atom positions of optimized structure B_4C_2 in $P\bar{6}m2$ with $a = 7.57828533 \text{ \AA}$ and $b = 4.11149348 \text{ \AA}$	244
13.36	Atom positions of optimized structure B_4C_2 in $P\bar{6}2m$ with $a = XXXX \text{ \AA}$ and $b = XXX \text{ \AA}$	244
13.39	Frequencies of Li_3AlP_2 and Li_3GaP_2 from frequencies analysis at Γ -point	247
13.40	Atomic coordinates of optimized Na_7TaP_4	250
13.41	Symmetry k-points for orthorhombic lattice for compounds Na_7TaP_4 . Brillouin zone path Γ -Y-C-E-A-X Z-D-Y is derived from the paths of Curtarolo et al. ^[4]	250
13.37	Atomic coordinates of optimized Li_3AlP_2 and Li_3GaP_2	251
13.38	Symmetry k-points for orthorhombic lattice for compounds Li_3AlP_2 and Li_3GaP_2 . Brillouin zone path Γ -S-Y-Z- Γ -Y-T-Z is derived from the paths of Curtarolo et al. ^[4]	251
13.42	Frequencies of Na_7TaP_4 from frequencies analysis at Γ -point	251
13.43	Atomic coordinates of optimized $KBi \cdot NH_3$ (DFT-PBE0/TZVP)	254
13.44	Atomic coordinates of optimized $KBi \cdot NH_3$ (DFT-PBEXC/TZVP). Atomic parameters are $a = 5.26408108 \text{ \AA}$, $b = 15.88009753 \text{ \AA}$, $c = 5.33503938 \text{ \AA}$ and $\beta = 87.776869^\circ$	254
13.47	Symmetry k-points for orthorhombic lattice for compounds $KBi \cdot NH_3$	254
13.45	Atomic coordinates of optimized KBi (DFT-PBE0/TZVP). Atomic parameters are $a = 14.07124071 \text{ \AA}$, $b = 7.30134576 \text{ \AA}$, $c = 13.39905252 \text{ \AA}$ and $\beta = 112.150986^\circ$	255
13.46	Atomic coordinates of optimized KBi (DFT-PBEXC/TZVP). Atomic parameters are $a = 14.0352994 \text{ \AA}$, $b = 7.42247064 \text{ \AA}$, $c = 13.40923965 \text{ \AA}$ and $\beta = 111.682852^\circ$	255
13.48	Frequencies of $KBi \cdot NH_3$ from frequencies analysis at Γ -point (DFT-PBE0/TZVP)	255
13.49	Frequencies of KBi from frequencies analysis at Γ -point (DFT-PBE0/TZVP)	256
13.50	Calculated Paboon and NPA charges for $[SnBi_3]^{5-}$ and $[CO_3]^{2-}$	262
13.51	Structural data of optimized cluster $[Co@Ge_9]^{5-}$	263
13.52	Structural data of optimized cluster $[Ru@Sn_9]^{6-}$	263
13.53	Structural data of optimized cluster $[Ge_9]^{4-}$ (C_{4v})	264
13.54	Structural data of optimized cluster $[Ge_9]^{4-}$ (D_{3h})	264
13.55	Structural data of optimized cluster $[Sn_9]^{4-}$ (C_{4v})	264
13.56	Structural data of optimized cluster $[Sn_9]^{4-}$ (D_{3h})	265

13.57	Atom contribution for IBOs per 2 electrons and in percentage for	
	$[\text{Co@Ge}_9]^{5-}$	266
13.58	Atom contribution for IBOs per 2 electrons and in percentage for	
	$[\text{Ru@Sn}_9]^{6-}$	267
13.59	Calculated Raman intensities for $[\text{Co@Ge}_9]^{5-}$	268
13.60	Calculated Raman intensities for $[\text{Ge}_9]^{4-}$	269
13.61	Calculated Raman intensities for $[\text{Ru@Sn}_9]^{6-}$	270
13.62	Calculated Raman intensities for $[\text{Sn}_9]^{4-}$	270